Improving High-speed Electrical Machines by Amorphous Metals

zur Erlangung des akademischen Grades eines

DOKTOR-INGENIEURS

von der KIT-Fakultät für
Elektrotechnik und Informationstechnik
des Karlsruher Instituts für Technologie (KIT)
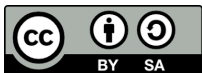
genehmigte

DISSERTATION

von

M.Eng. Jing Ou

geb. in: Guangdong, China

Tag der mündlichen Prüfung: 06.12.2019
Hauptreferent: Prof. Dr.-Ing. Martin Doppelbauer
Korreferent: Prof. Dr. Dianguo Xu
(Harbin Institute of Technology, China)

Preface

This dissertation was written at the Institute for Electrical Engineering (ETI) at Karlruhe Institute of Technology (KIT) and it could not have been finished without the help of my supervisor and colleagues.

I would like to thank my supervisor Prof. Dr.-Ing Martin Doppelbauer, who provided me with the opportunity to pursue my PhD in Karlsruhe Institute of Technology and provided me continuous support. His advice and insight have helped me to reach a higher research level. I highly appreciated the constructive feedback and helpful guidance given by Prof. Doppelbauer. In order to ensure the scientific quality of my work, Prof. Doppelbauer also encouraged me to participate in international conferences, which benefit me a lot.

I would like to thank my second referee, Prof. Dr. Dianguo Xu from Harbin Institute of Technology, China, for his scientific input and linguistic improvements, which helped a great deal to finish the final version of this dissertation.

Special thanks go to my colleagues for their help in the dissertation work. During the motor design phase, Patrick Breining helped me in measuring the electromagnetic properties of the materials and my wife Yingzhen Liu helped me in measuring the mechanical strength of the materials. Markus Schiefer helped me in building the prototypes and the testbench. Marc Veigel helped me in implementating the PWM inverters and the control strategy. Dominik Krahe, Hongfei Lu and my wife offered me helpful suggestions on the structure of the dissertation and English language as well. Their outstanding, technical supports greatly speeded up the whole work. Kim Oebel, Rouven Burgert, Andreas Maier, Helmut Strumberger, Bernhard Saschin provided me many help in building the prototypes and the testbench. Andreas Wolf and Alexander Stahl provided me help in the measurement of the prototype. Thanks also goes to Markus Schiefer, Jan Richter, Mario Greule, Bo Zhang and Patrick Winzer for their suggestions in determining my research topic. I finally followed the idea provided by Markus Schiefer to use the amorphous magnetic material for a high-speed interior permanent-magnet rotor and he provided me a primary structure of this rotor. My thanks will also go for the entire ETI employees for many on- and off-topic discussions, social activities, which have always been a recreating highlight during a busy week. I would also like to thank Klaus-Peter Becker for his help in life.

Finally, I would like to express my sincere gratitude to my mother, my brothers and sisters, my lovely wife and my little baby Pinyi Ou. I would never have made it so far if I did not have that much support of my family, to whom I shall ever be indebted.

06.12.2019 Karlsruhe, Jing Ou

Kurzfassung

Diese Dissertation wurde am Elektrotechnischen Institut (ETI) des Karlsruher Instituts für Technologie (KIT) verfasst und könnte ohne Hilfe von meinem Doktorvater und meinen Kollegen nicht zum Schluss kommen.

Ich würde mich bei meinem Doktorvater Prof. Dr.-Ing Martin Doppelbauer bedanken, der mir die Möglichkeit zur Promotion am Karlsruher Institut für Technologie gegeben und mich kontinuierlich unterstützt hat. Seine Vorschläge und Einblicke haben mich auf ein höheres Niveau der akademischen Forschung gebracht. Über die konstruktiven Feedbacks und die hilfreichen Beratungen von Prof. Doppelbauer bin ich sehr dankbar. Um die wissenschaftliche Qualität meiner Ausarbeitung zu garantieren, hat mich Prof. Doppelbauer auch ermuntert, an internationalen Konferenzen teilzunehmen, von denen ich viel profitierte.

Ich möchte mich auch bei meinem Korreferenten, Prof. Dr. Dianguo Xu vom Harbin Institut für Technologie, China, für seine wissenschaftlichen Beiträge und sprachliche Verbesserung zu dieser Dissertation bedanken, die in besonderem Maße zur Fertigstellung endgültiger Fassung dieser Dissertation beigetragen haben.

Spezieller Dank zu meinen Kollegen für ihre Hilfe bei der Unterstützung dieser Dissertation. Während des Entwurfs des Motors hat Patrick Breining mir bei der Messung elektromagnetischer Eigenschaften des Materials und meine Frau Yingzhen Liu bei der Messung mechanischer Festigkeit des Materials geholfen. Markus Schiefer half mir beim Aufbau des Prototyps und der Testumgebung. Marc Veigel half mir bei der Implementierung der PWM-Wechselrichters und der Regelungsstrategie. Dominik Krahe, Hongfei Lu und meine Frau haben mir hilfreichen Vorschläge über Struktur dieser Dissertation sowie englische Sprache gegeben. Ihre hervorragende technische Unterstützung hat die gesamte Arbeit erheblich beschleunigt. Kim Öbel, Rouven Burgert, Andreas Maier, Helmut Strumberger, Bernhard Saschin boten mir auch viele Hilfe beim Aufbau des Prototyps und des Prüfstands an. Andreas Wolf und Alexander Stahl boten mir viele Hilfe bei der Messung des Prototyps. Außerdem möchte ich Jan Richter, Mario Greule, Bo Zhang und Patrick Winzer für ihre Vorschläge zur Bestimmung meines Forschungsthemas bedanken. Ich folgte schließlich der Idee von Markus Schiefer, das amorphe magnetische Material für einen Hochgeschwindigkeitsrotor mit vergrabenen Permanentmagneten zu verwenden, und er stellte die erste Auslegung dieses Rotors zur Verfügung. Weiterhin gebührt den gesamten Mitarbeitern des ETIs mein großer Dank für viele themenbezogene Diskussionen und soziale Aktivitäten, die stets eine erholsame Weile in einer arbeitsreichen Woche waren. Ich möchte mich auch bei Klaus-Peter Becker für seine Hilfe im Leben bedanken.

Zum Ende möchte ich meiner Mutter, meinen Geschwistern sowie meiner lieben Frau und meinem kleinen Baby meinen herzlichen Dank aussprechen. Ich könnte es nicht schaffen, was ich heute geschafft habe, ohne so viel Unterstützung von euch, die ich jemals zu Dank verpflichtet sein werde.

06.12.2019 Karlsruhe

Jing Ou

Abstract

This dissertation is about the application of an amorphous magnetic material (AMM) to a sleeve-free interior permanent-magnet (PM) rotor of high-speed synchronous motors. Currently, surface-mounted PM rotors are commonly used in the high-speed motors. In order to protect the high-speed rotors from centrifugal forces, high-strength non-ferromagnetic sleeves are required. This results in a reduced torque density, lowered flux-weakening ability, and highen losses of the motor caused by pulse-width-modulation (PWM) voltage. Hence, a sleeve-free rotor structure is beneficial.

AMM has been used for transformers and inductors for decades. It is well-known due to its low core losses. However, because of its high hardness and brittleness, slotting becomes a key obstacle to its application in electrical machines. Hence, this material has not been widely applied in the electrical machines yet. An important property, the high mechanical strength of the AMM has been ignored eagerly. In this work, an interior PM rotor made from AMM for high-speed operation is studied. The high mechanical strength and the low core losses of the AMM are fully taken use of. Because of the difficulty in slotting of the AMM, this material is not used for the stator and a conventional silicon steel will be used.

In order to fulfill the proposed high-speed rotor, the properties of the AMM in terms of electromagnetics and mechanics are experimentally studied. The influences of the mechanical stress and temperature on the electromagnetic properties of the AMM cores are well studied. Based on the measured data, a prototype is designed and optimized in terms of electromagnetics, mechanics and thermal behaviors. To ensure the success of the prototype, the slotting methods are also investigated and wire electrical discharge machining method is selected for manufacturing of the AMM rotor core. In order to show the advantages and disadvantages of the proposed high-speed AMM rotor, a surface-mounted PM rotor covered by a carbon-fiber sleeve is designed as a comparison. Since the influences of the PWM inverter on the losses of the high-speed motors are significant and this problem has not been thoroughly investigated before, the dissertation goes into a further research on it to fill the gap in this field.

Finally, two prototypes are built and tested. The design results are verified through experiments. It is verified that by applying the AMM to the proposed rotor, the performance of the high-speed PM motor is significantly improved, such as better flux weakening ability, higher torque and power densities and higher efficiency. Based on the tested data of the prototypes, it is confirmed that the AMM has high potential in the application of high-speed high-power-density PM motors.

Abbreviations

AMM	amorphous magnetic material
AR	amorphous rotor
AWJ	abrasive water jet
CFD	computational fluid dynamic
EC	eddy current
FEA	finite element analysis
FEM	finite element method
FESS	flywheel energy storage system
FFT	fast Fourier transform
FPGA	field programmable gate array
FSCW	fractional slot concentrated winding
HSPM	high-speed permanent-magnet
ICE	internal combustion engine
IGBT	insulated gate bipolar transistor
IM	indution motor
IPM	interior permanent-magnet
ISDW	integral slot distributed winding
PM	permanent-magnet
PWM	pulse width modulation
RT	room temperature
SF	stacking factor
SI	silicon iron
SPM	surface-mounted permanent-magnet
SR	silicon steel rotor
SRM	switched reluctance motor
SVPWM	space vector PWM
UTS	ultimate tensile strength
WEDM	wire electrical discharge machining
YASA	yokeless and segmented armature

Index of symbols

A	vector magnetic potential
A_e	effective cross area of the specimen
B	flux density
B_r	radial magnetic flux density component
B_r	remanence of the PM
B_0	the magnetic flux density of the PM on the working point
B_θ	tangential magnetic flux density component
b_0	slot opening width
C	integration constant
C_f	air friction coefficient
D_h	the hydraulic diameter
d	nominal depth of penetration for a conductor
dm	the mass per unit length
E	the modulus of elasticity
$E_{flywheel}$	energy of the flywheel
e	induced voltage
e_{AN}	A phase back-EMF
F_g	geometrical factor
f	the frequency
f_i	natural frquency of the ith mode
H	the magnetic field strength
H_m	thickness of the PM
H_θ	tangential component of the magentic field strength
h	convective heat transfer coefficient
h_{core}	the thickness of the toroidal specimen
h_{sleeve}	the thickness of the carbon fiber sleeve
I	the area moment of inertia
I_{AN}	A phase current
I_u	the amplitude of uth temporal current harmonic
i	current
i_a	a phase current
i_b	b phase current
i_c	c phase current
i_d	d-axis current
i_q	q-axis current
i_1	current of the primary winding

i_2	current of the secondary winding
J	current density
J_a	a phase current density
J_b	b phase current density
J_c	c phase current density
J_e	eddy current density
J_{rotor}	moment of inertia of the rotor
J_s	total current density along stator inner circumference
K_{de}	a factor to modify the conductivity of PMs
K_n	coefficient of the Fourier series of the modulation function
$K_{n,Rx}$	coefficient of the Fourier series of the flux density at the radius Rx
K_t	the stress concentration factor
k	roughness coefficient
k	fluid conductivity
k_{core}	the stacking factor of the toroidal specimen
L	axial length of magnet
L_d	d-axis inductance
L_{fe}	the length of the rotor stack
L_q	q-axis inductance
L_S	phase inductance
l_e	the equivalent length of the magnetic path of toroidal specimen
m	phase number
$\dot{m}_a$	the air mass flow rate
$\dot{m}_f$	the fuel mass flow rate
N	the crankshaft rotational speed
N	the number of turns in one slot
N_s	the slot number of the stator
Nu	Nusselt number
N_1	the number of turns of primary winding
N_2	the number of turns of secondary winding
n_R	the number of crank revolution per power stroke
P	power
P	centrifugal force working on a ring
P_{core}	core losses of the toroidal core
P_e	eddy current loss
P_{engine}	indicated power of the internal combustion engine
$P_{f,air}$	rotor air-friction loss
$P_{f,end}$	air-friction loss on the end surface of the rotor
P_{mag}	eddy current loss of one PM segment
p	pole-pair number

p_{air}	absolute pressure
p_{im}	the intake manifold air pressure
Q_{fuel_LHV}	the mass specific lower heating value of the fuel
R	resistance
Re	Reynolds number
Re_r	tip Reynolds number
Re_δ	Couette-Reynolds number
R_r	outer radius of rotor core
R_S	phase resistance
R_s	inner radius of the stator core
R_{shaft}	radius of shaft
$R_{specific}$	the specific gas constant for dry air
R_1	rotor radius
r_a	the outer radius of the toroidal specimen
r_i	the inner radius of the toroidal specimen
$r\Delta\theta$	width of magnet cell unit in polar coordinate
T	period of PWM
T	sampling time
T	torque
T_a	the absolute air temperare
Ta	Taylor number
T_b	width of the flux bridge
T_C	Celsius temperature
T_K	the absolute (kelvin) temperature
t	time
u_1	voltage of the primary winding
u_2	voltage of the secondary winding
V_{AO}	voltage between A and O points of PWM inverter
V_{AN}	A phase voltage
V_{BO}	voltage between B and O points of PWM inverter
V_{CO}	voltage between C and O points of PWM inverter
V_{DC}	DC-bus voltage
V_e	the engine swept volume
v	the kinematic viscosity of the fluid
v	the order of the spatial harmonics
W_m	width of the PM
α_u	phase angle of uth temporal current harmonic
Δr	thickness of magnet cell unit in polar coordinate
δ	the air-gap length
η_{comb}	the combustion efficiency

η_{th}	the thermal efficiency
η_v	the volumetric efficiency
θ	current leading angle
θ_c	width of slot opening in polar coordinate
θ_t	width of tooth in polar coordinate
θ_0	initial angular position of the rotor
θ_1	start angular position of the rotor magnet segment
θ_2	end angular position of the rotor magnet segment
$\lambda_{d,PM}$	d-axis flux linkage generated by PM
μ	the dynamic viscosity of air
μ_r	the relative magnetic permeability of the conductor
μ_{rpm}	the relative permeability of the PM
μ_0	a physical constant $\mu_0 = 4\pi \times 10^{-7}$ H/m
ρ	the density of the rotor core
ρ	the resistivity of the conductor
ρ_{air}	density of the air
ρ_{im}	the air density in the intake manifold
ρ_0	the air density at the state of 0 °C, 0.1013 MPa and ρ_0=1.293kg/m^3
σ	conductivity of magnets
σ_f	conductivity of magnets at a specific frequency
σ_{max}	maximum stress
Φ_{max}	maximum flux provided by the PM
Φ_{max_rotor}	flux supplied by the rotor to the stator
ψ	flux linkage
ψ_{PM}	flux linkage provided by magnet
Ω	velocity of the fluid
ω	fundamental frequency
ω_e	electrical angular velocity
ω_{max}	maximum angular speed of the fly-wheel rotor
ω_{min}	minimum angular speed of the fly-wheel rotor
ω_{rotor}	angular speed of the rotor

Contents

1   Introduction

1.1   Motivation

With the development of high-energy rare-earth permanent-magnet (PM) materials, the power and torque densities of the PM motors have been increasing. To further increase the power/volume and power/weight ratios of the motors, a good way is to increase the surface velocity of the rotors because the tangential force density of the rotors, which generates rotating torque, is determined by the electrical and magnetic loadings. And these loadings are subjected to the heat dissipation ability of the motors. For example, the maximum speed of the 4th generation of Prius motor P610 was increased from 13,500 /min of the 3rd generation P410 to 17,000 /min in order to reduce the overall volume and weight. The corresponding rotor surface velocity of P610 was increased from about 114 m/s of P410 to 125 m/s. In addition, because advanced winding technology and better cooling method were employed, the new generation was reduced by 20 % in motor loss and 35 % in size while its power density was increased by up to 36 % [1], [2]. It can be expected that by further increasing the angular speed to increase the surface velocity of the rotor, the power of the motor might be further increased and higher power/volume and power/weight of the motors can be achieved. However, higher speed means higher frequency even though the pole-pair number of the rotor is only 1. The iron losses, the copper AC loss and the rotor losses increase significantly when the frequency increases. The electrical and magnetic loadings at a higher speed need to be reduced to avoid the overheated problem. Then the torque/volume ratio of the motors is reduced and consequently the power/volume ratio of the motors cannot be infinitely increased by increasing the angular speed of the rotors. For instance, currently, a speed up to 1,000,000 /min has been reached by Swiss Federal Institute of Technology Zurich (ETH Zurich). However, the power of this motor is low and it is only 100 W [3].

To fulfill a motor with high speed and high power density is faced with many challenges: 1) high centrifugal forces in the high-speed rotor require a structural protection; 2) poor heat dissipation condition of the rotor may cause irreversible demagnetization of the PMs; 3) high core losses at high speed decrease the electric loading of the stator windings in order to limit the total losses of the whole motor; 4) requirement of the rotor stiffness at high speed limits the axial length of the rotor. All these aspects limit the power of the high-speed motors. Hence, a solution to help to increase the speed and the power density of the PM motors is of high importance for the motors' development.

Generally, surface-mounted permanent-magnet (SPM) rotors are often employed in high-speed permanent-magnet (HSPM) motors. The structure of a 2-pole SPM rotor is presented in Fig. 1.1(a). One of the main problems of the SPM structure is that the adhesive forces

of the glue between PMs and the rotor core are no more able to overcome the centrifugal forces of the PMs at a high speed. Hence, sleeves to protect the PMs from being thrown out by high-speed centrifugal forces are required. Currently, carbon fiber and metal materials such as titanium, inconel and stainless are commonly applied as sleeves. Since these sleeves are non-ferromagnetic, the equivalent air-gap length of the motor becomes large. This results in relatively low air-gap magnetic flux density. As the torque of the motor is proportional to the magnetic flux density and the armature current, which are well-known as magnetic and electric loadings respectively, higher armature current is required to generate a specific torque because of relatively low magnetic loading. However, the armature current subjects to the insulation grade and the cooling ability of the copper winding. Consequently, the torque of the motor is limited. In addition, the eddy current losses in the solid-conductive sleeves at a high speed are very high. Although the fiber sleeves have lower conductivities, they generally have higher thermal resistances and much lower maximum working temperature than the metal sleeves. Moreover, the manufacture of the rotor with fiber sleeves is difficult. Even though fiber sleeves have much higher yield strength than metal sleeves, fiber sleeves are easily degraded during the manufacture and assembly process. Hence, sleeve-free structure is attractive for the HSPM motors.

The interior permanent-magnet (IPM) rotors do not need sleeves. A 2-pole IPM rotor is presented in Fig. 1.1(b). Without sleeves the equivalent air-gap length can be smaller and the flux weakening ability is better. However, the IPM rotors need flux-bridges to withstand the centrifugal forces of the rotors. The existence of the flux-bridges not only occupies the rotor space for PMs, but also increases the flux leakage. These problems are serious of the HSPM motors because the volume of the high-speed rotors is limited by the mechanical strength of the rotor core material and the stiffness of the rotor. Hence, the material of the rotor core plays a critical role of the high-speed IPM rotors. Firstly, the yield strength of the core material should be high enough in order to reduce the thickness of the flux bridges and the flux leakage. Secondly, the losses of the rotor-core material should be low to avoid rotor overheated due to high-frequency losses.
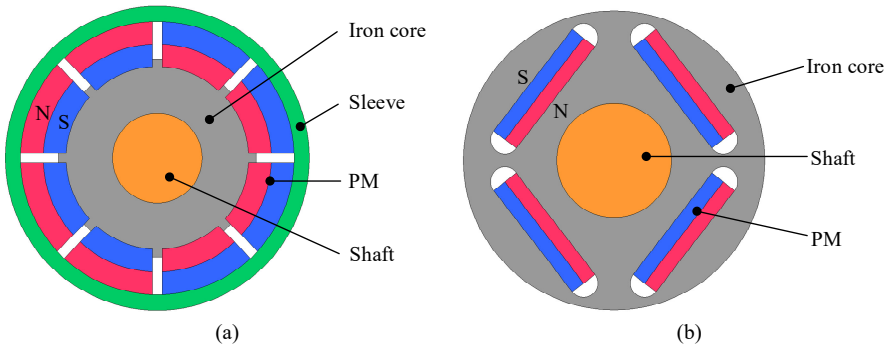

Figure 1.1:   Structures of 2-pole high-speed permanent-magnet rotors. (a) SPM rotor. (b) IPM rotor.

A special electrical steel, amorphous magnetic material (AMM) has been commercially available for decades. It is well-known because of much lower core losses than silicon irons (SIs). The AMM ribbons are produced by the rapid quenching method. The molten metal is solidified at a fast cooling rate (10^5 to 10^6 °C/s) to prevent crystallization. Insulation layer about 10 nm is formed during cooling. To meet the cooling rate requirment, avaible methods include splat quench, twin-roll casting, single roll free jet and melt spinning casting [4]. The scheme of the melt spinning casting process to produce the AMM ribbons is shown in Fig. 1.2 [5] and the produced AMM ribbon roll is presented in Fig. 1.3. The liquid metal is extruded from the nozzle to the cooling roll. The width of the AMM ribbon is decided by the sizes of the nozzle and the cooling roll. Currently, the maximum commercially available width of the AMM ribbon is 213 mm produced by Metglas, Inc. The thickness of the AMM ribbon 2605SA1 is about 23 μm and it is subjected to the cooling process.
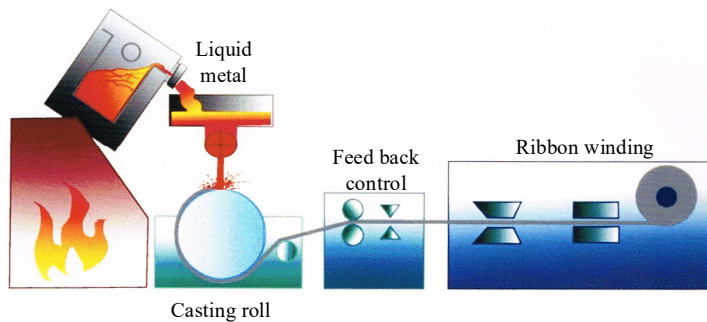
Figure 1.2:   Melt spinning casting process [5].

Figure 1.3:   Photo of amorphous ribbon roll.

Due to much small thickness and relatively high resistivity, the eddy current loss of this material is very low. However, currently its application to electrical machines still lacks of break-through progress. In the previous researches, the researchers focused on utilizing the low core losses of the AMM and the AMMs were mainly applied to the stators in order to reduce the core losses and to increase the efficiencies of the electrical machines. Because

the AMM ribbon was very thin and hard, and it became brittle after heat treatment, the difficulty in slotting of the AMM came to be a barrier to its wide application to the electrical machines. Due to the complex structure of the stator, the slotting problem is crucial. At present, electronic beam cutting, laser cutting, shear cutting, wire electrical discharge machining (WEDM), chemical etching and water jet cutting are possible techniques for producing of AMM cores [6]-[8]. However, either the cutting efficiency or the flexibility of these methods is generally lower than those of the widely applied punching method. Moreover, higher core losses are commonly observed in the prototypes due to the influence of the manufacturing process. These reduce the attractiveness of using AMM in electrical machines. Therefore, even though the AMM has attractive characteristics and has been applied in electronics, sensors and distribution transformers for decades [9], [10], the application of the AMMs to the electrical machines is still in research phase.

AMM 2605SA1 meets the requirements of the high-speed IPM rotor core very well. The mechanical strength and the specific losses of some commercially available high-performance electric steels are compared with the AMM 2605SA1 and shown in Fig. 1.4. It can be noticed that these materials distribute as 'V' shape in the figure.
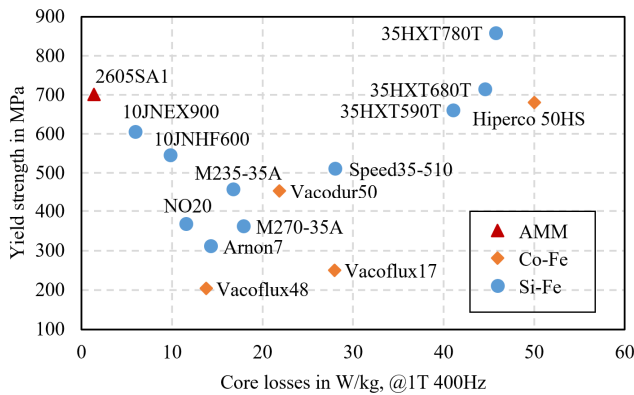

Figure 1.4:   Comparison of the yield strength and core losses of commercially availabel high-performance electric steels with AMM 2605SA1 [11], [O9].

The widely used SIs such as M235-35A and NO20, which locate at the bottom of the figure, have neither high strength nor low loss. Although silicon steel (Si-Fe) 35HXT780T and cobalt steel (Co-Fe) Hiperco 50HS have high yield strength, their losses are also high. According to Fig. 1.4 it can be found that the AMM 2605SA1 is the best because it has not only high yield strength but also lowest core losses. Its core losses are only one fourth of the super core material 10JNEX900. Besides the high yield strength and the low core losses, the AMM has high relative permeability. In addition, the saturation flux density of the

AMM is relatively low and it is about 1.56 T, which are not presented in this figure. Generally, the low saturation flux density is not welcome because it reduces the torque ability of the motor. However, for the high-speed IPM rotor structure, this characteristic may has positive effect because it can help to reduce the flux leakage in the flux-bridge regions. Since the core losses of the AMM are much lower than those of the widely used silicon steels, it is more suitable for high-speed and high-frequency applications. Hence, in this dissertation, the potential of using the AMM to improve the performance of the high-speed electrical machine will be studied.

1.2 Objectives

In this work, a new application for the AMM is proposed. The advantages of low core losses and high mechanical strength of the AMM are fully taken use of in the new application. Furthermore, the slotting difficulty can be in some way mitigated because the structure of the high-speed rotor is simple and the cutting length is small. This helps to reduce the cutting time. Meanwhile, by using the AMM to an IPM rotor, the problems of the high-speed SPM motors caused by the sleeves can be avoided. To evaluate the feasibility and the performance of the high-speed IPM rotor made from AMM core, the following works will be conducted.

Firstly, in order to better utilize the AMM in the design, the properties in terms of electromagnetics and mechanics of this material will be experimentally studied. The influences of manufacturing and working conditions, such as the stacking factor and the temperature, on the properties of the AMM will be investigated in order to avoid unacceptable design. These can provide a better reference for the designer who wants to use the AMM in the electrical machines.

Secondly, in order to study the feasibility of the proposed high-speed rotor, a demonstrator motor will be designed, built and tested. Currently, the HSPM motors are employed in variety of applications, including air compressor, flywheel energy storage system, turbocharger and electrified supercharger, spindle, micro-turbine, vacuum pump and so on. The power-speed ranges of these applications are shown in Fig. 1.5. It can be seen that the power demand of these applications is generally higher than 1 kW. In addition, the speed ranges of them are also wide and the maximum speed is generally close to 100,000 /min. In [12] a high-speed SPM motor of 15 kW and 120,000 /min for an air blower for cooling fuel cells has been developed by Korea Electrotechnology Research Institute. This motor used metal sleeve and the rotor diameter is 34 mm. The target speed and power of the motor have been experimentally measured. In [13] a high-speed SPM motor of 150,000 /min and 1.5 kW for supercharger mounted on a 1.5-liter class gasoline engine was developed and tested by Prof. Toshihoko Noguchi from Shizuoka University, Japan. Now, he is working on a higher power of 15 kW and 150,000 /min high-speed SPM motor and this motor is also used for automobile [14], [15]. The rotor diameter of this motor is 37.2 mm. Based on

the power, it is probably used for the bus [16]. To study the feasibility of the proposed IPM rotor made from AMM, a demonstrator motor of similar specification but a smaller size will be designed and tested. Because realization of a higher power high-speed PM motor is more difficult than that of a lower power high-speed motor, the target power of the demonstrator motor is over 15 kW at a relatively lower speed of 125,000 /min to show the superiortiy of the proposal. The potential applications of the demonstrator motor include air blower, electrified supercharger or turbochargers, flywheel energy storage systems, turbo-molecular pump and spindles, etc.
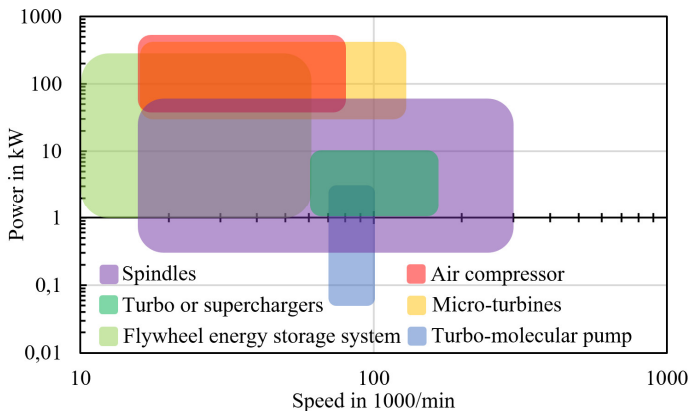

Figure 1.5:   Power-speed ranges of high-speed motors for different applications [17].

Thirdly, because the pulse-width-modulation (PWM) frequency of the high-power power module such as insulated gate bipolar transistor (IGBT) is limited, at a high speed, the modulation ratio between the PWM frequency and the frequency of the fundamental phase current is low. This will cause much higher amplitudes of current harmonics. Consequently, the losses of the motor including the core loss, the copper AC loss and the eddy current losses of the PMs and the metal sleeves are significantly increased. Since this is the main reason why the power/volume of the high-speed PM motors cannot be further increased by increasing the speed of the motors, this problem will be thoroughtly studied.

1.3   Structure of the dissertation

This dissertation is focused on the high-speed (high angular speed) motors and the application of the AMM in electrical machines. The detailed works of the dissertation are presented in Fig. 1.6, including experimental study of the propertis of AMM, design, manufacture and test of a demonstrator motor and comparison with a SPM motor.

In Chapter 2, the application and the state-of-the-art of the high-speed PM motors, and the state-of-the-art of the AMM electrical machines are introduced. Based on the literature, the

challenges and the opportunities of the high-speed motors and the AMM electrical machines are clarified. Then a high-speed IPM rotor structure made from AMM rotor core is proposed. Because slotting is the first concern when applying AMM, a review of the slotting techniques and the results of experimental studies will be illustrated in this chapter.
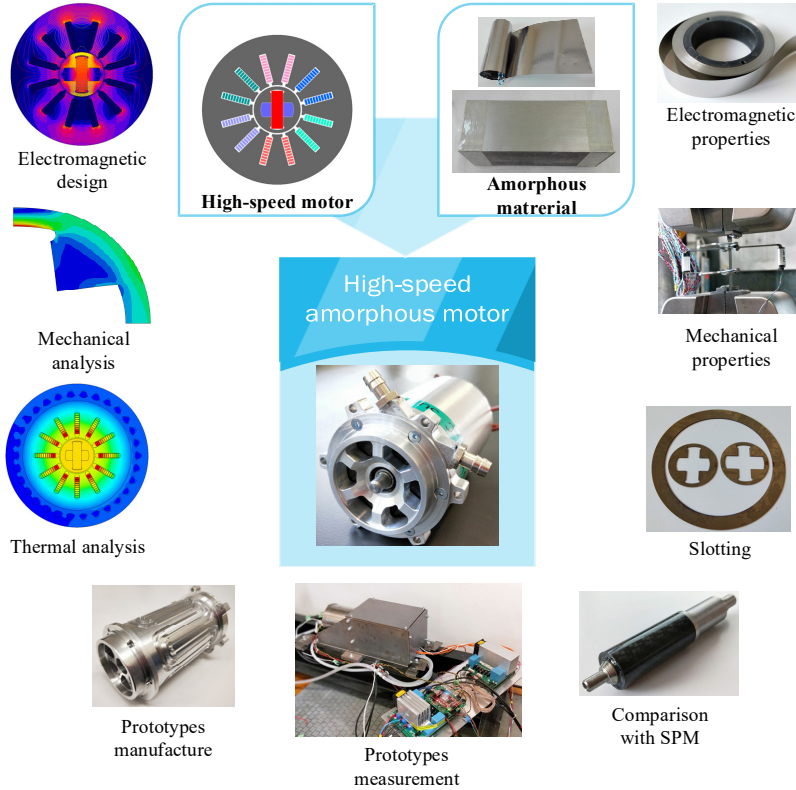

Figure 1.6:   Contents of this dissertation.

In order to better utilize the AMM and to build the material database for the design of the AMM electrical machines, in Chapter 3, the properties of the AMM in terms of electromagnetics and mechanics are experimentally studied. Since the electromagnetic properties of the AMM cores are sensitive to the manufacturing processes and the working conditions, the influences of the stacking factor, the temperature, the mechanical stress and the heat treatment are investigated.

In Chapter 4, a prototype of the proposed high-speed rotor is designed in terms of electromagnetics, mechanics and thermal behaviors. The structure of the stator core, the selection of the winding, the structure of the water-cooled housing for the high-speed PM motors are

discussed. The heat transfer ability of the air gap and the rotor air-friction losses are calculated. The importance of the AMM for the proposed IPM rotor is studied by conducting a comparison between different rotor core materials. A SPM rotor protected by a carbon fiber sleeve is also designed for a comparison study.

Chapter 5 studies the influence of the PWM inverter on the motor losses, including the copper AC loss, iron losses and the eddy current losses of the solid-conductive rotor components. The current harmonics caused by PWM inverter are theoretically derived and proved by coupled simulation.

To validate the design and analysis, in Chapter 6, the prototypes of the designed IPM and SPM motors are built and tested. The feasiability of the proposed IPM rotor made from AMM is evaluated.

Chapter 7 concludes the whole works of the dissertation. The advantages and disadvantages of the proposed high-speed rotor made from AMM are discussed. Further work to improve the rotor and some pieces of advice for using the AMM in the high-speed rotors are summarized.

2 High-speed PM motors and AMM electrical machines

In this chapter, the state-of-the-art of both the high-speed PM motors and the AMM electrical machines are summarized. The challenges and the opportunities of using AMM in electrical machines are discussed. In order to ensure the success of the prototypes, the slotting approaches of the AMM are experimentally studied. Finally, an IPM rotor made from AMM for high-speed operation is proposed.

2.1 Applications of the high-speed PM motors

Currently, high-speed motors are used in a variety of applications, including turbochargers and electrified superchargers, flywheel energy storage systems (FESSs), turbomolecular pumps, more electric engines, high-speed spindles, gas compressors, as well as microturbines [11], [18]-[22], etc. The working principle and requirements of these applications are briefly introduced in the following sections.

2.1.1 Turbocharger and electrified supercharger

Generally, the indicated power of an internal combustion engine (ICE) can be estimated by [23]:

$$P_{\text{engine}} = \rho_{\text{im}} \eta_{\text{v}} \eta_{\text{th}} \eta_{\text{comb}} \left(\frac{\dot{m}_{\text{f}}}{\dot{m}_{\text{a}}} \right) Q_{\text{fuel\_LHV}} N \left(\frac{V_{\text{e}}}{n_{\text{R}}} \right) \qquad (2.1)$$

where P_{engine} is the indicated power; ρ_{im} is the air density in the intake manifold; η_{v} is the volumetric efficiency; η_{th} is the thermal efficiency; η_{comb} is the combustion efficiency; $\dot{m}_{\text{f}}$ is the fuel mass flow rate; $\dot{m}_{\text{a}}$ is the air mass flow rate; $Q_{\text{fuel\_LHV}}$ is the mass specific lower heating value of the fuel; N is the crankshaft rotational speed; V_{e} is the engine swept volume; and n_{R} is the number of crank revolution per power stroke.

The air density is

$$\rho_{\text{im}} = \frac{p_{\text{im}}}{R_{\text{specific}} T_{\text{a}}} \qquad (2.2)$$

where p_{im} is the intake manifold air pressure; R_{specific} is the specific gas constant for dry air, and T_{a} is the absolute air temperature.

It is easy to notice that by increasing the air pressure in the intake manifold to increase the air density, the power of the ICE can be increased. This is because higher air pressure means more oxygen is present in each cylinder after the intake stroke, which helps more fuel to be burned and leads to higher produced power. In order to increase the air pressure, forced induction system with an air compressor is needed. Generally, according to the power supply of the compressor, the forced induction system can be categorized into two types: supercharger and turbocharger. The conventional supercharger is driven by the ICE and its speed is limited. Moreover, it consumes the energy of the ICE. Hence, the new electrified supercharger uses a high-speed motor to drive the compressor. In order to utilize the energy of exhaust stream, the compressor of a turbocharger is connected with a coaxial turbine and the turbine is driven by the exhaust stream. Because the turbocharger is driven by the exhaust gas from the engine, during start/stop conditions as well as during gear change, a low speed of the engine will reduce the discharge rate of the exhaust gas and cause low speed of the turbine, which reduces the charging capacity of the compressor as called turbo lag [21], [24]. In addition, a wastegate valve is needed in order to avoid turbine overspeed, which results in a potential waste of energy [23]. One way to overcome these problems is to regulate the speed of the turbocharger by installing a motor/generator be-tween the turbine and the compressor. When the speed of the engine is low and the energy of the exhaust gas is insufficient, the motor/generator works as a motor to improve the transient response delay (turbo lag); in high-speed zone of the engine, it works as a gener-ator to recover the excess exhaust gas energy [25].
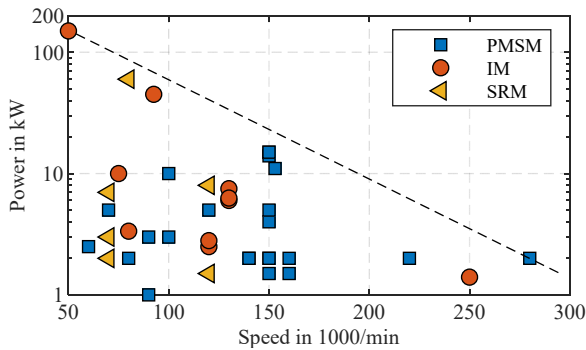

Figure 2.1: Power as a function of speed of the high-speed motors used for turbochargers and electrified superchargers [13], [18], [21], [23], [24], [28]-[43].

The power as a function of speed of the high-speed motors used for turbochargers and electrified surperchargers are shown in Fig. 2.1. It can be found that the PM synchronous motors (PMSMs) are more commonly applied. For high power ratings (higher than 40 kW), induction motors (IMs) and switched-reluctance motors (SRMs) may be better. The power decreases when the speed increases and they are generally below the dashed line. Since the

turbocharger does not deliver the typical target boost pressure until speeds of 60,000 /min to 100,000 /min are reached [26], the speed of the high-speed motors for this application are generally higher than 60,000 /min.

2.1.2 Flywheel energy storage system

Flywheel energy storage system (FESS) is an energy storage unit, which stores kinetic energy in a flywheel. Its energy $E_{flywheel}$ is linearly proportional to the moment of inertia J_{rotor} and the difference of the square of maximum and minimum angular velocities of the rotor ω_{max} and ω_{min}, as shown in (2.3) [44].

$$E_{flywheel} = \frac{1}{2} J_{rotor} \left(\omega_{max}^2 - \omega_{min}^2 \right) \tag{2.3}$$

Since the moment of inertia J_{rotor} of a certain FESS is constant, the energy of the FESS drops quickly when the rotation speed of the rotor decreases. Hence, the energy density of FESS is relatively low. However, the power density of FESS can be very high. Thus, FESS is commonly used as a short time high-power source (pulsed-power source). For example, it is used to mitigate the power fluctuation and enhance the dynamic-stability of an offshore wind farm and marine-current farm, which is connected to a power grid [45]. The application of FESS in electric vehicle helps to shorten the acceleration time of the vehicle. Currently, commercial FESS is available. A 100 kW, 25 kWh FESS produced by Beacon Power is shown in Fig. 2.2. By connecting multiple of FESSs together as shown in Fig. 2.2 as a matrix, higher energy up to 1 MW for 15 minutes can be delivered [46].
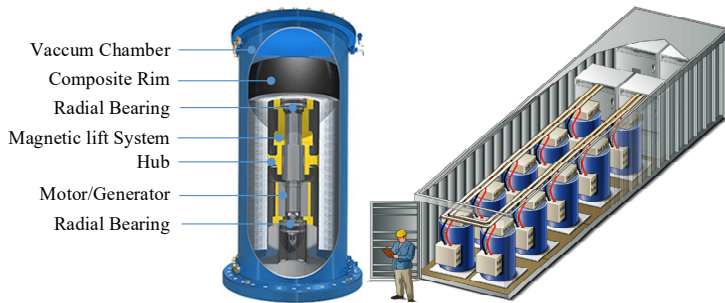

Figure 2.2: Beacon Power's flywheel matrix (250 kWh) [46].

Based on (2.3) it can be seen that there are two ways to increase the energy of the FESS. It is more effective to increase the rotation speed rather than to use a heavier flywheel with bigger diameter. An overview of the power and energy storage of different FESSs is present in Fig. 2.3. It can be found that the speeds of the high-speed motors used for FESSs are

around 20,000 /min to 60,000 /min. The power level is around 100 kW while the energy storage is generally not higher than 10 kWh. Most of the high-speed motors for this application are PM synchronous motors.
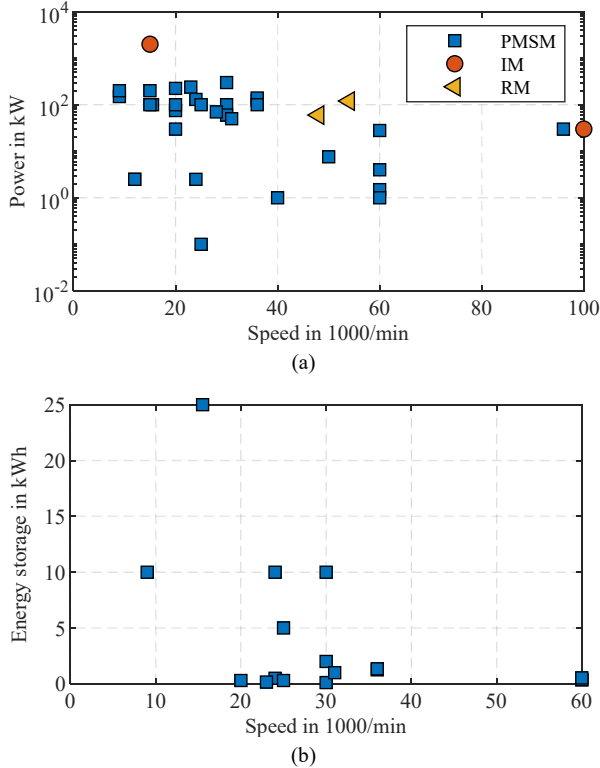

Figure 2.3:   An overview of power and energy storage of different FESSs. (a) Power-speed ratings of high-speed motors. (b) Energy-speed ratings of high-speed PM motors [47]-[76].

2.1.3   Turbomolecular pump

Turbomolecular pump is employed to obtain and maintain a high vacuum level. It is used in advanced technology applications, such as semiconductor manufacturing, thin film deposition, mass spectrometry, high energy physics, fusion technology, and general ultra-high vacuum research [77]. The turbomolecular pump consists of a turbine and a motor (as shown in Fig. 2.4). The motor runs at a high speed (typically 33,000 /min–75,000 /min, depending on the pump size) [77]. The turbine is driven by the motor and the blades of the turbine hit the gas molecules from the inlet of the pump toward the exhaust in order to create and maintain the vacuum condition. Currently, a rotation speed up to 1,000,000 /min is the future target of this application [78].

Figure 2.4:   Turbomolecular pump [11].

2.1.4   High-speed spindle

The conventional spindles are driven by the external motors through belt drive or through a coupling [79]. They cost less and allow flexible power and torque configurations. However, the maximum speed of the conventional spindles is limited because the belts at high speed produce unacceptable levels of vibration. Therefore, for the high-speed spindles, integrated motor spindle is a better choice. The speed and power ranges of the spindles are very spread out, varying from 4,500 /min to 300,000 /min, with a corresponding power level approximately from 60 kW down to 300 W [11], [80]. The speeds of the milling applications depend on the processed material type. For example, the speeds of some commonly processed materials in the milling application are listed in Table 2.1. The speeds for grinding applications are higher than those reported in Table 2.1 and it can be up to hundreds of thousands revolutions per minute [11].

Applications	Speed range in /min
Metal	4,500 – 12,000
Stones	8,000 – 12,000
Glass/Marble	8,000 – 14,000
Wood	18,000 – 25,000
Aluminum	30,000 – 40,000

Table 2.1:   Typical milling application speeds [11].

2.2   High-speed PM motors

Since PM motors have high power densities and efficiencies, they are popular for high-speed applications [12], [18]-[22], [81]-[91]. Generally, the high-speed PM motors can be classified into interior permanent-magnet (IPM) and surface-mounted permanent-magnet (SPM) types based on the rotor configurations. In this section, the characteristics and the

state-of-the-art of the two different configurations of the high-speed PM rotors are summarized and discussed.

2.2.1 SPM high-speed motors

The structure of a general 2-pole high-speed SPM rotor has been presented in Fig. 1.1(a). A significant feature of the high-speed SPM rotors is that sleeves are required to protect the rotors from cracking. In order to avoid flux leakage through the sleeves, non-ferro-magentic materials are commonly used for the sleeves. This results in a large equivalent air-gap length and a poor flux-weakening ability of the motor. In addition, when the sleeve is solid-conductive, the eddy current losses of the sleeves are very high. Furthermore, when fiber composite sleeves are used to reduce the eddy current losses, the heat dissipation ability of the rotor is relatively poor due to relatively high thermal resistivity. Moreover, the fiber sleeves are easily degraded at a high temperature and the maximum working temperature of fiber sleeves are much lower than that of the metal sleeves. The PMs of the SPM rotors can be either mounted on the rotor core or directly on the shaft. It is worth to mention that without the guidance of the rotor core, the flux lines directly pass through the solid-conductive shaft and high eddy current loss of the shaft will be induced. When a cylindrical PM is used as illustrated in [22], the shaft can be also avoided. The stiffness of the SPM rotor can be higher when the rotor stack is not employed because the axial stiffness of the stacked core is lower than that of the solid shaft. This can help to increase the natural frequencies of the rotor to some extent.

Generally, the maximum speed of a SPM rotor is much higher than that of an IPM rotor. Typical rotor surface velocity limitation for the IPM rotors is only 80 m/s, whereas for the SPM rotors is 280 m/s [92].Currently, the maximum speed reported is 1,000,000 /min and this motor was developed by ETH Zurich [3]. They adopted cylindrical PM covered by a titanium sleeve structure. A 100 W, 500,000 /min SPM drive system developed by them is presented in Fig. 2.5.
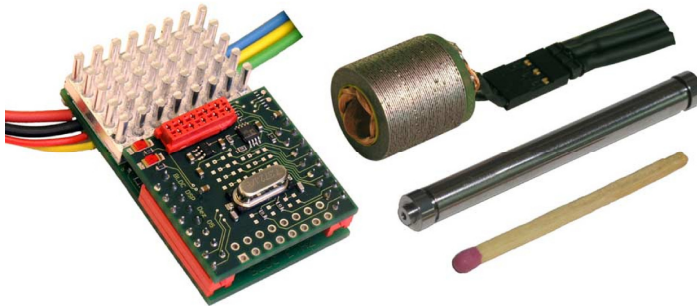

Figure 2.5:   A 100 W, 500,000 /min SPM drive system developed by ETH Zurich [3].

Table 2.1 lists some ultra-high-speed SPM prototypes with speed higher than 60,000 /min from published literature. It can be seen that metal sleeves are more frequently used. An important reason is that the fiber sleeves are sensitive to the manufacturing process and they maximum working temperature is relatively low. The strength of the fiber sleeves is easily degraded during manufacture. Generally, a thicker sleeve is used in the prototype than theoretically calculated thickness. One reason is that pressing axially the sleeve into the rotor may cause a shear stress and destroy the inner layers of the fiber sleeve. Moreover, the uncertain tolerances of the PMs and the shaft may cause unproper prestress. The bending stress caused by the edges of the PMs and the stress induced by the thermal expansion of the rotor are also harmful to the sleeve and may cause sleeve crash. Moreover, the rotor eddy current losses cuased by current harmoincs are very high. A failure example of a SPM rotor covered by the carbon-fiber sleeve built at TU Darmstadt is shown in Fig. 2.6 [93].

| (a) | (b) |
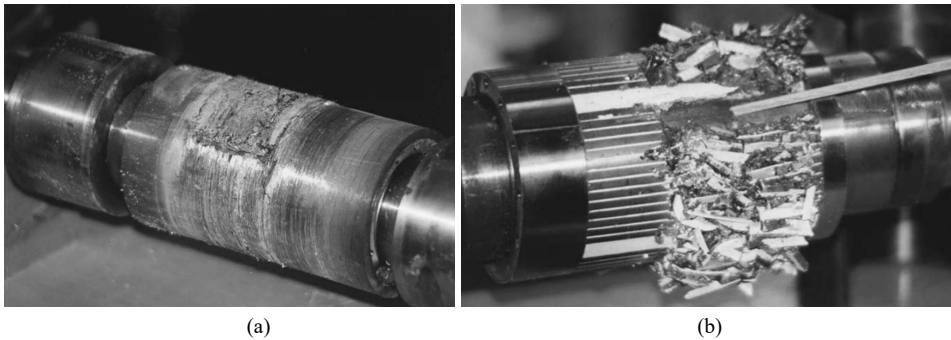
Figure 2.6:   Failure of a high-speed SPM rotor built at TU Darmstadt [93]. (a) Bandage crash at speed of 35,000 /min. (b) Destruction of brittle magnets underneath the broken bandage.

In order to strengthen the rotor, three major changes were made in a new rotor in terms of the rotor design, material selection and the assembly technique, which were very important for the design and the realization of high-speed SPM motors. Firstly, a thin layer glass-fiber was added to the inner layer of the carbon-fiber sleeve to withstand the bending stress. Secondly, cold shrink fitting method was used instead of axial pressing by immersing the rotor into the liquid nitrogen LN_2 to cool down the rotor. Thirdly, the mechanical air gap was increased from 0.7 mm to 3.2 mm to reduce the air friction losses and the eddy current losses of the rotor caused by the current harmonics; the sleeve undersize was reduced from 0.24 mm to 0.13 mm to decrease the prestress; the thickness of the PMs was also decreased from 7 mm to 4.5 mm to reduce the centrifugal forces of the PMs; and the interpole gap was avoided to mitigate the bending effect [93]. In this case, this improvement of the mechanical strength of the rotor sacrificed the power density of the motor.

Literature	Sleeve type	Max. speed in /min	Power in kW	Rotor diameter in mm	Sleeve thickness in mm	Air-gap length in mm	Stator diameter in mm	Stack length in mm
[91]	Titanium	200,000	2	22	-	0.8	35	21
[83]	Titanium	200,000	2.19	16.48	2	1.36	-	30
[81]	Titanium	500,000	1	10	0.5	-	25	30
[88]	Titanium	280,000	1	11	-	0.75	27.5	30
[90]	Titanium	500,000	0.1	6	-	-	16	15
[89]	Inconel 718	400,000	0.5	11.6	-	0.35	30	50
[12]	Inconel 718	120,000	15	34	4.5	1	120	50
[84]	Inconel	240,000	5	20	2	0.5	74	40
[87]	Stainless steel	80,000	0.05	5.5	0.25	0.7	22	29
[86]	Carbon fiber	60,000	0.5	29.2	1	1.4	60	30
[82]	Carbon fiber	220,000	2	25	5		110	29
[85]	Glass fiber	150,000	1.5	19.5	4.25		70	30

Table 2.2: Parameters of some high-speed SPM prototypes over 60,000 /min as reported in literature.

Even though metal sleeves such as titanium and inconel alloys have much stable mechanical strength than the fiber sleeves, the shrink fit (radial interference fit) between the sleeve and the PMs is still very difficult to control. When the shrink fit amount is not sufficient, because of expansion of the sleeve at a high speed, the sleeve becomes loose and then tensile stress inside the cylindrical PM is induced and the PM may crack. This phenomenon was reported in [89] and a broken rotor is presented in Fig. 2.7. A big shrink fit amount also cause difficulty in assembly. Hence, to fulfill a high-speed SPM rotor is challenging.
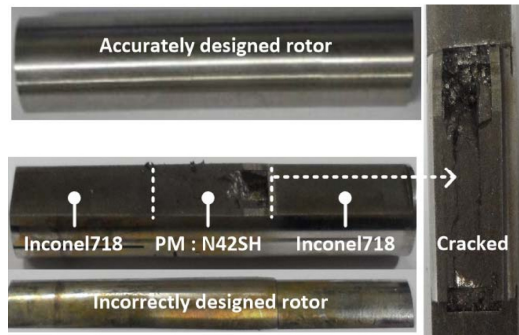
Figure 2.7:   Broken rotor caused by an incorrectly selected shrink fit [89].

2.2.2   IPM high-speed motors

The structure of a 2-pole high-speed IPM rotor has been shown in Fig. 1.1(b). It can be seen that the IPM rotor does not need a sleeve. Instead, the centrifugal forces of the rotor iron core and the PMs are withstood by the flux-bridges of the iron core. This enables the motors to have a small air-gap length, better flux-weakening and better rotor heat dissipation abilities. Due to a small air-gap length, the phase inductance of the IPM motor is generally higher than that of the SPM of the same volume and power levels. This helps to reduce the amplitudes of the current harmonics generated by the pulse-width-modulation (PWM) inverters. However, because the mechanical strength of the silicon steel is much lower than that of the titanium sleeve, the maximum speed of the IPM rotor is lower than that of the SPM rotor. Due to the volume limitation of the high-speed rotor, the usage of the PMs in the IPM rotor is also limited. In addition, because of the flux leakage in the flux-bridges, the air-gap magnetic flux density of the IPM motor is low. Moreover, since the rotor iron core is laminated along the axial direction, the stiffness of the rotor is also reduced. Hence, the IPM rotor is uncommonly used in the high-speed applications.

2.2.3 State-of-the-art of the high-speed PM motors

Based on the literature, the torque density, power density, rotor diameter and rotor stack length of different HSPM motors are summarized in Fig. 2.8 to Fig. 2.11. It can be noted from these figures that the SPM rotors are more commonly used than the IPM rotors in HSPM motors and that the metal sleeves are more popular than the fiber sleeves even though the eddy current losses of the metal sleeves at a high speed are much higher than that of the latter. In order to clearly show the levels of the target motor designed in this dissertation, the specifications of the designed motor are added to these figures in advance. The determination of the motor dimentions of the designed motors will be introduced in Chapter 4.
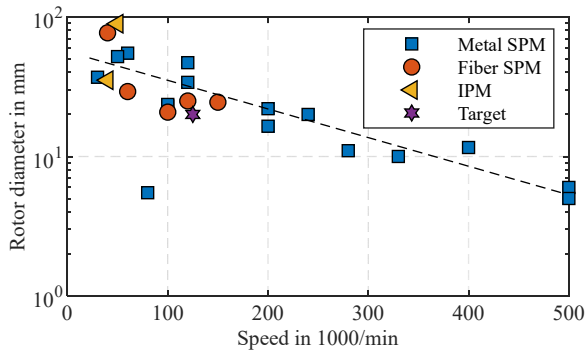
Figure 2.8: Rotor diameter of different high-speed PM motors as a function of rotor rotation speed [12], [21], [30], [81], [83], [85]-[104].
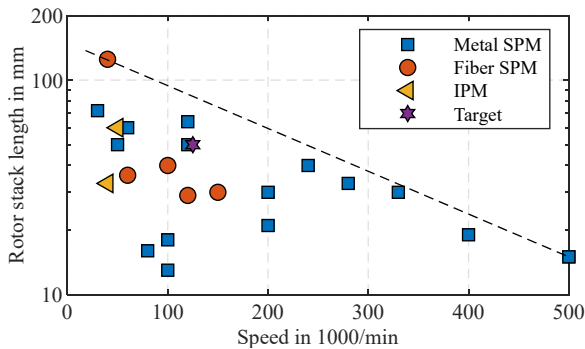

Figure 2.9: Rotor stack length of different high-speed PM motors as a function of rotor rotation speed [12], [21], [30], [81], [83], [85]-[104].

The rotor diameter and rotor stack length of some high-speed PM motors developed by other researchers are summarized in Fig. 2.8 and Fig. 2.9. It can be seen that the logarithm

of the rotor diameter and the logarithm of the rotor stack length decrease almost linearly when the speed increases. A small rotor diameter, which is below the dashed line is designed, it is because the maximum surface velocity of the IPM rotors is much lower than that of the SPM rotors. The effective axial stack length of the designed rotor is also below the dashed line in order to increase the natural frequency. Fig. 2.8 and Fig. 2.9 show that the dimentions of the designed rotor is reasonable in order to enable the rotor to run at the maximum speed.

Because the designed rotor has relatively small dimention, the torque density and the power density of this rotor are higher than those of the rotors reported in the literature. Fig. 2.10 shows the rotor torque density of differernt HSPM motors as a function of the rotor circumference velocity. It can be found that the rotor torque density decreases when the rotor velocity increases. As aforementioned, this is because the influence of the PWM inverter on the losses of the motor at higher speed is greater. This problem will be illustrated in Chapter 5. It is necessary to reduce the electrical and magnetic loadings of the motors at a higher speed. Hence, the rotor torque density is reduced when the rotor surface velocity is increased. The dashed lines in Fig. 2.10 denote the power density levels on the rotor surfaces. It can be seen that generally the SPM rotors have much higher power density than the IPM rotors. Moreover, the metal sleeves generally can help the SPM rotors to achieve higher power densities than the fiber sleeves. However, as regards the target motor designed in this dissertation, it has not only the highest rotor torque density but also highest power density, even though it is an IPM rotor.
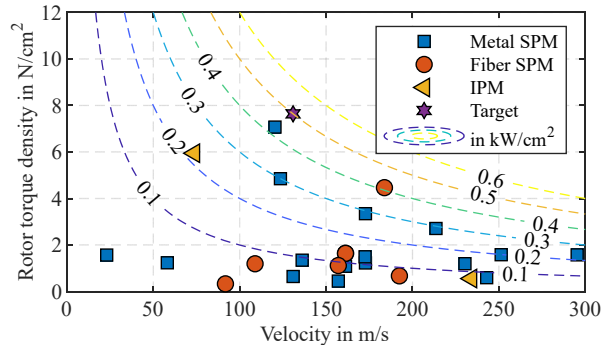
Figure 2.10:   Rotor torque density of different high-speed PM motors as a function of rotor surface velocity [12], [21], [30], [81], [83], [85]-[104].

The power density of different HSPM motors as a function of rotor rotating speed is presented in Fig. 2.11. The calculation of the power density of the motor is based on the radius and the axial length of the stator (all the motors shown in the Fig. 2.8 to Fig. 2.11 are inner rotor type). Fig. 2.11 shows that the IPM and fiber sleeve SPM rotors are mainly used at

the speed lower than 150,000 /min. No matter which rotor is used, the power density at the speed lower than 150,000 /min is generally lower than 50 kW/L. At a higher speed, only the metal sleeve SPM is employed. The power density is significantly increased and the highest value is about 100 kW/L. Even though the target motor is IPM type and the maximum speed is 125,000 /min, its power density can also reach about 100 kW/L. Hence, the target motor has a high power density.
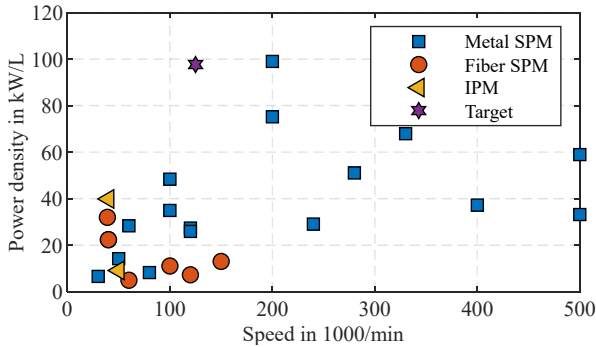

Figure 2.11:   Motor power density of different high-speed PM motors as a function of rotor rotating speed [12], [21], [30], [81], [83], [85]-[104].

2.3   Slotting challenge of AMM

The first challenge of using AMM for electrical machines is slotting. In the previous researches, many slotting approaches have been studied and many novel structures of the electrical machines have been proposed in order to avoid or to reduce the difficulty in slotting to some extent. However, up to now the slotting problem has not been completely solved. Hence, the AMM is not widely applied in the electrical machines even though this material has attractive benefits. In this section, the slotting experiments will be conducted in order to find out a proper approach for manufacturing of the prototype to ensure the high mechanical strength of the AMM rotor core.

2.3.1   Review of previous slotting studies

After several decades of the AMMs' commercially available for transformers, their application to electrical machines still stays in the research phase. The key problem is their difficulty in slotting. In the early 1980s, the slotting challenge has attracted attention and been investigated thoroughly as this is the primary challenge when considering quantity production [105]. In [105] directly slotting in casting phase by using three different methods were pursued. The idea was to make a parting line in the AMM ribbon by applying a pattern in the surface of the casting wheel, which has a lower quench rate than the bulk of

the casting wheel. Because of the low quench rate, the ribbon of this pattern region was crystallized and became brittle and then the parting line was generated. Firstly, they used unfilled shallow grooved pattern. The main drawback of this method was that the molten alloy flew slightly into the groove and formed a ridge on the underside of the ribbon. All or part of this ridge remained attached to the ribbon after cut-out separation and this ridge prevented the individual layers from lying flat and thus decreased the stacking factor. Fig. 2.12 shows the casting results over the unfilled shallow groove pattern.
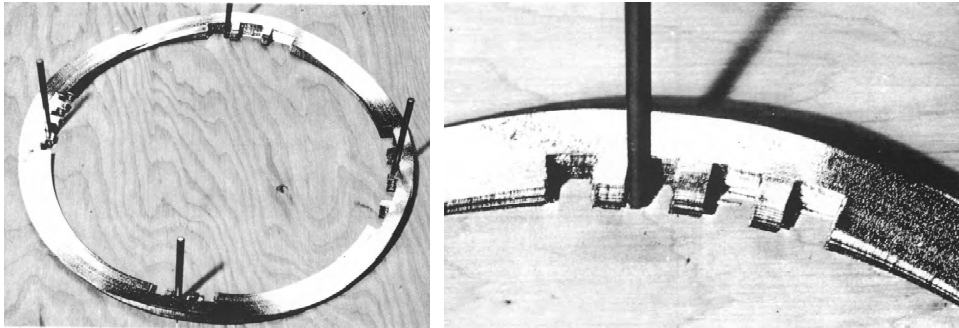
Figure 2.12:   Helical ribbon cast over unfilled shallow groove pattern [105].

In order to eliminate the burr cast on the downstream edge of the slot, a wheel was made with deep, straight-sided, open narrow grooves. A high pressure gas within the grooves was also supplied to prevent the molten metal from penetrating and sticking in the grooves. However, the ribbon still stuck to the grooves after several revolutions of casting as the surface tension of the molten metal was not sufficient to prevent its penetration into the groove. To avoid the penetration problem, the third method was proposed. They inserted low conductivity material in the groove. Various braze alloys, solid metal strips, and nickel-base alloy were tried. The casting response to all three metals was very similar and the ribbon did not show any marked tendency for embrittlement or separation at these parting lines. Then glass was applied due to its low thermal conductivity and non-wetting characteristics which were good for achieving a slower quench rate in the patterned regions and the casting wheel with glass filled grooves is shown in Fig. 2.13. However, these low temperature glasses suffered from thermal shock failure and did not meet the rigorous requirement for a long life under high erosion condition and thermal cycling. Fig. 2.14 shows the casting results over glass filled grooves and Fig. 2.15 shows the typical deterioration of the glass insert after casting. A partially dense ceramic was also employed but it was also faced with gradual erosion problem.

Since directly casting the slots was not successful, forming the slots after casting was also investigated. Four approaches were proposed: 1) by using a hot, resistance heated wire to heat the ribbon for a short time to create a crystallized, brittle outline, 2) by using a stylus

with electric current flowing through it into the ribbon to "draw" the embrittling pattern in the ribbon, 3) by using a magnetically steered electron beam to form the pattern, and 4) by using a heated die punch to punch the ribbon.
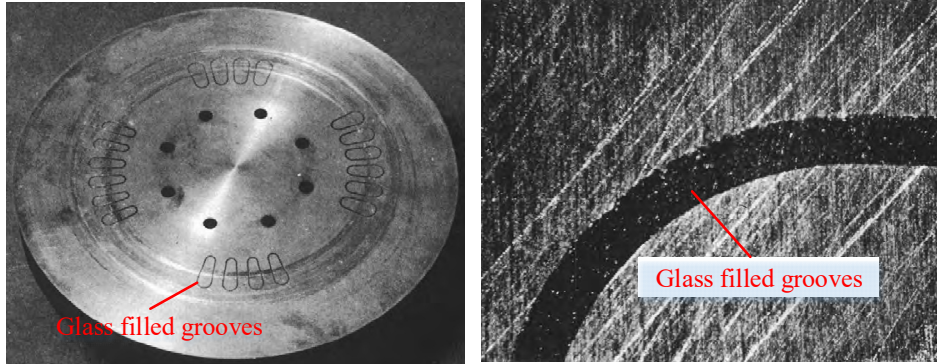

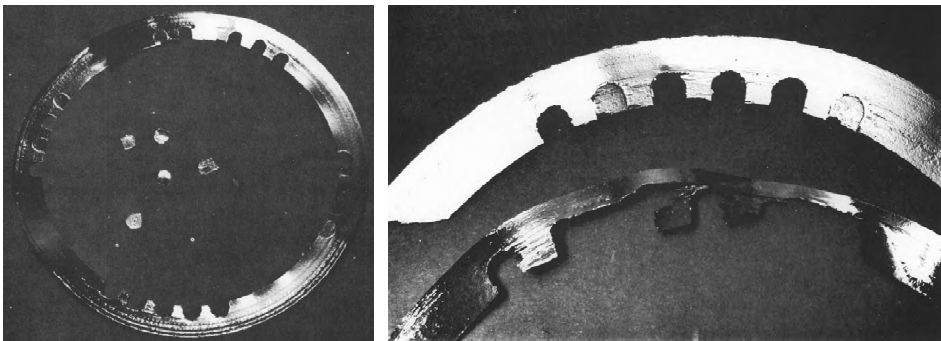Figure 2.13:   The casting wheel with glass filled grooves [105].

Figure 2.14:   The casting results over glass filled grooves [105].

Figure 2.15:   Typical deterioration of the glass insert after casting [105].

In the hot wire method nichrome wire was firstly bent into the shape of a slot and heated with an electric current to about 800 °C. Then the hot wire was pushed against the ribbon to embrittle the ribbon along the hot wire. This method required a high slotting speed to improve the quality of the slot edges. However, as the speed increased higher current had to be provided to keep the wire hot enough to accomplish the embrittlement. Further increasing the speed was limited by the cooling effect on the hot wire. This method was limited by life of the hot wire and economical slotting speed is unlikely to be achieved in the long term.

The stylus heating experiments were carried out by placing the amorphous ribbons on a conductive plate, which was connected to one terminal of a low voltage, current limited power source. The other terminal of the power source was connected to metallic probes. Because the resistivity of the amorphous metal was relatively high, the current was constrained to a narrow contact region when the probes were drawn across the amorphous metal. The contact region was heated and became embrittled. Because the contact area changed, the current density through the amorphous metal varied and differential stresses, varying embrittlement and the transverse cracks were caused along the crystallized line as can be seen in Fig. 2.16.
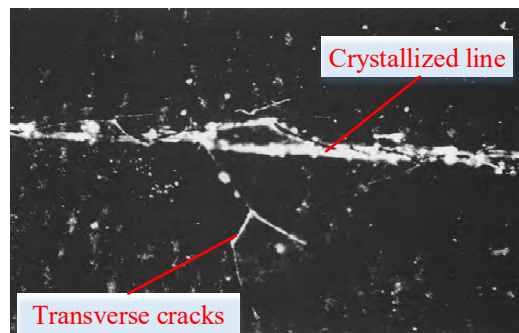
Figure 2.16:   Crystallized line and transverse cracks drawn by stylus heating [105].

To form the embrittling lines by using electron beam at economical speed was feasible according to their studies. Over 3,000 in/s, which was equivalent to high speed punching, could be attained with reasonable deflection systems. Moreover, high quality burrless edges could be attained by this method. In [106] a patent of using laser or electron beam method to cut the slots in the ribbon was introduced. The scheme of the cutting system is shown in Fig. 2.17. However, this method needs to take place in a vaccum chamber.
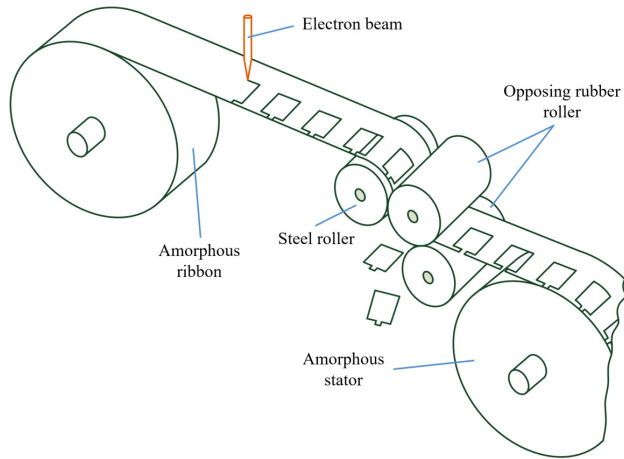
Figure 2.17:   Scheme of the cutting system by using electron beam approach [106].

The hot die punch method did not rely on creating brittle region but the hot temperature was used to avoid abrasion of the die due to high strength of the amorphous material. Usually about 100 °C below the crystallization temperature was applied and the strength of the amorphous ribbon dropped rapidly and the material became very easy to cut without any detectable tool wear. However, amorphous material underwent internal structureal relaxation when heated and it caused embrittlement. Hence, simply heated the material, cut and then cooled it again was unfeasibile for amorphous material. Moreover, because the amorphous was thin and soft after heated, a long deep-draw lip was formed after punching as can be seen in the left figure of Fig. 2.18. In order to minimize the ductile lip the tolerance of the die set needed to be reduced or an abrasive belt could be applied to remove the lip and the result can be seen in the right figure of Fig. 2.18. However, it was still unknown that can the lip be completely avoided or not by reducing the tolerance of the die set. Because heating and cooling processes are required, can the punching speed be improved to an economical rate or not was not sure. In addition, the effects of the punching process on the electromagnetic and mechanical properties of the amorphous material are still unknown.

To sum up, electron beam is the most feasible method considering quantity manufacturing. Besides the research report [105], there are fewer literatures concerning the slotting problem. Since the slotting of individual layer is difficult to achieve a good quality and high manufacturing efficiency, researchers turn to investigate the slotting of the amorphous blocks. For example, the amorphous ribbons were firstly wound and encapsulated as a solid, then abrasive water jet was applied to make the slots in [107]. Similar idea was proposed and milling method was used instead of abrasive water jet method in [108].
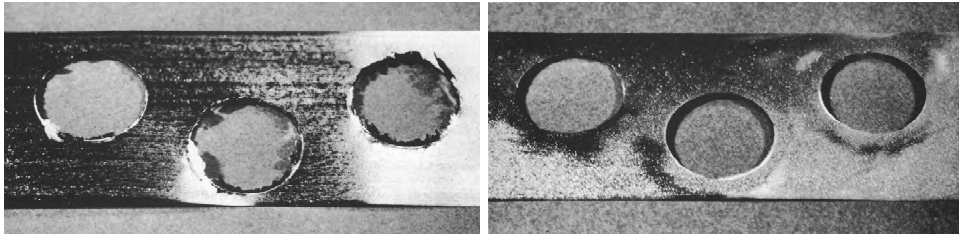
Figure 2.18:   Hot die punch holes (left) and after abrasive process (right) [105].

2.3.2   WEDM cutting experiments

WEDM method is commonly applied when the cutting amount is small. For quantity production of the core with a big dimention, this method is not recommended due to its low cutting efficiency. Even though this method is time-consuming, its cutting quality is the highest among the three methods tested in this dissertation and it is applicable for both annealed and non-annealed amorphous blocks. The cutting results of WEDM are shown in Fig. 2.19. The cutting edge is smooth and the tolerance is small. Moreover, the cutting contour shows that the layers are not burnt to connect together. This is important for the application in electric machines because the cutting surface is perpendicular to the air-gap magnetic field. High eddy current losses will be induced if short circuit occurs between the adjacent layers. Howerver, because of high temperature during cutting, the edge might be overheated and crystalized. Because this dissertation ustilizes the high mechanical strength of the AMM core and this material is brittle, any defect on the cutting contour will result is the rotor crack, the cutting influence on the mechanical strength of the core is the first consideration. Hence, a cutting method will only be selected when it has small influence on the mechanical strength of the AMM core based on the mechanical strength measurement.

(a)   (b)
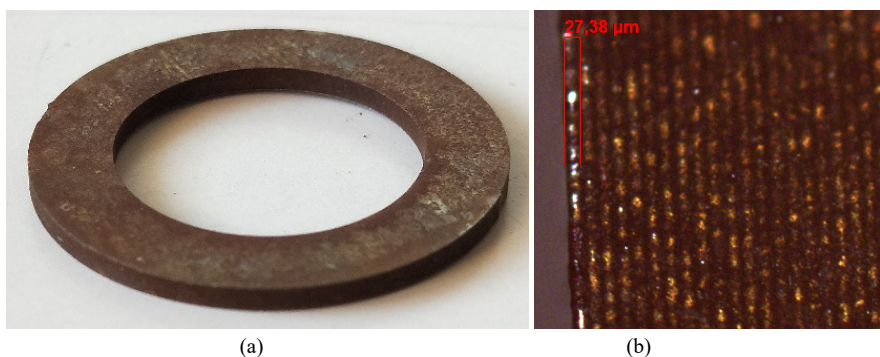
Figure 2.19:   AMM core cut by WEDM method. (a) Ring core. (b) Enlarged cutting contour.

2.3.3   Laser cutting experiments

Laser cutting is popular for prototyping when conventional silicon steels are employed. This method can obtain a high cutting precision and cutting efficiency. The cutting speed can reach a few tens meter per minute. A major problem of this method is that the insulation and the bonding varnish on the surface of the steel may be burnt out along the cutting contours. This may cause short circuits on the cutting contours when the stacking stress is high. When this method is applied to the AMMs, new problems emerge. Because the AMM ribbon is very thin, if single layer is cut, the stacking process becomes difficult. Hence, it is preferred to cut a laminated block in one time. However, this may also result in low cutting efficiency or poor cutting quality. For example, ribbons of 10 layers are firstly stacked and solidified, and then cut. In order to cut the 10-layer stack at a high cutting efficiency, the cutting power of the laser is high. The cutting results are shown in Fig. 2.20. It can be seen that a ridge is generated on the cutting contour. This ridge will reduce the stacking factor. Moreover, the cutting contour shown in Fig. 2.20(b) indicates that the AMM layers are burnt to connect together.

| (a) | (b) |
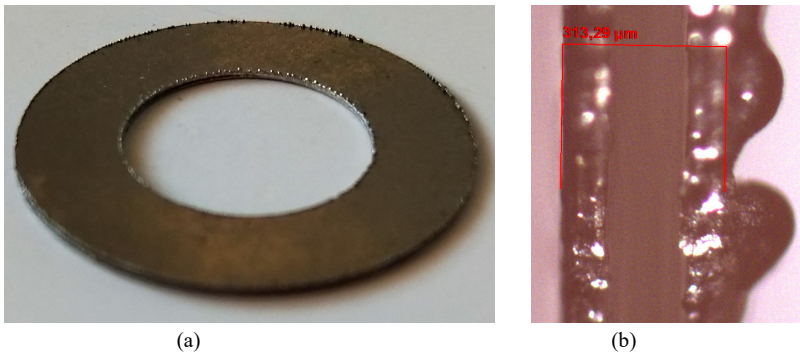
Figure 2.20:   AMM core cut by laser method. (a) Ring core. (b) Enlarged cutting contour.

In order to avoid ridges on the cutting contour, it is necessary to decrease the power of the laser. Then the cutting depth is limited. If the power is decreased to 10 W or 20 W, the cutting depth of each round is reduced to micrometer level. It will need a long time to finish the cutting. For example, it takes about one and half hours to finish cutting work of the rings (thickness 0.25 mm, outer diameter of the big ring is 55 mm as shown in Fig. 2.21).

Although the low power laser is suitable for cutting of the single-layer ribbon, the power of the laser still needs to be optimized to balance the cutting time and quality. For multi-layer amorphous stack, not only the cutting efficiency is low, but also the cutting quality is difficult to control. Sometimes the AMM ribbon may be burnt.

<table>
<tr><td>(a)</td><td>(b)</td></tr>
</table>
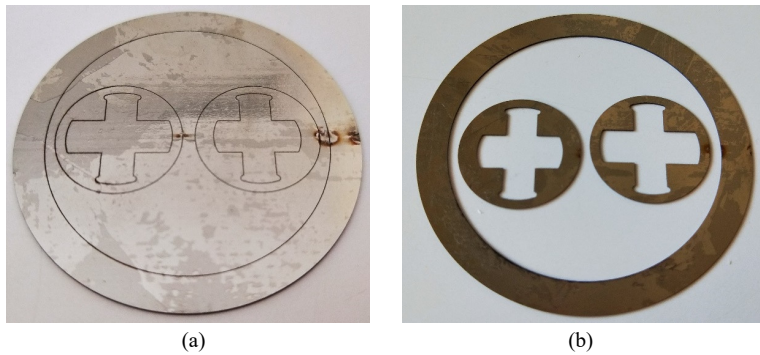
Figure 2.21: Amorphous Core produced by low power laser method. (a) Cutting trajectory. (b) Manufactured samples.

2.3.4 Punching experiments

Punching is the most widely used technique for quantity production of electrical machines because of its high efficiency and high quality. However, since the AMM has high hardness and brittleness after heat treatment, to use punching method for the AMM is challenging. Because the AMM ribbon is only about 23 μm in thickness, the tolerance of the punching die is required to be small if it is applied for a single layer punching. To avoid this problem, multi-layer stack may be better. The punching results of the annealed and non-annealed AMM stacks laminated by 20 layers are presented in Fig. 2.22 and Fig. 2.23, respectively. It can be noted that the annealed stack is easier to break after punching due to its high brittleness. Even though the non-annealed stack has higher quality than the annealed stack, it is still inapplicable with the current punching quality. Lip is formed along the punching contour after punching. The punching results of the non-annealed amorphous stacks by using the other two punching dies are presented in Fig. 2.24. It shows the same problem but also a potential of further improvement.

Figure 2.22: Punching results of the annealed amorphous stacks.

Figure 2.23:   Punching results of the non-annealed amorphous stacks.

Figure 2.24:   Punching results of the non-annealed amorphous stacks with different punching dies.

2.4   State-of-the-art of AMM electrical machines

2.4.1   Axial-flux AMM electrical machines

Since the slotting problem of the AMM has not been sloved, the researchers attempted to propose a proper machine structure to avoid or reduce the difficulty in slotting. Axial-flux topology was considered as a suitable way to employ AMMs. In order to avoid slotting, slotless tape-wound core with air-gap winding structure was proposed in 1990 [109]. However, the equivalent air-gap length of the slotless motor was relatively large which decreased the torque density of the motor. In order to decrease the equivalent air-gap length and avoid the slotting problem simultaneously, yokeless and segmented armature (YASA) axial-flux structure was more frequently proposed [109]-[111]. In this structure, modular stator cores could be either wound or laminated. In [110], cylindrical wound AMM cores were proposed. However, this structure could not make full use of the stator space. To increase the space usage of the stator, rectangular slot shape for the winding is a better

choice. Hence, trapezoidal or triangular wound AMM cores were used in [111]. The trapezoidal wound cores are shown in Fig. 2.25. These cores were wrapped from AMM tape and vacuum infused with resin for insulation between AMM layers. However, due to incompletely insulation between layers, the eddy current may be induced and the eddy current loop is shown in Fig. 2.25(a). In order to decrease the eddy current losses, a section was removed to cut off the eddy current loop as illustrated in Fig. 2.25(b). The experimental results of the prototype proved that by cutting a section along axial direction, the no-load iron losses were dramatically reduced. The no-load iron losses at 3,000 /min were reduced from around 110 W to 12 W. However, it brought cutting problem again.

A section removed

(a)   (b)   (c)
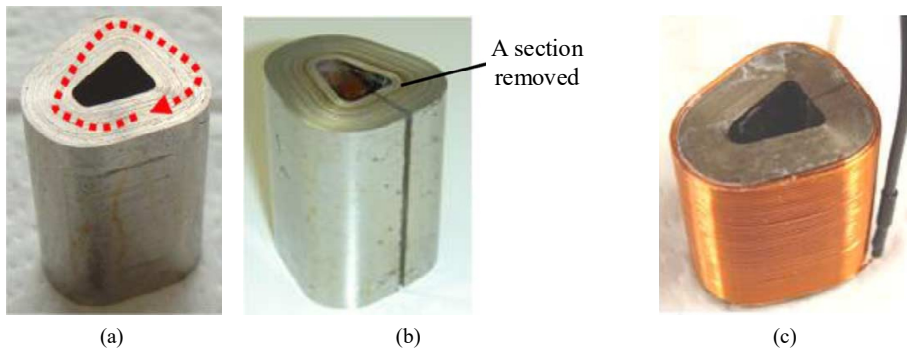
Figure 2.25:   AMM stator core for an axial-flux PM motor [111]. (a) Wound AMM core. (b) A section removed to decrease the eddy current losses. (c) Wound AMM core with copper coil.

Obviously, the wound AMM cores are hollow in the middle which increases the motors' size (as shown in Fig. 2.25). In order to reduce the total space occupied by the cores, the researchers from Hitachi also proposed another type of AMM core in [112]. They firstly wrapped the thin AMM ribbons into a core. Then, the core was encapsulated in resin to increase the strength. Finally, the molded AMM core was cut into several separate cores with trapezoidal surfaces. The iron losses measurement results showed that this new core had 30 % lower iron losses compared with the wound core shown in Fig. 2.25(b). However, cutting process after solidification of the AMM core is required and it is difficult.

Since the cutting time increased in proportion to the cutting area and these cores required a longer time for impregnation, a new AMM stratified core was proposed in [113]. The structure of the new stratified core is presented in Fig. 2.26(a) and the widths of the laminations are gradually changed. To fulfill this requirement, a manufacturing equipment consisting of transport and press systems was also made as shown in Fig. 2.26(b). Since after heat treatment the AMM ribbon becomes brittle, this process should be done before heat treatment. The final stratified core is shown in Fig. 2.26(c) and the prototype is shown in Fig. 2.26(d). For the new proposed stratified core, the iron losses were almost 30 % lower than those of wound core as shown in Fig. 2.25(b). After the heat treatment the core losses

were further reduced by 60 %. The developed motor had high efficiency and reached IE4. Even though the slotting problem can be avoided by using modular AMM cores, new challenges emerge. For example, it is difficult to form and assemble the AMM cores to attain a strong stator.

Laminate

(a)   (b)

AMM stratified core   Developed resin

(c)   (d)
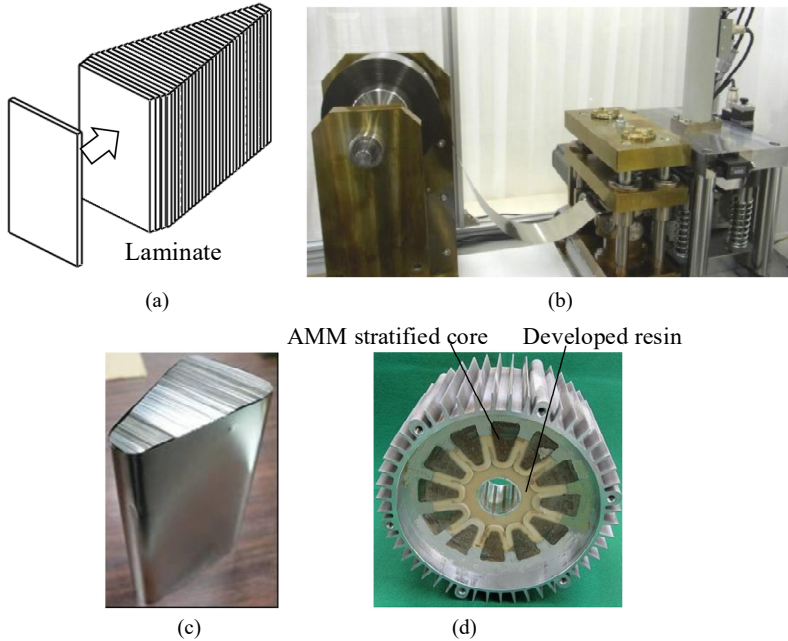
Figure 2.26:   Manufacturing of an axial-flux AMM stator by Hitachi [113]. (a) Lamination of AMM core. (b) Manufacturing equipment. (c) AMM stratified core. (d) Prototype of 11 kW at 3,000 /min.

In order to ease the slotting difficulty and save the manufacturing cost, a toroidal stator core cut from a tape-wound toroidal AMM core by using abrasive water jet (AWJ) technique was introduced in [8]. Since the tapered field machine can provide a larger air-gap surface area compared with the flat axial-field machine, which helps to increase the torque, in [107] a tapered AMM stator as shown in Fig. 2.27 was built by using the same method as illustrated in [8]. The experimental results of the prototype showed a moderate efficiency (~90 % at 7,000 /min).

Although axial-flux topology can ease the slotting difficulty to some extent, the disadvantages of this topology with AMM cores cannot be overlooked. For example, the low core losses of the AMM at high frequency are not fully taken use of and the low saturation flux density of the AMM is not easy to compensate, because the axial-flux motors generally run at a relatively low speed due to their mechanical strength limitation. Even though the slotting requirement can be eased or avoided, other manufacture process is still necessary. Due to high hardness and brittleness of the AMM, the difficulty in prototyping remains.
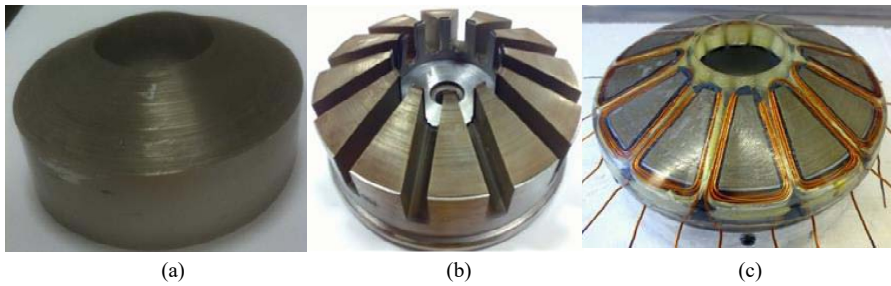
Figure 2.27:   Tape-wound tapered AMM stator [107]. (a) Wound tapered AMM core. (b) After waterjet cut. (c) With windings.

2.4.2   Radial-flux AMM electrical machines

As for the radial-flux AMM electrical machines, the slotting becomes more difficult. In order to avoid slotting process, a stator which has a plurality of segments and each segment includes a plurality of layers of AMM strips was proposed in [108]. A similar structure with a different manufacturing method for the 'U' type modular cores used for linear machines was also proposed in [O6]. In [114] a stator with separate AMM yoke and teeth was proposed. The yoke used helical AMM ribbon whereas the teeth used straight ribbon. Manufacturing method of the helical ribbon was introduced in [115]. Even though many structures have been proposed, experimental studies on the prototypes are unsufficient.

Despite of the slotting difficulty, some radial-flux prototypes made of the AMM cores have been built as shown in Fig. 2.28, including PM synchronous motors, induction motors and switched reluctance motors [116]-[125], [O1], [O9]. Their performances were evaluated and it was proved that the core losses of the AMM motors were reduced.
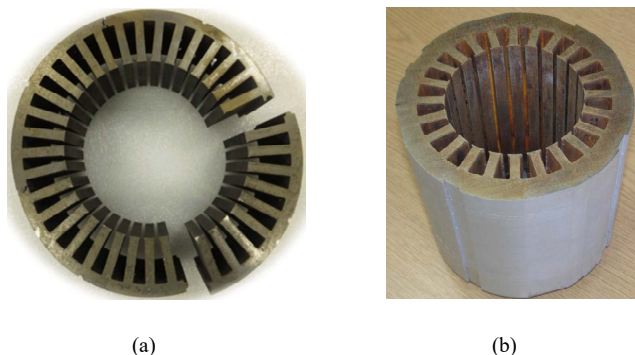
Figure 2.28:   Radial-flux AMM stator cores. (a) Modular AMM stator core for an interior PM motor [122]. (b) AMM core for an induction motor [125].

In [122] modular AMM stator cores were applied due to the dimension limitation of the AMM ribbons. It was observed that a prototype made from AMM stator was 31 % smaller in volume and 42 % lighter in weight than the baseline motor, which used conventional silicon iron, while the steady-state temperature rise at rated working condition was kept more or less unchanged. Moreover, it was reported that by using the AMM for a SRM, the efficiency of the prototype was improved by 6 % and reached 95.1 % at a speed of 8,500 /min with an output power of 2.4 kW [116]. In [121] an IPM synchronous motor employing the AMM stator core was tested and the test results illustrated that the AMM stator core can reduce the motor core losses by about 50 %. However, the experimental core losses were much higher than the finite element analysis (FEA) losses. The authors mentioned that this increase was highly likely due to the fact that the iron loss characteristics of the AMM were deteriorated by the mechanical stress during the core manufacture process.

Higher experimental core losses than those of FEA were observed not only in [121], but also in [107]. In [107] the experimental results of the prototype showed only a moderate efficiency (~90 % at 7,000 /min). In order to apply the AWJ method, the toroidal core must be strongly formed. The AMM core was degraded due to the stress caused by the strongly forming.

In [113] the core losses of the AMM cores were measured. It was found that the core losses at 400 Hz and 1 T of the wound core as shown in Fig. 2.25(b) were about 15 W/kg, while the core losses of the stratified core shown in Fig. 2.26(a) at this condition were only about 10 W/kg. After the heat treatment of the stratified core, the core losses were reduced to about 4 W/kg. Even though the stratified core after heat treatment has much lower core losses than the aforementioned cores, its losses were still much higher than those provided by the AMM ribbon manufacturer. Based on the manufacturer, at 1 T and 400 Hz, the core losses of the AMM are lower than 2 W/kg, and about 2.5 W/kg is observed in our measurement with an inside magnetic field annealed AMM core.

The AMM cores after mechanical process were degraded and the core losses were 7.5 times higher after the AMM core was manufactured as reported in [113]. When this core is applied to a demonstrator motor, higher core losses and lower efficiency will be obtained. By taking the slotting difficulty and the degradation of the AMM into consideration, the advantage and the attractiveness of the AMM motors are dramatically reduced.

The disadvantages of the AMM are summarized as follow. Firstly, because of relatively low saturation flux density, the torque and the overload performances of the AMM electrical machines are reduced. Secondly, the magnetic properties of the AMMs are easily influenced by the mechanical processes, especially the mechanical stress. Generally, higher mechanical stress leads to higher core losses. Thirdly, the thickness of the AMM ribbon is

very small which is only 0.023 mm. This reduces the stacking factor of the core. Moreover, small thickness requires a high precise punching die. Fourthly, the high hardness of the AMM will abrase and reduce the lifetime of the punching die. Fifthly, in order to release the internal stress in the AMM, annealing treatment is recommended. After annealing treatment the AMM becomes brittle, which increases the difficulty of the slotting. The high-efficiency punching method which is commonly applied for the conventional silicon steels is no applicable for the AMM at the moment.

2.5   Proposed high-speed AMM PM rotor

Since the AMM has higher mechanical strength and much lower iron losses than the conventional silicon steels, it is benefitial for the high-speed IPM rotors. In order to eliminate sleeves, Dr. Markus Schiefer proposed to use the AMM for a high-speed IPM rotor and he suggested to put the PM in the middle of the shaft. But the magnetization direction of the PM and the material of the shaft were not decided. After analyzing the performance of the proposed rotor and compared it with some other rotor types in [O5], I proposed a detail structure as presented in Fig. 2.29. The studied rotor consists of three components: an AMM rotor core, a PM, and a ferromagnetic hollow shaft.

In order to avoid high magnetic resistance of the main flux path, ferromagnetic shaft is required. To avoid the influence of flux leakages at the ends of the shaft, the ends should be non-ferromagnetic. Hence, a welded shaft made from two different materials is required.

By inserting the PM into the rotor center, ideally there is no additional stress on the rotor core from the PM. Moreover, since a rectangular PM is used, the manufacture and assembly of the PM are simple, and the pole-pitch factor is high. In order to strengthen the rotor, the gaps between the three components of the rotor will be filled with high-strength adhesive. The gaps between them lead to a slightly larger equivalent air-gap length and they have a small influence on the performance of the motor based on the analysis.

Due to relatively low saturation flux density of the AMM, the AMM rotor flux leakage is lower than the rotor made from silicon iron. For the proposed rotor structure, because its diameter is small due to mechanical strength limitation, the cutting cost and time can be dramatically reduced. This helps for the mass production. By using the proposed rotor structure and AMM for the rotor core, not only the sleeve can be avoided, but also the performances of the high-speed motor can be improved, such as better flux-weakening ability, higher efficiency and lower rotor temperature rise.

The disadvantages of the proposed high-speed rotor made from AMM are stated as follows. Firstly, the magnetic properties of the AMM are easily influenced by mechanical processes and temperature. Secondly, the thickness of the AMM ribbon is very small which is only

0.023 mm. This reduces the stacking factor of the core. Thirdly, due to relatively low saturation flux density of the AMM, the shaft loss at a high speed with high load is high.
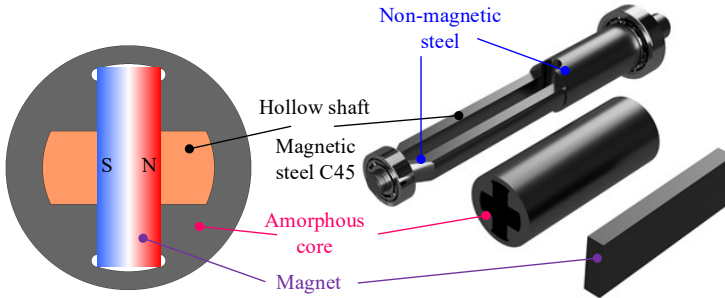
Figure 2.29:   Proposed high-speed IPM rotor structure.

As regards the proposed high-speed IPM rotor, due to its small volume, the PM usage is smaller than the SPM rotor. Although a special shaft made of different materials are in need, currently, friction welding technology is feasible and the cost is also comparable with a normal shaft. The price of the AMM is also comparable with the commonly used silicon steel and is cheaper than that of the low losses silicon steel, for example 10JNEX900. The most expensive part of the rotor is the cutting cost of the rotor core. However, due to a small cutting area of the high-speed rotor core, this cost is also acceptable. Moreover, because this motor has a high power density and a much small volume, which are more important than the cost in some specific application, such as turbomolecular pump, the manufacturing cost of the rotor is not a major problem. It is promising for a wide range of applications.

3 Experimental characterization of AMM

To better utilize the AMM and ensure the success of the design, the properties of the AMM are experimentally studied in this chapter. Since the electromagnetic properties of the AMMs are easily affected by the stacking factor, annealing and temperature, their influences are also studied in this chapter. In addition, according to the literature review in the Chapter 2, the AMM cores are usually applied for the stator cores of the machines to decrease the core losses. However, the high yield strength of the AMM lacks attention. As it is one of the most important properties to ensure the proposed rotor to successfully run at high speeds, the yield strength of the AMM is tested as well. In addition, the properties of some other electric steels, such as 10JNEX900, M235-35A, M330-35A, M330-50A and Vacodur49, are tested for a comparison. Moreover, the measured data in this chapter can extend the available database for the machine designers.

3.1 Measurement of electromagnetic properties

3.1.1 Measurement principle

The structure of the measurement system for measuring electromagnetic properties of electric steels is shown in Fig. 3.1. In this figure a toroidal specimen is tested. This system is also applicable for Epstein frame test. The size of the toroidal specimen used in the test is based on the norm DIN IEC 60404-6. The outer diameter is 55 mm; the inner diameter is 45 mm and the height is 20 mm as presented in Fig. 3.2. All the toroidal AMM cores tested are cut by the wire electrical discharge machining (WEDM) method. As it can be seen in Fig. 3.1, the toroidal specimen is wound with two sets of windings. The primary winding is excited with AC current i_1, which is generated by a linear power amplifier. Then, voltage u_2 is induced in the secondary winding. In order to ensure the flux variation inside the toroidal core is sinusoidal, the voltage u_2 is controlled to be sinusoidal by regulating the primary voltage u_1. The regulating variable of the primary voltage u_1 is obtained by comparing the secondary voltage u_2 with a sinusoidal reference. Due to flux leakage, the core magnetization and resistance loss, the primary current i_1 and voltage u_1 are not sinusoidal. Typical primary current and secondary voltage waveforms are shown in Fig. 3.3. Considering the magnetic field in the ring specimen is homogeneous, the *B-H* curve and the core losses can be calculated by using i_1, u_2, and the parameters of the toroidal specimen. More details about the realization of the measurement system can be found in [126].
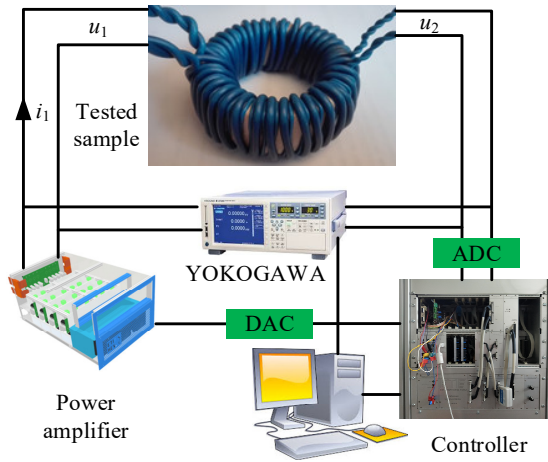
Figure 3.1:   Structure of the measurement system for electromagnetic properties.
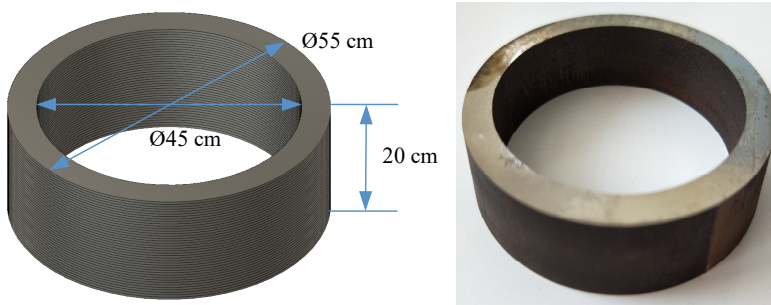
Figure 3.2:   Toroidal core used for electromagnetic property measurement.
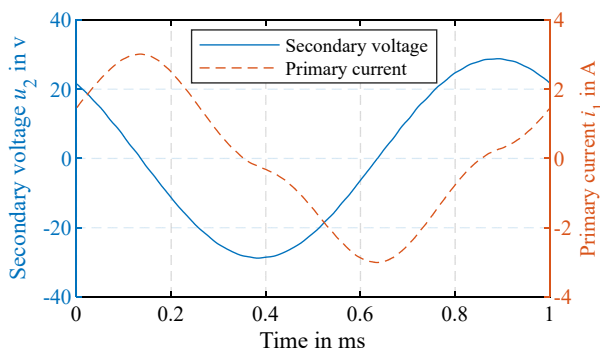
Figure 3.3:   Typical primary current and secondary voltage waveforms when the frequency is 1 kHz.

Based on the Ampère's law, the magnetic field strength can be calculated by

$$H = \frac{N_1 i_1}{l_e} \tag{3.1}$$

where H is the magnetic field strength; N_1 is the number of turns of primary winding; i_1 is the current in the primary winding and l_e is the equivalent length of the magnetic path of the toroidal specimen.

Because the circumference of the toroidal core varies with the radius, the magnetic field strengths of different radii are different. Then, an equivalent length l_e is adopted and it is expressed as [127]

$$l_e = 2\pi \frac{\ln\left(\frac{r_a}{r_i}\right)}{\frac{1}{r_i} - \frac{1}{r_a}} \tag{3.2}$$

where r_a and r_i are the outer and inner radius of the ring specimen, respectively.

The magnetic flux density B is calculated by the induced voltage u_2, the number of turns of the secondary winding N_2 and the effective cross area of the specimen A_e as expressions of (3.3) to (3.5) [127].

$$u_2 = \frac{d\psi}{dt} = N_2 \frac{d\phi}{dt} = N_2 A_e \frac{dB}{dt} \tag{3.3}$$

$$B = \frac{1}{N_2 A_e} \int_T u_2(t) dt \tag{3.4}$$

$$A_e = h_{core} k_{core} \frac{\ln^2\left(\frac{r_a}{r_i}\right)}{\frac{1}{r_i} - \frac{1}{r_a}} \tag{3.5}$$

where h_{core} and k_{core} are the thickness and the stacking factor of the toroidal specimen, respectively.

The core losses of the toroidal specimen can be calculated by using the secondary voltage through

$$P_{\text{core}} = \frac{1}{T} \int_T \frac{N_1 u_2(t) i_1(t)}{N_2} \, dt \qquad (3.6)$$

where T is the sampling time.

3.1.2 Measurement results

The electromagnetic properties of the AMM core 2605SA1 after inside magnetic field annealing process are measured. In order to evaluate the performance of the AMM core, a high-silicon steel 10JNEX900 (6.5% Silicon) and three widely used conventional electric steels named M235-35A, M330-35A and M330-50A and a high saturation flux density Cobalt-based steel named Vacodur 49 are also measured and compared with the AMM. M235-35A means the thickness of this steel is 0.35 mm and the typical iron loss of this steel at 50 Hz and 1.5 T is 2.35 W. The compositions of the Vacodur 49 are 49% Cobalt, 2% Vanadium and the rest is Iron. The thickness of the AMM strip is about 0.023 mm, while the thickness of the 10JNEX900 and Vacodur 49 are 0.1 mm and 0.35 mm, respectively.

Due to power limitation of the measurement system in our institute, the tested maximum magnetic field strength is about 3000 A/m. The tested B-H loops, the commutation curves and the core losses of these materials are compared in Fig. 3.4 to Fig. 3.6. Because the magnetization current is not seperated from the primary current i_1, the calculated magnetic field strength presented in Fig. 3.4 is slightly higher than the real value. The areas of the B-H loops as shown in Fig. 3.4 consist of not only the hysteresis loss but also the eddy current loss. Fig. 3.4 shows that the high-silicon steel 10JNEX900 has the lowest flux density among the tested cores when the magnetic field strength is lower than 3000 A/m. AMM 2605SA1 has the narrowest B-H loops. Cobalt steel Vacodur 49 has the highest flux density when the magnetic field strength is 1000 A/m. The magnetization abilities of the three widely applied silicon steels are silimar. Because M330-50A has larger thickness than the other two steels, it has larger B-H areas than the others due to higher eddy current loss. Because M330-35A has higher iron loss than M235-35A, the B-H areas of the former are larger than the later. The superior of the AMM 2605SA1 over the other materials is clear when the magnetic field strength is lower than 3,000 A/m based on the tested results.
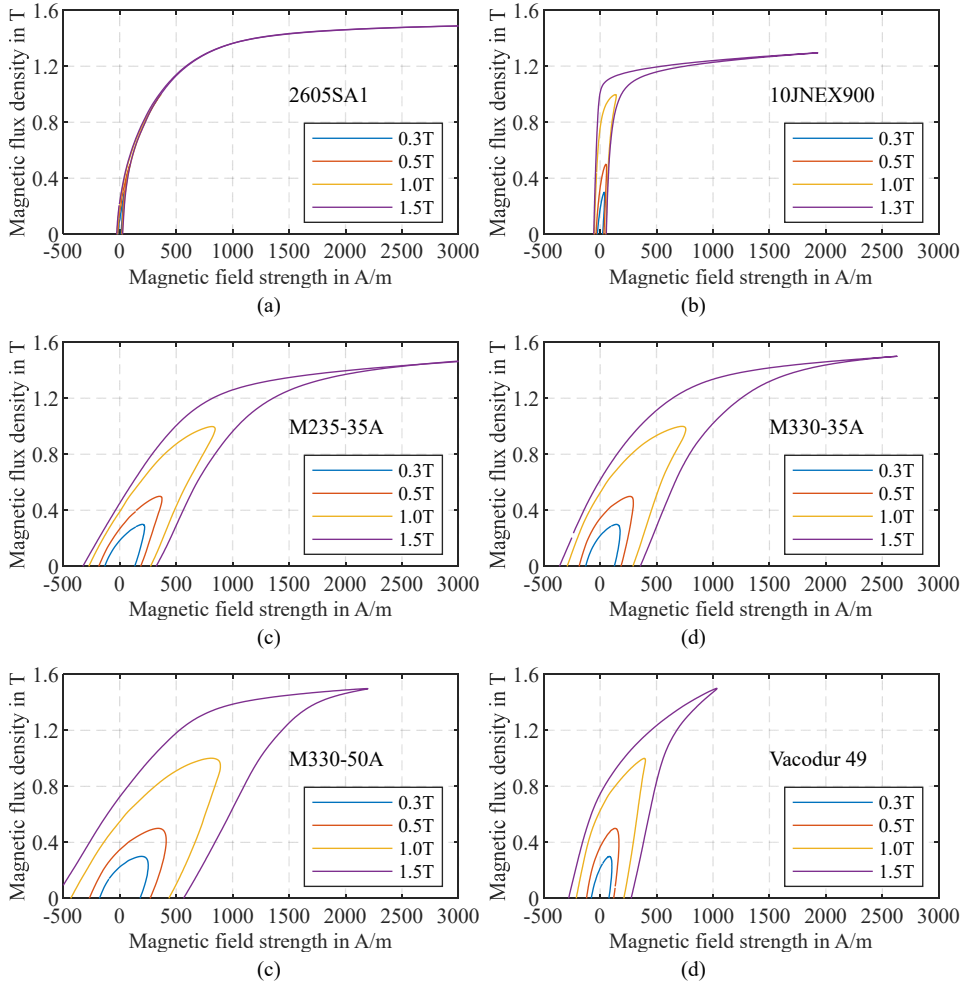
Figure 3.4:   *B-H* loops at 1000 Hz. (a) AMM 2605SA1. (b) 10JNEX900. (c) M235-35A. (d) M330-35A.
(e) M330-50A. (f) Vacodur 49.

The comparison of the commutation curves of the six cores is shown in Fig. 3.5. The commutation curves are obtained by connecting the peak points of the *B-H* loops of different frequencies and peak flux densities. It clearly shows that the magnetization abilities of 2605SA1 and 10JNEX900 are frequency-independent, whereas the magnetization abilities of the other materials decreases significantly when the frequency increases. This is mainly because the eddy current losses of the steels with larger thickness increase significantly when the frequency increases. For example, M330-35A and M330-50A are the same material with different thickness. At low frequencies, the commutation curves of the two cores are similar. However, when the frequency increases, the magnetic flux density of the

M330-50A decreases faster than the M330-35A due to a larger thickness. Fig. 3.5 also shows that the magnetic flux density of the 10JNEX900 increases faster than the other materials when the magnetic field strength increases from the beginning. This means the 10JNEX900 has the highest maximum relative permeability.
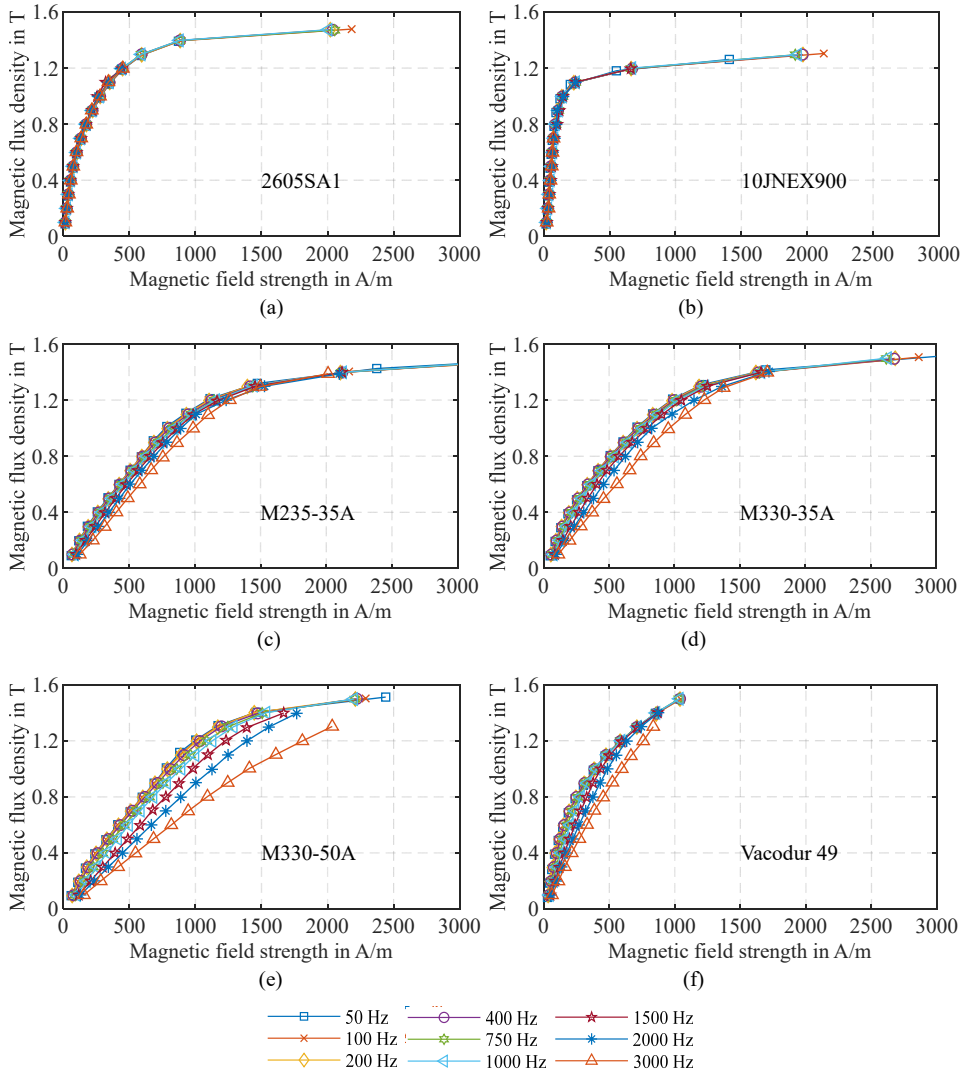
Figure 3.5:   Commutation curves. (a) AMM 2605SA1. (b) 10JNEX900. (c) M235-35A. (d) M330-35A. (e) M330-50A. (f) Vacodur 49.
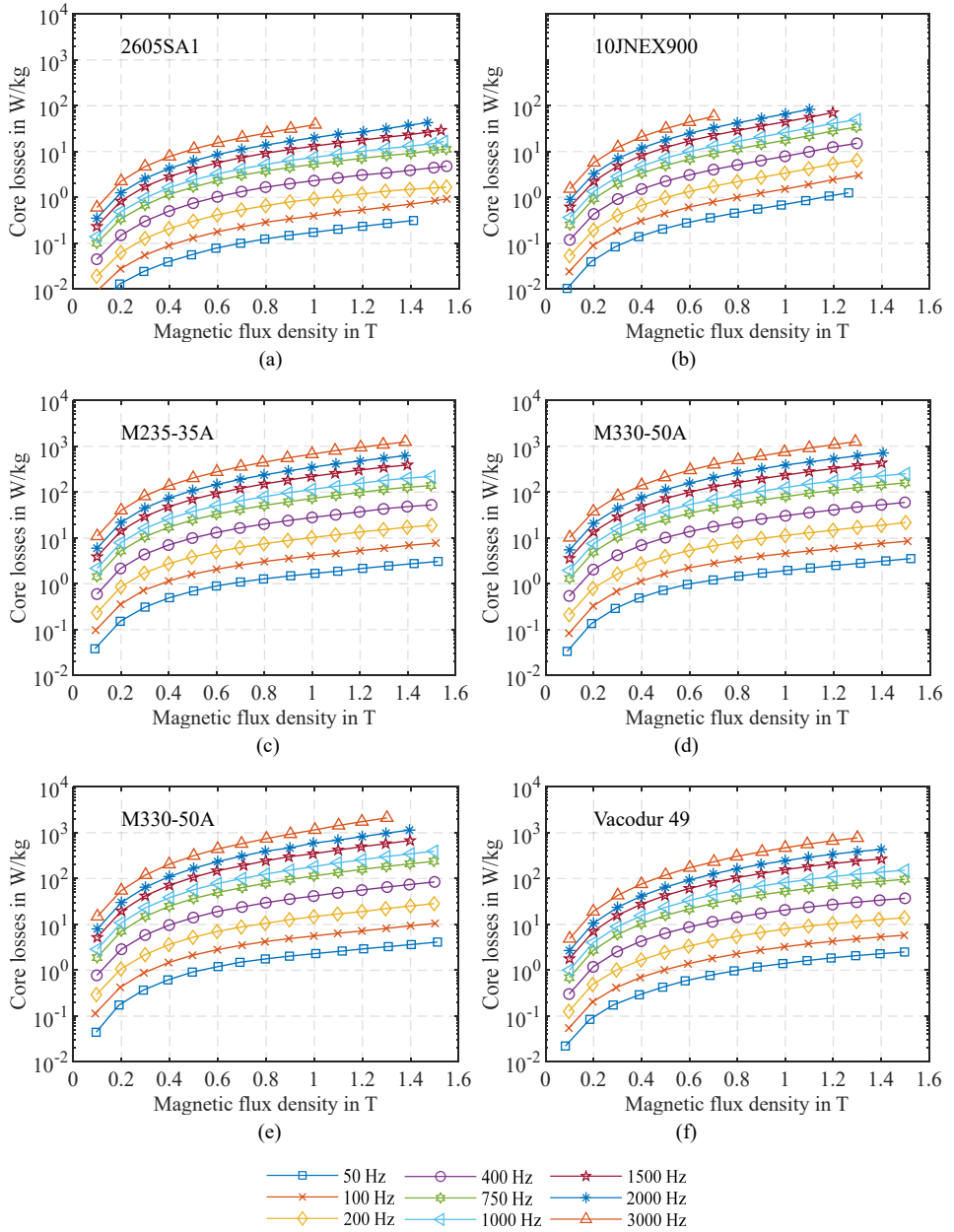
Figure 3.6:   Core losses comparison. (a) AMM 2605SA1. (b) 10JNEX900. (c) M235-35A. (d) M330-35A. (e) M330-50A. (f) Vacodur 49.

By comparing the commutation curves as presented in Fig. 3.5 of the materials with a same thickness, M235-35A, M330-35A and Vacodur 49, it can be found that the differences of the commutation curves between low and high frequencies are similar. It can be concluded that when the eddy current loss of the core is dominant, the magnetization ability of the core is frequency-dependent. In other words, when the commutation curves are frequency-dependent, the eddy current loss is high. This conclusion is useful for the later study of the influence of the stacking factor on the properties of the AMM cores.

The core losses of all the tested steels are compared in Fig. 3.6. AMM has the lowest core losses; the second lowest is 10JNEX900; the next are Vacodur 49 and M235-35A, followed by M330-35A and M330-50A. The ranking of the materials regarding losses can be more clearly seen according to the *B-H* loops as presented in Fig. 3.4. The core losses of 2605SA1, 10JNEX900, M235-35A, M330-35A, M330-50A, and Vacodur 49 at 1,000 Hz and 1.2 T are 8.98 W, 41.29 W, 155.89 W, 175.08 W, 257.59 W, 110.31 W, respectively.

Since the tested magnetic field strength is lower than 3,000 A/m, in order to show the flux densities of these materials at the higher magnetic field strength region, the magnetization curves provided by the manufacturers of these electrical steels are presented in Fig. 3.7. Based on the test results and the data provided by the manufacturers, it can be concluded that the AMM has the lowest core losses and moderate saturation flux density.
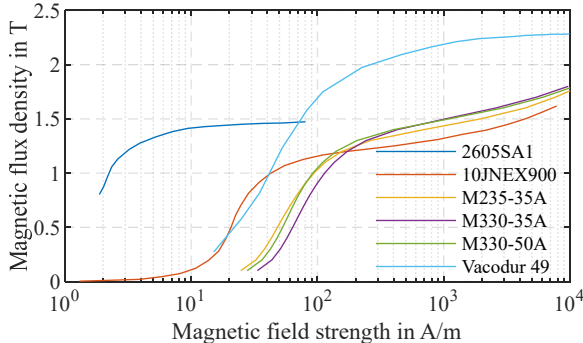
Figure 3.7:   Typical *B-H* curves at 50 Hz provided by the manufacturers.

3.2 AMM core degradation

According to the experimental results of the AMM cores, it is found that the performances of different AMM cores are much different. Especially, the core losses of the degraded AMM core are a few times the AMM ribbon. Hence, in order to better utilize the AMM cores and avoid serious degradation, a thorough study of the core degradation problem is necessary. In this section, the influences of the stacking factor, the external stress from the

housing, the working temperature and the annealing treatment on the AMM cores are studied.

3.2.1   Non-annealed AMM ribbon

Firstly, in order to avoid the influence of the aforementioned factors, the non-annealed raw AMM ribbon without any further process such as stacking, is measured by using Epstein method. A cast width of 30 mm as is shown in Fig. 3.8(a) is used to avoid the influence of the cutting on the edge of the ribbon. The Epstein frame is shown in Fig. 3.8(b). The measured results are presented in Fig. 3.9. Fig. 3.9(a) shows that the area of the *B-H* loop at a higher frequency is larger because of higher core losses. By comparing Fig. 3.9(a) with Fig. 3.4(a) it can be found that the saturation flux density of the non-annealed AMM ribbon is higher than that of the inside magnetic field annealed AMM core. For example, the flux density of the non-annealed AMM ribbon reaches 1.5 T when the magnetic field strength is about 1,500 A/m, while the annealed core reaches 1.47 T at about 2,000 A/m. The core loss of the raw AMM ribbon at 1,000 kHz and 1.2 T is about 10.13 W. It is about 13 % higher than the inside magnetic field annealed AMM core presented in section 3.1.2.

| (a) | (b) |
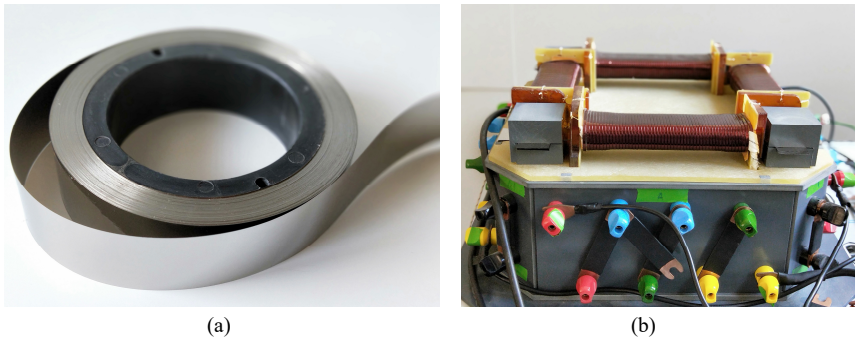
Figure 3.8:   Test of the non-annealed AMM robbon by using Epstein frame method. (a) AMM ribbon. (b) Epstrein frame.

To evaluate the measurement accuracy, the test losses (abbreviation as "E") are compared with the data from the AMM ribbon manufacturer Hitachi (abbreviation as "H") as presented in Fig. 3.10. It is easy to find that the tested data has a very high accuracy and it can be used as a benchmark for the later influence study. For example, the tested loss at 1,000 Hz and 1.2 T is 10.13 W while the loss from Hitachi is about 9.76 W, which is about 3.7 % lower. From an engineering view this error is acceptable and the accuracy of the tested data is adequate for the design of the electrical machines.
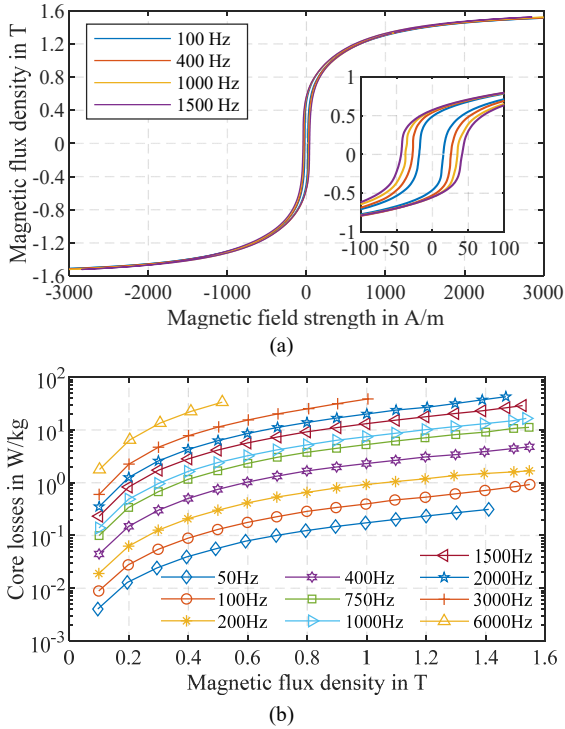
Figure 3.9: Test results of the non-annealed AMM robbon by using Epstein method. (a) *B-H* loops. (b) Core losses.
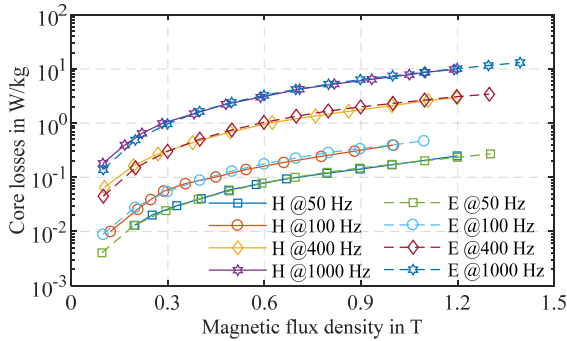
Figure 3.10: Epstein frame test results (E) compared with Hitachi data (H).

3.2.2 Influence of the stacking factor

As the thickness of the 2605SA1 ribbon is only 23 μm, the stacking factor of this material is much lower than that of the silicon irons (SIs). Generally, the stacking factor of the AMM

cores is about 0.88 to 0.92, while the stacking factor of the SI core is about 0.95 to 0.98. There are two kinds of glue used in making the AMM cores: one can strongly form the cores while the other can weakly form the cores. Both strongly and weakly formed AMM cores look like a solid component. However, the strongly formed core has a high stiffness in laminated direction. The AMM layers of the strongly formed AMM core cannot be separated any more because of high adhesive force between the layers. The AMM layers of the weakly formed core can be easily separated as can be seen in Fig. 3.11. Weakly formed AMM core has a low stiffness in laminated direction. Because of high stress induced during stacking and this stress cannot be released when it is strongly formed, the strongly formed cores may have higher losses than the weakly formed cores.
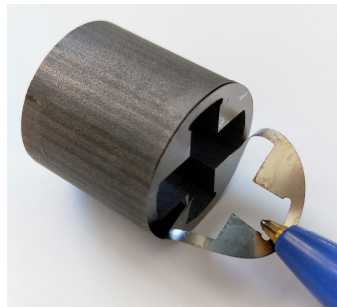
Figure 3.11:   Layers can be easily separated of the weakly formed AMM core even though it looks like a solid component.

Four AMM cores cut by the same method (wire electrical discharge machinning) with the same dimensions are tested. Two of them are strongly formed and the other two cores are weakly formed. The four cores have different stacking factors. The stacking factors (SF) of the two strongly formed cores are about 0.934 and 0.925 respectively, while the SFs of the two weakly formed cores are about 0.929 and 0.905 respectively. The tested results of them are shown in Fig. 3.12 and Fig. 3.13.

The measurement results illustrate that the commutation curves of them are similar; and that the maximum relative permeabilities occur at about 0.2 T and are generally increased when the stacking factor is decreased. When the stacking factor is higher, the magnetic field strength needed to reach the same magnetic flux density is generally higher as shown in Fig. 3.11(c). However, the core losses of these cores are much different. No matter the cores are strongly formed or weakly formed, higher stacking factor will cause higher core losses. Moreover, the strongly formed cores have higher core losses than the weakly formed cores even though the stacking factor of the strongly formed core is lower than that of the weakly formed core. For example, the core losses of the weakly formed core of SF 0.929 are about 83% of the strongly formed core of SF 0.925. Hence, it is better to avoid strongly formed cores. This means that the core losses can be reduced by releasing the

stacking stress of the core, for instance, by means of further heat-treatment. However, the working temperature of the glue needs to be taken into consideration. Generally, the working temperature of the glue is lower than the heat-treating temperature. In order to obtain low core losses, the stacking factor needs to be relatively low. For example, the core losses of the weakly formed core of the SF 0.905 are only about 1.4 times of the non-annealed AMM ribbon.
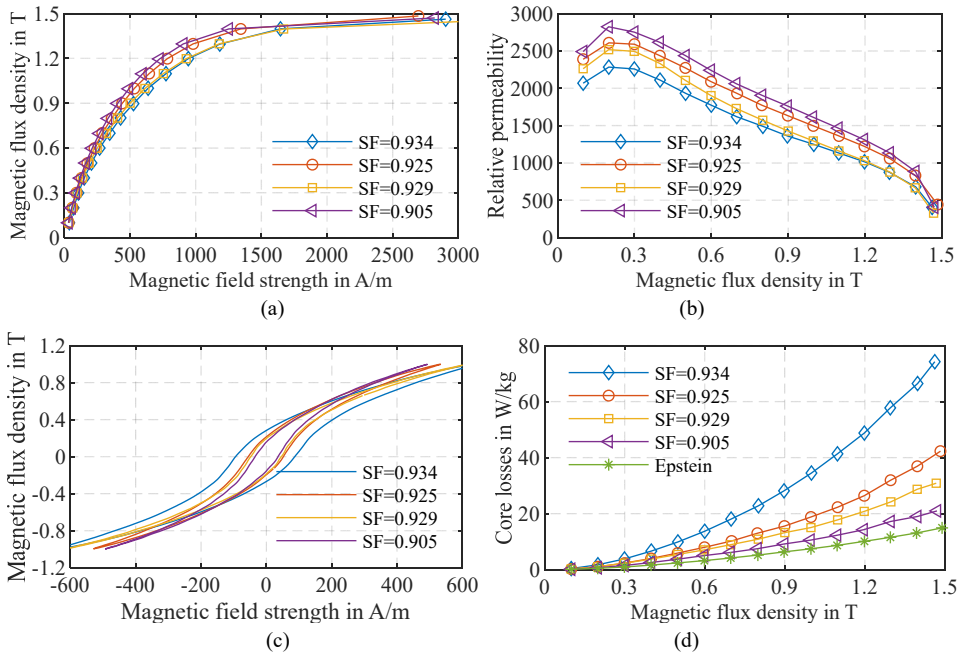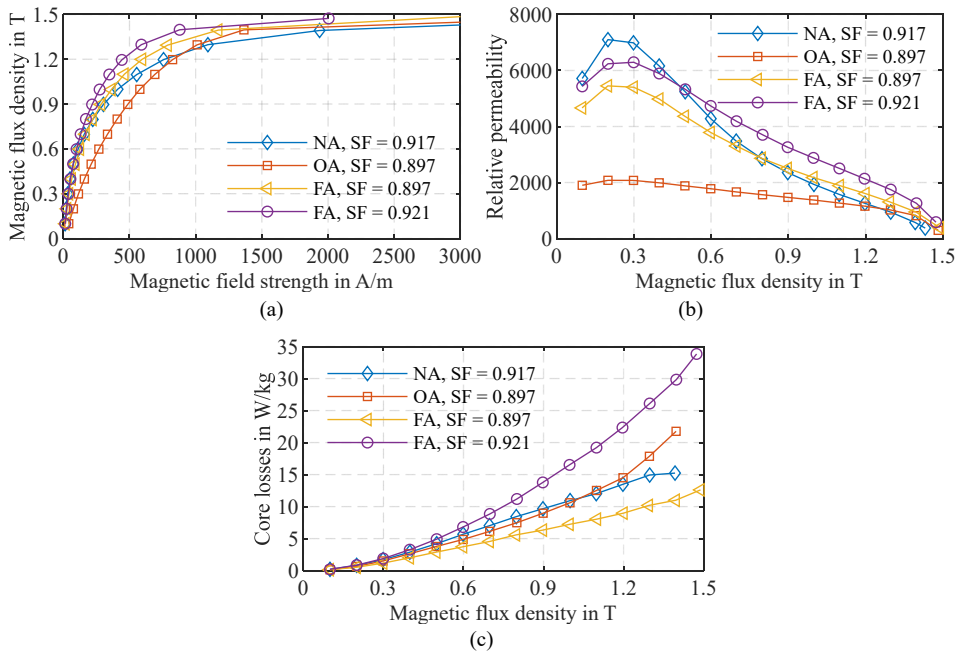

Figure 3.12:   Influences of the stacking factor on the magnetic properties of the AMM cores at 1,000 Hz.
(a) Commutation curves. (b) Relative permeability. (c) *B-H* loops. (d) Core losses.

The commutation curves of one strongly formed and one weakly formed AMM cores are presented in Fig. 3.13. It shows that the magnetization abilities of both cores are frequency-independent. In oterh words, the eddy current losses of both cores are not significantly increased with frequency even though the total core losses are increased. This results from the stable insulation of the AMM ribbon even though the insulation is very thin.
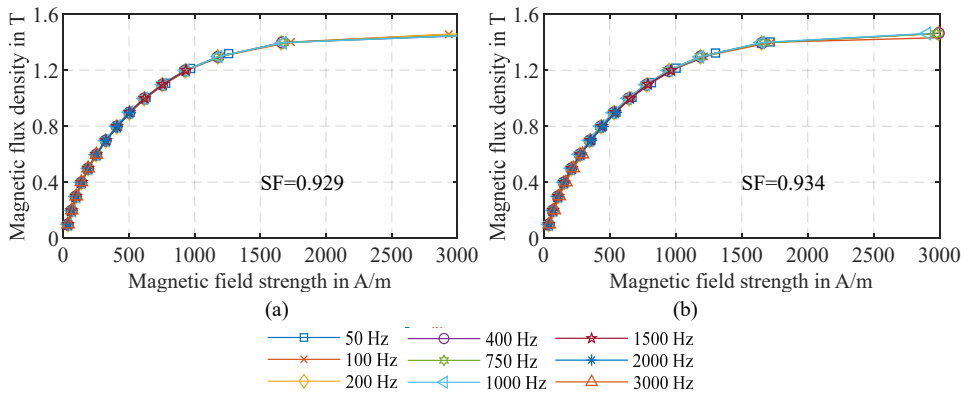
Figure 3.13:   Commutation curves of different stacking factors (a) SF = 0.929 weakly formed. (b) SF = 0.934 strongly formed.

3.2.3 Influence of the external stress

To further study the influence of the stress, external stresses are added to the toroidal cores by using auxiliary components as presented in Fig. 3.14. Force sensors are installed to measure the stress value. Because the size of the force sensors used is small, the maximum tested pressure is only 2 MPa. Both radial and axial stresses working on the strongly formed core of the stacking factor of 0.934 are investigated and the results are illustrated in Fig. 3.15. The experimental results show that both radial and axial pressures (RP and AP) will cause the degradation of the AMM cores, including the decrease of the saturation flux density and the increase of the core losses.

Figure 3.14:   Methods to add mechanical stress to the cores. (a) Device to apply axial force. (b) Device to apply radial force.
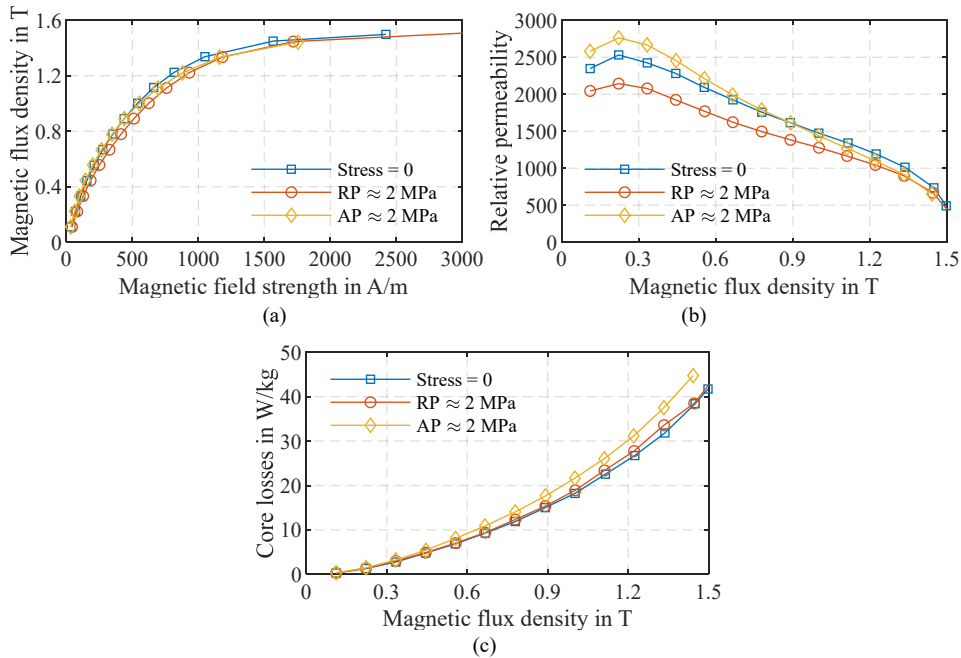
Figure 3.15: Influences of the external stresses on the magnetic properties of the AMM cores at 1,000 Hz. (a) Commutation curves. (b) Relative permeability. (c) Core losses.

The radial pressure has a greater influence on the decrease of the relative permeability, whereas the axial pressure results in higher core losses. When the axial pressure is about 2 MPa, the core losses are increased by about 15%. Compared with the influence of the stacking factor, the influence of the external stress at 2 MPa is smaller. The reason might be that the axial pressure cannot cause further deformation, because the internal stress of the core caused by stacking process is high and the core is very tight.

3.2.4 Influence of annealing treatment

It is well-known that annealing treatment can help to improve the performance of the AMM. The annealing condition plays an important role in the magnetic properties of the AMM core. In this dissertation, to find out the best annealing condition is not my research focus since we are not able to conduct the annealing treatment in our institute. The aim of this part is to show whether the annealed core is always better than the non-annealed core or not.

The test results of four cores of non-annealed (NA), ordinary heat-treated (OA) and inside magnetic field heat-treated (FA) AMM core are compared in Fig. 3.16. From Fig. 3.16 it can be seen that after heat treatment, the maximum relative permeability is decreased,

whereas the saturation flux density is increased. However, the core losses of the annealed core may be higher than those of the non-annealed core. For example, as presented in Fig. 3.16(c), when the magnetic flux density is higher than 1 T, the core losses of the ordinary heat-treated core are higher than those of the non-annealed core even though the stacking factor of the former is lower. As for the inside magnetic field annealed core of stacking factor 0.921, the core losses are much higher than those of the non-annealed core. Because the stacking factor of this annealed core is higher than that of the non-annealed core, it is not clear whether the higher core losses are caused by the higher stacking factor or the annealing treatment. By comparing the two cores of the same stacking factor of 0.897, it is believed that inside magnetic field annealing can obtain a better performance. To summarize, the experiment results show that annealing treatment may not dramatically improve the performance of the AMM core. In addition, the AMM cores become brittle after heat treatment. Therefore, it is necessary to keep these points in mind in the application of the AMM cores.

Figure 3.16:   Influence of heat-treating on the magnetic properties of the AMM cores at 1,000 Hz. (a) Commutation curves. (b) Relative permeability. (c) Core losses.

3.2.5   Influence of temperature

The AMM cores are not only sensitive to stress, but also very sensitive to the temperature. Fig. 3.17 and Fig. 3.18 illustrate the properties of the heat-treated and non-heat-treated

AMM cores as a function of the temperature, respectively. The influences of the temperature on both AMM cores are very similar. The magnetization abilities of the AMM cores at high temperature are still frequency-independent. It can also be noticed that when the temperature is increased, the saturation flux densities of the two cores are dramatically decreased and the core losses are slightly reduced, whereas the maximum relative permeability is increased. When the working temperature is increased from room temperature (RT) to 150 °C, the reduction of the saturation flux density of the heat-treated core is about 9 % and 10 % for the non-heat-treated core; the core losses of the heat-treated core are reduced by 13.3 %, while the non-heat-treated core are reduced by 6.1 %.

The core losses reduction at a high temperature might be mainly because the resistivity of the AMM is increased when the temperature is increased. Meanwhile, the maximum relative permeability at 150 °C is almost twice that at room temperature for the heat-treated core, while as regards the non-heat-treated core, this value is about 1.5 times.
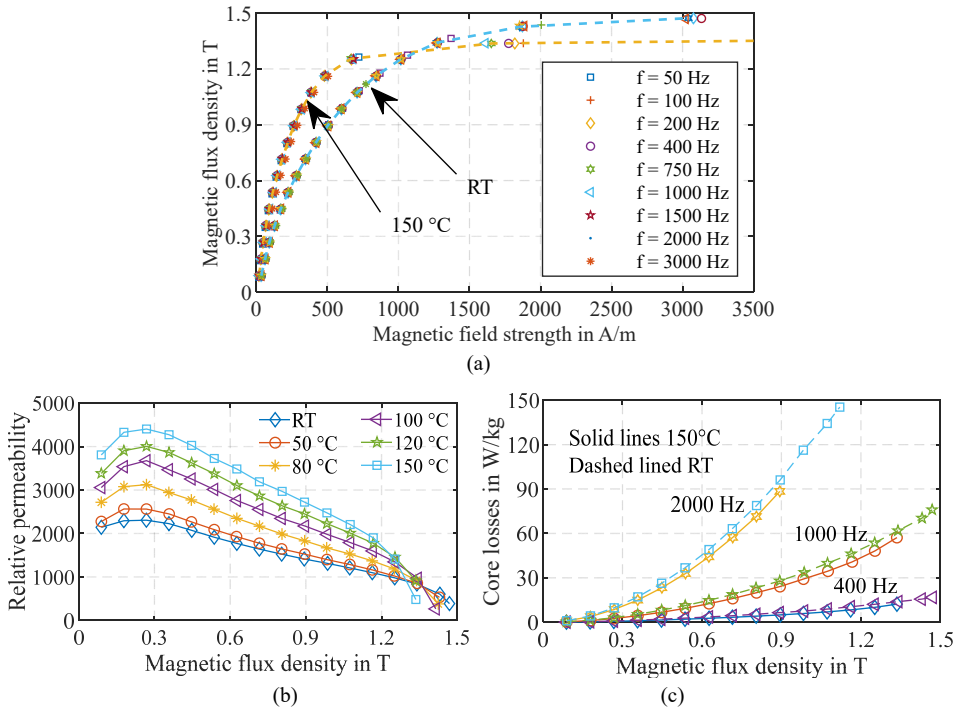
Figure 3.17:   Influences of the temperature on the magnetic properties of the ordinary heat-treated AMM core. (a) Commutation curves. (b) Relative permeability. (c) Core losses.
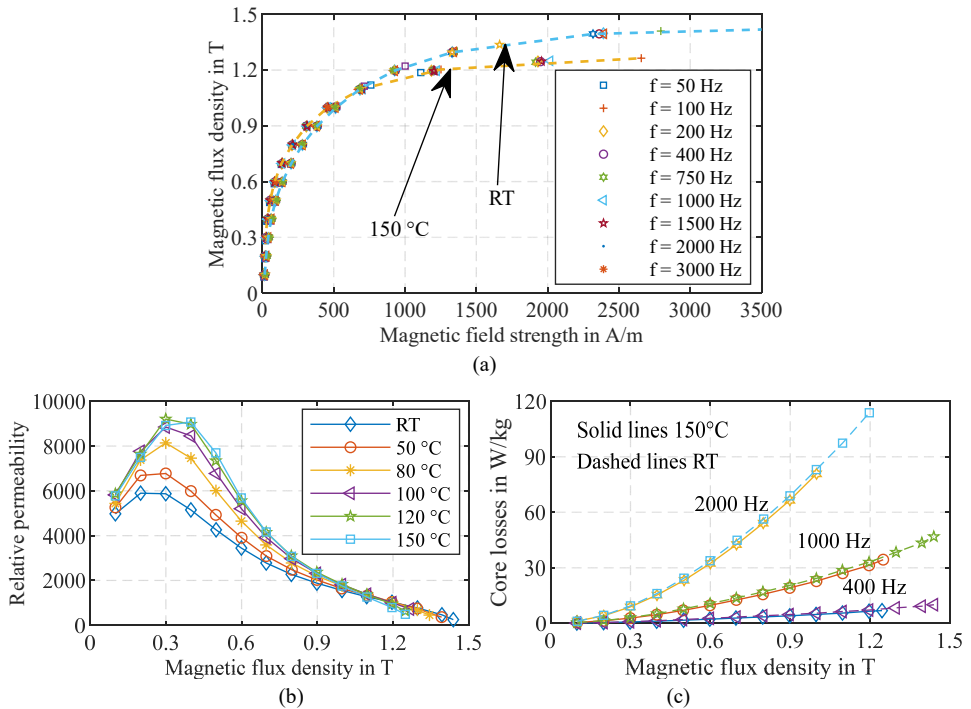
Figure 3.18:   Influences of the temperature on the magnetic properties of the non-annealed AMM core. (a) Commutation curves. (b) Relative permeability. (c) Core losses.

3.2.6   Influence of temperature on M235-35A

Compared with the AMM cores, the silicon iron M235-35A has much stable properties when the temperature is increased from RT to 150 °C as presented in Fig. 3.19. However, its variation trend is different from the AMM cores. When the temperature is increased, not only the saturation flux density and the core losses are slightly reduced, but also the relative permeability of the core is reduced. When the temperature is increased, the magnetic field strength required to reach a specific flux density is higher. Because the resistivity of the M235-35A increases when temperature increases, the eddy current loss decreases. Hence, it is believed that the magnetization ability of the M235-35A decreases when temperature increases. The core losses of M235-35A at 150 °C are about 5.6 % lower than those at RT, which is comparable with the non-heat-treated AMM core. The tested results show that M235-35A has much lower relative permeability than the AMM cores.
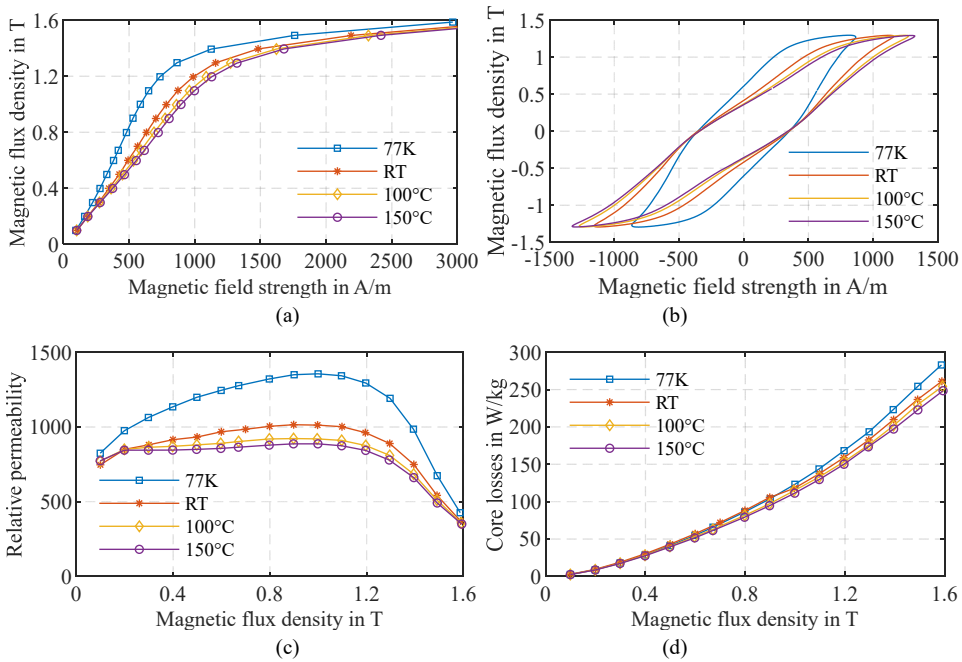
Figure 3.19:   Influences of the temperature on the magnetic properties of the M235-35A at 1,000 Hz. (a) Commutation curves. (b) *B-H* loops (c) Relative permeability. (d) Core losses.

3.2.7   Influence of temperature on 10JNEX900

The influence of the temperature on the magnetic properties of the core 10JNEX900 is presented in Fig. 3.20. It is easy to find that the variation of the saturation flux density and the relative permeability of this core are similar to the the conventional silicon iron M235-35A when the temperature is increased. The magnetic field strength required to reach a specific flux density at a higher temperature is higher. However, the core losses at a higher temperature are higher than those at a lower temperature, which is completely different from the AMM and the M235-35A cores. When the temperature is increased from RT to 100 °C, the properites of the 10JNEX900 core change sharply. When the temperature is increased from RT to 150 °C, the core losses of 10JNEX900 are increased by 24.7 %; and the relative permeability is reduced by about 60 %. Because the resistivity of 10JNEX900 is not measured, it is not sure whether the eddy loss increases or the magnetization ability decreases when the temperature increases.
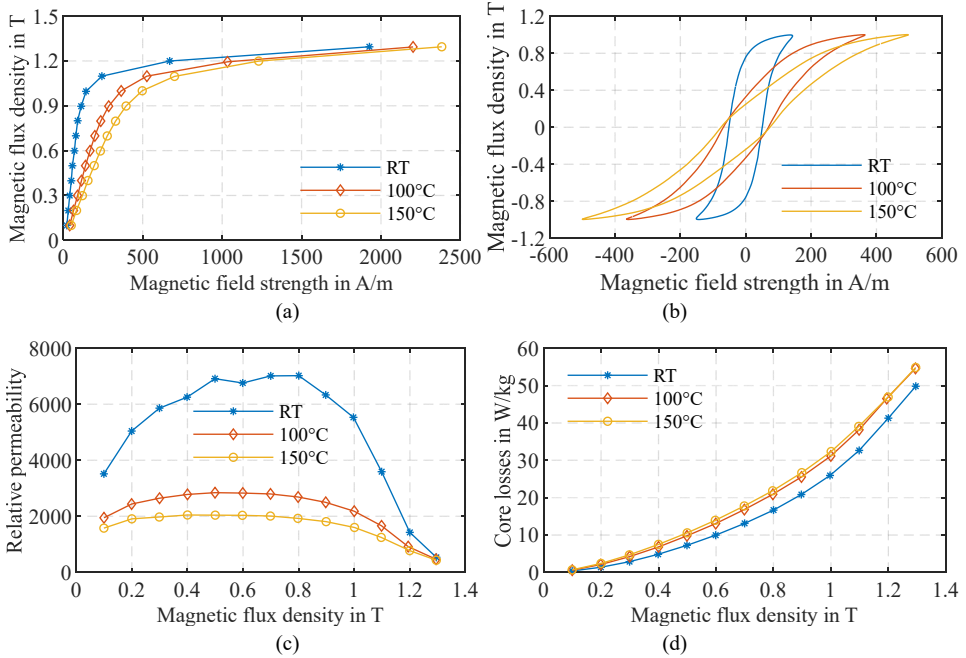
Figure 3.20:   Influences of the temperature on the magnetic properties of the 10JNEX900 at 1,000 Hz. (a) Commutation curves. (b) *B-H* loops (c) Relative permeability. (d) Core losses.

3.3   Mechanical properties measurement

Based on the data from the manufacturer, the yield strength of the AMM core is higher than 700 MPa [128]. However, it is unclear whether heat treatment and mechanical machining will decrease the strength of the AMM cores or not. Hence, it is necessary to measure the mechanical properties of the AMM in order to ensure the success of the prototype.

The measurement specimen and device are shown in Fig. 3.21. The dimension of the specimen is based on the norm ASTM E8 and the dimension is shown in Fig. 3.21(a). The specimens are cut by WEDM method. In order to measure the deformation under the tensile stress, clip-on extensometers consist of a titanium alloy or copper-beryllium frame are used as shown in Fig. 3.21. The extensometer is equipped with a Wheatstone bridge of 350 Ω strain gauges. The introduction of the test device and the design of the extensometer are introduced in [129] and [130]. Because the AMM ribbon after heat treatment is brittle, the clip-on extensometers may crack the sample before or during the measurement, which causes failure of the test. Hence, the specimens consisting of 3-layer are tested. However, for multi-layer test, because the strains of each layer are not identical, the stresses of them are also different. The sample might be cracked layer by layer and the tested strength is much lower than the real strength of each layer. The test results of four specimens are

shown in Fig. 3.22. Because the AMMs are brittle, they do not have non-linear elastic region, as can be seen from Fig. 3.22. The ultimate tensile strength (UTS) is tested instead of yield tensile strength.

(a)

(b)

(c)
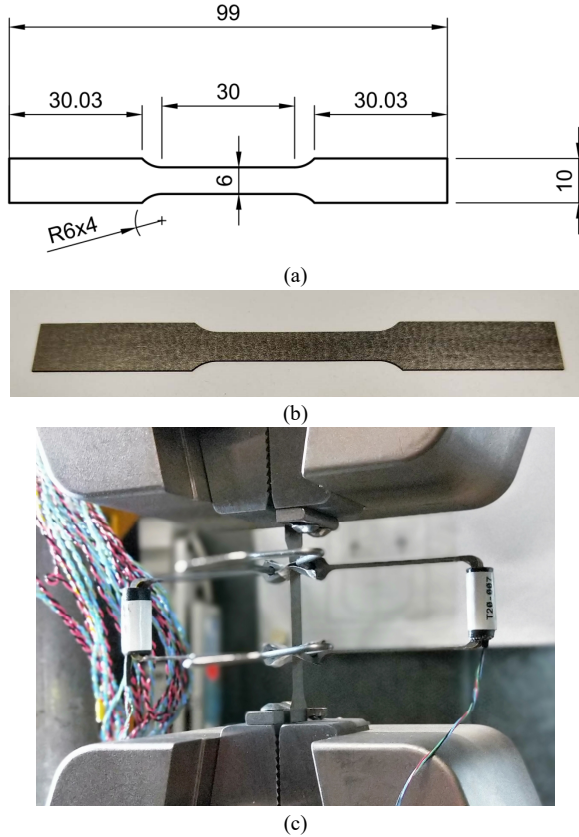
Figure 3.21:   Tensile strength measurement. (a) Dimension of the AMM Specimen. (b) AMM Specimen. (c) Measurement device.

The tested results show that the UTS of the single sheet can be higher than 1,000 MPa. The mulit-layer samples have a lower UTS than the single sheet. The UTS of the annealed 3-layer samples are higher than 600 MPa. Based on the tested results and the data from the manufacturer, it is believed that the yield strength of the AMM ribbon is higher than 700 MPa. However, it is worth to point out that any defect in the AMM core may significantly reduce the strength of the core. The prototype may not have the same strength as the tested specimens due to the impacts of the machining and assambly.
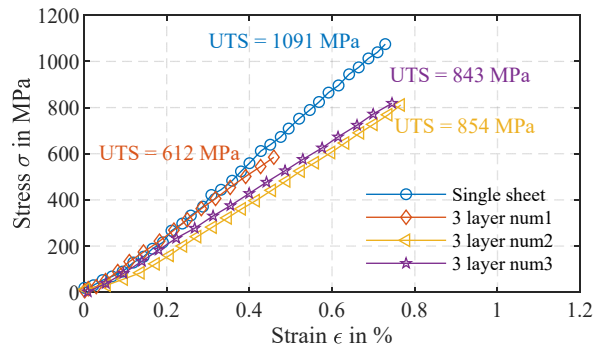
Figure 3.22:   Tensile strength measurement results.
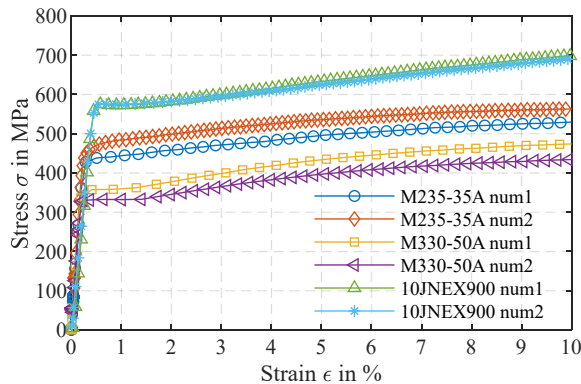
Figure 3.23:   Tensile strength measurement results of M235-35A, M330-50A and 10JNEX900.

In this dissertation, WEDM is used to cut the toroidal cores, the ASTM E8 specimens and the rotor cores. The electromagnetic and mechanical tests have proved the feasibility of this cutting method. However, if another cutting technique is used for this high-speed rotor core, the mechanical properties must be tested again in order to evaluate the influence of this method on the tensile strength of the core. The strength of the silicon steels are also tested as presented in Fig. 3.23. The tested yield strengths of the M235-35A, M330-50A and 10JNEX900 are about 450 MPa, 350 MPa and 570 MPa, respectively.

3.4   Summary of the material properties

The properties of the materials tested are summarized and compared in Table. 3.1. It can be seen that the AMM has not only the highest tensile strength but also the lowest core losses. To ensure that the rotor has high mechanical strength and to minimize the rotor core losses, the best choice of the rotor core material is AMM. The second choice is 10JNEX900 in terms of yield strength and core losses. However, although the core losses of

10JNEX900 are much lower and the strength is higher than the other crystalline steels, its flux density is relatively low. More importantly, the 10JNEX900 also faces with slotting difficulty. This material is brittle as well. The shearing and laser edges of this material are shown in Fig. 3.24. It clearly shows that the shearing edges are uneven. The cutting result of laser is unsatisfactory, either. Hence, AMM is the best choice in this high-speed application.

Material	Resistivity in $\mu\Omega\cdot$cm	Yield strength in MPa	Flux density at 1 kHz, 2 kA/m in T	Loss at 1 kHz, 1.2 T in W/kg
2605SA1	130	>700	1.46	8.98
10JNEX900	82	570	1.30	41.29
M235-35A	59	450	1.38	155.89
M330-35A	42	350	1.45	175.08
M330-50A	42	350	1.47	257.59
Vocadur 49	40	390	2.17	110.31

Table 3.1:   Eletromagnetic and mechanical properties of the electrical steels.

(a)   (b)
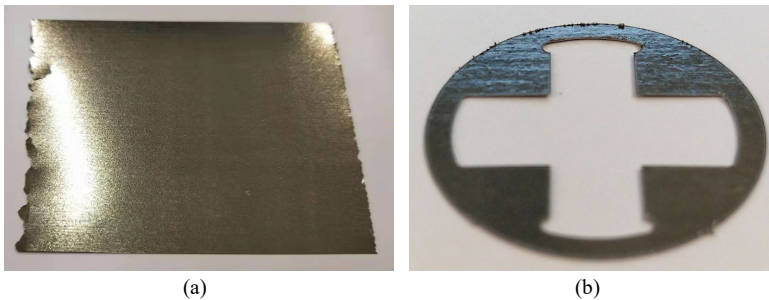
Figure 3.24:   Cutting results of the 10JNEX900. (a) Shearing. (b) Laser.

4 Multiphysics design of the proposed IPM motor

To study the feasibility of the proposed application of the AMM cores, a demonstrator motor is designed in this chapter. The electromagnetic, mechanical and thermal behaviors of the demonstrator motor will be analyzed. Moreover, in order to clearly show the advantages of using the AMM rotor core for the proposed interior PM rotor structure, the performance of a rotor made from M330-35A is analyzed and compared with the AMM rotor. Furthermore, a surface-mounted PM rotor is also designed for a comparison study.

4.1 Stator design

4.1.1 Slot/pole number combinations

Considering the switching frequency of the power electronic module, it is better to minimize the fundamental frequency of the motor. Hence, the pole-pairs number of 1 is chosen to reach a high speed of 125,000 /min. In this case, the maximum fundamental frequency of the motor is equal to 2,083 Hz.

Generally, fractional-slot concentrated-winding (FSCW) is attractive for low-speed motors, since this winding is single-tooth type and it can help to reduce the end-length of the winding which results in a compact size of the motor. A possible slot/pole combination of this high-speed application is 3-slots/2-poles as presented in Fig. 4.1. However, because the armature reaction magnetic field in the air gap of this winding consists of abundant spacial field harmonics, the rotor losses caused by the field harmonics are high and may result in the rotor PM demagnetization. In addition, since the windings are concentrated in a small number of stator slots, the heat dissipation condition of the conductor in the middle position of the slot is critical. It is necessary to reduce the electric loading and this results in reduced torque. Moreover, due to unsymmetrical flux distribution of FSCW as shown in Fig. 4.1, the rotor suffers from high unbalancing forces. This will aggravate the burden of bearings and damage them. In views of noise, vibration and harshness, the FSCW is also very bad. Hence, it will not be considered in this work.

Compared with FSCW motors, the integral-slot distributed-winding (ISDW) motors consist of much lower spacial field harmonics. This is beneficial for reducing the rotor iron and PM losses. Furthermore, the ISDW motors can avoid unbalancing forces problem. The structure and the noload flux distribution of a 12-slot/2-pole ISDW motor is shown in

Fig. 4.2. However, because ISDWs are overlapped, they have long end-windings, which not only occupy large axial space but also cause high copper losses. Since the performance of the high-speed rotor is more important in high-speed PM motors, in this work, ISDW configuration is used.
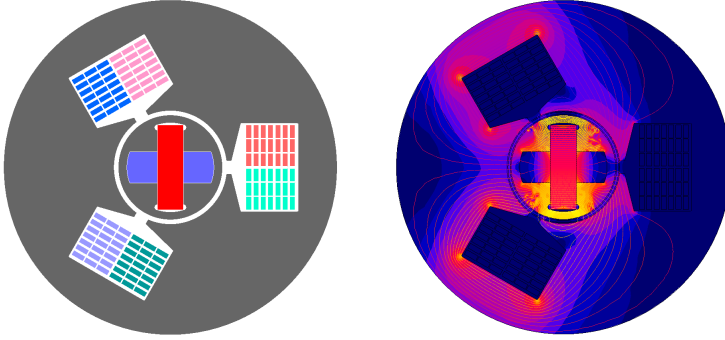
Figure 4.1:   Structure and noload flux distribution of a 3-slot/2-pole PM motor.
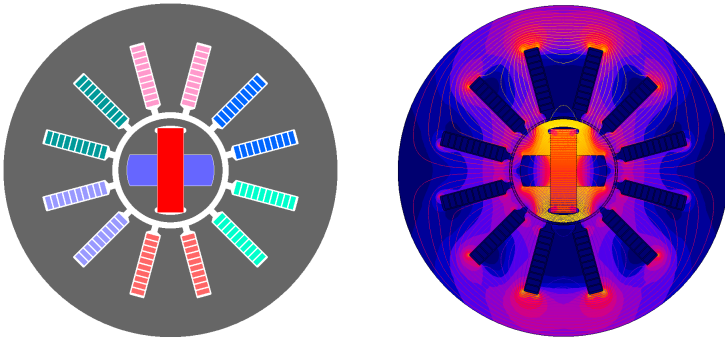
Figure 4.2:   Structure and noload flux distribution of a 12-slot/2-pole PM motor.

4.1.2   Slot and winding types

The torque of a PM synchronous motor is proportional to the magnetic and the electric loadings. These two loadings are limited by the heat dissipation ability of the motor. Because the current density of the winding is limited by the heat dissipation ability of coil, in order to increase the electric loading, a large area of the stator slots are in need. However, bigger slot will reduce the stator core region which is the main path of the flux. The magnetic loading will be decreased due to core saturation when the electric loading is increased. Hence, to fully take the advantage of the stator volume, a high copper filling factor of the slot is the design target. Generally, parallel tooth is more frequently adopted in the electrical machines of large volume. Since the copper filling factor of the parallel-tooth stator

configured with flat wire is low, round wire is better as shown in Fig. 4.3(a). Compared with the parallel tooth, parallel slot configured with flat wire as shown in Fig. 4.3(b) generally has a higher copper filling factor. Higher electric loading and shorter end-winding can be attained by using the winding technologies of Dr. Markus Schiefer's company SciMo – Elektrische Hochleistungsantriebe GmbH. Dr. Markus Schifer highly recommoned this type of stator. Hence, these two types of stators are considered.

(a)   (b)
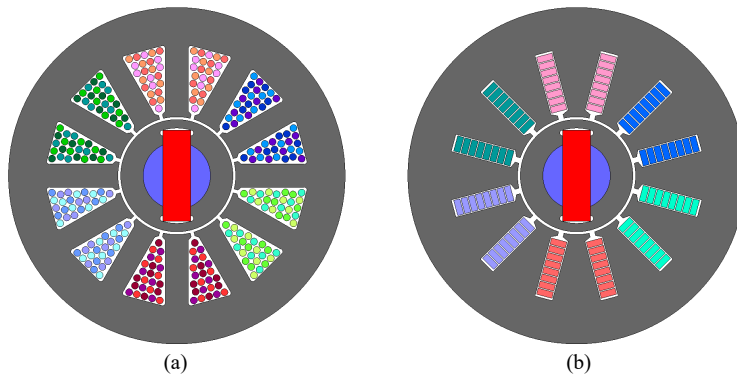
Figure 4.3:   Stator configurations. (a) Parallel tooth with round coils. (b) Parallel slot with flat coils.

Generally, a larger cross sectional area of conductor is better for reducing the copper DC Joule losses (ohmic losses). However, because the high-speed motors operate at high frequency, the AC copper losses might be dominant and a bigger conductor might bring a higher loss. Hence, the selection of the windings for the high-speed motor needs to consider the AC copper losses. There are three more types of copper losses besides DC Joule losses in the conductors, including the eddy current losses caused by the slot flux leakage and the additional losses caused by the skin effect and the proximity effect. Their principles and effects are illustrated in Fig. 4.4. The eddy current loss and the loss due to skin effect are very high at a high frequency. To reduce these two types of losses, the size of the conductor needs to be limited. As for the loss due to the proximity effect, it can be mitigated by reducing the electric loading of one slot.

(a)   (b)   (c)
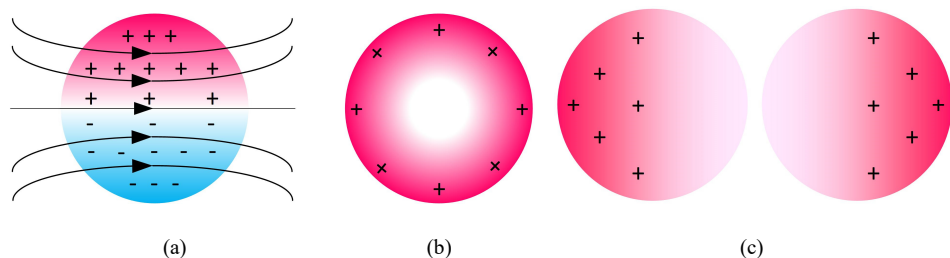
Figure 4.4:   Current distribution in the conductors of one slot. (a) Eddy current caused by magnetic field. (b) Skin effect. (c) Proximity effect.

To avoid high loss due to the skin effect at high speeds, the diameter of the conductors need to be limited. The penetration depth d of a conductor is expresses as [131]

$$d = \sqrt{\frac{\rho}{\pi f \mu_0 \mu_r}} \tag{4.1}$$

where ρ is the resistivity of the conductor in $\Omega\cdot$m; f is the frequency in Hz; μ_r is the relative magnetic permeability of the conductor; μ_0 is a physical constant which is commonly called the permeability of vacuum and it is $4\pi\times10^{-7}$ H/m.

At the maximum speed of 125,000 /min, the frequency is 2083 Hz. The penetration depth of the copper winding is about 1.43 mm. It means the diameter of the copper conductor must be smaller than 2.86 mm. In this work, a smaller diameter of 1.25 mm is selected in order to increase the copper filling factor. As shown in Fig. 4.3(a), a multi-strand wire of three-strands parallelly connected is used. The number of turns of the two stators shown in Fig. 4.3 is 8 in each slot. In Fig. 4.3(b) a flat wire of 1.12 mm thick and 2.8 mm wide is used. When the phase current is 60 A, the current distributions on the windings are shown in Fig. 4.5. Although the cross sectional area of the round wires is higher than that of the flat wire (4.32 mm² of multi-strand round wire and 3.14 mm² of flat wire), the maximum current density on the round wires is higher than that of the flat wires because high eddy current is induced in the conductors at a high frequency. Since the Joule losses is proportional to the square of the current density, the maximum Joule losses density of the round wires is higher than that of the flat wire. This may bring heat dissipation problem. Moreover, the torque of the parallel tooth motor is only 1.35 Nm while the torque of the motor using parallel slot is 1.45 Nm when they have the same electric loading and rotor. The torque of the motor with parallel slot is about 7.4% higher because of relatively low magnetic saturation of the stator core.
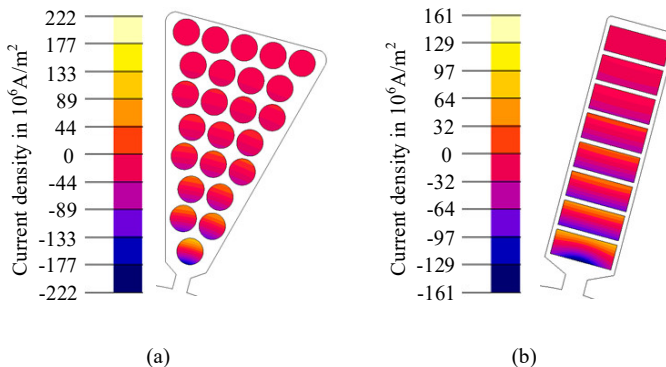
Figure 4.5:   Current densities of the windings. (a) Parallel tooth with round conductors. (b) Parallel slot with flat conductors.

It can be noticed from Fig. 4.5 that the current distribution of the conductors in one slot is uneven. The conductors close to the air gap have much higher current densities than those of the bottom conductors at the same slot. Based on Fig. 4.4 it can be known that this problem is mainly caused by the slot flux leakage. For instance, for the parallel slot with flat wire configuration, when the phase current is positive, the flux line of the armature field slot leakage is shown in Fig. 4.6(a). To avoid the influence from the PM field, the remanence of the PM is set to zero. Since the phase current is sinusoidal, when the phase current reaches its peak value, the flux density distribution in the conductors's regions is shown in Fig. 4.6(b). It can be found that the flux density of the conductor 1 is much higher than that of the other conductors as the flux line pass through the conductor 1 is generated by the currents of conductors 2 to 8. Based on Lenz's law, the eddy currents will be induced in the conductors. The maximum eddy current occurs at the moment of the phase current is zero. When the phase current is zero and it is increasing, the current distribution is shown in Fig. 4.6(c). It can be seen that the eddy current caused by slot flux leakage is much higher than the phase current by comparing the current densities of conductor 1 and conductor 8. To reduce the eddy current losses of the windings, it is necessary to use a wider slot and thinner flat wire. In addition, when the electric loading of one slot is reduced, this loss can also be decreased.
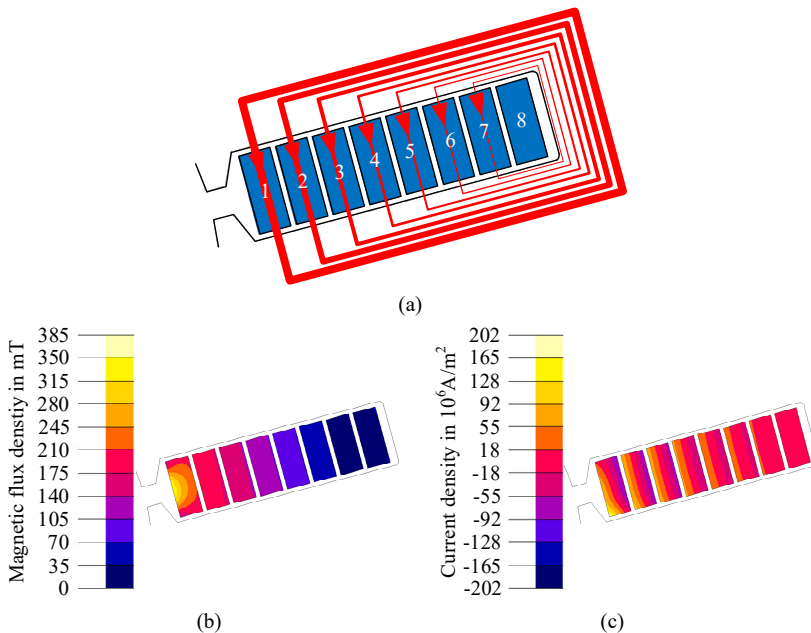
Figure 4.6: Eddy currents caused by armature reaction magnetic field leakage. (a) Flux leakage. (b) Flux density distribution. (c) Current distribution.

4.1.2.1 **Multi-strand round wires**

In order to reduce the eddy current losses and mitigate the skin effect, multi-strand wires with a smaller diameter are more commonly used. Based on the previous analysis, the parallel tooth stator is employed when the round wires are used. Because the width of the slot close to the air gap is very small, the eddy current losses of the conductors which are close to the air gap are much higher than those of the condutors at the bottom. Hence, the slot area close to the slot opening is unusable.

Moreover, the flux linkage of the high-speed motor is generally low in order to avoid overvoltage at a high speed. This requires less number of turns of the windings. A small difference of the strands such as end-length and the position in the slot may cause much different induced voltage at a high speed. For the multi-strand round wires, the difference of the induced voltages among strands will cause loop current within the phase. This aggravates the copper losses. To calculate the influence of the multi-strand wires, the strands at one slot are connected as shown in Fig. 4.7. Then the strand currents and the Joule losses of each conductor of three different distributions as shown in Fig. 4.8 are calculated and drawn in Fig. 4.9.
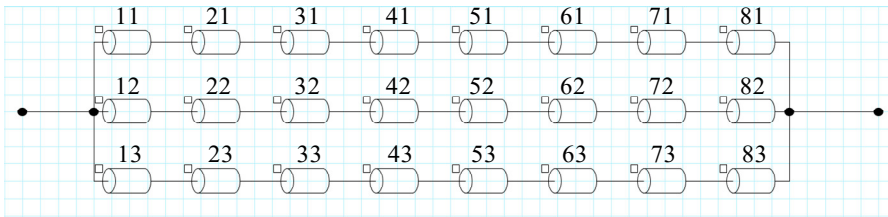
Figure 4.7:   Connection of a 3-strand wire in one slot.

In Fig. 4.8 three cases are compared and the difference of end-length of the windings is not considered. They are ideal case which has small current difference among the strands; normal case which is more similar to a real motor and the worst case which has maximum current difference among strands. The corresponding strand currents of these cases are shown in the left column of Fig. 4.9. It clearly shows that the currents in the strands of the ideal case and the normal case are very similar, while the currents of the worst case are much different in both the amplitude and the phase angle. The losses of the ideal case and the normal case are comparable. Even though the maximum current in the strands of the worst case is higher than twice that of the other two cases, the Joule losses of the worst case is still not much higher as it can be seen in the right column of Fig. 4.9. It is because the eddy current caused by the slot leakage is dominant.
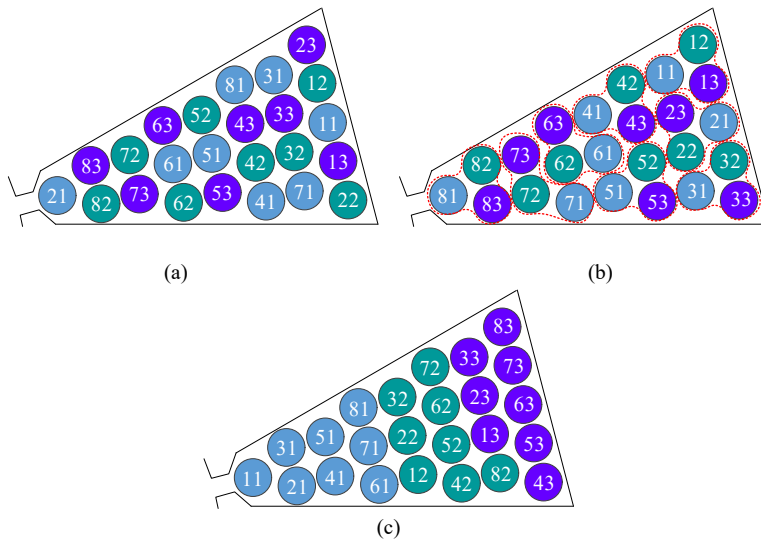
Figure 4.8: Three different distributions of multi-strand wires (each color represents a strand) in one slot. (a) Ideal distribution. (b) Normal distribution. (c) Worst case.

Based on the previous analysis it is known that the conductor which is close to the slot opening has highest current density. In order to reduce the total losses, these areas which are close to the slot opening are not used. When a smaller size of wire consisting of 5-strand is used, and the distribution of the conductors as is shown in Fig. 4.10(a), the Joule losses of the strands are presented in Fig. 4.10(b). It shows that the Joule losses difference among the conductors of different positions is reduced. This is because the slot leakage flux density decreases along the radial direction of the slot.

The comparison of the Joule losses of the wires consisting of 3-strand and 5-strand respectively is presented in Table 4.1. In Table 4.1 the nominal current density is equal to the phase RMS current divided by the wire area. Although the nominal current density of the big wire is lower than that of the small wire consisting of higher number of strands, the Joule losses of the big wire are still higher than those of the small wire as aforementioned. It is because the eddy current losses in the conductors which are close to the slot opening are dominant.
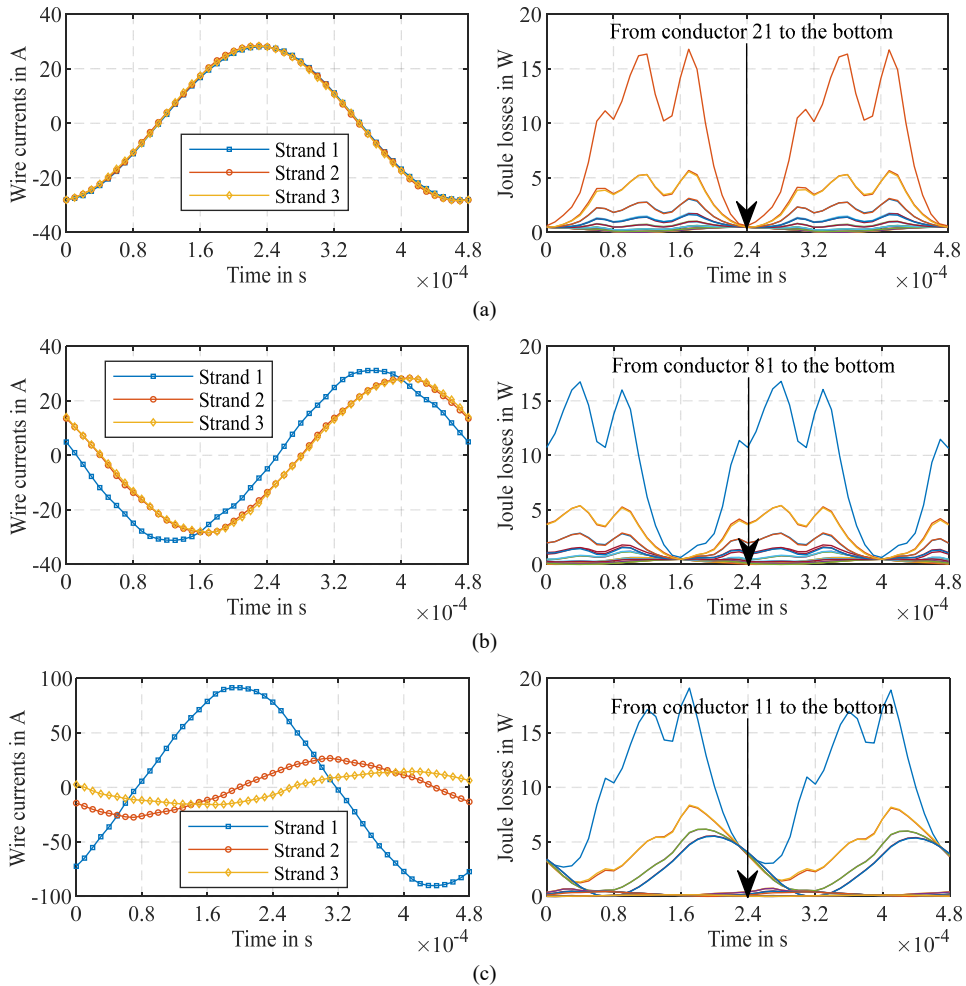
Figure 4.9: Wire currents and wire Joule losses of the multi-strand wires corresponding to differen wire distributions. (a) Ideal distribution. (b) Normal distribution. (c) Worst case.

Although the compact windings as shown in Fig. 4.10 can dramatically reduce the Joule losses, to realize such a high filling factor is challenging. The copper filling factor of the stator in this case is higher than 0.54, even though part of the slot is not used. Moreover, the overload performance is reduced due to the narrow tooth. For example, when the magneto motive force of one slot is 700 A-RMS, the torque of the parallel tooth motor is only 1.88 Nm while the torque of the parallel slot motor is 2.44 Nm, which is about 30% higher.
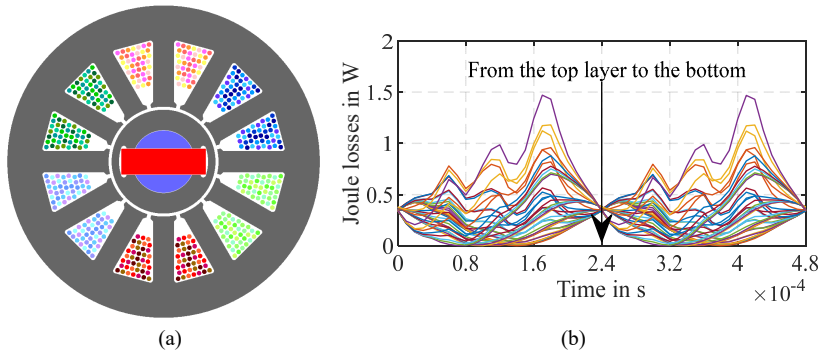
Figure 4.10: Conductors distribution and Joule losses of the stator using 5-strands wire. (a) Conductors distribution. (b) Joule losses of the conductors in one slot.

Winding type	3-strand	5-strand
Area of one strand in mm^2	1.44	0.69
Total area of one phase in mm^2	4.32	3.45
Nominal current density in A/mm^2	15.05	18.84
Torque in Nm	1.47	1.46
Max. conductor losses density in W/cm^3	139.40	24.40
Total Joule losses in one slot in W	31.74	14.47

Table 4.1: Joule losses comparison of 3-strand and 5-strand wires at 125,000 /min.

4.1.2.2 Flat wires

Different from the parallel tooth stator, the slot width of the parallel slot stator is constant. Based on the analysis as presented in Fig. 4.6 it is known that the eddy current of the conductors are induced by the currents of the other conductors in the same slot. Hence, even though all the conductors are far away from the air gap, the one closest to the air gap still has a high Joule loss. Hence, it is better to use a wide slot. However, this may decrease the magnetic conductivity of the stator. By changing the number of turns of the coil in one slot, the Joule losses of the conductor which is closest to the air gap may be reduced. However, this improvement is limited. For example, when the number of turns of one slot is changed, the maximum conductor losses and the total Joule losses of one slot are compared in Table 4.2. It can be found that when the number of turns of one slot is equal to 8, the maximum conductor losses is lowest and the total Joule losses of one slot is also low. However, a smaller number of turns results in a lower back-EMF, and a higher phase current is required to generate a specific torque. Because the current limitation of the power electronic module, higher number of turns is preferred to fit the specifications of the PWM inverters.

Number of turns per slot	6	8	10
Phase rms current in A	80	60	52
Torque in Nm	1.46	1.45	1.46
Max. conductor losses in W	7.53	6.85	6.99
Joule losses in one slot in W	22.80	23.50	29.03

Table 4.2:   Joule losses comparison of different number of turns per slot.

4.1.2.3 Litz wires

To decrease the Joule losses of the conductors caused by the slot flux leakage, an effective method is to apply litz wire. When a flat litz wire is used, the current density and the Joule losses of the conductors in one slot are presented in Fig. 4.11. It shows that the difference of the eddy current losses of the conductors of one turn distributed in different position is very small. This menas the Joule losses caused by the slot leakage are significantly reduced. However, although the litz wire is better than the flat wire in terms of the high-frequency Joule losses, the copper filling factor of the litz wire is much lower than that of the solid flat wire. This reduces the efficiency of the motor at a low speed and limits the overload performance of the motor.

(a)   (b)
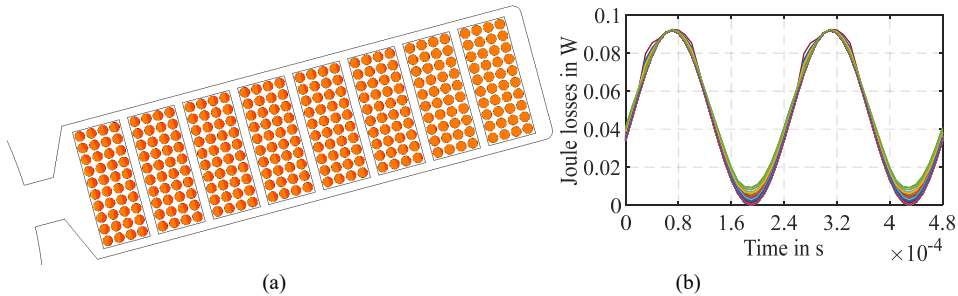
Figure 4.11:   Current density distribution and Joule losses of the flat litz wire. (a) Conductors distribution. (b) Joule losses of the conductors in one slot.

4.1.3 Slotless

In order to decrease the rotor losses, slotless stator is a good choice. However, besides the manufacture difficulty of the slotless windings, the performance of the motor configured with the slotless winding is also not competitive with the slotted motors in terms of torque and power densities. Since the equivalent air-gap length of the slotless motor is much larger than that of the slotted motor, the air-gap flux density is relatively low which results in a low torque. Moreover, without the stator teeth to guide the flux line, the windings are directly exposed to the rotor PM field. This causes high eddy current losses in the windings.

This problem becomes more serious at a high speed. The losses and the torque of the motors equiped with slotted and slotless windings as shown in Fig. 4.12 are compared in Table 4.3. It can be found that even though the current densities of the slotless windings are much higher than that of the slotted winding, the torques of the slotless motors are much lower than that of the slotted motor. Moreover, the losses of the slotless windings are much higher than those of the slotted windings. Therefore, the slotted stator is better because of higher torque and lower winding Joule losses.

| | (a) | | | (b) | |
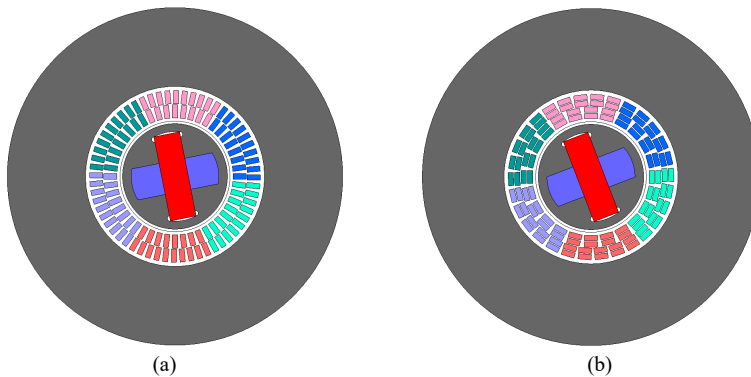
Figure 4.12:   Slotless motors. (a) Slotless 1. (b) Slotless 2.

Stator type	Slotted	Slotless 1	Slotless 2
Nominal current density in A/mm^2	18.40	28	28
Torque in Nm	1.21	0.51	0.45
Copper losses* in W	249.96	1349.78	2981.33
Stator core losses in W	290.44	8.82	7.81
Rotor core losses in W	2.45	0.60	0.57
PM losses in W	2.60	0.05	0.07
Shaft losses in W	25.81	0.01	0.01
Total losses in W	571.26	1359.26	2989.79

*End-winding copper losses are not included.

Table 4.3:   Performances comparison of slotted and slotless motors at 125,000 /min.

4.2   Rotor design

It is well-known that the load ability of a motor generally depends on the heat dissipation ability. However, for the high-speed motors, besides the thermal limitation, the torque is also subjected to the diameter and the axial length of the rotor. The diameter of the rotor is

determined by the mechanical stress on the rotor and the axial length of the rotor is limited by the natural frequencies of the rotor. In order to protect the rotor from centrifugal force, the mechanical stress on the rotor must be lower than the yield strength of the rotor core or the sleeve materials. To ensure the natural frequencies of the rotor are higher than the fundamental frequency at maximum speed of the motor, the effective length of the rotor cannot be very long. Hence, mechanical analysis is essential for the design of the high-speed motors.

4.2.1 Rotor stress analysis

4.2.1.1 Maximum stress of the rotor core

For the proposed rotor structure, the PM is buried into the rotor and its volume is limited. Consequently, the flux linkage provided by the PM is limited. To withstand the centrifugal forces of the rotor, flux bridges are needed. Then, the width of the flux bridges plays an important role on both the electromagnetic and mechanical performances of the rotor. In order to reduce the flux leakage, it is necessary to reduce the width of the flux bridges. However, higher stress will be induced when the width of the flux bridges is reduced. Hence, it is necessary to optimize the size of the rotor diameter and the width of the flux bridges in parallel. The width and the thickness of the PM, W_m and H_m, are limited by the rotor radius R_1 and the width of the flux bridge T_b and they have a relationship of

$$W_m^2 + H_m^2 = 4\left(R_1 - T_b\right)^2 \tag{4.2}.$$

The parameters of the rotor are indicated in Fig. 4.13. The maximum flux Φ_{max} provided by the PM can be expressed as

$$\Phi_{max} = B_0 W_m L_{fe} \tag{4.3}$$

where B_0, W_m and L_{fe} are the magnetic flux density of the PM on the working point, the width of the magnet and the length of the rotor stack, respectively.

When the influences of the slot opening and the saturation of the iron core are not considered, the magnetic flux density of the PM on the working point is expressed as

$$B_0 = B_r \frac{1}{1 + \mu_{rpm} \dfrac{2\delta}{H_m}} \tag{4.4}$$

where B_r and μ_{rpm} are the remanence and the relative permeability of the magnet, respectively; δ and H_m are the air-gap length and the PM thickness, respectively.

When the flux leakage on the flux bridge area is considered and the flux density on this area is assumed to be 1.5 T which is the saturation flux density of the amorpous core, the flux supplied by the rotor to the stator $\Phi_{\text{max\_rotor}}$ can be written as

$$\Phi_{\text{max\_rotor}} = \left(B_{\text{r}} \frac{\sqrt{4(R_1 - T_{\text{b}})^2 - H_{\text{m}}^2}}{1 + \mu_{\text{rpm}} \dfrac{2\delta}{H_{\text{m}}}} - 3T_{\text{b}} \right) L_{\text{fe}} \tag{4.5}.$$

To simplify the stress analysis, the shaft is not considered and the rotor core is shown in the left figure of Fig. 4.13. Since the maximum stress happens at the positions A, the rotor core can be seperated into three parts as presented in the middle figure of Fig. 4.13 and then it can be equivalented into two concentrated forces working at a ring as presented on the right figure of Fig. 4.13. The centrifugal force of the two yellow parts on a ring, P, is equal to

$$P = \frac{2}{3} \rho \omega_{\text{rotor}}^2 \left(R_1^3 + (\sin(\theta_1) - 1)(R_1 - T_{\text{b}})^3 - \tan(\theta_1)\left((R_1 - T_{\text{b}})\cos(\theta_1)\right)^3 \right) \tag{4.6}$$

$$\theta_1 = \arccos\left(\frac{H_{\text{m}}}{2(R_1 - T_{\text{b}})} \right) \tag{4.7}$$

where ρ and ω_{rotor} are the density of the rotor core and the rotation angular speed of the rotor, respectively.

Then the maximum stress σ_{max} on the flux bridge area can be calculated by

$$\sigma_{\text{max}} = \frac{P}{T_{\text{b}}} K_{\text{t}} \tag{4.8}$$

where K_{t} is the stress concentration factor and it is decided by the PM thickness, the radius of the rotor core, the width of the flux bridge, and the parameters of the shaft, etc.

For example, when the PM thickness is constant and it equals to 5 mm, in order to keep the maximum stress on points A constant to about 600 MPa, the thickness of the flux bridge and the stress concentration factor (SCF) as a function of the rotor radius are shown in Fig. 4.14. It shows that the stress concentration factor decreases non-linearly when the radius of the rotor increases. Hence, finite element method (FEM) is better to be used for the analysis of the stress on the rotor.
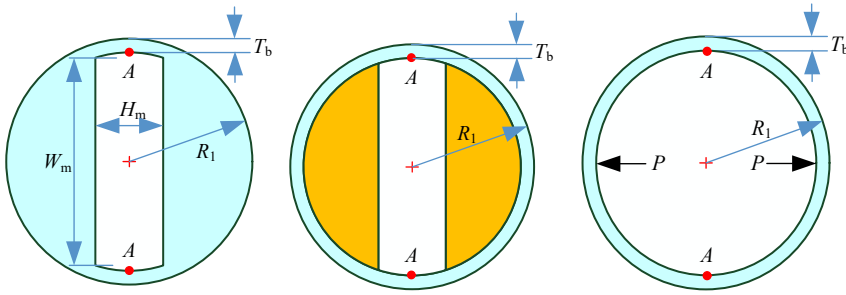
Figure 4.13: Rotor core without considering the shaft and its equivalent to a ring.
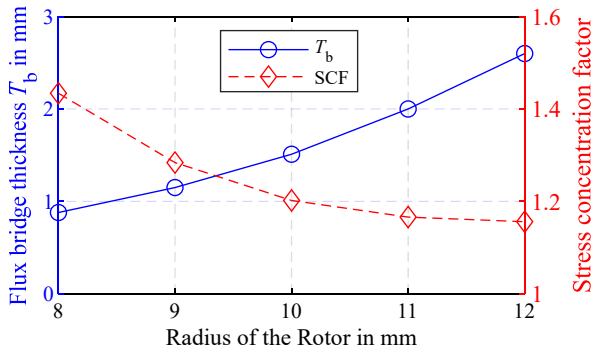
Figure 4.14: The thickness of the flux bridge and the stress concentration factor as a function of rotor radius.

Based on FEM, by keeping the maximum stress at points A constant to about 600 MPa, the width of the flux bridge for different magnet thicknesses as a function of the rotor radius are shown in Fig. 4.15. It can be found that the influence of the magnet's thickness on the rotor stress is not very high when the rotor radius is constant. Hence, an equation can be used to describe the relationship between T_b and R_1 as

$$T_b = -0.0014R_1^4 + 0.0569R_1^3 - 0.8349R_1^2 + 5.4669R_1 - 12.9825 \qquad (4.9)$$

When the air-gap length is 0.5 mm and the rotor stack is 50 mm; a high temperature FeNdB magnet N35AH which can work over 200 °C is employed; and the remanence and the relative permeability of the magnet are 1.024 T and 1.057, respectively, the maximum flux linkage provided to the air gap $\Phi_{\text{max\_rotor}}$ according to (4.5) as a function of the PM thickness and the rotor radius can be drawn as shown in Fig. 4.16. It clearly shows that when the rotor radius is about 10 mm, the rotor can provide a maximum flux linkage to the air gap. Hence, the radius of the designed rotor is 10 mm and the thickness of the flux bridge is 1.5 mm. Since the maximum flux linkages generated by the PM are almost the same when

the PM thickness is about 5 mm to 7 mm, and by considering the shaft stiffness at the same time, a small value of 5 mm is chosen for the PM thickness.
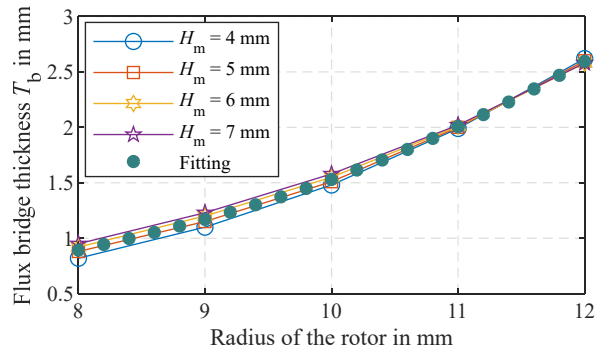
Figure 4.15: Influence of PM thickness on the thickness of the flux bridge as a function of rotor radius.
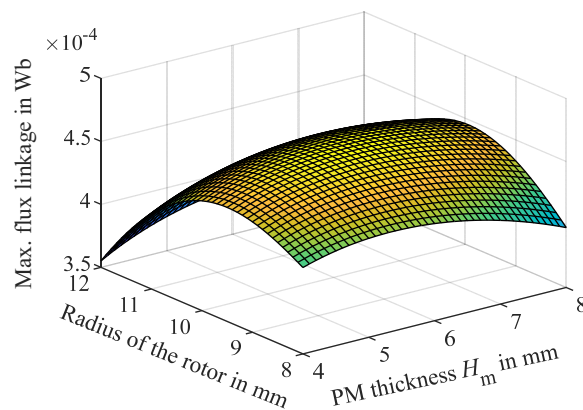
Figure 4.16: Influence of PM thickness on the thickness of the flux bridge as a function of rotor radius.

4.2.1.2 Maximum stress of the PM

In order to avoid high-temperature demagnetization of the PM, a high-temperature magnet is necessary. Commonly, high-temperature high-performance magnets, such as sintered Neodymium (NdFeB) magnets and sintered Samarium Cobalt (SmCo) magnets are employed in the motors of high-power density. In general, the NdFeB magnets have higher remanence and mechanical strength whereas SmCo magnets can work at higher temperature. The characteristics of the NdFeB and SmCo magnets are compared in Table 4.4. In this work, because the rotor runs at a high speed, the mechanical strength of the PM is more important. Moreover, because the electrical resistivity of the SmCo magnet is lower than that of the NdFeB magnet, higher rotor eddy current loss will be induced when SmCo

magnets were used. Since the Curie temperature of the AMM 2605SA1 is only 395 °C [132] and its saturation flux density is easily influenced by the temperature, a higher working temperature of the PM is unnecessary and a lower eddy current losses of the PM is prefered. Hence, the NdFeB magnet is chosen in this work.

PM type	NdFeB	SmCo
Density in g/cm^3	7.6	8.3
Maximum remanence in T	>1.35	<1.20
Flexural strength in MPa	240	120
Tensile strength in MPa	75	45
Young's modulus in GPa	150	140
Electrical resistivity ρ in $\mu\Omega\cdot$cm	190	90
Maximum operating temp. in °C	230	350
Specific heat in J/(kg·K)	450	350
Thermal conductivity in W/(m·K)	8.5	10
Curie temperature in °C	380	825

Table 4.4:   General characteristics comparison of NdFeB and SmCo magnets. [133]-[136].

Based on the finite element analysis, the maximum stress of the PM without the support from the AMM rotor core is 42 MPa as shown in Fig. 4.17. In this figure, the horizontal and vertical directions represent the thickness and the height of the PM, respectively. Since the maximum stress at the maximum speed is lower than the tensile strength, the PM is safe at the maximum speed. In order to strengthen the rotor, the gaps among the PM, the shaft and the rotor core are filled with high-strength epoxy.
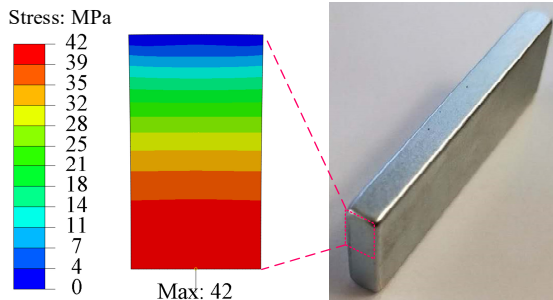
Figure 4.17:   Stress in the PM at maximum speed.

4.2.2 Rotor natural frequencies

In order to make sure the rotor can run to a high speed, dynamic analysis of the rotor is necessary. The natural frequencies of the rotor should be higher than the mechanical frequency of the rotor, i.e. 2083.3 Hz at 125,000 /min, to avoid resonance.

The natural frequency is defined as [137]

$$\text{Natural Frequency} = \sqrt{\frac{\text{Stiffness}}{\text{Mass}}} \tag{4.10}.$$

For a simple beam structure supported by pin joints at each end, the natural frequencies can be expressed as [137]

$$f_i = \frac{(i\pi)^2}{2\pi L^2}\sqrt{\frac{EI}{dm}} \tag{4.11}$$

where L is the length, E is the modulus of elasticity, I is the area moment of inertia and dm is the mass per unit length.

It is easy to find that the natural frequencies are inversely proportional to the square of the rotor length. Hence, it is necessary to shorten the length between the two bearings. By using Ansys software, the natural frequencies of the rotor are analyzed. Fig. 4.18 shows the first mode of the rotor supported by the two bearings. Table 4.5 lists the natural frequencies of different rotor stack lengths. Because the bearings are considered as fixed in the model, to have a large safety margin, the rotor stack length of 50 mm is chosen for the prototype.
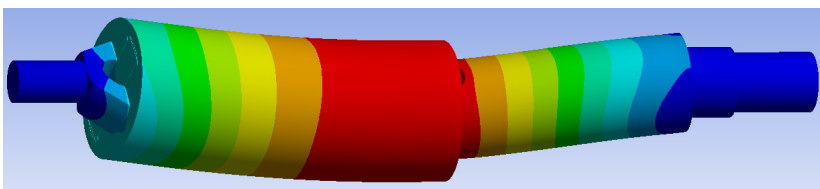
Figure 4.18:   First mode of the rotor.

Rotor stack length	50 mm	60 mm
1st mode	4374.1 Hz	3706.6 Hz
2nd mode	4588.1 Hz	3849.3 Hz
3rd mode	6773.6 Hz	6171.6 Hz

Table 4.5:   Natural frequencies of first three modes of the rotor.

4.2.3 Rotor eddy current losses

4.2.3.1 Losses of the PM and the shaft

For the proposed rotor structure, the PM magnetic flux needs to pass through the solid shaft, and the flux lines from the armature reaction need to pass through the solid shaft and the PM. Moreover, the flux lines of the armature reaction are easier to pass through the shaft than the magnet because the relative permeability of the iron is much higher than that of the PM. The flux lines generated by different sources are shown in Fig. 4.19. Thus, the eddy current losses in the shaft are high for the proposed rotor. In order to keep the PM safe, the losses in the rotor should be limited. Hence, the calculation and optimization of the losses of the shaft is of great importance. To promise the calculation precision, the meshes of the PM and the shaft regions are dense and mapped mesh is used. The mesh result is shown in Fig. 4.20(a). The eddy current densities of the PM and the shaft at 125,000 /min and 1.2 Nm generated by armature reaction are illustrated in Fig. 4.20(b). The eddy current distribution shows that the eddy current of the shaft concentrates on a thin depth from the surface of the shaft. In addition, the eddy current losses of the PM is much lower than those of the shaft. Hence, the design of this rotor is focused on the losses of the shaft instead of the losses of the PM. A trade-off design of the shaft to consider the shaft losses and the rotor stress is necessary.

(a)   (b)
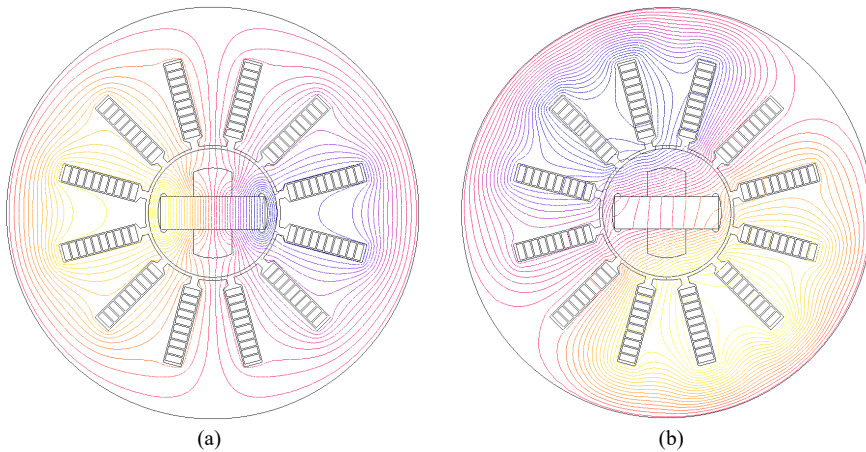
Figure 4.19:   Flux lines of no-load and armature reaction. (a) No-load. (b) Armature reaction.
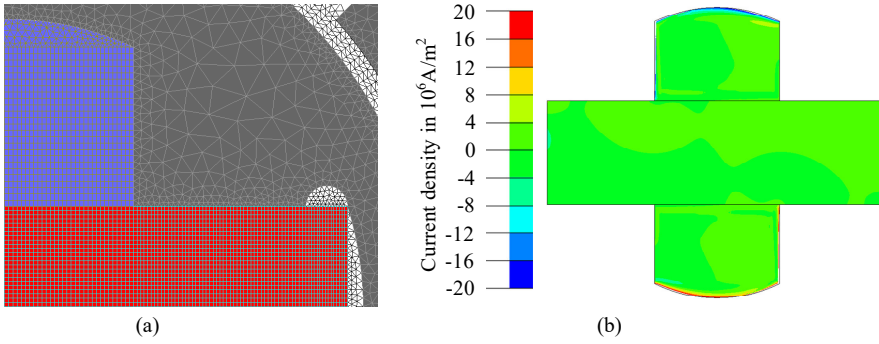
Figure 4.20:   Calculation of the eddy current losses of the shaft and PM. (a) Mesh of the rotor. (b) Eddy current distribution of the shaft and PM caused by armature reaction field.

4.2.3.2   Influence of the current leading angle

For the proposed IPM rotor structure, the d-axis inductance L_d is smaller than the q-axis inductance L_q. Hence, the torque T of this motor can be separated into two parts, i.e. permanent magnet torque and reluctance torque. It can be expressed as

$$T = \frac{m}{2} p \left(\lambda_{d,PM} i_q + \left(L_d - L_q \right) i_d i_q \right) \tag{4.12}$$

where m is the phase number; p is the pole-pair number; $\lambda_{d,PM}$ is the d-axis flux linkage generated by PM; i_d and i_q are the d-axis and q-axis current, respectively.

Based on the torque equation it can be known that in order to take full advantages of the torque performance of the motor, it is necessary to use negative d-axis current, i.e. the current leading angle θ is larger than zero. To determine this angle, the torque and the shaft losses need to be considered at the same time. When a round shaft is used, and the radius of the shaft is 7 mm, the torque and the shaft losses as a function of current and current leading angle are shown in Fig. 4.21.

Fig. 4.21 shows that when the current leading angle θ is increased, the torque is firstly increased and then decreased, while the losses of the shaft are decreased. In order to minimize the shaft losses, it is better to use a large current leading angle. However, considering the maximum torque ability, it is better to choose 30 degree for the current leading angle. When the current is decreased and the current leading anlge is set to 30 degrees, to generate a same torque of 1.2 Nm, the shaft losses are 34.5 W, while the shaft losses of a higher current with the current leading angle equals to 52 degrees are lower than 30 W. Hence, high current with large current leading angle is better to reduce the shaft losses. However, even though a higher current with a larger current leading angle is helpful to decrease the shaft losses, the armature current is limited by the stator heat dissipation ability.
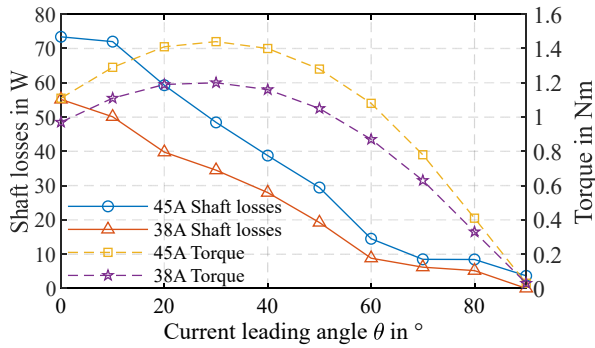
Figure 4.21:   Torque and shaft losses as a function of current and current leading angle.

4.2.3.3   Trade-off design of the shaft

In order to reduce the shaft eddy current losses, a small radius of the shaft R_{shaft} is preferred. However, the smaller the rotor shaft radius, the higher the rotor core stress. For example, when the radius of the shaft is reduced from 8.35 mm to 7 mm, the maximum core stress is increased as illustrated in Fig. 4.22. Hence, a trade-off design of the shaft dimensions is necessary.
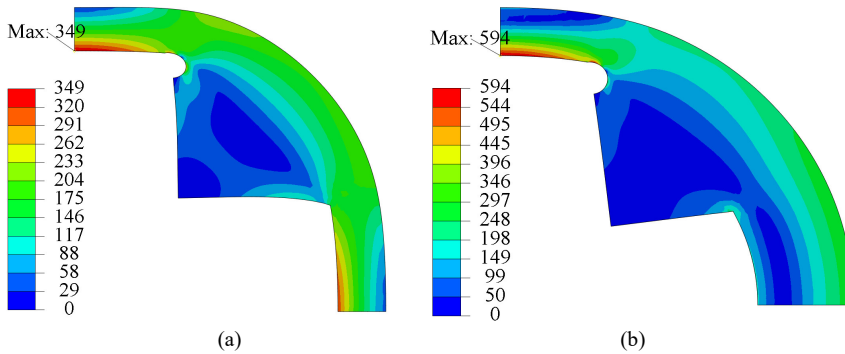
Figure 4.22:   Stress distribution of the rotor core (Unit: MPa). (a) R_{shaft} = 8.35 mm. (b) R_{shaft} = 7 mm.

The rotor stress and the shaft losses as a function of the shaft dimensions are shown in Fig. 4.23. It can be seen that when the radius of the round shaft (left figure in Fig. 4.24) is increased, the stress on the rotor is decreased, whereas the shaft losses are increased. As for the flat shaft (right figure in Fig. 4.24), when the radius of the shaft is increased, the shaft losses are increased, while the stress on the rotor is firstly decreased and then increased. When the radius of the shaft is increased, the width of the rotor core near to the shaft is decreased. Then the maximum stress will happen at this position instead of at the flux bridges. Hence, the maximum stress of the rotor firstly decreases and then increases when the radius of the shaft increases. The shaft losses of the flat shaft are always lower

than those of the the round shaft when the shaft radius is fixed. Since the round shaft cannot significantly decrease the rotor stress and it may add stress to the magnet, it is not selected for the demonstrator motor. For different combinations of shaft thickness and radius, when the rotor stresses are comparable, the shaft losses are also comparable. Hence, in this work the shaft thickness is selected to 6 mm which is equal to the bore diameter of the rear bearing, by considering the manufacture of the shaft and assembly of the rotor. To verify of the high strength property of the AMM core, a small shaft radius of 7 mm is chosen for the prototype.
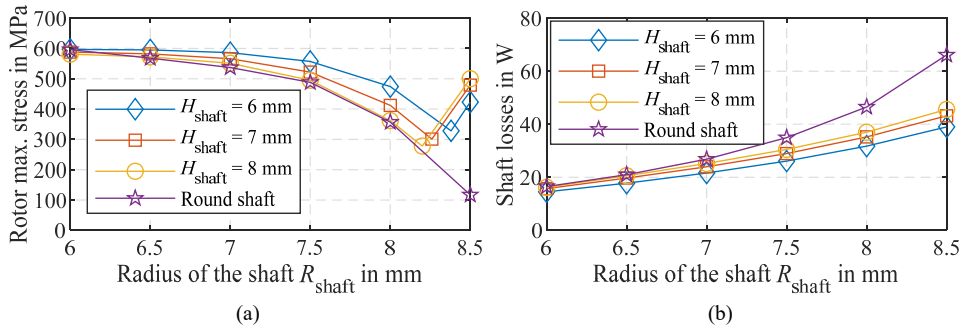
Figure 4.23:   Rotor stress and shaft losses as a function of shaft dimensions. (a) Rotor stress. (b) Shaft losses.
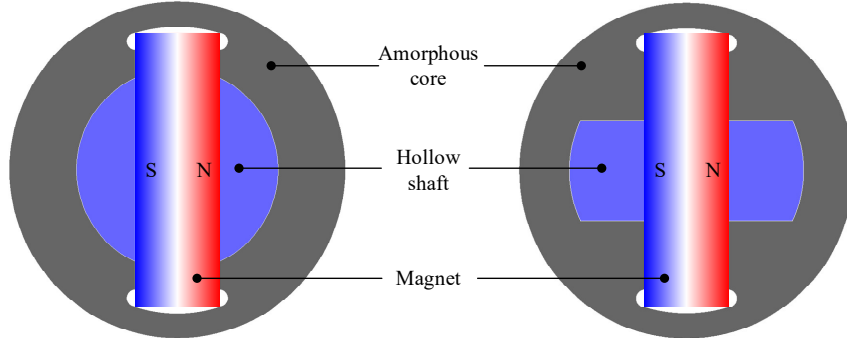
Figure 4.24:   Difference of the round shaft (left, Dr. Markus Schiefer proposed) and the flat shaft (right).

4.2.4   Rotor air-friction loss

Besides the mechanical limitation, rotor air-friction loss is also a challenge for the high-speed motors. Generally, the rotor air-friction loss can be calculated by [138]

$$P_{f,air} = k C_f \pi \rho_{air} \omega^3 R_l^4 L \tag{4.13}$$

where $P_{f,air}$ is the rotor air-friction loss; k is the roughness coefficient, its value is 1 for smooth surfaces and 2.5 for axially slotted surface [139]; C_f is the friction coefficient; ρ_{air} is the density of the air in kg/m³; ω is the angular velocity of rotor in rad/s; R_1 is the radius of rotor in m; L is the length of the rotor in m.

In order to improve the heat dissipation ability of the stator, the stator will be encapsulated with epoxy resin. Then, the inner surface of the stator becomes a smooth surface and the roughness coefficient is equal to 1. It can be found that by encapsulating the stator with epoxy resin, not only the heat dissipation ability of the stator is improved, but also the rotor air-friction loss can be reduced.

In Equation (4.13), the air-friction coefficient C_f depends on the air-gap length, the radius of the rotor and the Reynolds number [140], and is expressed as

$$\begin{cases} C_f = 0.515 \dfrac{\left(\delta / R_1\right)^{0.3}}{\mathrm{Re}_\delta^{0.5}}, & 500 < \mathrm{Re}_\delta < 10^4 \\[3mm] C_f = 0.0325 \dfrac{\left(\delta / R_1\right)^{0.3}}{\mathrm{Re}_\delta^{0.2}}, & 10^4 < \mathrm{Re}_\delta \end{cases}$$

(4.14).

The Couette-Reynolds number Re_δ describing the nature of tangential gas flow inside the air gap is expressed as

$$\mathrm{Re}_\delta = \frac{\rho_{air} \omega R_1 \delta}{\mu}$$

(4.15)

where δ is the air-gap length in m; μ is the dynamic viscosity of air in Ns/m².

The dynamic viscosity is given by [141]

$$\mu = \frac{1.458 \times 10^{-6} T_K^{1.5}}{T_K + 110.4}$$

(4.16)

where T_K is the absolute (kelvin) temperature.

The air-friction loss on the end surface of the rotor can be calculated as

$$P_{f,end} = 0.5 C_f \rho_{air} \omega^3 \left(R_1^5 - R_{shaft}^5\right)$$

(4.17)

where R_{shaft} is the radius of shaft in m.

The corresponding number describing the nature of tangential gas flow at the end surfaces is the tip Reynolds number, defined as

$$\mathrm{Re_r} = \frac{\rho_{air}\omega R_1^2}{\mu}$$ (4.18).

According to the Reynolds number $\mathrm{Re_r}$, the air-friction coefficient C_f is:

$$\begin{cases} C_f = \dfrac{64}{3\,\mathrm{Re_r}}, & \mathrm{Re_r} < 30 \\[2mm] C_f = \dfrac{3.87}{\mathrm{Re_r^{0.5}}}, & 30 < \mathrm{Re_r} < 3\times10^5 \\[2mm] C_f = \dfrac{0.146}{\mathrm{Re_r^{0.2}}}, & 3\times10^5 < \mathrm{Re_r} \end{cases}$$ (4.19).

Since the air-friction loss is proportional to the cube of the rotor angular speed, the air-friction loss is very high and they cannot be neglected. To consider the influence of temperature and pressure, the density of the air is expressed as [141]

$$\rho_{air} = \rho_0 \frac{273.15}{273.15+T_C} \frac{p_{air}}{0.1013\times10^6}$$ (4.20)

Where ρ_0 is the air density at the state of 0 °C, 0.1013 MPa and ρ_0=1.293kg/m³; T_C is the Celsius temperature and p_{air} is the absolute pressure in Pa.
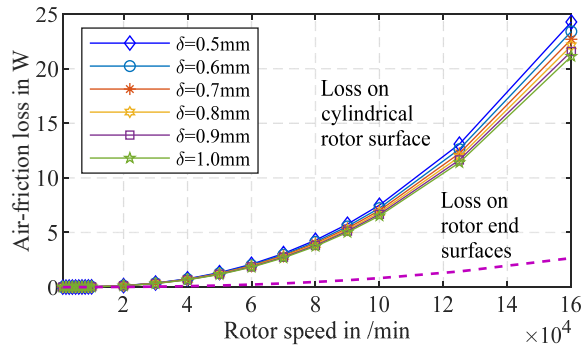
Figure 4.25:   Air-friction losses on the rotor surface and the end surface.

For a temperature of 100 °C and standard pressure of 0.1013 MPa, the dynamic viscosity is 2.173×10^{-5} Ns/m² and the air density is 0.946 kg/m³. The air-friction losses of the rotor

at different speeds and air-gap lengths are shown in Fig. 4.25. Since the air-friction losses of different air-gap length are not much different, a small air-gap length of 0.5 mm is selected to reduce the air-gap magnetic resistance of the motor.

4.3 Water-cooled housing

In order to increase the electric loading of the stator to increase the torque density of the motor, forced water-cooled system is employed. Generally, a spiral water-cooled channel as shown in Fig. 4.26 is used since its inlet pressure is low and the manufacture of this type of channel is simple. However, in this case, the axial stiffness and the wall area of this water-cooled housing are restricted by the tooth dimensions of the channel. When the tooth depth of the channels is increased, the axial stiffness is decreased, on the contrary, the wall area is decreased. In order to improve the cooling performance without significantly decreasing the stiffness of the housing, a special water-cooled channel as presented in Fig. 4.27 is designed. The cross section of the proposed channel as shown in Fig. 4.27(b) is designed to increase the wall area so as to increase the cooling performance. This special design can obtain almost two times larger area than the spiral channel.

(a)   (b)
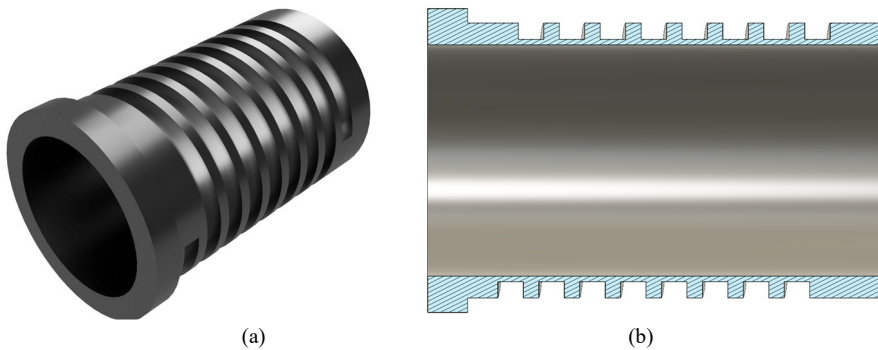
Figure 4.26:   Spiral water-cooled channel. (a) 3-D rendergraph. (b) Cross section.

(a)   (b)
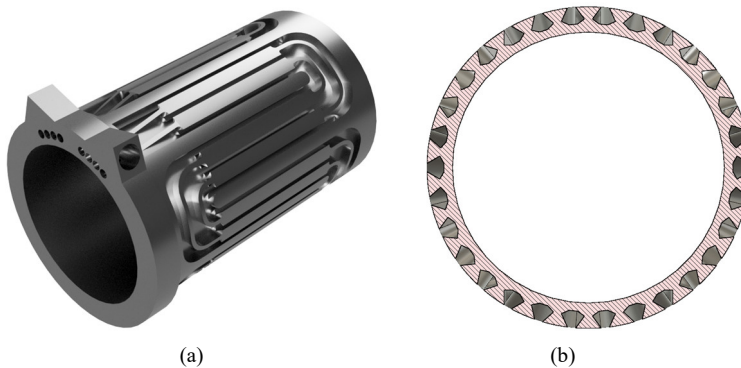
Figure 4.27:   Proposed water-cooled channel. (a) 3-D rendergraph. (b) Cross section.

4.3.1   Natural frquencies of the water-cooled housing

When both the two ends of the housings are fixed, the natural frequencies of the two water-cooled housings with the stator core inside are compared in Fig. 4.28 and Table 4.6. Based on the results it can be found that the proposed water-cooled housing has slightly higher natural frequencies. Because the cover of the water-cooled housing is not added to the analyzed model, the first bending frequency of the water-cooled housing is relatively low.

(a)   (b)
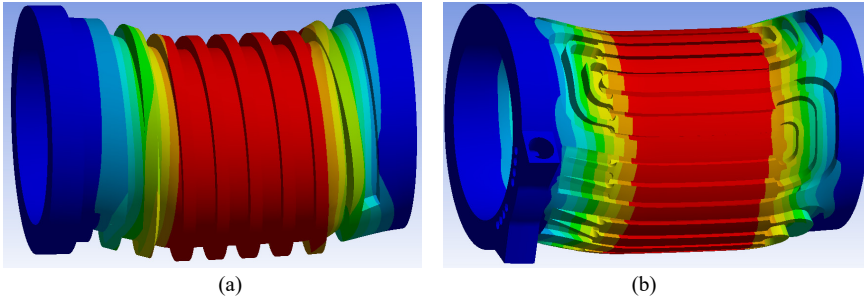
Figure 4.28.   First bending mode of the housings with stator core inside. (a) Spiral channel. (b) Proposed channel.

Water channel	Spiral	Proposed
1st mode	3113.8 Hz	3262.9 Hz
2nd mode	3131.6 Hz	3270.9 Hz
3rd mode	5572.9 Hz	5171.4 Hz

Table 4.6:   Natural frequencies of the first three modes of the housings.

4.3.2   Heat conduction coefficient of the water-cooled housing

As for this special water channel design, when the inlet velocity is fixed, the inlet pressure is higher than that of the spiral type. If the inlet pressure is kept constant, when the inlet velocity of the proposed water channel is 1 m/s, the corresponding inlet velocity of the spiral channel is 1.616 m/s. The wall heat conduction coefficients of the two housings are compared in Fig. 4.29 and Fig. 4.30. It can be seen that the spiral channel has higher wall heat transfer coefficient than that of the proposed channel. However, because the proposed channel has almost two times larger wall area than the spiral channel, the cooling performance of the spiral channel might not be better.
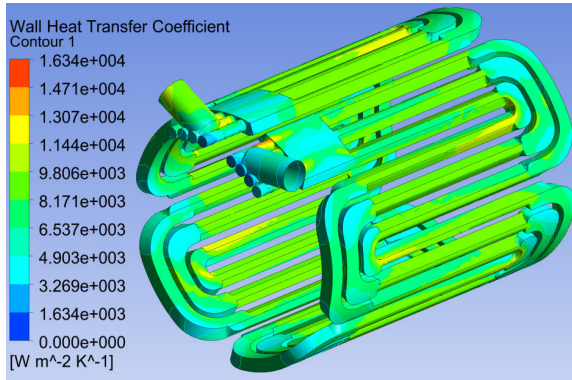
Figure 4.29:   Wall heat conduction coefficient of the proposed channel at inlet velocity of 1.0 m/s.
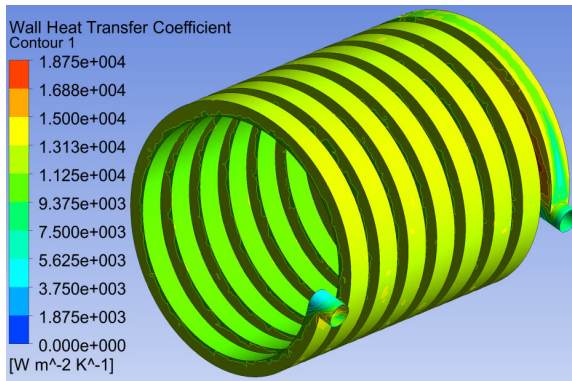
Figure 4.30:   Wall heat conduction coefficient of the spiral channel at inlet velocity of 1.6162 m/s.

4.4   Thermal field analysis

4.4.1   Heat transfer coefficient of the air gap

Heat can transfer from the rotor to the stator across the air gap by convection and radiation. For the rotor in the designed motor, the heat convection ability of the air gap is the most important, because there is no forced cooling device on the rotor. In order to predict the temperature rises of the rotor, the heat transfer coefficient of the air gap is needed.

4.4.1.1   Flow modes

With the increase of the rotor speed, the flow mode of the air gap transforms from purely laminar flow to Taylor vortices and finally to turbulent and the heat convection ability keep

improving. Generally, the flow modes of the air gap are divided into four modes as following [142]:

1) Purely laminar flow;
2) Laminar flow mix with Taylor vortices;
3) Turbulent flow mix with Taylor vortices;
4) Turbulent flow.

To predict the transition of the flow modes, Reynolds number (Re) is commonly used. It is a dimensionless quantity, which is the ratio of intertial forces to viscous forces within a fluid. In an annular air gap between stator and rotor, it can be expressed as [142]

$$\mathrm{Re} = \frac{\Omega \delta R_1}{v} \tag{4.21}$$

where Ω is the velocity of the fluid in m/s; δ is the air gap length in m and v is the kinematic viscosity of the fluid in m^2/s.

Another nondimensional quantity, which is more appropriate to be used in annular geometries is Taylor number (Ta). It is the ratio of the centrifugal to the viscous forces and can be expressed as [143]

$$\mathrm{Ta} = \frac{\omega_{\mathrm{rotor}}^2 \delta^3 R_1}{v^2} \frac{1}{F_{\mathrm{g}}} \tag{4.22}$$

where ω_{rotor} is angular speed of the rotor in rad/s and F_{g} is a geometrical factor which has many different forms proposed by different authors. Gardiner and Sabersky proposed [144]:

$$F_{\mathrm{g}} = \frac{\pi^4 \left(2R_1 + \delta \right)}{2 R_1 P} \tag{4.23}$$

$$P = 1697 \left(0.0571 \left(1 - 0.652 \frac{\delta}{R_1} \right) + 0.00056 \left(1 - 0.652 \frac{\delta}{R_1} \right)^{-1} \right) \tag{4.24}.$$

4.4.1.2 Critical speed

Once the rotor rotating speed exceedes the critical speed, the flow in the annular air gap presents instabilities which is known as Taylor vortices. Taylor determined the critical speed with Tac = 1708 [143]. As the speed continues to rise, once the Taylor number is above 1300 times Tac, the flow turns into turbulent flow. For the designed motor with rotor

radius $R_1 = 10$ mm, the Taylor number as a function of the air-gap length and the rotor speed is shown in Fig. 5.31. This figure shows that a larger air-gap length and higher speed can achieve a higher Taylor number.
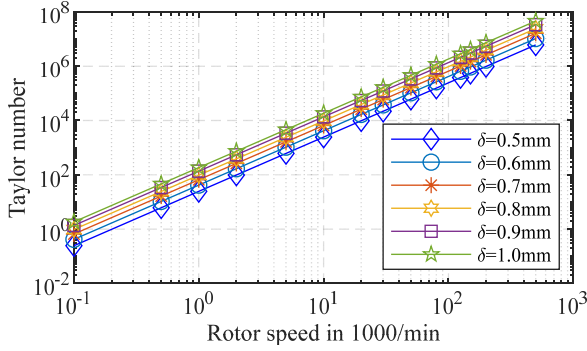
Figure 4.31:   Taylor number as functions of the air-gap length and the rotor speed.

4.4.1.3 Heat transfer coefficient

In order to evaluate the convection intensity, the Nusselt number (Nu), which is the ratio between convective and conductive heat transfer, is used [142]:

$$\text{Nu} = \frac{hD_\text{h}}{k} \tag{4.25}$$

where h is the convective heat transfer coefficient, k is the fluid conductivity, D_h is the hydraulic diameter, and $D_\text{h} = 2\delta$.

The value of Nu is based on the Taylor number Ta and is expressed as [142]

$$\begin{cases} \text{Nu} = 2\delta / \left(R_1 \ln\left(1 + \delta / R_1\right)\right), & \text{Ta} < 1700 \\ \text{Nu} = 0.128\text{Ta}^{0.367}, & 1700 < \text{Ta} < 10^4 \\ \text{Nu} = 0.409\text{Ta}^{0.241}, & 10^4 < \text{Ta} < 10^7 \end{cases} \tag{4.26}$$

Through (4.22) to (4.26), the convective heat transfer coefficient h of the air gap with rotor radius $R_1 = 10$ mm, as a function of the air-gap length and the rotor speed is shown in Fig. 4.32. It shows that the convective heat transfer coefficient of a smaller air-gap length at a low speed is higher. When the speed is higher than 10,000 /min, the difference of convective heat transfer coefficient of different air-gap lengths is small.
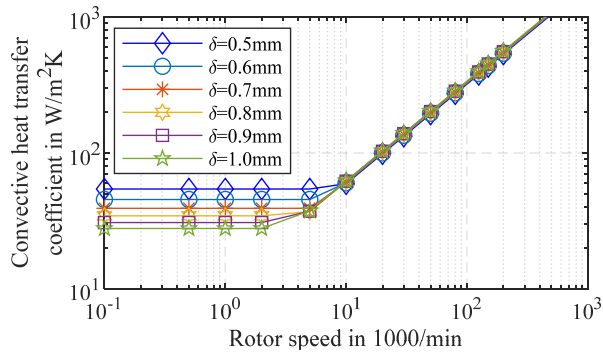
Figure 4.32:   Convective heat transfer coefficient as a function of the air-gap length and the rotor speed.

The thermal conductivity as a function of speed and air-gap length is presented in Fig. 4.33. It can be noticed that the thermal conductivity of the air gap is increased when the air gap is enlarged or the speed is increased. However, compared with the thermal conductivity of the iron, the thermal conductivity of the air is still much lower. For example, at 125,000 /min, the convective heat transfer coefficient of the air in the air gap is about 409 W/m²K, the corresponding thermal conductivity is only 0.2045 W/mK. However, the thermal conductivity of the AMM core is about 10 W/mK. Since the thermal resistance of the air gap is proportional to the air-gap length and inversely proportional to the thermal conductivity, a large air-gap length cannot significantly help to reduce the air-gap thermal resistance. Hence, by considering the heat dissipation and the torque density, a small air-gap length of 0.5 mm is adopted.
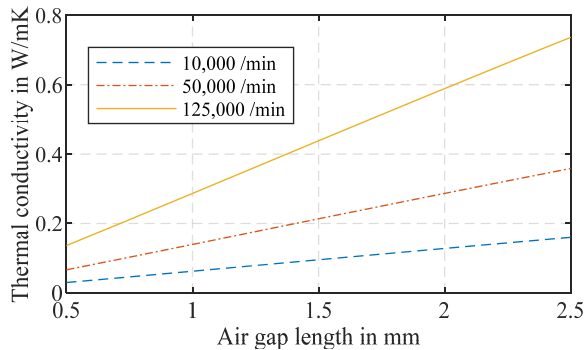
Figure 4.33:   Thermal conductivity as a function of the air-gap length and the rotor speed.

4.4.2   CFD analysis of the temperature rises

Because the windings, the AMM rotor core and the NdFeB magnet can be damaged at a high temperature, and the high temperature always happens at a high speed with high load, it is necessary to predict the temperature rises at the maximum speed and the rated load. To consider the water-cooling, computational fluid dynamics (CFD) is employed in this work. A complete 3-D model of the prototype is better in order to consider the temperature difference between the end-windings and the windings in the slots. The overall structure of the designed motor is presented in Fig. 4.34. The mesh of the 3-D model and the mesh on the radial cross section of the motor are shown in Fig. 4.35. Different from the electromagnetic FEA method, the finite element method used for the structural and thermal analyses does not require a consistent mesh of the contacted surfaces of two components.
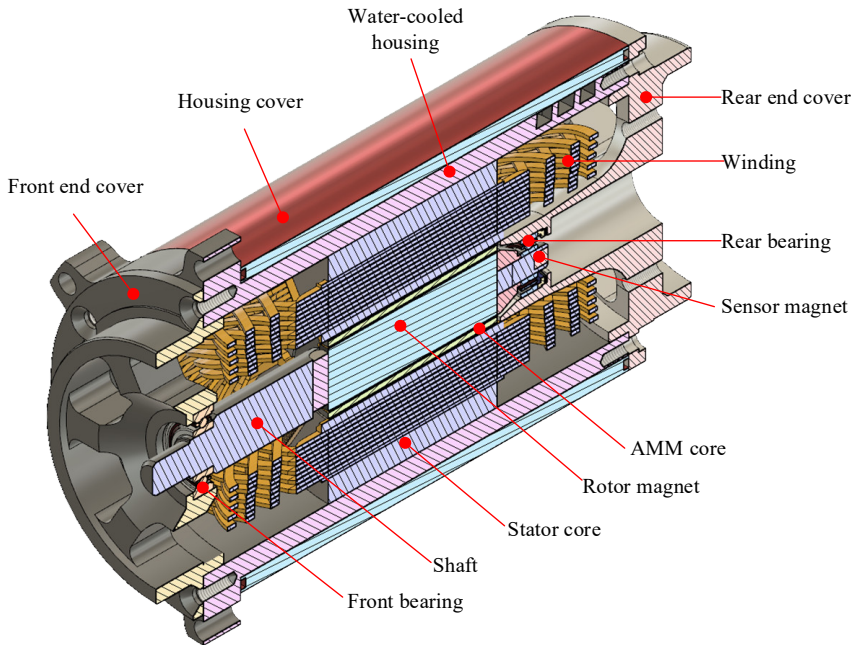
Figure 4.34:   Overall structure of the designed motor.
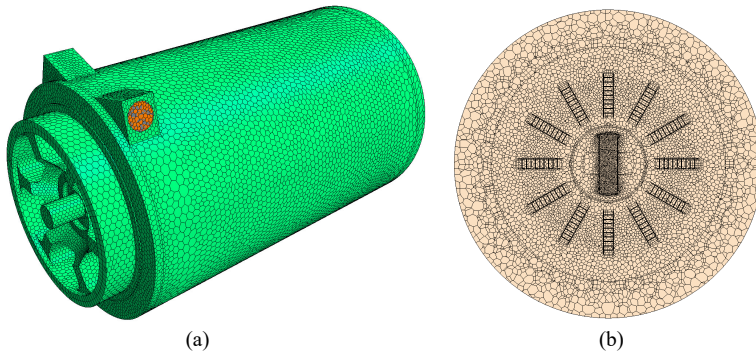
Figure 4.35: Mesh of the CFD model. (a) 3-D mesh. (b) Mesh on the radial cross section.

The thermal properties of the materials used in the models of this disseration are listed in Table 4.7. One point to note is that the AMM has only half the thermal conductivity of the silicon steel.

Materials	Thermal conductivity in W/mK	Specific heat capacity in J/kgK
Carbon fiber/epoxy [145]	0.87	970
2605SA1 [146]	10	540
NdFeB [147]	9	440
Copper winding [147]	390	383
Silicon steel [147]	20	447
Carbon steel shaft	46	500
Insulation [147]	0.175	1500
Aluminum housing [148]	180	896
Epoxy resin	0.6	1000

Table 4.7: Thermal properties of materials used.

4.4.2.1 Cooling performance comparison of the two water-cooled housings

When the ambient and the inlet water temperature is 26.85 °C (300 K), the inlet water speed of the proposed water channel is 1 m/s and the corresponding inlet velocity of the spiral channel is 1.616 m/s, at 125,000 /min and 1.2 Nm, the temperature distributions of the motors with two different water-cooled housings are compared in Fig. 4.36. The maximum temperature rises are compared in Table 4.8. The CFD results show that the proposed

water-cooled housing has better cooling performance due to its larger cooling area. According to the former analyses, it is known that the proposed water-cooled housing has higher natural frequencies. Hence, this water-cooled housing will be used for the prototype.

	Temperature (C)	
27.026	49.794 72.563 95.332	118.10 140.87
	(a)	

	Temperature (C)	
27.259	50.977 74.694 98.412	122.13 145.85
	(b)	
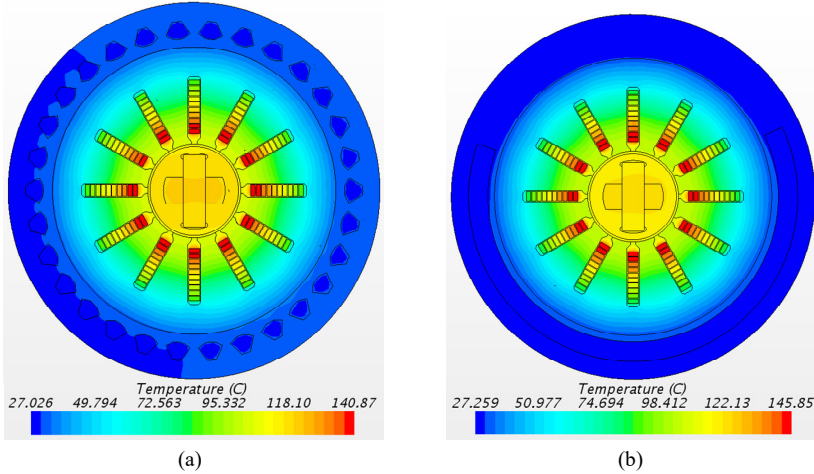
Figure 4.36:   Radial sectional temperature distribution at 125,000 /min and 1.2 Nm. (a). Proposed channel. (b). Spiral channel.

Water channel	Proposed	Spiral
Rotor	93.85 K	95.74 K
Windings	129.19 K	144.07 K

Note: the maximum temperature rise at the windings is located at the end-winding.

Table 4.8:   Comparison of the two water-cooled housing.

4.4.2.2   Cooling performance enhanced by encapsulating the stator with epoxy resin

In order to improve the cooling performance and increase the natural frequencies of the motor, the stator will be encapsulated in a vacuum tank. An epoxy resin with higher thermal conductivity is preferred. However, by filling high thermal conductive powders to increase the thermal conductivity of the composition may result in degradation problem of electrical insulation [149]. In addition, the cure temperature and cure time and maximum working temperature are also important for electrical machines. Currently, the thermal conductivity of the epoxy resin used for the electric machines is generally lower than 1 W/m·K. To evaluate the performance of the epoxy resin, the axial and radial temperature distributions of the motor at the maximum speed and rated torque are analyzed through CFD as pre-

sented in Fig. 4.37 to Fig. 4.40. When the stator is not encapsulated, the temperature distributions are shown in Fig. 4.37. It can be found that the highest temperature of the stator is at the left end-windings. When the stator is encapsulated with epoxy resin of the thermal conductivity of 0.2 W/m·K, the highest temperature of the stator is still the same as the stator without encapsulation. It can be seen that the hottest point of the stator moves from the left to the right side after encapsulation. It is because without encapsulation, the right side of the stator will be cooled down by the surrounding high-speed air caused by the high-speed rotor.
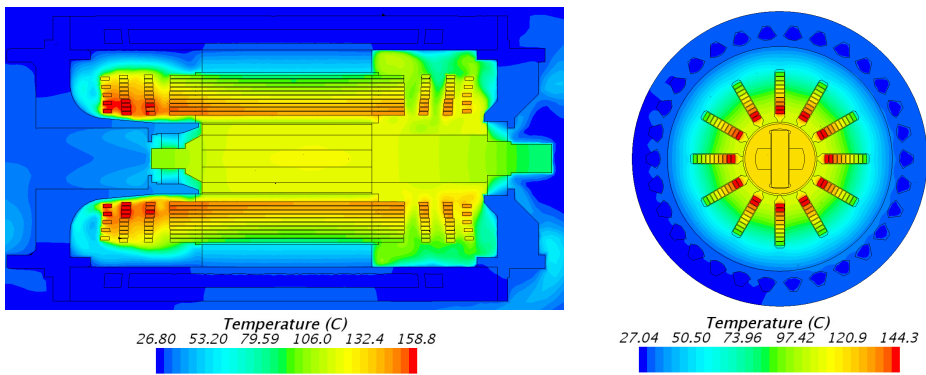
Figure 4.37:   Temperature distribution when the stator is not encapsulated with resin epoxy.
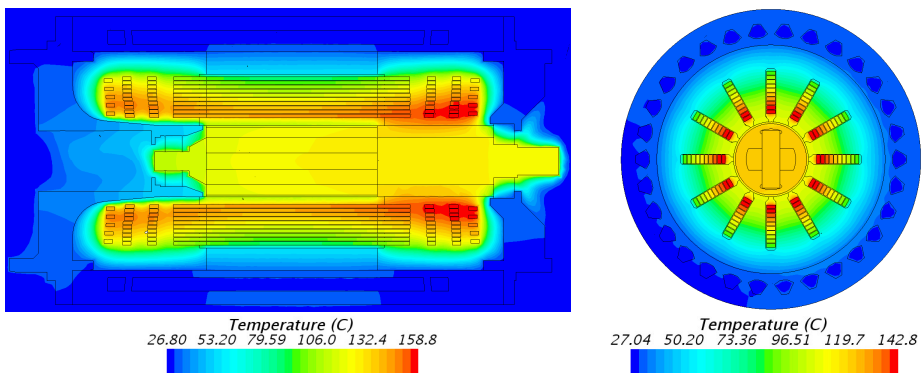
Figure 4.38:   Temperature distribution when the stator is encapsulated with resin epoxy of thermal conductivity 0.2 W/mK.

When higher thermal conductive epoxy resins are used, the hottest points will move from the right end-windings to the middle windings as presented in Fig. 4.39 and Fig. 4.40. The temperature rises of both the stator and the rotor are significantly decreased. The CFD results show that when the thermal conductivity of the epoxy resin is low, the heat dissipation ability of the motor might not be improved. However, a high thermal conductive epoxy

resin is helpful to decrease the temperature rise and increase the power density of the motor. Hence, the prototype will be encapsulated.

Temperature (C)
26.85 48.96 71.08 93.19 115.3 137.4

Temperature (C)
27.03 47.67 68.30 88.94 109.6 130.2
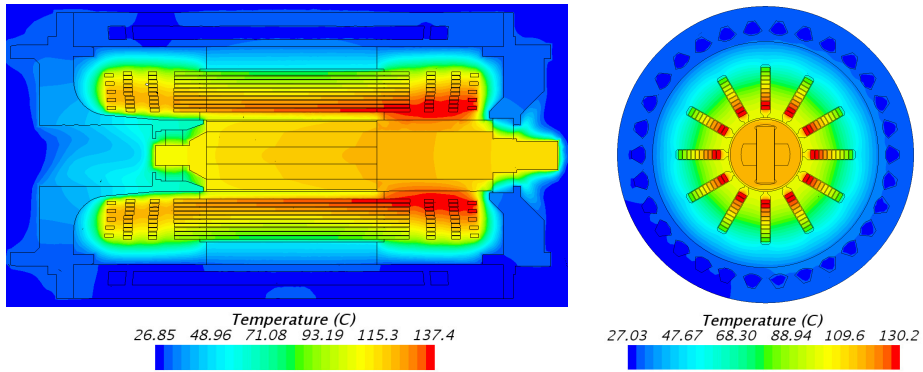
Figure 4.39:   Temperature distribution when the stator is encapsulated with resin epoxy of thermal conductivity 0.6 W/mK.

Temperature (C)
26.85 45.54 64.23 82.93 101.6 120.3

Temperature (C)
27.04 45.18 63.33 81.47 99.62 117.8
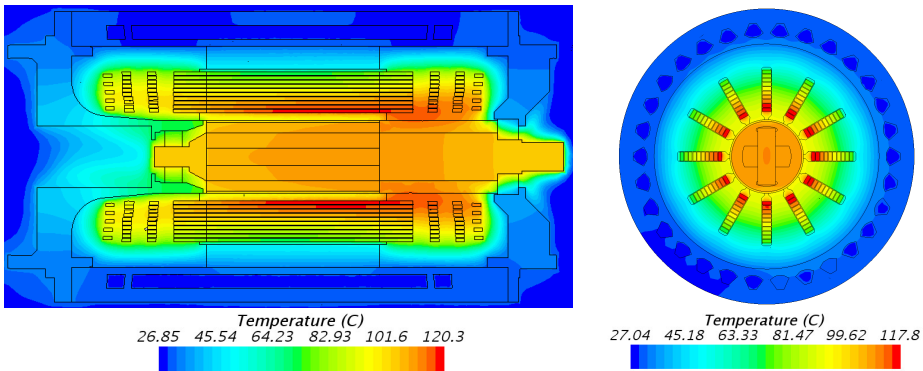
Figure 4.40:   Temperature distribution when the stator is encapsulated with resin epoxy of thermal conductivity 1.4 W/mK.

4.5   Comparison with rotor made from M330-35A

As for the proposed rotor structure, it is better to employ AMM for the rotor core. This is not only because the AMM has much lower core losses at high frequency than the silicon steels, but also because AMM has lower saturation flux and higher mechanical strength than the silicon steels. The high mechanical strength of the AMM is suitable for the proposed rotor to avoid sleeves. In addition, the width of the flux bridge exsisting in IPM rotor can be reduced. Consequently, the flux leakage is also decreased. This is also a very important aspect as the diameter of the high-speed rotor is limited. The relatively low saturation flux density of the AMM further helps to reduce the flux leakage in the flux bridge area. To evaluate the advancement of the proposed rotor made from the AMM core, the

electromagnetic, mechanical and thermal performances of the proposed rotor structure with amorphous 2605SA1 rotor (AR) core are compared to those of the silicon steel M330-35A rotor (SR) core.

4.5.1 Mechanical limitations

To ensure that the rotor can run at a high speed, the maximum stress on the rotor at the highest speed should be below the yield strength of the rotor core material. Because the mechanical strength of the M330-35A is much lower than that of the AMM, the flux-bridge width of M330-35A rotor core is larger than that of the AMM. The maximum stress of the two rotors is compared in Fig. 4.41 and the designed dimensions of them are listed in Table. 4.9. Based on the analysis in Section 4.2.3.3 it is known that the maximum stress of the AR can be reduced by increasing the radius of the shaft. However, the stress of the SR cannot be further reduced in the same way. In order to reduce the stress of SR, the thickness of the flux bridge must be increased and this will result in a worse electromagnetic performance of the motor. Hence, it is believed that the AMM is more suitable for the proposed high-speed IPM rotor in terms of mechanics.
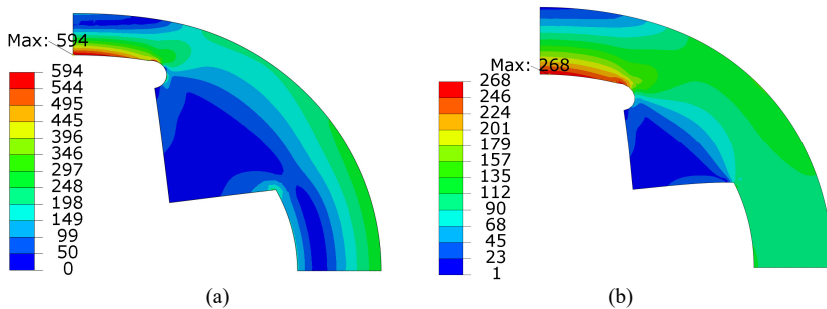
Figure 4.41:   Mechanical stress on the rotor cores at 125,000 /min (unit: MPa). (a). 2605SA1. (b). M30-35A.

Rotor core material	2605SA1	M330-35A
PM thickness H_m	5 mm	5 mm
Radius of the shaft R_{shaft}	7 mm	7 mm
Thickness of flux bridge T_b	1.5 mm	2.55 mm
Thickness of the shaft H_{shaft}	6 mm	6 mm

Table 4.9:   The dimensions of the rotor cores made from different materials.

4.5.2 Electromagnetic analysis

For both AR and SR, the *d*-axis and *q*-axis inductances are unequal. Fig. 4.42 shows the torque and the rotor losses as a function of the current leading angle for different values of the phase RMS current. The curves are plotted for both the AMM and M330-35A materials and they are labeled with A and M, respectively, in front of the phase RMS current value. For example, A 20A means that amorphous material is used for the rotor core and the RMS current is 20 A; M 20A means that M330-35A is used for the rotor core and the RMS current is 20 A. It can be noted that the rotor losses of AR are much smaller than those of SR, and the torque of AR is higher than that of SR. Table 4.10 compares the phase current, the current leading angle and the corresponding losses of the motors with different rotor core materials. To generate a torque of 1.2 Nm at 125,000 /min, the motor with M330-35A rotor has higher copper losses and rotor losses.
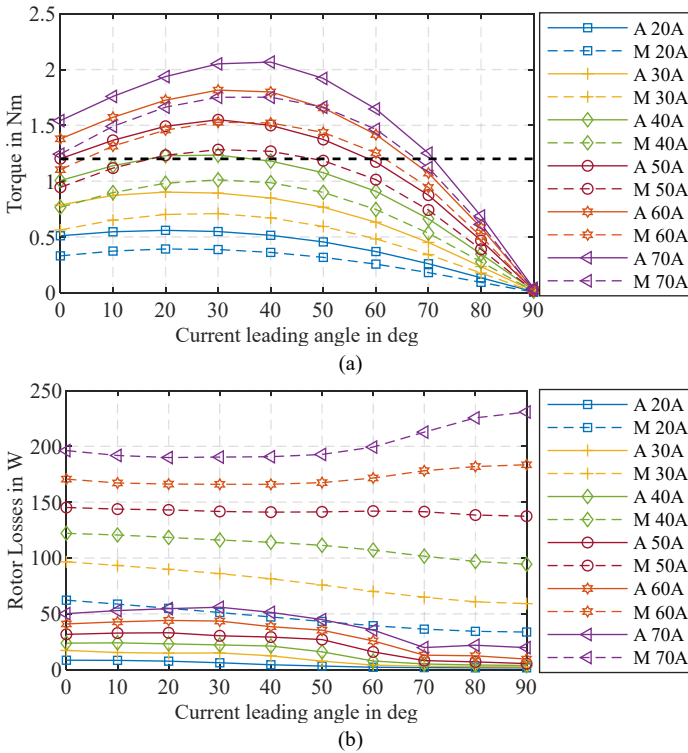
Figure 4.42:   Torque and rotor losses of the rotors with different rotor core materials. (a) Torque.(b) Rotor losses.

Rotor core material	2605SA1	M330-35A
Phase rms current in A	45	47

Current leading angle in deg	52	35
Shaft losses in W	16.63	3.03
PM losses in W	3.30	1.59
Rotor core losses in W	3.00	139.99
Air-friction losses in W	15.96	15.96
Stator core losses in W	275.55	428.65
Winding losses in W	467.40	537.96
Total rotor losses in W	38.89	160.57
Total stator losses in W	742.95	966.61
Total losses in W	781.84	1127.18

Table 4.10: Losses of the proposed rotor structure with different core materials

4.5.3 Temperature rise

Although the thermal conductivity of the silicon steels is higher than that of the AMM core, the rotor temperature rise of the SR is still much higher than that of the AR due to much higher core losses of the SR. The temperature distributions of the rotors with different core materials at 125,000 /min and 1.2 Nm are compared in Fig. 4.43. The radial cross sectional temperature distributions of the motors are compared in Fig. 4.44.

Because the flux leakage of the SR is higher than that of the AR, the stator current needed is higher for the SR motor to generate a specific torque. Hence, the temperature rise of the windings of the motor with the SR is also higher. The analyzed results show that the AMM rotor has better performance than that of the M330-35A rotor. The superiority of the performance of AR over SR is very clear. Hence, experimental verification is unnecessary.
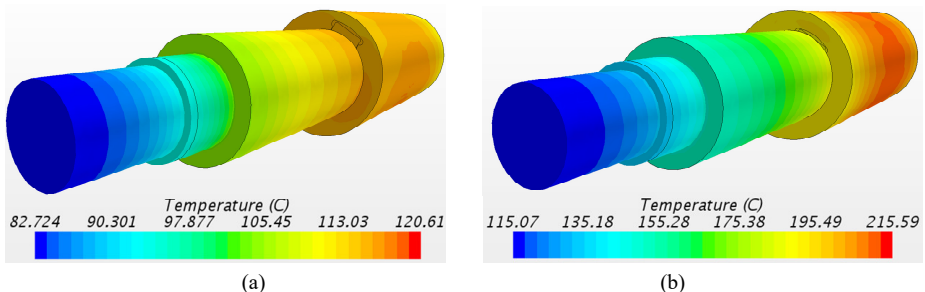
Figure 4.43: Temperature distribution of rotors at 125,000 /min and 1.2 Nm. (a). AMM. (b). M330-35A.
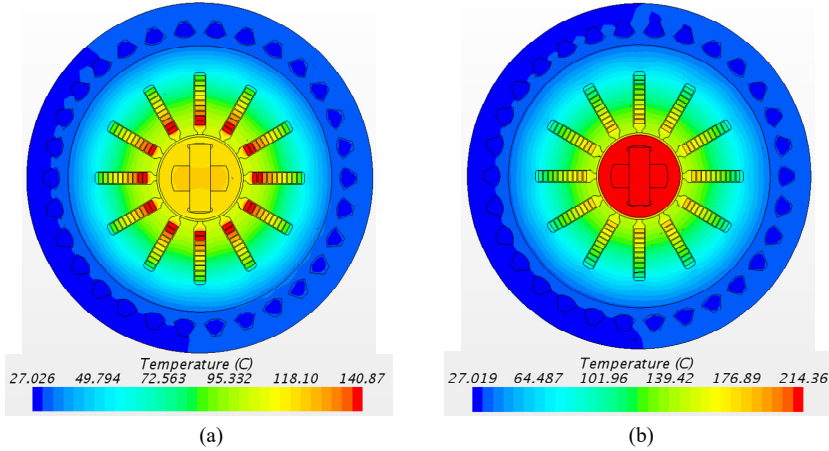
Figure 4.44:   Radial section temperature distribution at 125,000 /min and 1.2 Nm. (a). AMM. (b). M330-35A.

4.6   Design of a SPM rotor for comparison

Because the eddy current losses of the SPM rotors caused by pulse-width-modulation (PWM) inverter are dominant. In order to avoid high eddy current losses of the sleeve, a carbon fiber sleeve made by CarbonForce company is used. The properties of the sleeve at 90 °C are listed in Table 4.11. It is worth to notice that the thermal conductivity and the tensile strength of this sleeve are higher than those of the AMM core. Furthermore, the electrical resistivity of the sleeve is about 12 times that of the AMM core. The tensile strength can be increased to 4,000 MPa by changing the alignment angle of the fiber. The disadvantage of this sleeve is that its temperature resistance (recommended maximum working temperature) is relatively low which is only 110 °C.

Because the SPM motor cannot provide reluctance torque, it is necessary to increase the air-gap flux density to obtain a high torque at a low electric loading. Generally, the air-gap flux density of the SPM motor is expressed as

$$B_{\text{air\_gap}} = \frac{B_{\text{r}} H_{\text{m}}}{H_{\text{m}} + \mu_{\text{rpm}}\left(\delta + h_{\text{sleeve}}\right)} \tag{4.27}$$

Where B_{r} is the remanence of the PM; H_{m} is the thickness of the PM; μ_{rpm} is the relative permeability of the PM; δ and h_{sleeve} are the air-gap length and the thickness of the carbon fiber sleeve.

However, equation (4.27) does not consider the non-linear properties of the ferromagnetic iron cores and the shaft. Moreover, as regards a high-speed rotor, the diameter of the rotor is small, which results in significant changes of PM width along the radial direction. A thicker PM may bring a lower air-gap flux density. This is not considered in (4.27) either.

Hence, to precisely predict the air-gap flux density, FEA method is used. Due to the limitation of the manufacturing, the mechanical air-gap length is kept the same as the IPM rotor which is equal to 0.5 mm. The thickness of the sleeve and the PM should be determined by the maximum stress and the air-gap flux density. However, to avoid high eddy current losses of the rotor, the optimal air-gap length is generally larger than the summation of the thickness of the sleeve and the mechanical air-gap length. Hence, in order to make full use of the air gap, a thicker fiber sleeve is generally used. This can not only help to reduce the rotor eddy current losses, but also help to reduce the maximum stress in the sleeve. A high safety factor of the fiber sleeve can be obtained.

Parameter	Value
Density in g/cm^3	1.5 - 1.6
Thermal conductivity in W/mK	17
Specific heat in J/kgK	710
Tensile strength in MPa	900
Youngs modulus in GPa	60
Electrical resistivity in $\mu\Omega\cdot$cm	1600
Temperature resistance in °C	Up to 110

Table 4.11: Properties of the carbon fiber sleeve made by CarbonForce company [150].

The air-gap flux density and the maximum stress in the sleeve as a function of the PM and sleeve thickness are presented in Fig. 4.45. It can be found that when the thickness of the sleeve is fixed, a thicker PM can bring a higher air-gap flux density. The air-gap flux density will reach the maximum value at a medium PM thickness. The most effective way to increase the air-gap flux density is to decrease the thickness of the sleeve. However, the rotor stress is increased at the same time. Moreover, it is necessary to increase the air-gap length to reduce the eddy current losses of the PMs caused by the PWM inverter. By considering all these aspects, the thickness of the sleeve of 1 mm and the thickness of the PM of 3 mm are selected. The design results of the SPM rotor is listed in Table 4.12.

In order to reduce the eddy current losses of the PMs caused by PWM inverter, the PM pole needs to be segmented along the circumferential direction. However, when the manufacture of the rotor is considered, the PM segment cannot be infinitely small. Hence, each PM pole is devided into four segments. To reduce the requirement on the manufacturing tolerance of the PM segments, a convex is designed between the PM segments to evenly locate and distribute the PMs as can be seen in Fig. 4.46. This special design will increase the manufacture difficulty of the shaft. In addition, the convex will reduce the PM usage

amount and decrease the air-gap flux density to some extent. Moreover, a gap in between the PM segments may bring a higher stress of the sleeve at the edge of the PM. Hence, it is necessary to reduce the thickness of the convex.

(a)

(b)
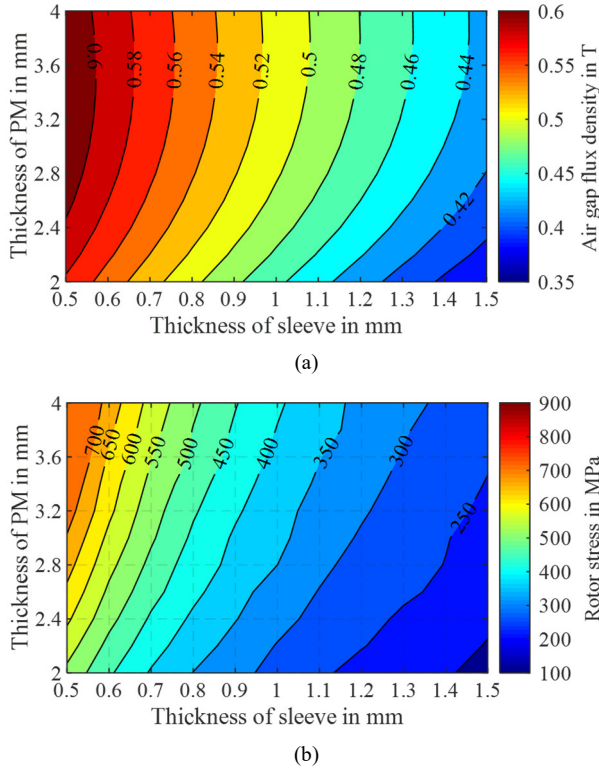
Figure 4.45:   The air-gap flux density and the maximum stress in the sleeve as a function of the PM and sleeve thickness. (a) The air-gap flux density. (b) Rotor maximum stress.

Sleeve type	Carbon fiber
Sleeve thickness	1 mm
PM thickness	3 mm
PM segments per pole	4
Radius of the shaft	6 mm

Table 4.12:   Design results of the SPM rotor.
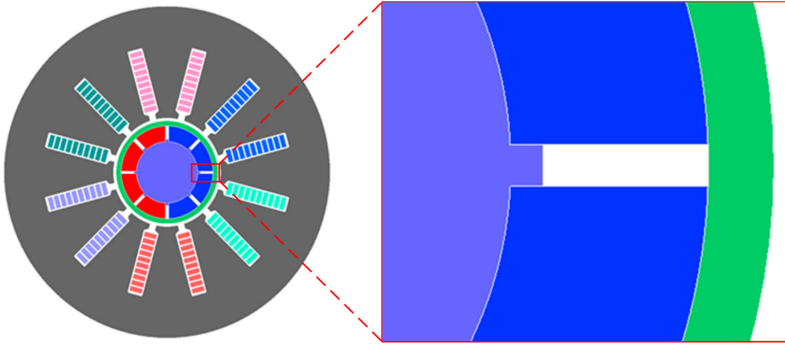
Figure 4.46:   Cross section of the designed SPM rotor.

4.7   Comparison of IPM and SPM rotors

In this work, high strength glue is used to fill the gap between the PM segments of the SPM rotor. The stresses of the sleeve of 2 segments per PM pole and 4 segments per PM pole are compared in Fig. 4.47. It shows that when the PM segments are evenly distributed, the maximum stress of the sleeve can be reduced by increasing the number of the segments per PM pole. The maximum stress of the sleeve locates at the edge of the PM segments.
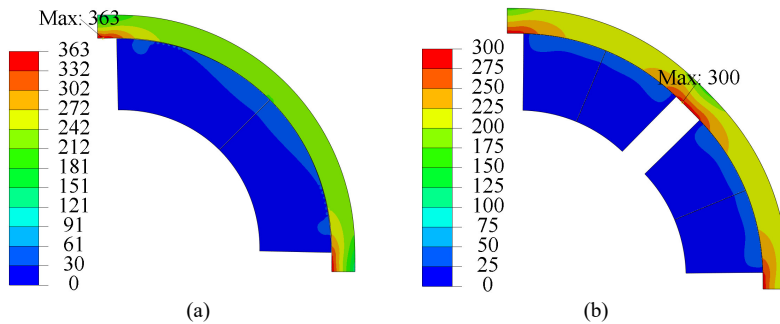
Figure 4.47:   Rotor stress at maximum speed when the thickness of sleeve is 1 mm and PM thickness is 3 mm (Unit: MPa). (a) 2 segments per PM pole. (b) 4 segments per PM pole.

The no-load air-gap flux density, back-EMF, torque and the torque as a function of the current leading angle of the SPM and the IPM motors are compared in Fig. 4.48 and Fig. 4.49. Even though the SPM motor has a little higher air-gap flux density and back-EMF than those of the IPM motor, the torque of the SPM motor is lower than that of the IPM motor as can be seen in Fig. 4.49 due to the reluctance torque in the IPM motor. When the current leading anlges of the IPM and SPM motors are 30 degrees and 0 degree respectively and the phase RMS current is 40 A, the torque of the IPM motor is 1.30 Nm, while the torque of the SPM motor is 1.12 Nm, which is about 14 % lower. Because the SPM

motor consists of high amplitudes of 5th and 7th orders of the air-gap flux, the torque ripple of the SPM motor is higher than that of the IPM motor.

When the influence of the PWM inverter is not considered, the phase currents fed to the motors are sinusoidal. The losses of the two motors, especially the rotor losses are much lower. When the motors run at the maximum speed of 125,000 /min and at the torque of 1.2 Nm, the temperature distributions of the two motors are presented in Fig. 4.50. It can be seen that the SPM motor has a little higher temperature than that of the IPM motor when both motors are fed with sinusoidal currents. Hence, it can be concluded that the IPM motor has better electromagnetic performance while the SPM motor has better mechanical performance.
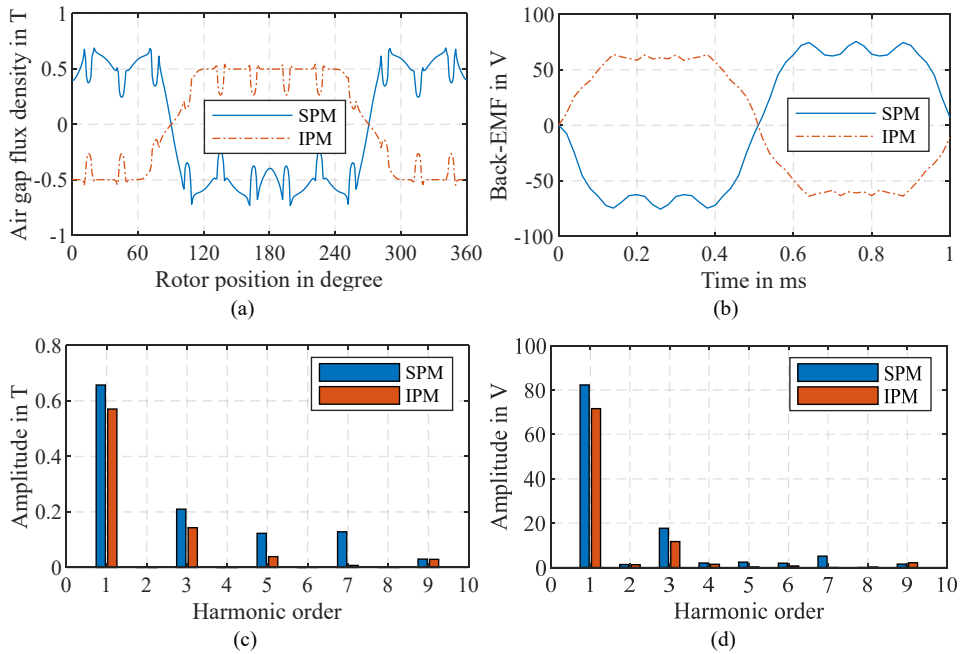
Figure 4.48:   Air gap flux density and phase back-EMF at 60,000 /min. (a) Air gap flux density. (b) No-load back-EMF. (c) FFT of air gap flux density. (d) FFT of back-EMF.
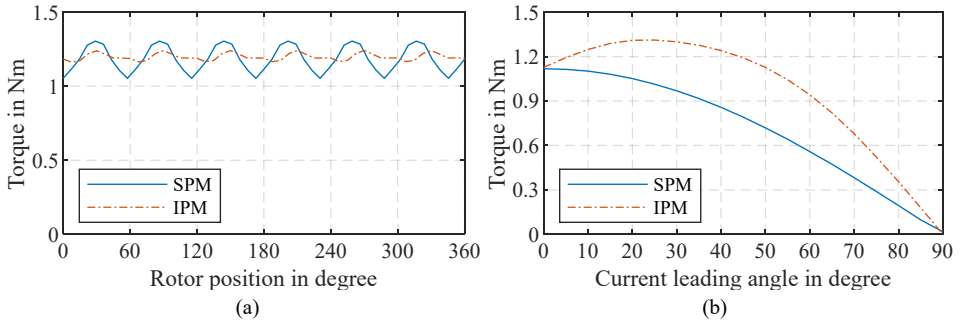
Figure 4.49: Torque ripple and torque as a function of current leading angle. (a) Torque. (b) Torque as a function of current leading angle when the phase current is 40 A-RMS.
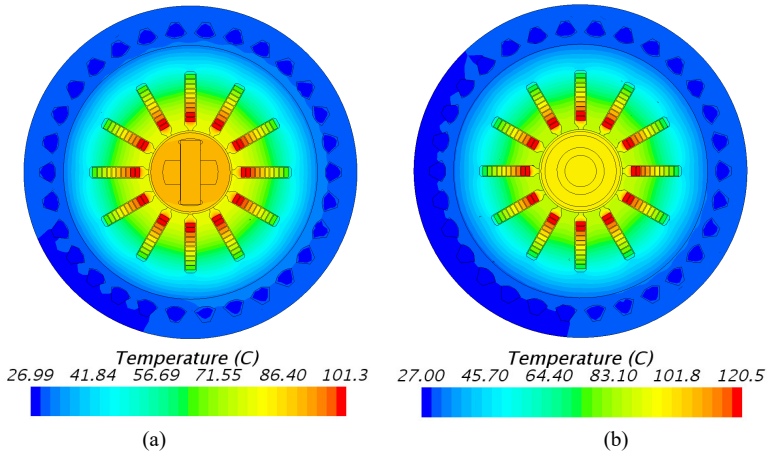
Figure 4.50: Temperature distributions of the motors at 125,000 /min and 1.2 Nm when the influence of the PWM inverter is not considered. (a) IPM motor. (b) SPM motor.

4.8 Temperature distribution of the designed IPM

The temperature distribution of each part of the IPM motor is presented in Fig. 4.51. The outlet water is about 3 °C hotter than the inlet water. Because the eddy current losses of the conductors in one slot are unevenly distributed, which has been analyzed in the Section 4.1.2, the temperature rises of the conductors close to the air gap are about 40 °C higher than that of the bottom conductors, which have lower losses and better heat dissipation condition. The maximum temperature rises of the rotor and the windings with rated torque at the maximum speed are about 68.8 °C and 79.0 °C based on the CFD analyses. The rotor has lower temperature rise than the windings because the losses caused by PWM inverter are not considered and this problem will be illustrated in the next Chapter. Based on the analytical results it is believed that the designed motor is feasible.
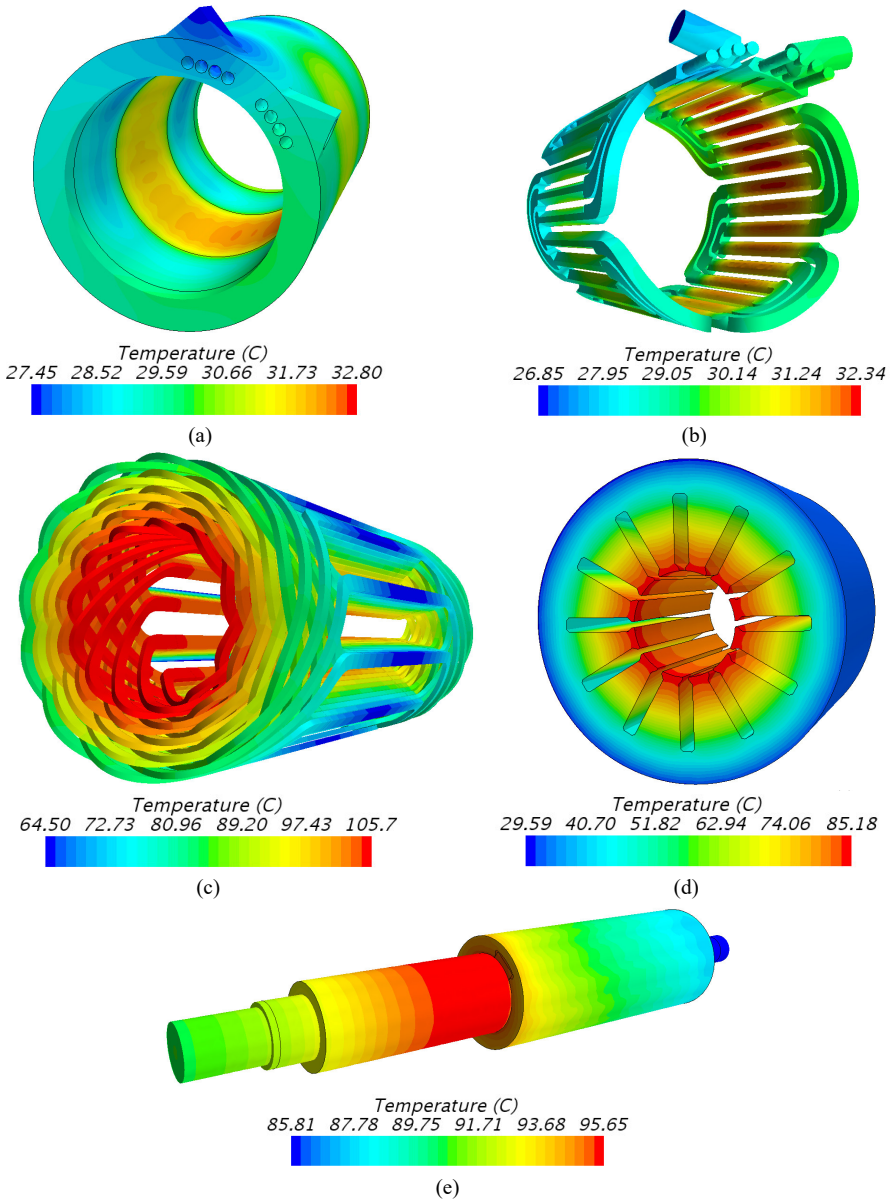
Figure 4.51: Temperature distributions of the components of the IPM prototype encapsulated with resin epoxy of thermal conductivity 0.6 W/mK. (a) Water-cooled housing. (b) Water. (c) Windings. (d) Stator core. (e) Rotor.

5 Influence of PWM inverter on the losses of the high-speed PM motors

The influence of the PWM inverter on the losses of the AC induction motors has obtained the attention from the international electrotechnical commission (IEC). Because this problem is very important and it will result in higher losses and lower efficiency of the motors, IEC has published specific test methods in IEC 60034-2-3 for determining losses and efficiency of converer-fed AC induction motors and a new version will be published soon. Since the influence of the PWM inverter on the losses of the motors was not considered in Chapter 4, the analytical results showed that the proposed IPM motor has only minor advantages in terms of electromagnetics compared with the SPM motor. However, when the influence of the PWM inverter is considered, the proposed IPM motor will has distinct advantages and this case will be studied in this chapter. In order to provide the motor designers valuable references for predicting the additional high-frequency losses of the motors caused by the PWM inverters in the design stage, analytical, FEA and coupled simulation methods will be introduced in detail in this chapter.

5.1 Calculation of current harmonics generated by the PWM inverter

To predict the additional losses of the motors, the phase currents fed by the PWM inverters need to be firstly calculated. There are four available methods to obtain the phase currents: 1) conduct coupled simulation between the magnetic field simulator and control simulator to calculate the phase currents [151]; 2) directly measure the phase currents from the experiments [152]; 3) feed PWM voltages to the FEA model to calculate the phase currents [153], [154]; and 4) calculatd through the mathematical model of the motor. Coupled simulation has a high prediction precise. Available coupled simulation softwares include Flux with Simulink, Ansoft with Simplorer, etc. However, coupled simulation takes a much longer time compared with the other methods. Directly measurement of the phase currents in the motor design stage is unfeasible. When the third method is applied, in order to take all the high-order voltage harmonics into consideration, the time-step needs to be very small and this again results in a long simulation time. Hence, analytical equations to predict the phase currents fed by the PWM inverter are valuable.

The schematic diagram of a PWM inverter connected with a PM motor is shown in Fig. 5.1. The equivalent circuit of the A phase circuit is shown in Fig. 5.2. When the power switch S_A^+ or S_A^- is turned on, the voltage V_{AO} is expressed as (5.1). Similarly, V_{BO} and V_{CO} can

be known. Since the voltage V_{ON} has the form of (5.2), the phase voltage V_{AN} can be expressed as (5.3). Then, the A phase current I_{AN} can be calculated by (5.4) according to the phase circuit shown in Fig. 5.2. In (5.4) the back-EMF e_{AN} can be obtained by FEA or analytical method.
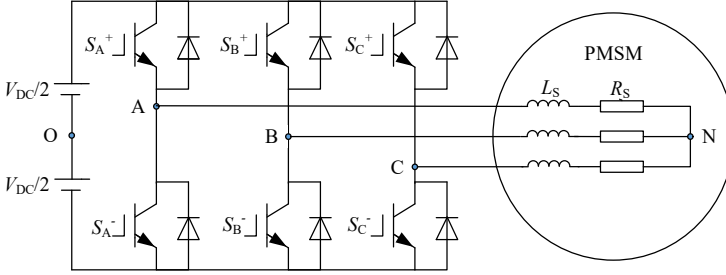
Figure 5.1:   Schematic diagram of a PWM inverter connected with a PM motor.
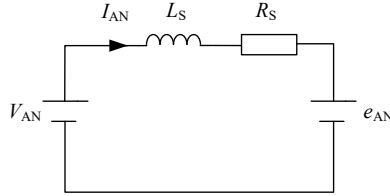
Figure 5.2:   Equivalent circuit of A phase.

$$\begin{cases} V_{AO} = \dfrac{1}{2}V_{DC}, & S_A^+ = 1 \\[2mm] V_{AO} = -\dfrac{1}{2}V_{DC}, & S_A^- = 1 \end{cases} \tag{5.1}$$

$$V_{ON} = -\frac{1}{3}\left(V_{AO} + V_{BO} + V_{CO}\right) \tag{5.2}$$

$$V_{AN} = V_{AO} + V_{ON} \tag{5.3}$$

$$V_{AN} - R_S I_{AN} - e_{AN} = L_S \frac{dI_{AN}}{dt} \tag{5.4}$$

When the fundamental frequency of the output current is 200 Hz and the PWM frequency is 5 kHz, the calculated voltage V_{AN} and the current I_{AN} are presented in Fig. 5.3. The spectrum of the phase current clearly shows that the 49th and 51st current harmonics have highest amplitudes. It is because the phase current rises and falls twice in one PWM period, which

is caused by the space vector PWM (SVPWM). The analysis of the phase voltage and current in a PWM period is shown in Fig. 5.4. When the output voltage of the PWM inverter is higher than the back-EMF of the motor, the phase current increases. Conversely, the phase current decreases. The corresponding current variations are expressed as (5.5). When the RMS value of the phase current is equal to 0, the phase voltage supplied by PWM inverter is equal to the back-EMF e_{AN}. Then the phase current variation satisfy (5.6) and t_2 is close to 0. Based on (5.5) to (5.7) the maximum current variation is derived as (5.8). Based on (5.8) it is known that the amplitudes of the current harmonics generated by the PWM inverter are determined by the phase inductance, the switching frequency, the DC-bus voltage and the speed of the motor (correspond to the back-EMF). When the DC-bus voltage is much higher than the back-EMF, the amplitudes of the current harmonics caused by the PWM inverter are proportional to the back-EMF (the speed of the rotor) and are inversely proportional to the PWM frequency. The amplitudes of the current harmonics can be reduced when the switching frequency is increased or the phase inductance can be increased. However, by increasing the PWM frequency to reduce the amplitudes of the current harmonics may be not very helpful in reducing the eddy current (EC) losses because the frequencies of the current harmonics are correspondingly increased.
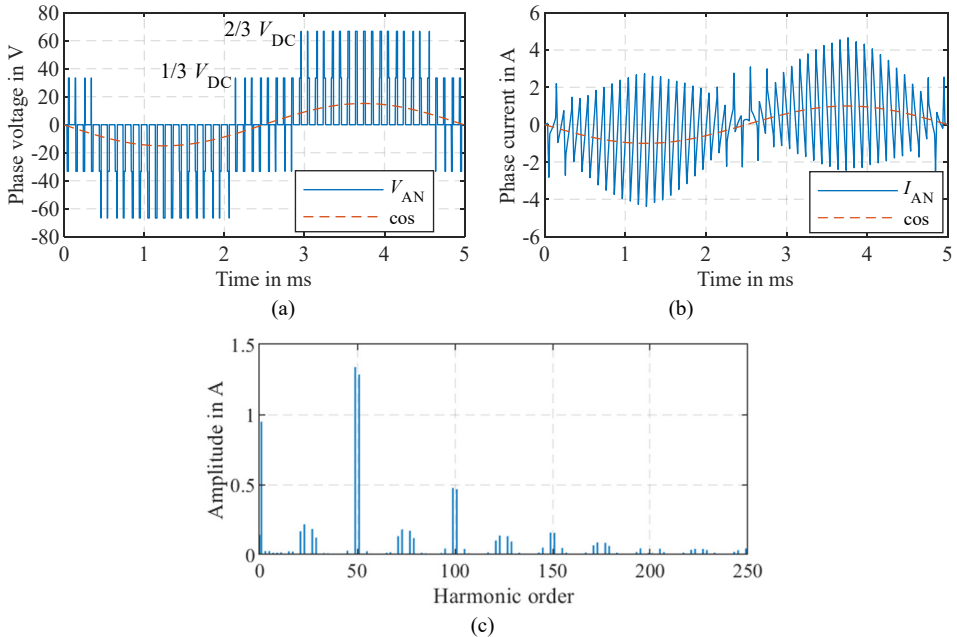
Figure 5.3:   Voltage and current of A phase. (a) Voltage waveform. (b) Current waveform. (c) Spectrum of the phase current.

103

$$\begin{cases} \Delta i_1 = \dfrac{1}{L_{\mathrm{S}}}\left(\dfrac{2}{3}V_{\mathrm{DC}} - e_{\mathrm{AN}} - R_{\mathrm{S}}i_{\mathrm{AN}}\right)t_1 \\[2mm] \Delta i_2 = \dfrac{1}{L_{\mathrm{S}}}\left(\dfrac{1}{3}V_{\mathrm{DC}} - e_{\mathrm{AN}} - R_{\mathrm{S}}i_{\mathrm{AN}}\right)t_2 \\[2mm] \Delta i_3 = \dfrac{1}{L_{\mathrm{S}}}\left(-e_{\mathrm{AN}} - R_{\mathrm{S}}i_{\mathrm{AN}}\right)t_3 \end{cases} \tag{5.5}$$

$$\Delta i_1 + \Delta i_2 + \Delta i_3 = 0 \tag{5.6}$$

$$t_1 + t_2 + t_3 = \frac{T}{2} \tag{5.7}$$

$$\Delta i_{3,\max} = -\frac{e_{\mathrm{AN}}T}{2L_{\mathrm{S}}}\frac{2V_{\mathrm{DC}} - 3e_{\mathrm{AN}}}{2V_{\mathrm{DC}}} \tag{5.8}$$
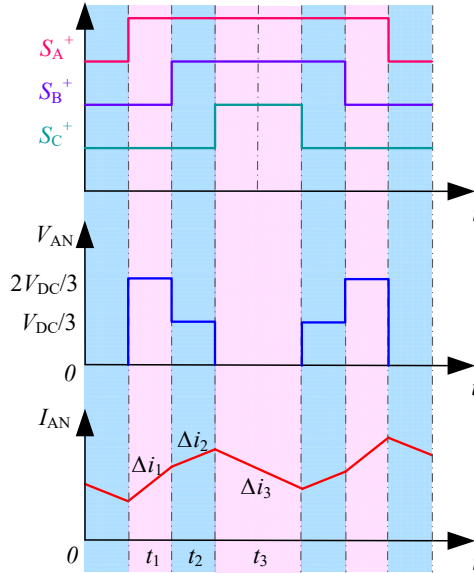
Figure 5.4:   Phase current analysis of one PWM period.

5.2   Prediction of eddy current loss of SPM rotor

Currently, the calculation of the EC losses of the PMs mainly depends on the FEA. Although FEA method has a high precision on the losses calculation, it is time-consuming because the calculation of EC losses needs to solve differential equations, which requires a small time-step to consider the high-frequency EC losses. Therefore, analytical methods

are popular. In [155] and [156] analytical methods to calculate the no-load EC losses of PMs caused by slotting are introduced. In order to predict the EC losses of PMs caused by armature reaction field, equivalent current sheets method is frequently employed [157]-[162]. However, using the winding and slot opening factors to calculate the equivalent current sheets lacks precision at high-order current harmonics. In [160]-[162] the equivalent current sheets are expressed as Fourier series, which are also adopted in this section. Then the EC distribution in the PMs can be calculated by solving the time derivative of the vector magnetic potential [160]. To take the slotting effect into account, the subdomain model is used in [163]. The analytical results presented in [157]-[163] show a high analytical accuracy at low frequency. However, the EC losses caused by the high-frequency current harmonics are not studied. Another method named Poynting vector method is also used for this purpose in [164], but there is no detailed derivation and verification. Thus, in this section, analytical equations to predict the EC density and losses of the PMs induced by current harmonics are derived in detail.

5.2.1 Theoretical analysis

Generally, an electrical machine consists of abundant temporal current harmonics and spatial magnetic field harmonics. If a spatial magnetic field harmonic rotates asynchronously with the rotor, EC losses are induced in the magnets as the magnets are solid and conductive. The induced current obeys the right-hand rule and the EC loops are shown in Fig. 5.5. To calculate the EC losses, the EC density in each PM unit cell must be calculated, as shown in the right side of Fig. 5.5. In each unit cell, the induced voltage e can be calculated by Faraday's law as expressed in (5.9). When the resistance along the tangential direction is ignored and the magnet is considered as a ring, the corresponding EC i and EC density J can be expressed as (5.10) and (5.11).
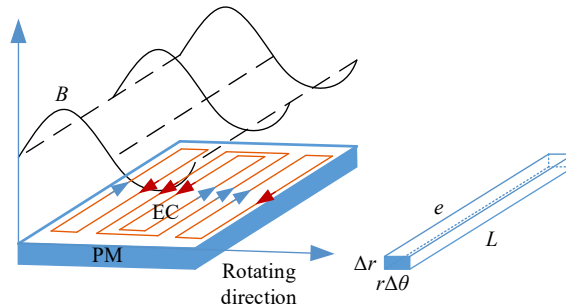
Figure 5.5: Principle of EC induced by magnetic field.

$$e = -\frac{d\psi}{dt} = -\frac{Lr\Delta\theta dB}{dt} \qquad (5.9)$$

$$i = \frac{e}{R} = \sigma \frac{er\Delta\theta\Delta r}{L} = -\sigma \frac{r^2 (\Delta\theta)^2 \Delta r dB}{dt} \qquad (5.10)$$

$$J = \frac{i}{r\Delta\theta\Delta r} = -\sigma \frac{r\Delta\theta dB}{dt} \qquad (5.11)$$

where e is induced voltage; ψ is flux; σ is conductivity of magnets; L is axial length of magnet; R is resistance; B is flux density; Δr and $r\Delta\theta$ are the thickness and width of magnet cell unit in polar coordinate and t is time.

Then, the resulted eddy current loss of one PM P can be calculated by [165]

$$P = \int_0^L \int_{\theta_1}^{\theta_2} \int_{R_r}^{R_m} \frac{J^2}{\sigma} r dr d\theta dz \qquad (5.12)$$

where R_m is the outer radius of the PM; R_r is the outer radius of the rotor core.

The problem of using (5.11) to calculate current density J is that its value is determined by $\Delta\theta$. Another method to calculate the current density is to use the vector magnetic potential A as expressed in [159]

$$J = -\sigma \frac{\partial A}{\partial t} + C \qquad (5.13)$$

where C is an integration constant which is a function of time t and to ensure the total current in one PM block is equal to 0.

5.2.1.1 Equivalent current sheets

In order to calculate the vector magnetic potential A, equivalent current sheet is employed as aforementioned [160]. As for the designed motor of 2-pole/12-slot, the phase currents can be expressed as (5.14). Since the stator current is distributed on the stator inner surface and is concentrated in the slot opening area with thickness equal to 0, the equivalent current sheets at time 0 are illustrated in Fig. 5.6.

$$\begin{cases} i_a(t) = \sum_u I_u \cos\left(u\omega t + \alpha_u\right) \\ i_b(t) = \sum_u I_u \cos\left(u\left(\omega t + \dfrac{2}{3}\pi\right) + \alpha_u\right) \\ i_c(t) = \sum_u I_u \cos\left(u\left(\omega t + \dfrac{4}{3}\pi\right) + \alpha_u\right) \end{cases} \qquad (5.14)$$

where, I_u is the amplitude of uth temporal current harmonic; α_u is the phase angle of uth temporal current harmonic; ω is fundamental frequency and i_a, i_b, i_c are the phase currents.
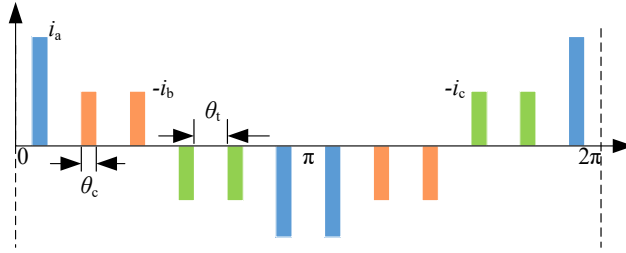
Figure 5.6: Distribution of armature current sheets.

With the use of fast Fourier transform (FFT) method, the phase current densities J_a, J_b, J_c can be expressed in (5.15) and (5.16). Then the total current distribution along stator inner circumference J_s is equal to (5.17).

$$\begin{cases} J_a(t,\theta) = \sum_v \dfrac{4Ni_a}{v\pi b_0} K \cos\left(v\theta\right) \\ J_b(t,\theta) = \sum_v \dfrac{4Ni_b}{v\pi b_0} K \cos\left(v\left(\theta + \dfrac{2}{3}\pi\right)\right) \\ J_c(t,\theta) = \sum_v \dfrac{4Ni_c}{v\pi b_0} K \cos\left(v\left(\theta + \dfrac{4}{3}\pi\right)\right) \end{cases} \qquad (5.15)$$

$$K = \sin\left(v\left(\frac{1}{2}\theta_t + \theta_c\right)\right) - \sin\left(\frac{v}{2}\theta_t\right) \qquad (5.16)$$

where N is the number of turns in one slot; v is the order of the spatial field harmonics; b_0 is slot opening width; θ_t is width of tooth and θ_c is width of slot opening in polar coordinate as shown in Fig. 5.6.

$$J_s(t,\theta) = J_a + J_b + J_c = \sum_{u=1,7,13\dots}\sum_{v=1,7,13\dots} \frac{6NI_u}{v\pi b_0} K\cos(u\omega t - v\theta + \alpha_u)$$

$$+ \sum_{u=1,7,13\dots}\sum_{v=5,11,17\dots} \frac{6NI_u}{v\pi b_0} K\cos(u\omega t + v\theta + \alpha_u)$$

$$+ \sum_{u=5,11,17\dots}\sum_{v=1,7,13\dots} \frac{6NI_u}{v\pi b_0} K\cos(u\omega t + v\theta + \alpha_u) \tag{5.17}$$

$$+ \sum_{u=5,11,17\dots}\sum_{v=5,11,17\dots} \frac{6NI_u}{v\pi b_0} K\cos(u\omega t - v\theta + \alpha_u)$$

$$= \sum_{u=1,5,7\dots}\sum_{v=1,5,7,11\dots} \frac{6NI_u}{v\pi b_0} K\cos(u\omega t \pm v\theta + \alpha_u)$$

In equation (5.17) the orders of the current harmonics which are multiplier of 3 are not considered because the windings of the motor are connected to star type. Theoretical, the phase currents do not consist of even-orders current harmonics. Hence, they are also not considered in equation (5.17). However, because of the influence of the cogging torque and torque ripple, the phase currents may consist of even-order current harmonics. Then they should be added to equation (5.17).

5.2.1.2 Armature reaction field

To avoid the influence of the stator slots and simplify the analysis, in the analytical model some assumptions are made as follows: 1) the stator is considered slotless and the stator current is distributed on the stator inner surface; 2) the nonlinear properties of the iron cores are not considered; 3) the permeability of the iron cores is infinite; 4) the losses of the sleeve are ignored; 5) the relative permeability of the magnet is equal to 1; 6) the effects of the EC in the PMs on the armature reaction field and on the EC distributions in the PMs are not considered. Then the boundary conditions of the air-gap magnetic field have the expressions as

$$B_\theta\big|_{r=R_r=0}, \qquad H_\theta\big|_{r=R_s=J_s} \tag{5.18}.$$

The armature reaction field in the air gap and magnet regions is governed by (5.19) and A is the magnetic vector potential. The general solution for (5.19) is equal to (5.20) [165].

$$\nabla^2 A = 0 \tag{5.19}$$

$$A(r,\theta,t) = \sum_u \sum_v \left(C_{u,v} r^v + D_{u,v} r^{-v}\right)\cos(u\omega t \pm v\theta + \alpha_u) \tag{5.20}$$

The radial and tangential magnetic flux components B_r and B_θ can be calculated by (5.21) and (5.22), respectively.

$$B_{\rm r}\left(r,\theta,t\right)=\frac{1}{r}\frac{\partial A\left(r,\theta,t\right)}{\partial\theta}=\sum_u\sum_v\mp v\left(C_{u,v}r^{v-1}+D_{u,v}r^{-v-1}\right)\sin\left(u\omega t\pm v\theta+\alpha_u\right) \quad (5.21)$$

$$B_{\theta}\left(r,\theta,t\right)=-\frac{\partial A\left(r,\theta,t\right)}{\partial r}=-\sum_u\sum_v v\left(C_{u,v}r^{v-1}-D_{u,v}r^{-v-1}\right)\cos\left(u\omega t\pm v\theta+\alpha_u\right) \quad (5.22)$$

According to the boundary conditions (5.18), the coefficients $C_{u,v}$ and $D_{u,v}$ can be expressed as (5.23) and (5.24), respectively.

$$D_{u,v}=-\frac{1}{v^2}\frac{1}{R_{\rm r}^{-2v}R_{\rm s}^{v-1}-R_{\rm s}^{-v-1}}\frac{6\mu_0 NI_uK}{\pi b_0} \quad (5.23)$$

$$C_{u,v}=D_{u,v}R_{\rm r}^{-2v} \quad (5.24)$$

where $R_{\rm r}$ and $R_{\rm s}$ are the radius of rotor and stator cores, respectively.

5.2.1.3 EC distribution and loss

To calculate the ECs and their losses in the rotor PMs, the vector magnetic potential A is transferred to the rotor frame firstly as expressed in (5.25). Then, the EC density J_e caused by the changing magnetic field can be calculated through (5.26) according to (5.13).

$$A\left(r,\theta,t\right)=\sum_u\sum_v\left(C_{u,v}r^v+D_{u,v}r^{-v}\right)\cos\left(u\omega t\pm v\omega t\pm v\theta_0+\alpha_u\right) \quad (5.25)$$

$$J_{\rm e}\left(r,\theta,t\right)=-\sigma\frac{\partial A\left(r,\theta,t\right)}{\partial t}+C\left(t\right) \quad (5.26)$$

In (5.26), $C(t)$ is an integration constant which forces the total ECs in one PM equal to 0 at any instant. For example, for a magnet which is from θ_1 to θ_2, it has the expression as (5.27). Based on (5.27) the integration constant has the expression as (5.28) and (5.29).

$$\int_{R_{\rm r}}^{R_{\rm m}}\int_{\theta_1}^{\theta_2}J_{\rm e}\left(r,\theta,t\right)rdrd\theta=0 \quad (5.27)$$

$$C\left(t\right)=\mp\frac{2}{\alpha_{\rm p}}\frac{\sigma}{R_{\rm m}^2-R_{\rm r}^2}\sum_u\sum_v\frac{2}{v}\left(u\omega\pm v\omega\right)K_{\rm ap}$$
$$\times\left[\frac{1}{v+2}C_{v,u}\left(R_{\rm m}^{v+2}-R_{\rm r}^{v+2}\right)+\frac{1}{-v+2}D_{v,u}\left(R_{\rm m}^{-v+2}-R_{\rm r}^{-v+2}\right)\right] \quad (5.28)$$

$$K_{\text{ap}} = \cos\left(u\omega t \pm v\omega t \pm v\theta_1 + \alpha_u\right) - \cos\left(u\omega t \pm v\omega t \pm v\theta_2 + \alpha_u\right) \tag{5.29}$$

where $\alpha_p = \theta_2 - \theta_1$; R_m and R_r are the PM and rotor core outer radii.

Then the expression of EC density in one PM J_e can be expressed as (5.30) and the EC loss density P_e is expressed as (5.31).

$$
\begin{aligned}
J_e\left(r,\theta,t\right) &= \sigma \sum_u \sum_v \left(u\omega \pm v\omega\right)\left(C_{u,v}r^v + D_{u,v}r^{-v}\right) \\
&\times \sin\left(u\omega t \pm v\omega t \pm v\theta_0 + \alpha_u\right) + C(t)
\end{aligned}
\tag{5.30}
$$

$$P_e\left(r,\theta,t\right) = \frac{J_e^2\left(r,\theta,t\right)}{\sigma} \tag{5.31}$$

where θ_0 is the initial angular position of the rotor.

Finally, the EC loss P_{mag} in one PM segment is equal to

$$P_{\text{mag}}\left(t\right) = \int_0^L \int_{R_r}^{R_m} \int_{\theta_1}^{\theta_2} P_e\left(r,\theta,t\right) r\,dr\,d\theta\,dz \tag{5.32}.$$

5.2.2 FEA verification

To verify the analysis above, the demonstrator SPM motor designed in Chapter 4 is analyzed. In order to avoid the influence of slotting of the stator, the phase currents are concentrated on small sheet regions with a thickness of 0.02 mm and the width is equal to the slot opening in FEA model. The carbon fiber sleeve is considered as non-conductive, because the resistivity of the used carbon fiber sleeve is $1.6e^{-5}$ Ωm, which is 10 times higher than that of the PM.

5.2.2.1 Influence of the fundamental current

Because the current sheets are concentrately distributed in the slot areas along the stator inner circumference, the armature reaction field consists of spatial field harmonics. For the designed integral-slot PM motors, the fundamental spatial field component is dominant, and this component caused by the fundamental current is synchronous with the rotor. Hence, this component does not induce EC loss in the rotor. However, the other spatial field harmonics caused by the fundamental current are asynchronous with the rotor. Thus, EC losses in the PMs are induced. The FEA and analytical results about EC losses caused by the fundamental current are compared and shown in Fig. 5.7 and Fig. 5.8, when the

rotation speed is equal to 20,000 /min and the peak value of the phase currents is equal to 20 A.

Fig. 5.7 shows the armature reaction field and the EC density in the PM region on the radius of 8.99 mm. Based on (5.30) the EC densities in any radius, angle and time can be calculated. The EC distributions in one PM pole by using analytical and FEA methods are compared in Fig. 5.8. It can be seen from Fig. 5.7 and Fig. 5.8 that a high accuracy is obtained by the analytical methods in calculating the magnetic field and EC densities caused by the fundamental current.

Fig. 5.8 shows that the EC caused by the high-order spatial field harmonics generated by the fundamental current is concentrated on the surfaces of the PMs. It is because the spans of the high-order spatical field harmonics are small. Due to the shielding effect, the penetration ability of the high-order spatial field harmonics is poor. Hence, the EC is concentrated on the surface.
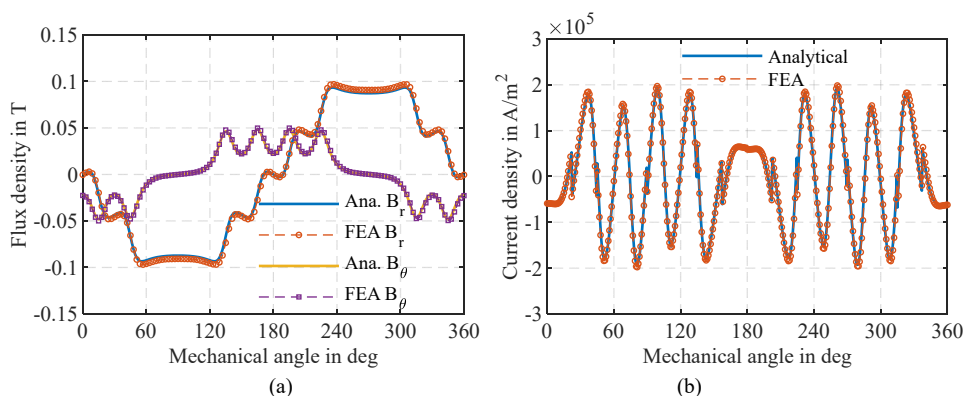
Figure 5.7: Armature reaction field and the induced EC density of the fundamental current in the PMs at radius of 8.99 mm. (a) Armature reaction field. (b) EC density.
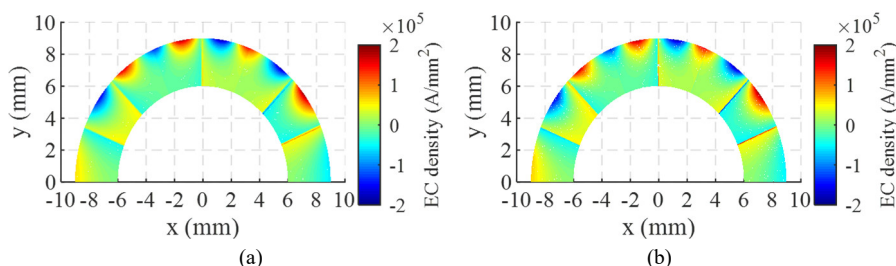
Figure 5.8: EC distribution of one PM pole caused by the fundamental current. (a) Analytical. (b) FEA.
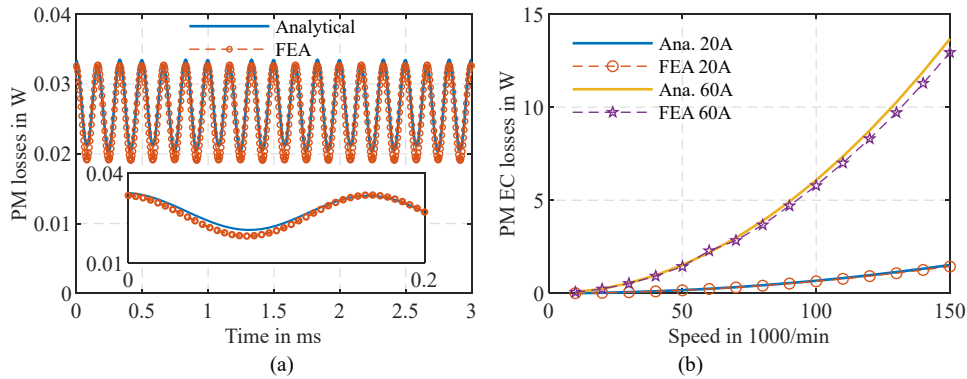
Figure 5.9: EC losses induced by fundamental currents. (a) Fundamental current 20 A at 20,000 /min. (b) EC losses caused by fundamental current as a function of speed and amplitude of the current.

Since the EC distribution has been precisely predicted, the EC losses of the PMs can be precisely calculated as shown in Fig. 5.9(a). The average error of the analytical EC losses is about 3.8%. When the amplitude of the fundamental current and the rotor speed are increased, the average losses in PMs are drawn in Fig. 5.9(b). The results show that the analytical method has a very high accuracy in calculating the EC losses caused by the fundamental current. In addition, from Fig. 5.9 it can be noted that the EC losses caused by the fundamental current are relatively low. This is mainly because the fundamental spatial field harmonic generated by the fundamental current is dominant and it is synchronous with the rotor. When fractional-slot single tooth windings are used, the EC losses of the PMs caused by the fundamental current will be much higher.

5.2.2.2 Armature reactions of the high-order current harmonics

The air-gap magnetic field generated by the high-order current harmonics has the same form with that generated by the fundamental current because they are decided by the winding configuration. The magnitudes of them are determined by the amplitudes of the currents. However, the rotating speed of those spatial field harmonics are decided by the frequencies of the current harmonics. For example, the rotating speed of the 1st spatial field harmonics generated by the 61st current harmonic is 61 times the rotor rotation speed. Furthermore, the amplitude of the 1st spatial field harmonic is the highest and it is much higher than those of the high-order spatial harmonics. Hence, this component will generate high EC losses in the PMs. When the PWM frequency is 10 kHz, at 20,000 /min, the 61st current harmonic has highest amplitude among current harmonics. When the amplitude of the 61st current harmonics is 1 A, by using (5.27) to force the total EC in each PM segment equal to 0, the analytical results are compared with FEA as shown in Fig. 5.10 and Fig. 5.11.

It can be found from Fig. 5.10(a) that the analytical error of the flux density is a little high. This is because the amplitude of the high-order current harmonic is low and the influence of the EC on the flux density is not considered. In this case, the error of EC losses in the PMs shown in Fig. 5.12(a) is about 2.9 %. By comparing Fig. 5.12 with Fig. 5.9 it can be known that the EC losses caused by high-order current harmonics are much higher than those caused by the fundamental current.

It can also be noticed that the EC distributions in the PMs caused by the high-order current harmoincs are not more concentrated on the surfaces of the PMs. Instead, the EC magnitudes along radial direction change slightly. This is because the 1st order spatial field is dominant and its rotating speed is n times the rotor speed when this spatial filed is generated by the nth current harmonic. Because the span of the 1st spatial field is larger than the width of the segmented PMs, the shielding effect is weak.
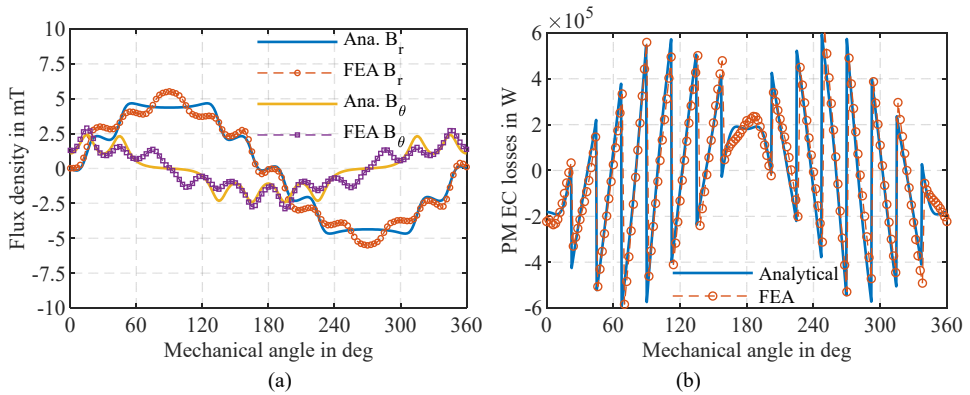
Figure 5.10:   Armature reaction field and the induced EC density of the 61st current harmonic in the PMs at radius of 8.99 mm. (a) Armature reaction field. (b) EC density.
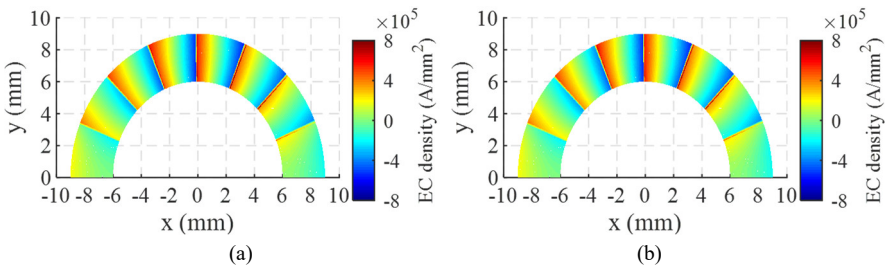
Figure 5.11:   EC distribution of one PM pole caused by the 61st current harmonic. (a) Analytical. (b) FEA.

Fig. 5.12(b) shows the EC losses as a function of speed caused by the 5th and 61st current harmonics with amplitude equal to 1 A, respectively. Because the analytical method does not consider the effects of ECs in the PMs on the armature reaction field and on the EC

distributions in the PMs, the difference between analytical and FEA EC losses at high speed caused by high-order current harmonics is high. Hence, to predict the real EC losses in the PMs, coupled simulation is also employed in the following section.
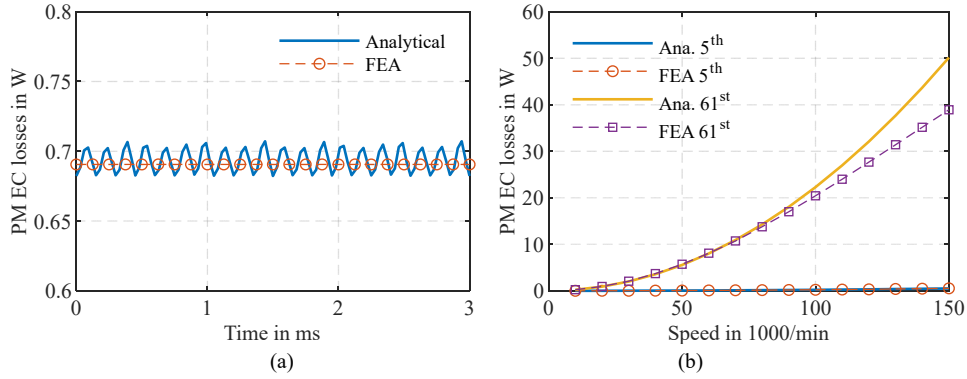
Figure 5.12: EC losses induced by current harmonics. (a) 61st current harmonic of 1 A at 20,000 /min. (b) EC losses caused by the 5th and 61st current harmonics of 1 A as a function of speed.

5.2.2.3 Diffusion effect

In order to correct the EC losses caused by the high-order harmonics at high speed, the diffusion effect is considered. The function of diffusion effect can be considered as the increase of the resistance of the PM [155]. A factor K_{de}, which is a function of the frequency of eddy current and the size of the PM can be used to modify the conductivity of PMs and it is expressed as

$$\sigma_f = K_{de}\sigma \tag{5.33}.$$

This factor is not higher than 1. Analytical calculation of the PM eddy current losses considering the diffusion effect can be found in [162]. In order to simplify the analysis, FEA method is used to determine this factor. For example, as regards the analyzed SPM motor, the factor K_{de} as a function of the frequency of eddy current for different size of PM segments is presented in Fig. 5.13. It shows that when the frequency of eddy current increases, the factor decreases because of greater diffusion effect. A larger size of PM segment also causes greater diffusion effect.
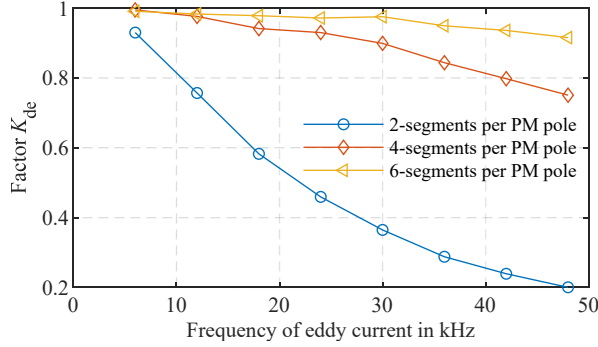
Figure 5.13:   A factor to modify the conductivity of PM because of diffusion effect as a function of the frequency of eddy current for different size of PM segments.

5.2.2.4 Influence of slotting and PM segmentation

In [155] a simplified method to determine the PM eddy current loss caused by slotting is presented. The mean value of the eddy current losses of PMs caused by slotting can be expressed as [155]

$$\hat{P}_e = \frac{\sigma L H_m B_0^2 \omega_{rotor}^2 R_s^2 w}{2} \sum_n K_n^2 \left[1 - \left(\frac{s}{\pi n w} \sin \frac{\pi n w}{s} \right)^2 \right] \tag{5.34}$$

where $B_0 = B_r(R_m - R_r)/(R_m - R_r + \mu_r(R_s - R_m))$; $w = R_m(\theta_2 - \theta_1)$; $s = 2\pi R_s/N_s$; $H_m = R_m - R_r$; B_r is the remanence of the PM; ω_{rotor} is the mechanical speed of the rotor; N_s is the slot number of the stator; K_n is the coefficients of the Fourier series of the modulation function, which is obtained using conformal mapping method [155], [O8]. To avoid complicate conformal mapping, the flux density of the middle air-gap position at static state can be used to calculate the coefficients K_n.

Because this method does not consider the variation of the eddy current in the thickness direction of PM, the calculation error at a high speed is large. To solve this problem, the PM is divided into x layers in thickness, then the coefficients K_n are replaced by $K_{n,Rx}$. The improved calculation equation is expressed as

$$\hat{P}_e = \int_{R_r}^{R_m} \frac{\sigma L H_m B_0^2 \omega_{rotor}^2 R_s^2 w_{Rx}}{2x} \sum_n K_{n,Rx}^2 \left[1 - \left(\frac{s}{\pi n w_{Rx}} \sin \frac{\pi n w_{Rx}}{s} \right)^2 \right] dR \tag{5.35}$$

where $w_{Rx} = Rx(\theta_2 - \theta_1)$; $K_{n,Rx}$ is the coefficients of the Fourier series of the flux density at the radius Rx.

Generally, the PM EC losses caused by the stator slot cannot be ignored. However, compared with the high-frequency EC losses caused by the high-order current harmonics, the losses due to slotting are very small. In table 5.1, the PM losses caused by slotting, fundamental current, high-order current harmonics of different segmental PM poles are compared. It shows that the EC losses caused by the slotting and the fundamental current are much lower than those caused by the high-order current harmonics. The total EC losses caused by these three aspects are close to those caused by the high-order current harmonics. In addition, segmentation cannot dramatically reduce the EC losses caused by the slotting and the fundamental current. However, it can dramatically decrease the EC losses caused by the high-order current harmonics.

5.2.3 Verification by coupled simulation

Because experimental measurement of EC losses is very difficult to conduct, to validate the feasibility of the analytical method and to predict the real EC losses in the motor, coupled simulation is used. The external circuit applied in the FEA software for coupled simulation is shown in Fig. 5.14. In this figure, "Udc" is the DC bus voltage source; "S1" is a power electronic switch which consists of a switch whose state is controlled by the PWM signal from the Simulink; a DC voltage to represent the on-state voltage drop and an anti-parallel diode. "Phase A" is the A-phase winding which consists of a coil, an inductance and a resistance to take the end-winding into consideration. In the coupled simulation model, the slots of the stator and the non-linear properties of the electrical steel are considered. The Simulink model is shown in Fig. 5.15. The component "Coupling with Flux" in this figure is an interface between Simulink and Flux softwares. They exchange input and output data through this interface.
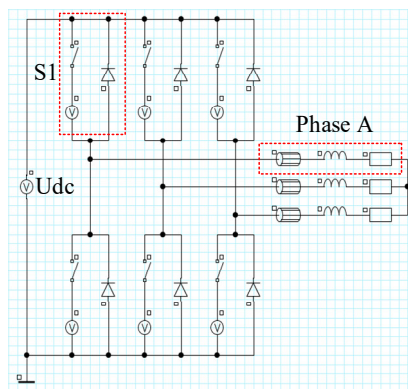
Figure 5.14:   External circuit of the FEA model.
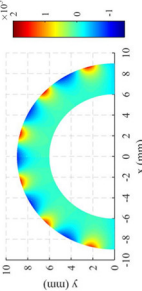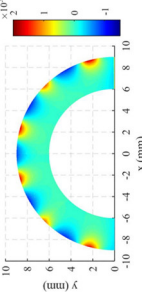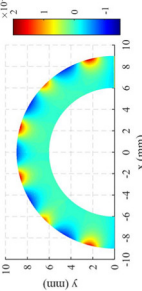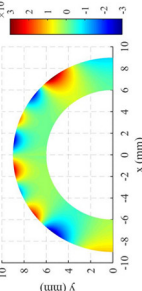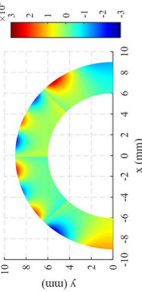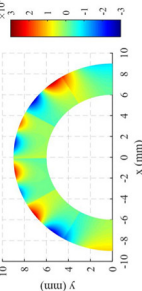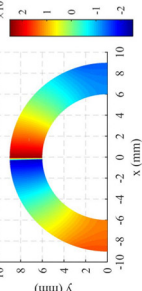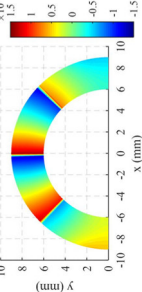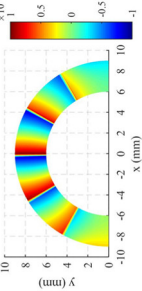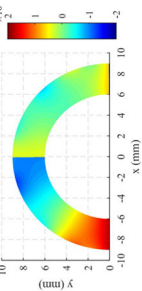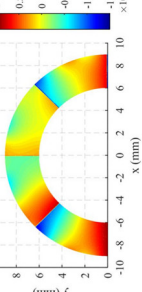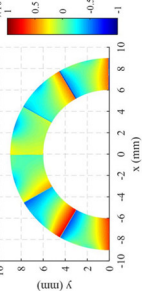
Segments	2	4	6
EC distribution caused by sloting effect			
FEA losses	0.013 W	0.013 W	0.013 W
Ana. Losses	0.016 W	0.016 W	0.016 W
EC distribution caused by 1st order of 30 A			
FEA losses	0.068 W	0.061 W	0.053 W
Ana. Losses	0.075 W	0.069 W	0.060 W
EC distribution caused by 61st order of 1 A			
FEA losses	5.24 W	2.44 W	1.16 W
Ana. Losses	5.63 W	2.63 W	1.25 W
EC distribution caused by slotted stator with 1st order of 30 A and 61st order of 1 A			
FEA losses	5.38 W	1.83 W	0.94 W

Table 5.1:   EC distribution and losses of PMs at 20,000 /min as a function of number of segments of one PM pole.
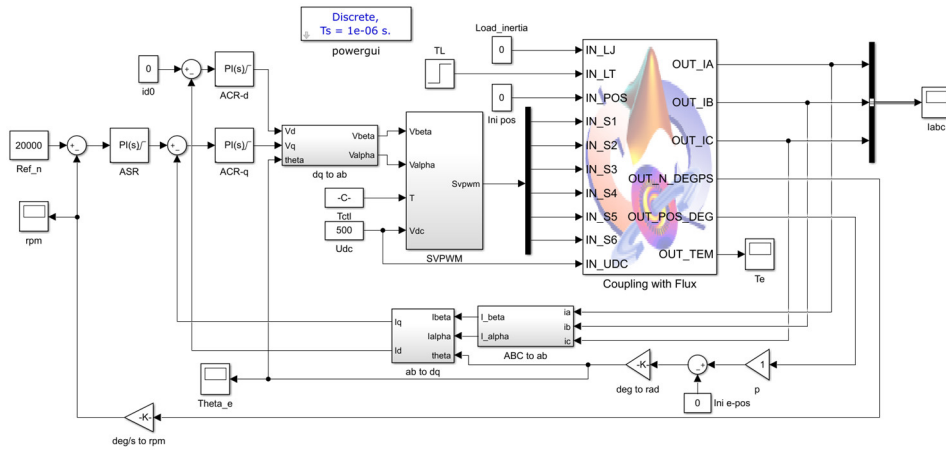
Figure 5.15:   Simulink model of coupled simulation.

Fig. 5.16 shows the phase currents, spectrum of the phase currents, the PM EC losses caused by currents with different orders and the total PM losses at different load conditions at 12,000 /min through different prediction methods, when the switching frequency is equal to 20 kHz. Because the phase current rises and falls twice in one PWM period which is caused by SVPWM as aforementioned, the phase current consists of high amplitudes of 199th and 401st current harmonics as shown in Fig. 5.16(b). It clearly shows that when the load increases, the amplitude of fundamental current increases in order to generate higher torque. The low-order current harmonics such as 5th and 7th also increase significantly. However, the amplitudes of 199th and 401st harmonics caused by the PWM inverter change slightly.

The PM EC losses generated by each current harmonics are shown in Fig. 5.16(c). It can be noticed that the low-order currents generate much lower EC losses than the 199th and 401st current harmonics, which are caused by the PWM inverter, even though the low-order currents have much higher amplitudes. Hence, the total losses change slightly when the load is changed as illustrated in Fig. 5.16(d). Fig. 5.16(c) and (d) also show that the analytical method is very accurate in predicting the PM EC losses.
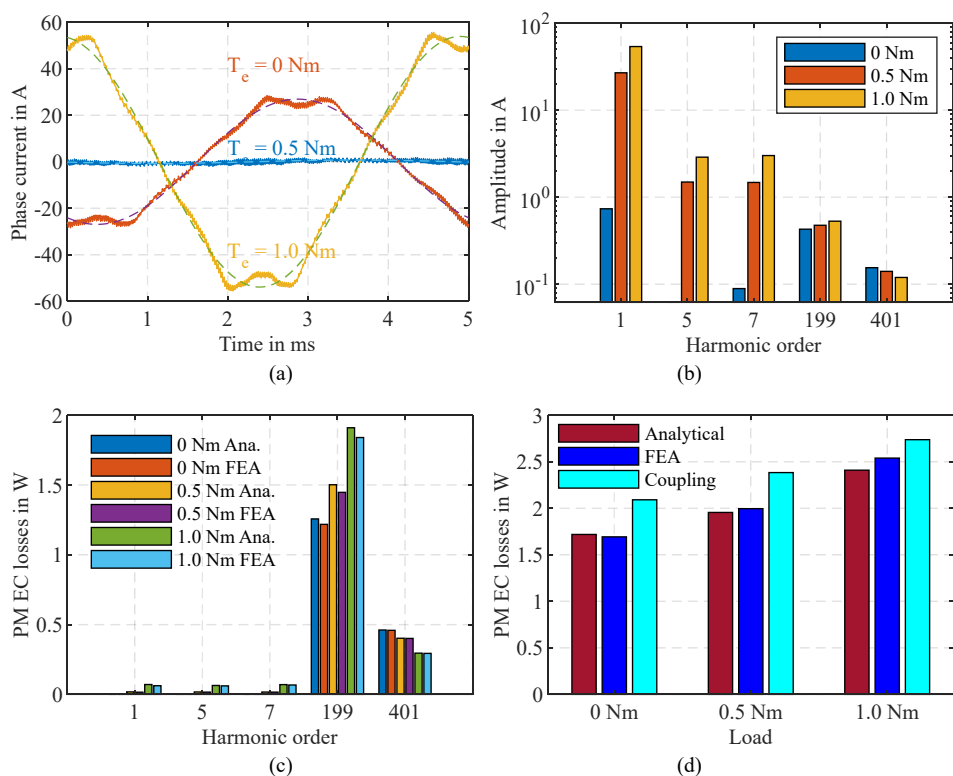
Figure 5.16: Comparison of analytical, FEA and coupled simulation resuts when the switching frequency is 20 kHz and the rotor speed is 12,000 /min. (a) A-Phase current. (b) Phase current FFT. (c) EC losses of PMs caused by current harmonics. (d) Total PM EC losses of PMs caused by sloting, 1st, 5th, 7th, 199th and 401st currents.

5.2.4 Methods to reduce the influence of PWM inverter

5.2.4.1 Increase the PWM frequency

When the switching frequency is increased, the orders of the current harmonics are proportional increased, whereas the amplitudes of the current harmonics are inversely proportional decreased. The EC losses variation under different switching frequencies and load conditions are compared in Fig. 5.17. It shows that when the switching frequency is increased, the EC losses are decreased. However, the reduction of the EC losses by increasing switching frequency is unsatisfied. When the PWM frequency is increased from 8 kHz to 80 kHz, which is ten times increased, the PM eddy current losses are only 42.6% reduced. Furthermore, Fig. 5.17 also shows that the EC losses in PMs are still very high even at

0 Nm torque condition. Considering the losses in power electronic module and the challenges of reducing the calculation and commutation time of the controller, by increasing the switching frequency to decrease the EC losses is not a prefered method.
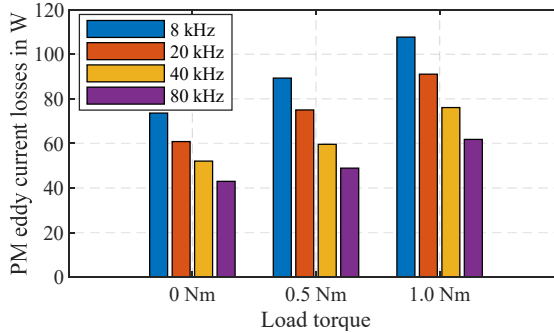
Figure 5.17:   PM eddy current losses at different PWM frequency and load when the rotor speed is 60,000 /min.

5.2.4.2 Increase the air-gap length

In terms of the machine design, increasing the physical air-gap length to reduce the armature reaction field is a possible way. If the mechanical air-gap, which is equal to 0.5 mm, is constant, by increasing the thickness of the fiber sleeve, the physical air-gap length is increased. In addition, the mechanical stress on the fiber sleeve is decreased. When the thickness of fiber sleeve is increased, the variation of the EC losses is presented in Fig. 5.18. It confirms that by increasing the thickness of fiber sleeve, the PM EC losses are decreased. The disadvantages of this method are that the torque and the efficiency of the motor are decreased. This method is generally adopted in the current design of the high-speed SPM motors and this is the reason why the power density of the high-speed SPM motor cannot be significantly increased by increasing the speed.
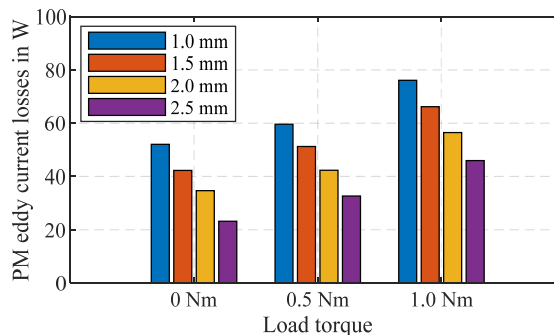
Figure 5.18:   PM eddy current losses at different sleeve thickness and load when the rotor speed is 60,000 /min and the PWM frequency is 40 kHz.

5.3 Losses comparison of IPM and SPM motors

Because of the existence of the rotor core, the analytical method for predicting EC losses of the SPM rotor cannot be directly applied to an IPM rotor. To compare the losses of the two motors, FEA and coupled simulation methods are adopted in this section.

5.3.1 Rotor eddy current losses

5.3.1.1 *d*-axis and *q*-axis inductances

Based on (5.8) it is known that the amplitudes of the current harmonics generated by the PWM inverter are inversely proportional to the phase inductance of the motor. Because the equivalent air-gap length of the IPM motor is smaller than that of the SPM motor, the IPM motor has higher phase inductance, which leads to lower amplitudes of the current harmonics. The *d*-axis and *q*-axis inductances of the two motors as a function of *d*-axis and *q*-axis currents are presented in Fig. 5.19. It can be found that the inductances of the SPM motor are constant, while the *q*-axis inductance of the IPM motor decreases dramatically, when the *q*-axis current increases. Because of a small air-gap length, the IPM motor is easily saturated. When the *q*-axis current is higher than 45 A, the *q*-axis inductance of the IPM motor is lower than that of the SPM motor as can be seen in Fig. 5.19. When the *q*-axis current is 60 A (rated torque current), the relative permeability of the two motors are compared in Fig. 5.20. It is easy to find that the *q*-axis inductance of the IPM motor is significantly decreased because the stator core is deeply saturated when the *q*-axis current is high. Hence, at a high load the IPM motor will have comparable amplitudes of the current harmonics caused by the PWM inverter with the SPM motor. The advantage of decreasing the amplitudes of the current harmonics of the IPM motor at a high load is not obvious.
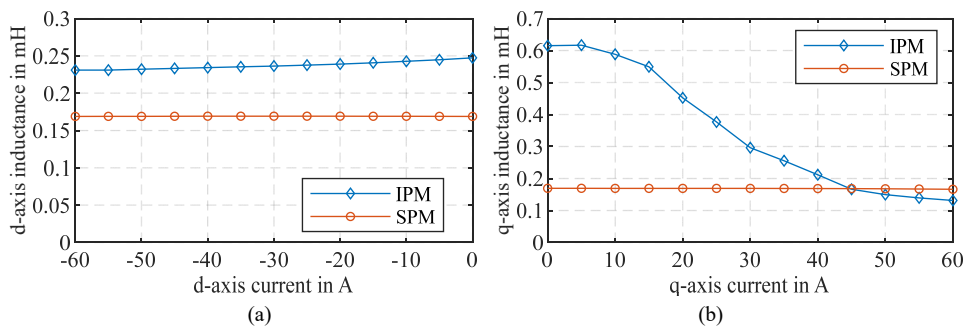
Figure 5.19:   *d*-axis and *q*-axis inductances of the two motors as functions of *d*-axis and *q*-axis currents. (a) *d*-axis inductances. (b) *q*-axis inductances.
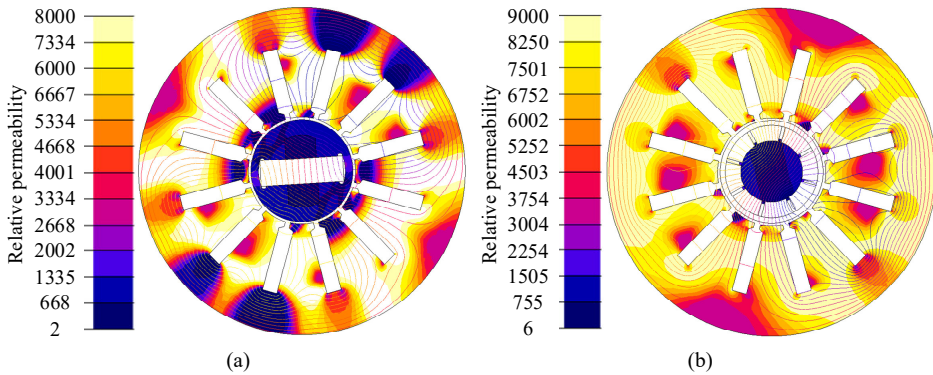
Figure 5.20:   Relative permeability of the two motors when the q-axis current is 60 A. (a) IPM motor.
(b) SPM motor.

5.3.1.2 Losses at no-load

When the speed is 60,000 /min and the PWM frequency is 25 kHz, the 49th current harmonic with high amplitude is generated based on the analysis in Section 5.1. Because the inductance of the IPM motor varies when the phase current changes, to compare the rotor losses of the two motors, a same current harmonic of a same amplitude is excited to the two motors. Fig. 5.21 shows the phase currents and the corresponding rotor losses of the two motors when the amplitude of the 49th order harmonic current is 1 A. Since the fundamental current is 0, the effective torque of the two motors is 0. The mean values of the rotor losses are compared in Table 5.2. It clearly shows that the SPM rotor has much higher losses than the IPM rotor even though the same current is fed to them. The shaft loss of the IPM rotor is very low, it is because the AMM has much higher permeability than the shaft when the phase current is low. However, because the armature reaction field generated by the high-order current harmonic needs to pass through the PM, the PM eddy current loss of the IPM rotor is high. Based on the FEA results it is believed that the IPM rotor has much lower losses than the SPM rotor when the load is low.
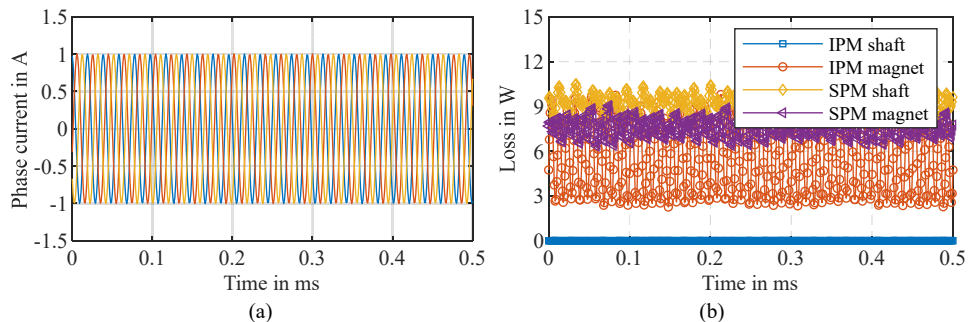
Figure 5.21:   Phase currents and corresponding eddy current losses of SPM and IPM motors caused by 49th current harmonic of 1 A at 60,000 /min. (a) 3-phase currents. (b) Rotor losses.

Mean loss in W	IPM	SPM
Shaft	0.01	9.26
PMs	5.50	7.63

Table 5.2:   Mean values of SPM and IPM rotors' eddy current losses caused by 49th current harmonic of 1 A at 60,000 /min.

5.3.1.3 Losses at load

When the fundamental current is 60 A and the 49th current is 1 A, the phase currents and corresponding rotor losses are presented in Fig. 5.22. It is worth to notice that the shaft loss of the IPM motor contains a low-frequency component. This component is caused by the fundamental current. Because the AMM rotor core is saturated at this load, the armature reaction field needs to pass through the shaft and causes high loss.
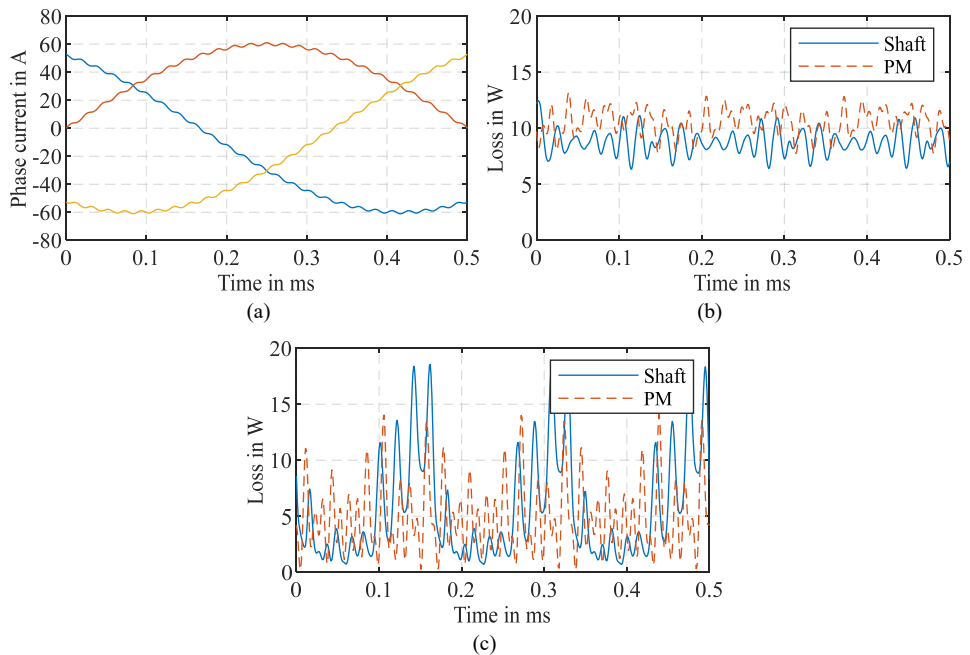
Figure 5.22:   Phase currents and corresponding eddy current losses of SPM and IPM motors caused by fundamental current of 60 A and 49th current harmonic of 1 A at 60,000 /min. (a) 3-phase currents. (b) SPM rotor losses. (c) IPM rotor losses.

The mean values of the two rotors are compared in Table 5.3. The total losses of IPM rotor is still much lower than that of the SPM rotor even though the same current is fed to the

two motors. The losses of the SPM rotor at no-load and load conditions are not much different. This is because the losses of the SPM rotor are mainly caused by the high-frequency current harmonics, which has been analyzed and proved in Section 5.2.

Mean loss in W	IPM	SPM
Shaft	5.72	8.77
PMs	4.93	10.51

Table 5.3: Mean values of SPM and IPM rotors' eddy current losses caused by fundamental current of 60 A and 49th current harmonic of 1 A at 60,000 /min.

When the current harmonics are not considered and the amplitudes of the fundamental currents are 60 A and 30 A respectively, the rotor losses of the IPM rotor are presented in Fig. 5.23. It can be found that the low-frequency loss component exists in the shaft loss when the load is high. At a lower load, because the AMM rotor core is unsaturated, the shaft loss is significantly reduced.

When all the current harmonics is considered, including the current harmonics caused by the PWM voltage and the controller's parameters, the rotors' losses are much higher than those presented in Table 5.3. Through coupled simulation, the rotor losses of the two motors at 60,000 /min and 1.2 Nm, when the PWM frequencies are 25 kHz and 100 kHz respectively, are calculated and presented in Fig. 5.24. It clearly shows that the rotor losses decrease when the PWM frequency increases. Moreover, the IPM rotor has much lower losses than the SPM rotor. When the PWM frequency is increased from 25 kHz to 100 kHz, the rotor losses of the IPM rotor are reduced by about 70.8 %, while the losses of the SPM rotor are reduced by about 56.5 %. The IPM rotor has significant advantage in terms of rotor losses compared with the SPM rotor.
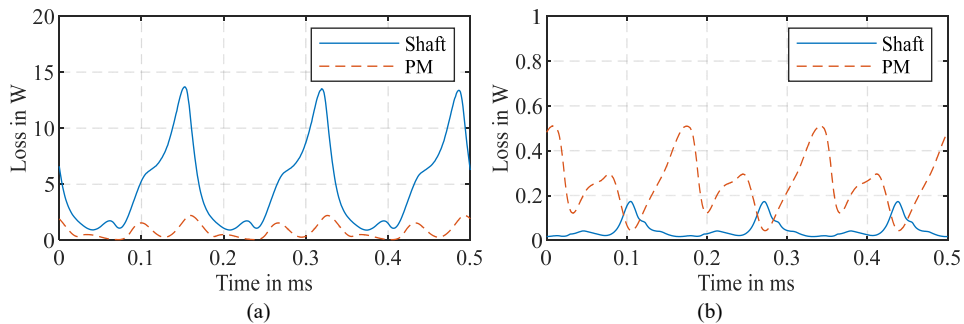
Figure 5.23: Rotor eddy current losses of IPM motor caused by fundamental current at 60,000 /min. (a) Fundamental current of 60 A. (b) Fundamental current of 30 A.
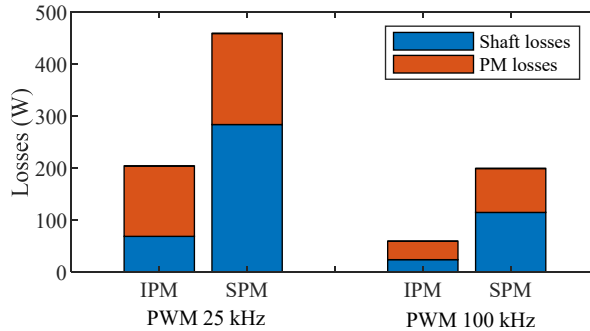
Figure 5.24:   Rotor eddy current losses of the two motors at 60,000 /min and 1.2 Nm through coupled simu-
lation when the PWM frequency is changed.

5.3.2   Copper losses

When a same current is excited to the two motors, the copper losses of them are almost the same because the AC copper losses are mainly caused by the slot flux leakage and they have a same stator. The conductors' losses of one slot at 60,000 /min are presented in Fig. 5.25. It is easy to find that the conductors' losses caused by the high-order current harmonics are influenced by the fundamental current. When the fundamental current has a lower amplitude as presented in Fig. 5.25(a), the conductors' losses generated by the high-order current harmonics are low. The influence of the high-frequency current harmonics on the conductor closed to the air gap is the greatest and this conductor has the highest losses, which has been analyzed in Section 4.1.2.

Because the AC copper losses are mainly caused by the slot flux leakage, all the current harmonics will cause loss in the copper windings. When the PWM frequencies are 25 kHz and 100 kHz respectively, the conductors' losses of one slot at 60,000 /min and 1.2 Nm of the two motors calculated by coupled simulation are compared in Fig.5.26 and Fig. 5.27. They show that the AC copper losses caused by the high-frequency current hamonics have much higher amplitudes. By increasing the PWM frequency, the phase currents becomes smooth and the losses can be significantly decreased. The mean values of the copper losses of the two motors are compared in Table. 5.4. It shows that the SPM motor has higher copper losses than the IPM motor. Moreover, when the PWM frequency is increased from 25 kHz to 100 kHz, the copper losses of the IPM motor are reduced by 53.5 %, while the copper losses of the SPM motor are reduced by only 34.1 %. Hence, it is believed that the IPM motor has much better performance in terms of copper losses.

(a)

(b)
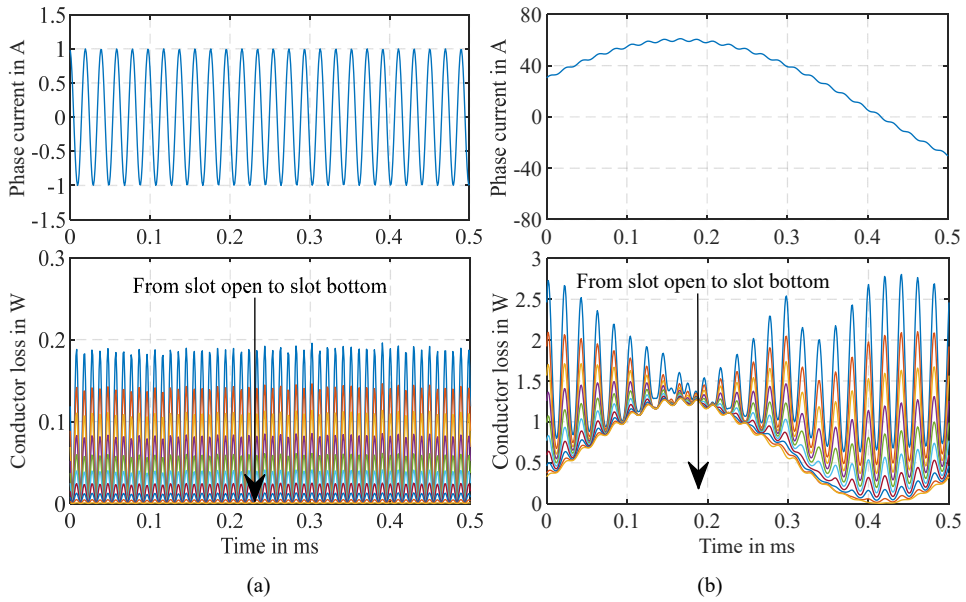
Figure 5.25: Conductors' losses of one slot caused by fundamental current and current harmonics at 60,000 /min. (a) 49th of 1 A. (b) 1st of 60 A and 49th of 1 A.

(a)

(b)
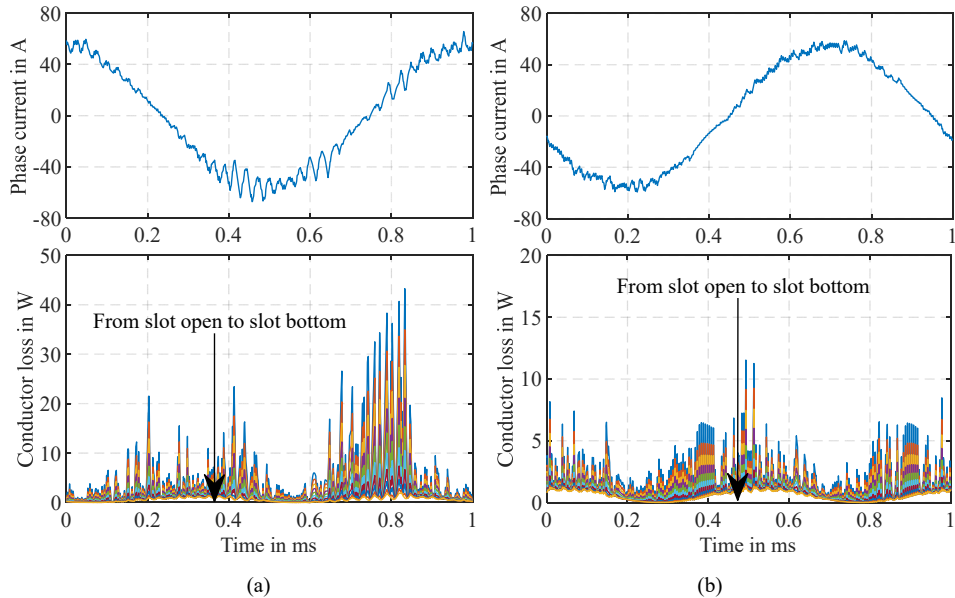
Figure 5.26: Conductors' losses of one slot of the IPM motor at 60,000 /min and 1.2 Nm calculated by coupled simulation. (a) PWM frequency is 25 kHz. (b) PWM frequency is 100 kHz.

126
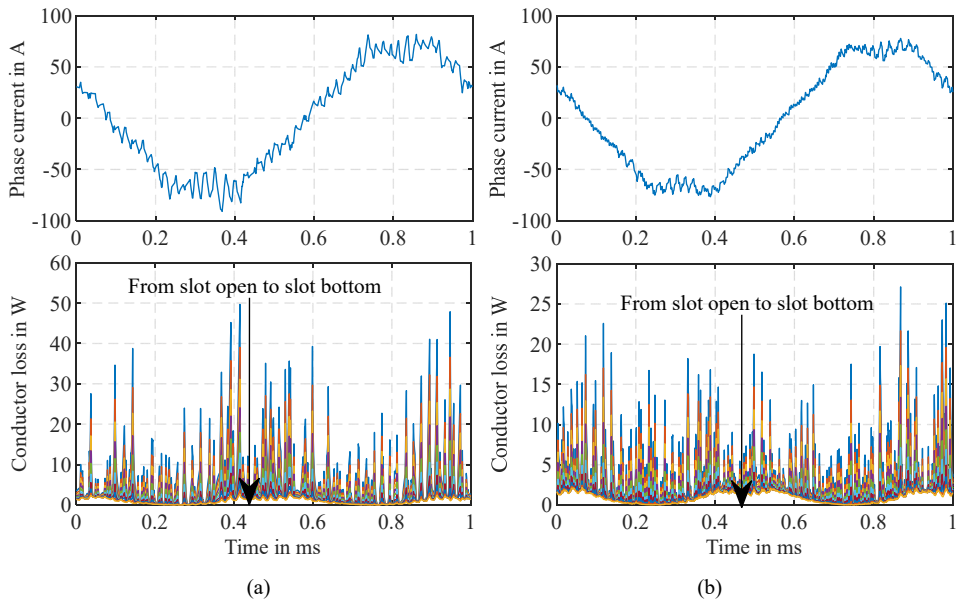
Figure 5.27: Conductors' losses of one slot of the SPM motor at 60,000 /min and 1.2 Nm calculated by coupled simulation. (a) PWM frequency is 25 kHz. (b) PWM frequency is 100 kHz.

Mean loss in W	IPM	SPM
PWM frequency 25 kHz	21.55	31.36
PWM frequency 100 kHz	10.03	20.66

Note: The losses of end-windings are not included.

Table 5.4: Mean values of the IPM and SPM motors' copper losses of one slot at 60,000 /min and 1.2 Nm calculated by coupled simulation.

5.3.3 Iron losses

The high-frequency current harmonics also cause higher core losses. In [166] the influence of the high-order current harmonics on the core losses has been studied. The DC-bus voltage and the PWM frequency were studied. A modulation index m which was the ratio between the amplitude of the sinusoidal reference voltage and the amplitude of the triangular carrier voltage was defined. It was found that a smaller modulation index resulted in a higher iron loss. A lower PWM frequency or a higher DC-bus voltage caused a smaller modulation index. When the maximum flux density is 1 T, the *B-H* loops of the core material 35A360 at 50 Hz are presented in Fig 5.28. The results in [166] can also be under-

stood as: a lower modulation ratio between the PWM frequency and the fundamental frequency, or a higher voltage ratio between the DC-bus voltage and the induced electromagnetic force (EMF) of the coil around the tested core, will result in a higher iron loss. This is because lower modulation ratio or higher voltage ratio will result in higher amplitudes of current harmonics as analyzed in Section 5.1. Hence, the core losses of the high-speed motor generated by the PWM inverter needs to be considered.
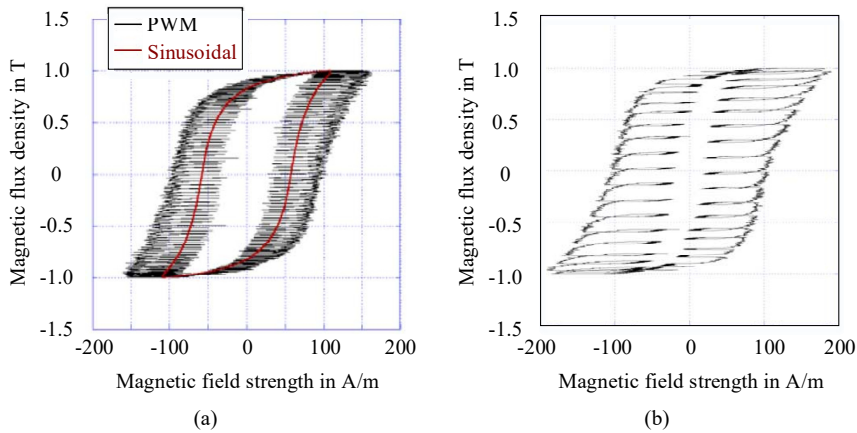
Figure 5.28:   *B-H* loops of the core material 35A360 at 50 Hz [166]. (a) PWM frequency is 5 kHz, DC-bus voltage is 40 V and modulation index is 0.26. (b) PWM frequency is 1 kHz, DC-bus voltage is 40 V and modulation index is 0.22.

Because the IPM motor has lower amplitudes of current harmonics than the SPM motor, the additional core losses caused by the PWM inverter of the IPM motor are lower than those of the SPM motor. Hence, the proposed IPM motor made from the AMM rotor core will have much lower losses and higher efficiency than the SPM motor. The superiority of the IPM motor over the SPM motor is clear.

5.4   Losses reduction by adding current filters

Because increasing the switching frequency is very difficult, to reduce the amplitudes of the high-order current harmonics in order to decrease the losses of the high-speed PM motors, another method is to connect a current filter between the PWM inverter and the motor in series. Because of the existence of the current filter, the phase inductance is increased and the dynamic response performance of the motor drive system is decreased. When the inductance of the current filter is increased from 0.15 mH to 0.45 mH, the phase current, torque, shaft and PM losses, and the conductor's loss of the designed IPM motor are compared in Fig. 5.29 to Fig. 5.32.
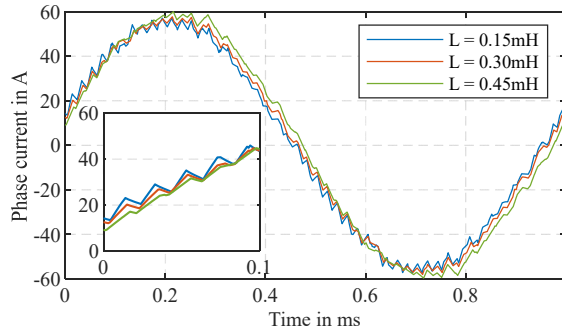
Figure 5.29:   Phase current of different current filter at 60,000 /min and 1.2 Nm when PWM frequency is 25 kHz.

Fig. 5.29 clearly shows that when the inductance of the current filter is increased, the phase current becomes smoother. The high-frequency torque ripple and shaft loss caused by the PWM current are correspondingly decreased as can be seen in Fig. 5.30 and Fig. 5.31. However, the low-frequency components of the torque ripple and the shaft loss are almost unchanged. Moreover, they have the same frequency because they are caused by the fundamental current. Hence, it is unnecessary to further increase the inductance of the current filter in terms of torque ripple and shaft loss.

The influence of the current filter on the losses of the PM and the conductor, which is the closest to the air gap, is presented in Fig. 5.32 and Fig. 5.33. They clearly show that when the inductance is increased, the amplitudes of the PM eand the conductor losses are significantly decreased. The mean values of the losses are compared in Table 5.5. It can be noticed that the current filter can help to dramatically reduce the losses of the motor, including the shaft loss, PM loss and copper AC losses. However, when the inductance of the current filter is further increased from 0.15 mH to a higher value, the losses of the shaft and the copper winding cannot be further reduced. Because of the existence of the current filter, the required output line-voltage of the PWM driver to drive the designed IPM motor to the maximum speed at rated torque is significantly increased. For example, when the filter is 0.15 mH, the line voltage at maximum speed and rated torque is increased from 391 V to 485 V.
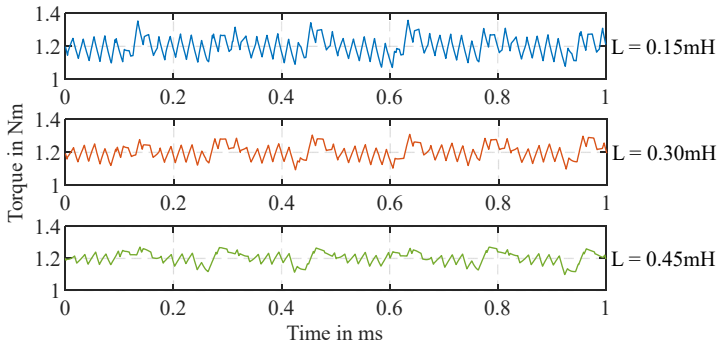
Figure 5.30: Torque of different current filter at 60,000 /min and 1.2 Nm when PWM frequency is 25 kHz.
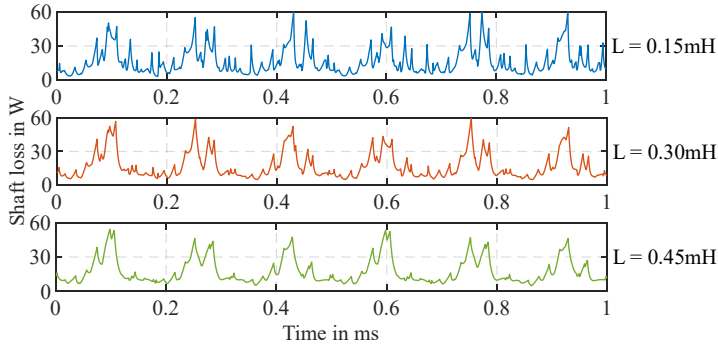
Figure 5.31: Shaft loss of different current filter at 60,000 /min and 1.2 Nm when PWM frequency is 25 kHz.
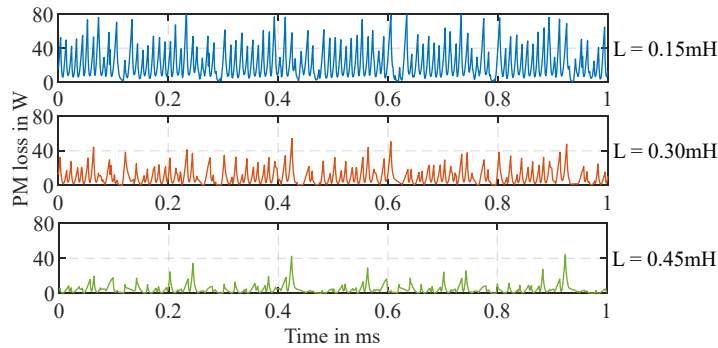
Figure 5.32: PM loss of different current filter at 60,000 /min and 1.2 Nm when PWM frequency is 25 kHz.
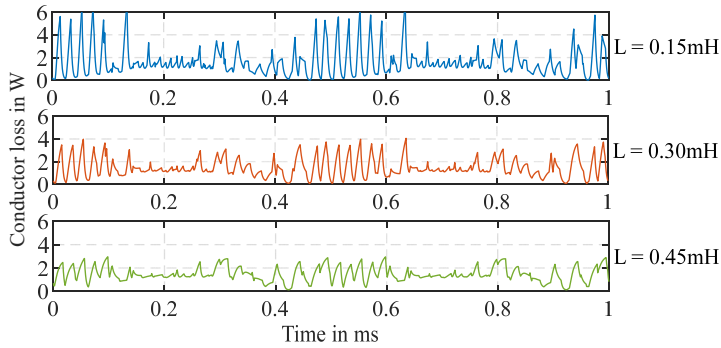
Figure 5.33:   Conductor loss of different current filter at 60,000 /min and 1.2 Nm when the PWM frequency is 25 kHz.

Inductance of current filter	0	0.15 mH	0.30 mH	0.45 mH
Rotor shaft loss in W	69.02	16.41	17.16	17.52
Rotor PM loss in W	135.38	22.24	10.06	4.71
Copper loss of one slot in W	21.55	9.06	8.66	9.02

Note: The losses of end-windings are not included.

Table 5.5:   Mean values of IPM motor's losses at 60,000 /min and 1.2 Nm calculated by coupled simulation.

5.5   Comparison of SPM and IPM motors fed with PWM currents

Because the influence of the PWM inverter cannot be avoided and higher losses and higher temperature rises of the motors will be induced. In order to protect the motors from high losses and high temperature failure, it is necessary to analyse the losses and the temperature rises of the motors driven by the PWM inverters. When the switching frequency is 25 kHz and the DC-bus voltage is 600 V, at the maximum speed of 125,000 /min and at the rated torque of 1.2 Nm, the losses and the temperature rises of the two motors are compared in Table 5.6. Because of existence of a current filter of 0.15 mH, the line voltage of the SPM motor is higher than the DC-bus voltage. In this case, the DC-bus voltage is increased to 700 V. The corresponding temperature distributions of the two motors with and without a current filter are compared and presented in Fig. 5.34 and Fig. 5.35.

Rotor type	IPM		SPM	
Current filter in mH	0	0.15	0	0.15
Shaft losses in W	20.05	19.38	87.30	40.53
PM losses in W	53.69	17.75	56.72	29.53
Rotor core losses in W	3.20	2.91	-	-
Stator core losses in W	332.88	308.16	237.46	207.24
1st conductor losses in W	4.50	3.94	6.08	4.98
2nd conductor losses in W	3.45	3.02	4.68	3.85
3rd conductor losses in W	2.80	2.47	3.79	3.14
4th conductor losses in W	2.25	1.99	3.01	2.52
5th conductor losses in W	1.77	1.58	2.35	2.00
6th conductor losses in W	1.37	1.25	1.80	1.56
7th conductor losses in W	1.06	0.98	1.36	1.21
8th conductor losses in W	0.82	0.77	1.03	0.95
9th conductor losses in W	0.67	0.64	0.81	0.77
10th conductor losses in W	0.59	0.58	0.70	0.69
Rotor temp. rise in K	137.71	99.57	196.80	126.84
Winding temp. rise in K	108.28	96.21	135.88	112.83

Table 5.6:   Losses and temperature rises of the two motors at the maximum speed of 125,000 /min and at the rated torque of 1.2 Nm.

Table 5.6 shows that by connecting a current filter in series, the losses of both motors are significantly reduced and the temperature of the motors are dramatically decreased. The rotors' temperature rises of the IPM and SPM motors are reduced by 34.18 °C and 69.94 °C, respectively. The shaft loss of the IPM motor is slightly reduced because it is mainly caused by the fundamental current as aforementioned. The PM loss of the IPM motor is reduced by about 67 %. The rotor losses of the SPM motor are reduced by about 51 %. The stator core losses of both motors are also reduced to some extent. Because the IPM stator has higher flux density than the SPM stator, which has been proved in Fig. 5.20, the stator core losses of the IPM motor are higher than those of the SPM motor. The copper losses of the two motors are also reduced because of existence of the current filter. The SPM motor has higher copper losses than the IPM motor, it is mainly because the SPM motors needs a higher RMS current to generate a high torque of 1.2 Nm. Hence, the SPM rotor is 59.09 °C hotter than the IPM rotor without a current filter in series connected and

the SPM rotor faces with high risks of irreversible demagnetization. Even though a current filter of 0.15 mH is connected, the SPM rotor is 27.27 °C hotter than the IPM rotor. The superiority of the IPM rotor over the SPM rotor is obvious.
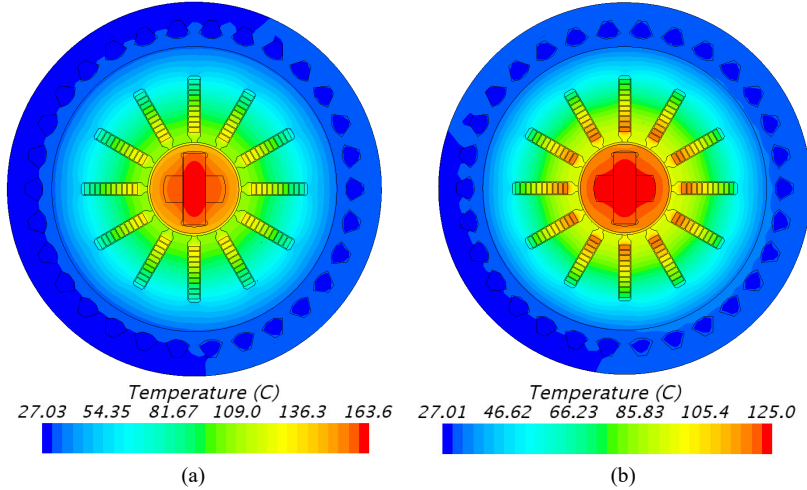
Figure 5.34:   Temperature distributions of the IPM motors at 125,000 /min and 1.2 Nm when considering the influence of the PWM inverter. (a) Without current filter. (b) With current filter of 0.15 mH.
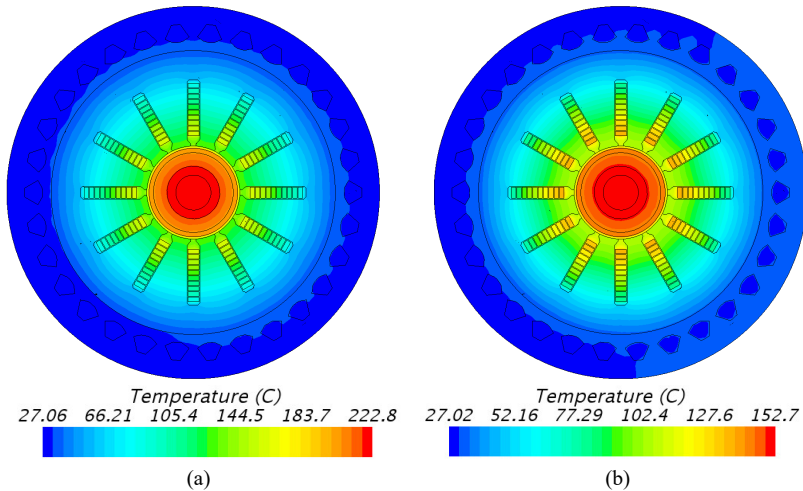
Figure 5.35:   Temperature distributions of the SPM motors at 125,000 /min and 1.2 Nm when considering the influence of the PWM inverter. (a) Without current filter. (b) With current filter of 0.15 mH.

6 Experimental verification

In this chapter, the prototyping techniques, the testbench and the driver are introduced. An AMM IPM prototype and a fiber sleeve SPM prototype are built and tested and their performances are compared to evaluate the feasibility and the superiority of the proposed application of the AMM. The no-load EMF, flux linkage, load torque, temperature rise and efficiency of the prototypes are measured. The influence of the PWM inverter on the losses of the rotor is verified.

6.1 Manufacture of prototypes

6.1.1 AMM rotor core

In order to run the rotor to the maximum speed, the mechanical strength of the AMM rotor core is the first concern. Hence, WEDM method is adopted for manufacturing of the rotor core because it has the highest cutting quality among the three methods tested in Chapter 2. To use the WEDM method, the amorphous ribbons are firstly laminated and solidified into a stack as shown in Fig. 6.1. Then, the AMM rotor cores produced by three different companies by using the WEDM method are presented in Fig. 6.2. It is worth to notice that the cutting quality depends on the operation and the technique employed by different companies. The cutting surface may be significantly overheated as can be seen in Fig. 6.2(b). Fig. 6.2(c) shows that the WEDM method may also cause a ridge which may decrease the mechanical strength of the core. When the temperature during the cutting process is higher than the crystallization temperature, the cutting contour will crystallize and the performance of the AMM will change. The electromagnetic and mechanical performances of the AMM cores might be influenced.

Figure 6.1:   Laminated and solidified AMM stack.

<div align="center">(a)　　　　　　　　　　　　　　　　　(b)</div>

<div align="center">(c)</div>
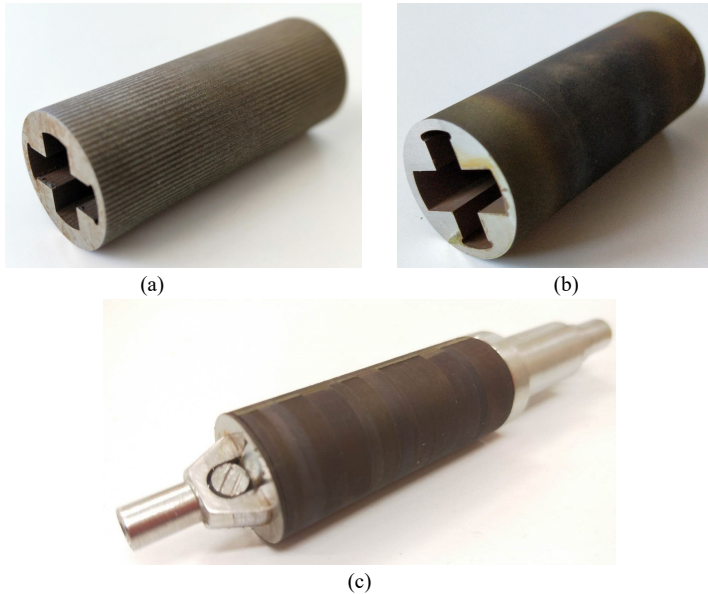
Figure 6.2:　　　AMM rotor cores made by WEDM method.

6.1.2　Hollow shaft

To realize a shaft with ferromagnetic and non-ferromagnetic segments, friction-welding technique is employed. Since the shaft will be shorten during the welding process, to ensure the required length of the ferromagnetic part, the raw material is about 11 mm longer than the expected length. For example, the designed length of the ferromagnetic part is 54 mm. The raw material used for welding is 65 mm. During the press process of the friction welding, the raw material is shortened to about 54 mm (each side is about 5.5 mm). The materials of the welded shaft are shown in Fig. 6.3. Because of high temperature during friction welding, the junctions of the two materials become very hard. It needs a high hardness tool to further process a hollow in the shaft. Then the shaft is milled under a clampling platform as can be seen in Fig. 6.4. After finishing the hollow shaft, the PM can be inserted to the shaft before assembling the rotor core. The hollow shaft inserted with the PM is presented in Fig. 6.5.
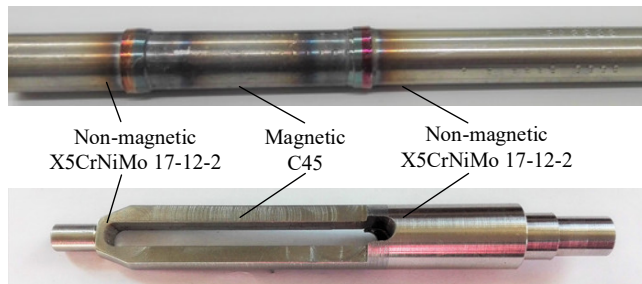
Figure 6.3:   Hollow shaft made from different materials by friction welding technique.
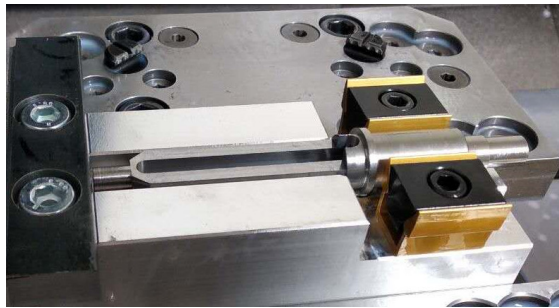
Figure 6.4:   A clampling platform for manufacturing of the hollow shaft.

Figure 6.5:   Hollow shaft inserted with PM.

6.1.3 Stator core

Because the slotting of the AMM is challenging, AMM is not used for the stator core even though its core losses are much lower than those of the conventional silicon steels. Instead, conventional silicon steel NO20, whose thickness is 0.2 mm, is employed for the stator core. The stator laminations are cut by laser and then are solidified by the bonding varnish on the surfaces of the laminations. The stator core is presented in Fig. 6.6(a). Because of

high temperature during laser cut, the insulation layer around the cutting contour is burned out. This may result in partial short circuit on the inner surface of the stator core and consequently higher core losses. In order to improve the cooling performance so as to increase the power density of the motor, the stator is encapsulated with high thermal conductivity epoxy resin as shown in Fig. 6.6(b).

(a)   (b)
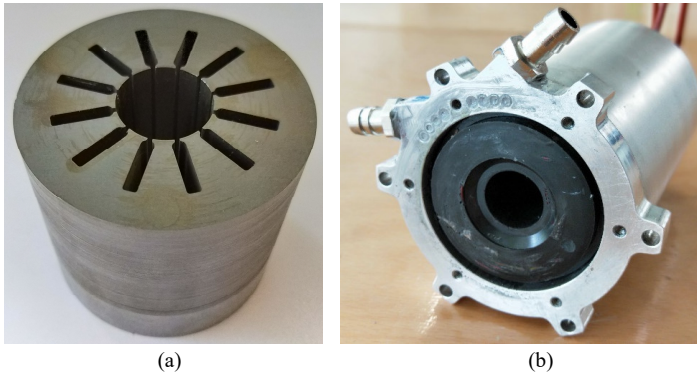
Figure 6.6:   Stators of the prototype. (a) Stator core. (b) Stator encapsulated with epoxy resin.

6.1.4 Water-cooled housing

To increase the torque density of the motor, forced water-cooled housing is implemented. As aforementioned, a special water channel is designed in order to increase the axial stiffness of the housing, instead of using a spiral channel. Then, the manufacture of the housing is challenging. It needs a device, which can work on four axes. The device to manufacture the housing developed by our institute is presented in Fig. 6.7. It consists of a spindle motor, which runs at a high speed and moves in z-axis, and a platform, which moves in x-y plane and a rotating axis mounted on the platform to fix and rotate the housing. The manufactured housing is presented on the right figure of Fig. 6.7.
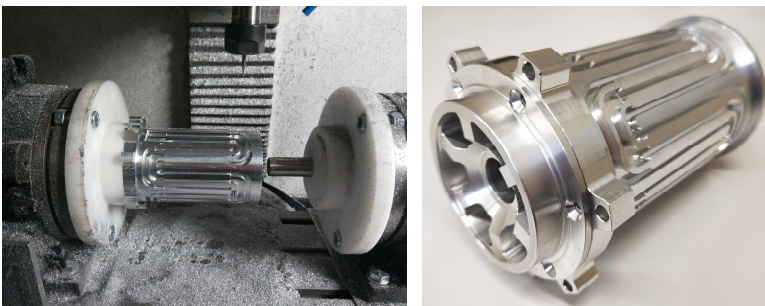
Figure 6.7:   Manufacture of the cooling channel on the housing.

6.1.5 Realization of the SPM rotor

The manufacture of the SPM rotor is challenging. When prestress is needed, a small undersize is required. The inner diameter of the sleeve should be a little smaller than the outer diameter of the PM rotor to add prestress. Then, heat shrinking or cold shrinking method is necessary to assemble the sleeve into the rotor. This small undersize is determined by the manufacturing tolerances of the shaft, PMs and sleeve. It is very difficult to obtain a proper tolerance in the mechanical process. Hence, undersize is not adopted in this prototype. Instead, the inner diameter of the sleeve is slightly bigger than that of the rotor. The gap between the rotor and the sleeve is filled with high strength adhesives Loctite 648.

To decrease the tolerance requirements of PMs, the shaft is designed to have convex as shown in Fig. 6.8(a). Because of the existence of the convex, the PM usage will be reduced when the segmental number per PM pole is increased. Consequently, the air-gap flux density will be reduced. Hence, each pole is cut into four segments considering the PM eddy current losses and the PM usage. The shaft, carbon fiber sleeve and the SPM rotor are presented in Fig. 6.8.

| (a) | (b) | (c) |
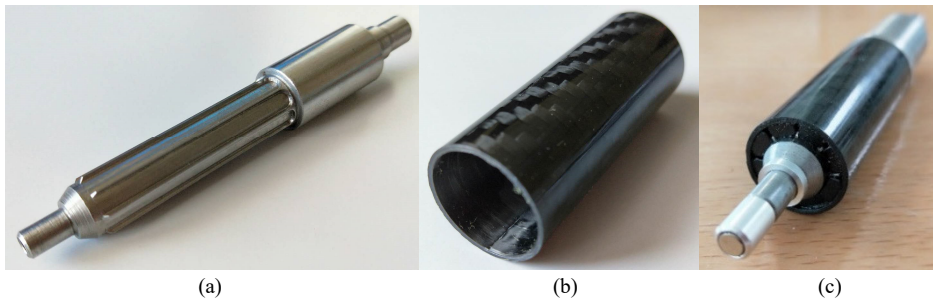
Figure 6.8: SPM rotor and components. (a) Shaft. (b) Carbon fiber sleeve. (c) SPM rotor.

6.1.6 Assembly of the prototypes

One of the most important components to ensure the rotor can be run to the maximum speed is the bearing. In this work, mechanical spindle bearings HY KH 61900 C TA and HY S 619/6 C TA produced by GMN are used. Their maximum speed are 135,000 /min and 165,000 /min, respectively. The finished IPM rotor is shown in Fig. 6.9. The complete SPM and IPM prototypes are presented in Fig. 6.10. The outer diameter of the prototypes after housing is 84 mm; the total length is about 160 mm; the rotor is about 200 g and the total weight of the prototype is about 2.8 kg.

Figure 6.9:   Finished AMM rotor.
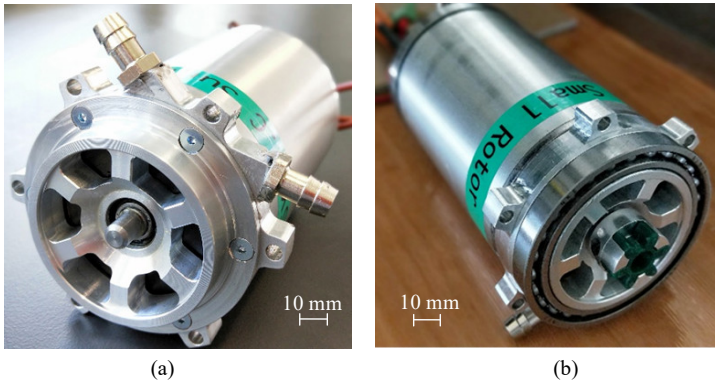
Figure 6.10:   Photos of the prototypes. (a) SPM. (b) IPM.

6.2   Design and manufacture of the testbench

Generally, a torque sensor is connected between the tested prototype and the load machine through couplings. However, because of high-speed operation, it is better to reduce the distance between the tested motor and the load machine. Hence, a special design for testing the torque is realized as presented in Fig. 6.11. The two prototypes are directly connected through a coupling. A strain gage based torque sensor TS70 produced by ME-Meßsystem GmbH is connected between the end-cap of the IPM prototype and the base. For this configuration, the stator is hold by two bearings as shown in Fig. 6.11 and Fig. 6.10(b). The prototypes are covered by thick steels in order to ensure the stiffness and the safety of the testbench.
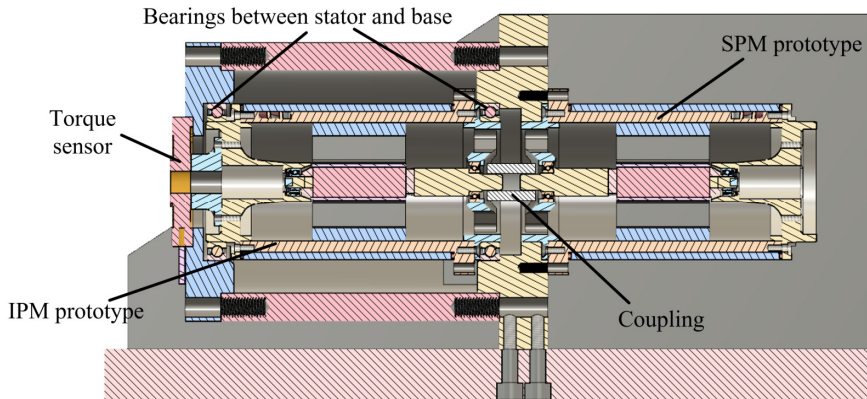
Figure 6.11:   Structure of the testbench.

The connection of the PWM inverters and the two prototypes is presented in Fig. 6.12. During the test, one of the prototypes is driven as a motor while the other is driven as a generator. In order to increase the modulation ratio, silicon carbide (SiC) power module CCS050M12CM2 is used. The two converters are connected to the same DC supply. The DC supply only need to provide power for the losses of the converters and the prototypes.
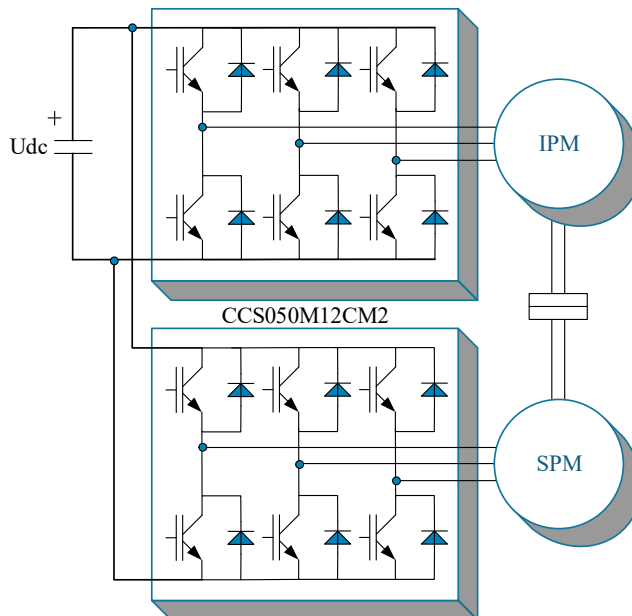
Figure 6.12:   Schematic diagram of the PWM inverters and motors.

141

The motor is controlled by speed mode while the generator is controlled by current mode. To test the angular position of the rotors, non-contact position sensor IC MHM produced by iC Haus is used. The control system is realized by using Xilinx Zynq SoC (system on a chip) XC7Z020. The structure of the hardware system is shown in Fig. 6.13. This SoC consists of two ARM Cortex-A9 cores and 85 k programmable logic cells (Artix-7 FPGA). One ARM core is used for communication while the other one is used to realize the control strategies. The two ARM cores share data through the on chip memory. The PC and ARM core 0 communicates through Ethernet. The PC sends the target values to and recieves the state parameters from the ARM core 0. All the sensors, including the current, DC-bus voltage, temperature and rotor angular position, are connected to the FPGA. If any error is detected by the FPGA, it will shut down the SVPWM immediately in order to protect the motors and the power converters. The control strategies for the two motors are realized in the ARM core 1. It calculates the duty cycles of the upper arms of the two PWM inverters and sends them to the FPGA. The FPGA will calculate the turn on and off times of each power electronic switches and add dead-time to avoid short circuit between the upper and lower arms of one phase.
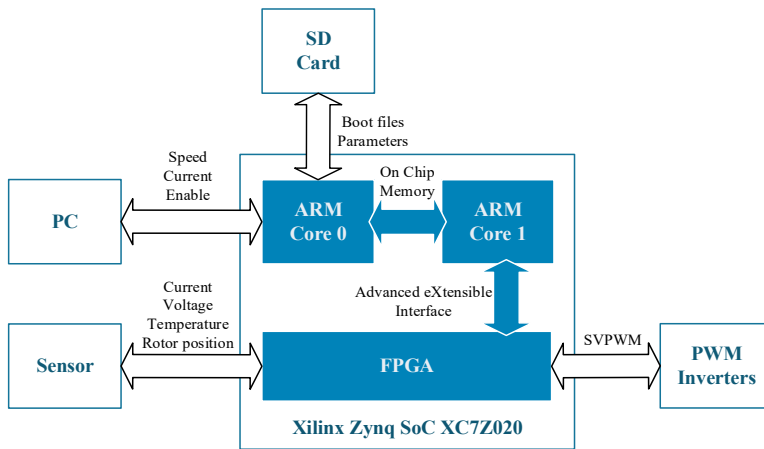
Figure 6.13:   Structure of the hardware system.

The schematic diagram of the speed control model is introduced in Fig. 6.14. Because the IPM motor can provide additional reluctance torque, the current leading angle (*Gamma* in the Fig. 6.14) is set based on the FEA and experimental results. In Fig. 6.14 the *d*-axis and *q*-axis reference currents are calculated based on the mathematical model of the motor according to the torque in need M_{req}. The motor and generator drive system is shown in Fig. 6.15.
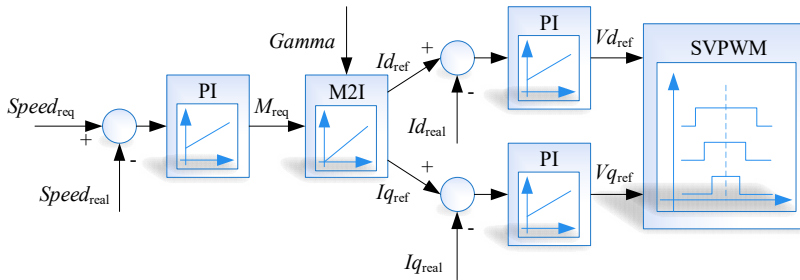
Figure 6.14:   Speed control model realized in ARM core 1.
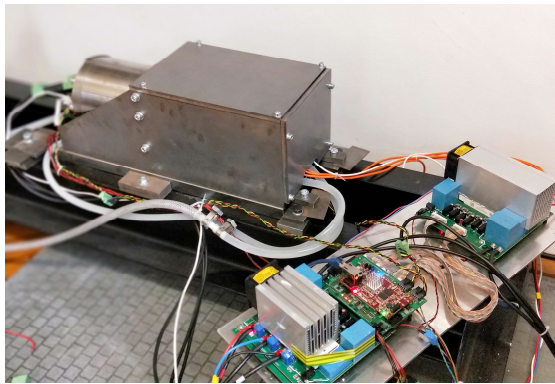
Figure 6.15:   Photo of the motor and generator drive system.

6.3 Measurement of the prototypes

6.3.1 No-load test

First of all, the no-load back-EMFs of the prototypes are measured to ensure that the prototypes are correctly built. To test the no-load EMFs, one of them is driven as motor to drive the two prototypes to a specific speed and the other prototype is open circuit. The phase current of the motor and the back-EMF of the counter prototype at 30,000 /min are presented in Fig. 6.16.

The voltage probe is ten times attenuated and the current probe is 20 A/V. Because of relatively low amount of PMs in the IPM rotor, the back-EMF of the IPM motor is about 18 % lower than that of the SPM motor. However, due to higher inductance of the IPM motor, the current harmonics generated by the PWM inverter of the IPM motor have much lower amplitudes than those of the SPM motor. Furthermore, the phase current needed for the

IPM motor is much lower than that of the SPM motor to drive the two rotors to 30,000 /min. The SPM motor needs about 1.28 A-RMS current while the IPM motor needs only 0.69 A-RMS when the current leading angle is equal to 30 degrees.

(a)

(b)
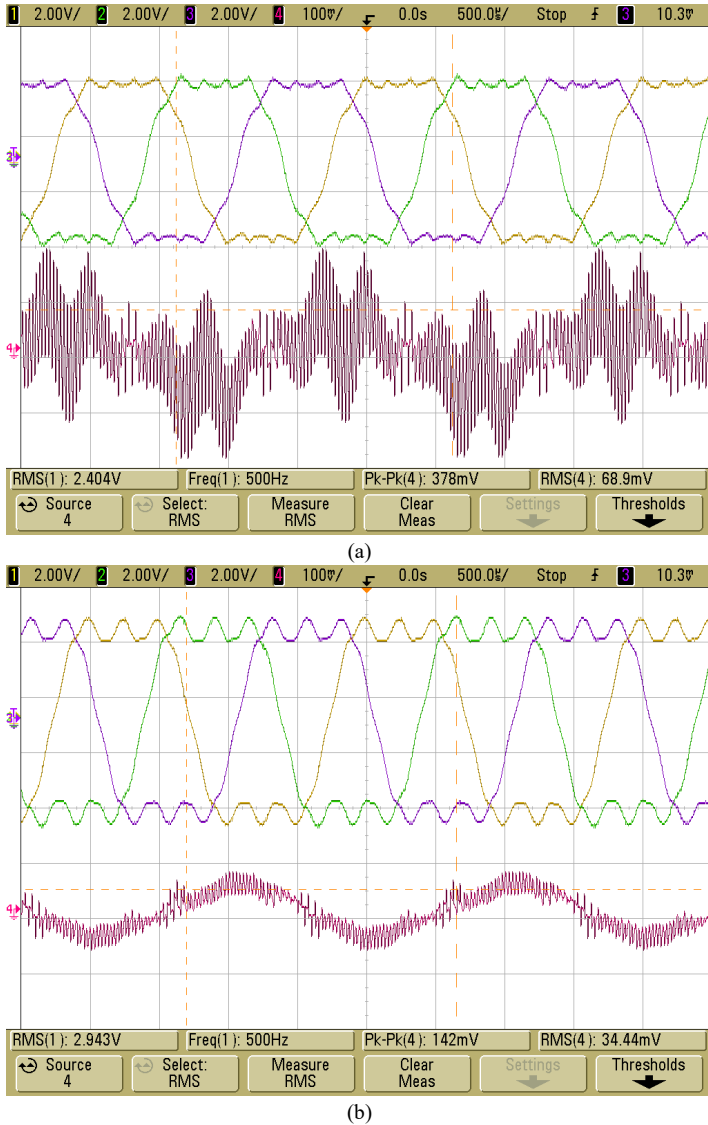
Figure 6.16:   Tested back-EMF and phase current at 30,000 /min. (a) EMF of IPM and current of SPM. (b) EMF of SPM and current of IPM.

The experimental results compared with the FEA results of the two prototypes are presented in Fig. 6.17 and Fig. 6.18, respectively. In can be seen that the back-EMFs of the

two prototypes contain high amplitudes of 3rd harmonic. Because the windings are connected in star type, the phase current does not contain 3rd current harmonic. However, the 5th and the 7th back-EMF harmonics of the SPM will generate corresponding current harmonics. The EMF errors between FEA and experimental results of the IPM motor is about 7.4 %, while the error for the SPM motor is about 1.7 %.
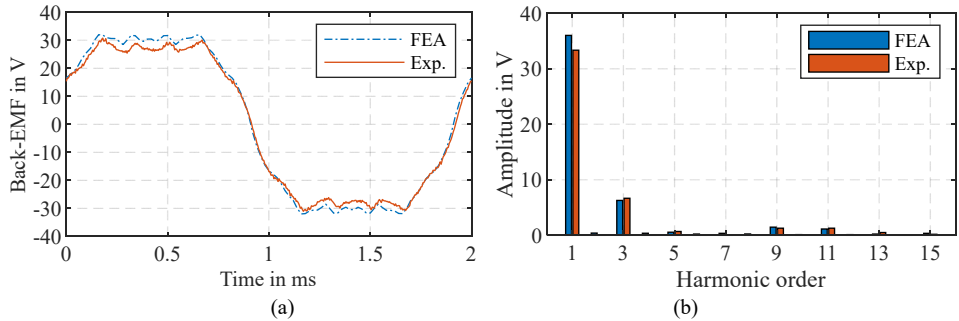
Figure 6.17: Comparison of the tested and the FEA back-EMF of the amorphous IPM motor at 30,000 /min. (a) Back-EMF waveform. (b) Spectrum of the back-EMF.
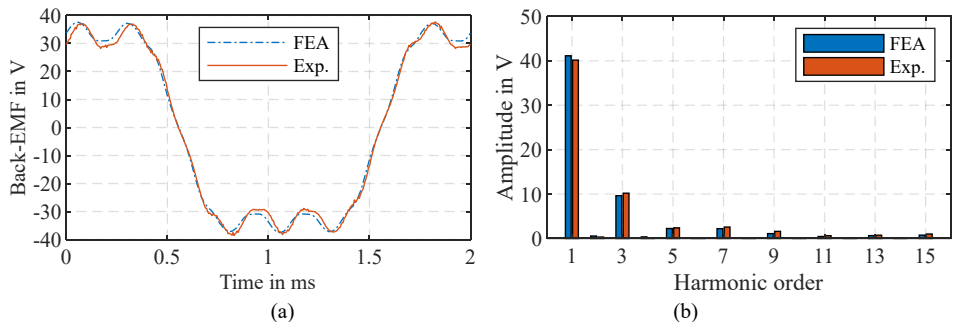
Figure 6.18: Comparison of the tested and the FEA back-EMF of the SPM motor at 30,000 /min. (a) Back-EMF waveform. (b) Spectrum of the back-EMF.

The back-EMFs of the two prototypes as a function of speed are presented in Fig. 6.19. The FEA results fit well with the experimental results and this proves that the FEA analysis is credible. The decrease of the experimental EMF of the IPM motor, compared to the FEA results, might be mainly caused by the flux leakage at the ends of the shaft, the inaccuracy of the stacking factor and the inaccurate electromagnetic properties of the AMM rotor core. Even though the error of the EMF of the IPM motor is a little higher than that of the SPM motor, this error is still reasonable from the engineering point of view.
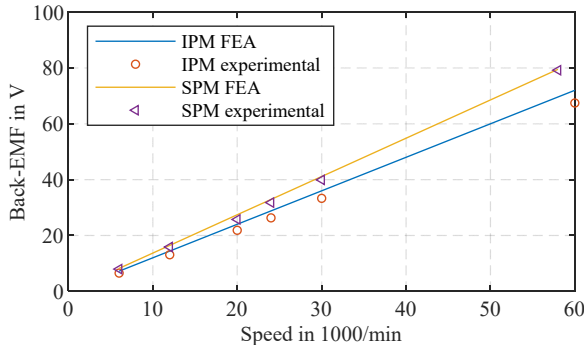
Figure 6.19:   Back-EMFs of the two prototypes as a function of speed.

6.3.2 Flux linkage measurement

Since the *d*-axis and *q*-axis inductances of the IPM motor are unequal and they are influenced by the *d*-axis and *q*-axis currents due to the non-linear property of the AMM rotor core, the *d*-axis and *q*-axis flux linkages are tested to optimize the torque control. The mathematical model of the IPM motor is

$$\begin{cases} u_\mathrm{d} = R_\mathrm{s}i_\mathrm{d} + L_\mathrm{d}\dfrac{di_\mathrm{d}}{dt} - L_\mathrm{q}\omega_\mathrm{e}i_\mathrm{q} \\[2mm] u_\mathrm{q} = R_\mathrm{s}i_\mathrm{q} + L_\mathrm{q}\dfrac{di_\mathrm{q}}{dt} + L_\mathrm{d}\omega_\mathrm{e}i_\mathrm{d} + \omega_\mathrm{e}\psi_\mathrm{PM} \end{cases} \tag{6.1}.$$

It can be known that to derive the flux linkages, the phase voltages and currents, and the rotor position need to be measured. For example, at 3,000 /min, when the *d*-axis current is -25 A and the *q*-axis current is 45 A, the phase voltages, currents and the angular position are illustrated in Fig. 6.20. Through Clarke and Park transformation, the *d*-axis and *q*-axis currents and voltages are presented in Fig. 6.21. It shows that the *d*-axis and *q*-axis currents are much stable. Their average values are used and the *d*-axis and *q*-axis currents are considered to be constant. Then the *d*-axis and *q*-axis flux linkage can be calculated through

$$\begin{cases} u_\mathrm{d} = R_\mathrm{s}i_\mathrm{d} - \omega_\mathrm{e}\psi_\mathrm{q} \\[1mm] u_\mathrm{q} = R_\mathrm{s}i_\mathrm{q} + \omega_\mathrm{e}\psi_\mathrm{d} \end{cases} \tag{6.2}.$$
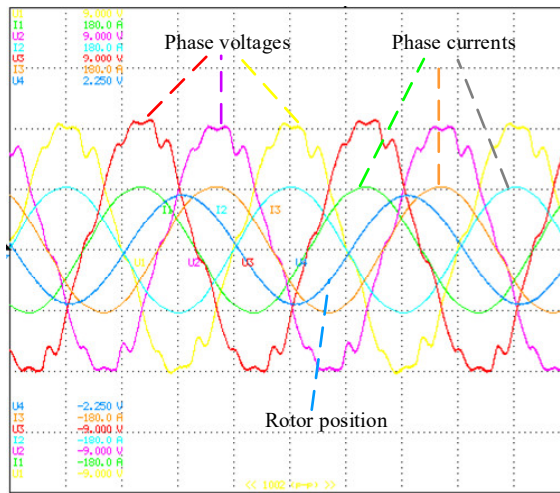
Figure 6.20: Experimental phase voltages and currents and rotor position at 3,000 /min.
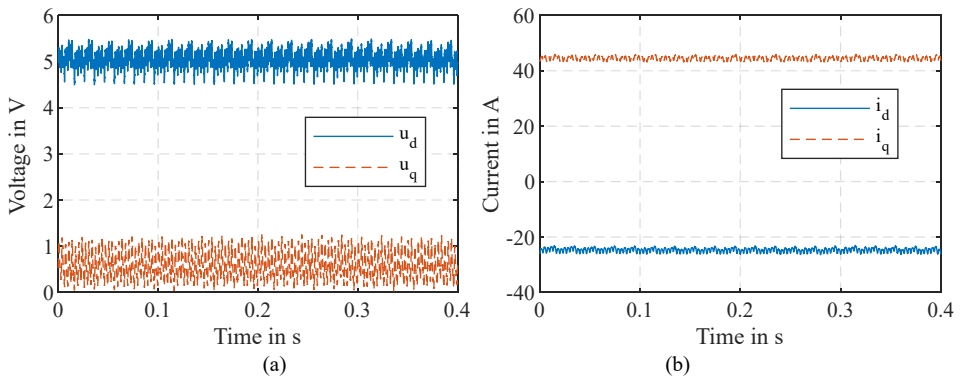
Figure 6.21: Experimental d-axis and q-axis voltages and currents at 3,000 /min.

The tested flux linkages as a function of d-axis and q-axis currents are compared with the FEA results and presented in Fig. 6.22 and Fig. 6.23, respectively. It shows a high accuracy in predicting of the flux linkages through the FEA and the optimum current leading angle can be determined. The FEA flux linkages of different currents fit well with the measured flux linkage because the measured B-H curve of the AMM core is used in the FEA analysis.
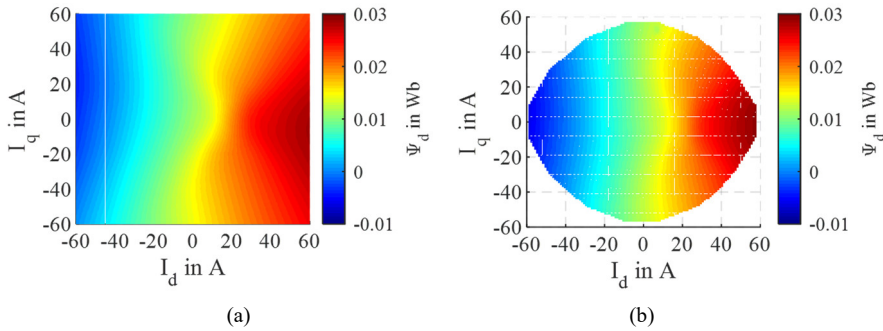
Figure 6.22:   *d*-axis flux linkage of the IPM motor. (a) FEA. (b) Measured.
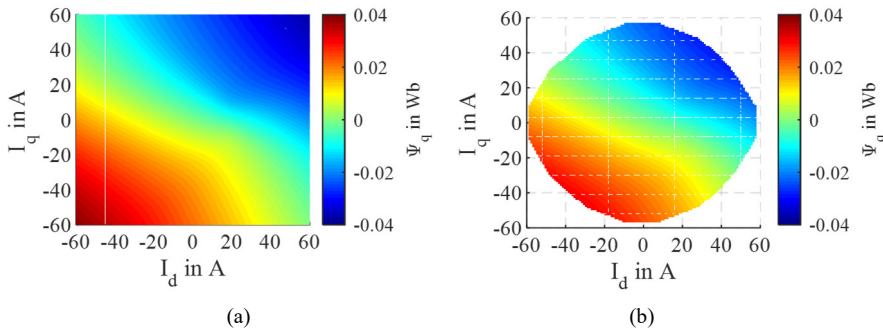
Figure 6.23:   *q*-axis flux linkage of the IPM motor. (a) FEA. (b) Measured.

6.3.3   Load torque test

Even though the SPM prototype has higher back-EMF than the IPM prototype, because the IPM motor can provide additional reluctance torque, the IPM motor has higher torque when the amplitude of the phase current is higher than 30 A based on the tested results as can be seen in Fig. 6.24. In this figure, the current leading angles of the IPM and the SPM motors are 30 degrees and 0 degree, respectively. The tested torque of the SPM prototype is about 9 % lower than the FEA value. As regards the IPM prototype, the tested error at low current is high while at a high current this error is decreased to 5 %. The tested error might be mainly caused by inaccurate magnetic properties of the solid shaft material and inaccurate stacking factor and *B-H* curves of the stator and rotor cores. It is worth to notice that at 3,000 /min, when the amplitude of phase current is 55 A, the tested peak torque of IPM motor is about 11% higher than that of the SPM motor. Compared with the analytical results as shown in Fig. 4.49, it is believed that the tested data is creditable. Because the losses of the SPM motor increase faster than those of the IPM motor when the speed increase, it can be expected that at a higher speed, the IPM motor will has much higher torque than the SPM motor. This will lead to a much lower efficiency of the SPM motor.
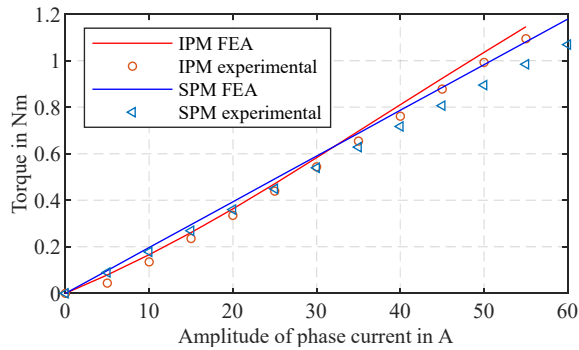
Figure 6.24:   Peak torque (test duration 30 seconds) of the two prototypes as a function of current amplitude at 3,000 /min.

The tested torque of the IPM prototype as a function of the *d*-axis and *q*-axis currents is compared with FEA results as shown in Fig. 6.25. Because the *q*-axis inductance is higher than the *d*-axis inductance, the maximum torque occurs at flux-weakening regions. Based on the comparison of the tested and FEA results, it is believed that the design of the motor based on the test data of the AMM is highly precise and creditable.

(a)   (b)
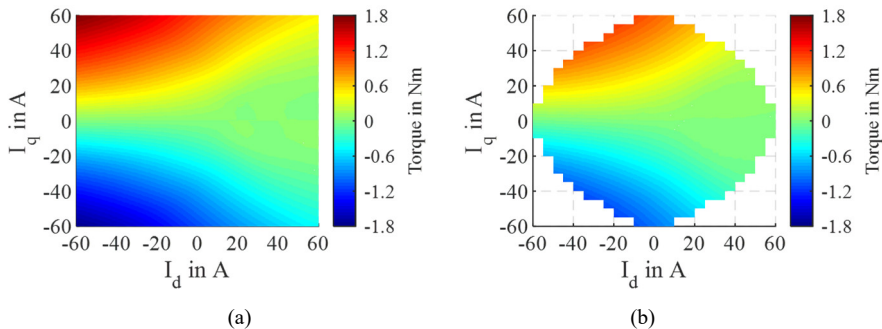
Figure 6.25:   Torque of the IPM prototype as a function of the *d*-axis and *q*-axis currents. (a) FEA. (b) Test.

6.3.4   Temperature rises

To evaluate the feasibility of the proposal, the thermal behavior of the prototype needs to be assessed. The temperature rises of the IPM prototype at 10,000 /min, 0.83 Nm and 30,000 /min, 0.51 Nm are measured and compared with the CFD calculation results. The CFD analytical thermal distributions of the prototype in these cases are illustrated in Fig. 6.26. The tested temperature rises of the prototype are compared with the simulation results in Table 6.1.

149
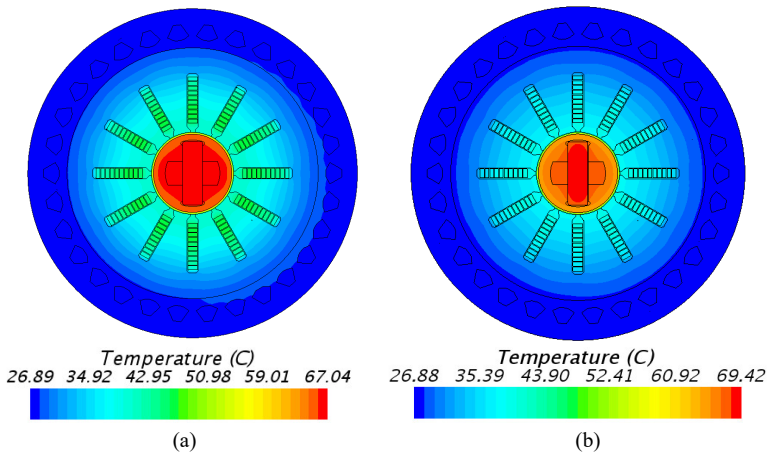
Figure 6.26:   Predicted thermal distributions of the IPM prototype at different speed and load conditions. (a) 10,000 /min and 0.83 Nm. (b) 30,000 /min and 0.51 Nm.

Speed and load	Temperature rise	CFD	Experimental
10,000 /min and 0.83 Nm	Windings in K	28.8	31.0
	Rotor in K	40.2	36.1
30,000 /min and 0.51 Nm	Windings in K	17.6	17.1
	Rotor in K	42.6	37.4

Note: the maximum temperature rise at the windings is located at the end-winding.

Table 6.1:   Comparison of the tested and the CFD temperature rises of the IPM motor at different speed and load conditions.

In Table 6.1, the temperature rises calculated through CFD software are the maximum values, while the tested temperature rise of the rotor is an average value and the tested temperature rise of the winding is at the end-winding. Because directly measurement of the rotor's temperature is difficult at a high speed, in the test, the temperature rise of the rotor is derived from the no-load back-EMF. Based on the temperature coefficient of the remanence of the PM, the temperature rise is calculated. The CFD results show that the maximum temperature rise of the rotor locates at the middle position of the PM, while the maximum temperature rise of the windings happens at the end-winding. The experimental results fit well with the predicted values through CFD software.

6.4 Influence of PWM inverter

6.4.1 Phase current fed by PWM inverter

Through (5.4) the phase current of the SPM prototype at different speed and load conditions can be precisely predicted because the phase inductance of the SPM prototype changes slightly when the load changes. For example, the predicted and experimental phase currents at 12,000 /min and light load are compared in Fig. 6.27.
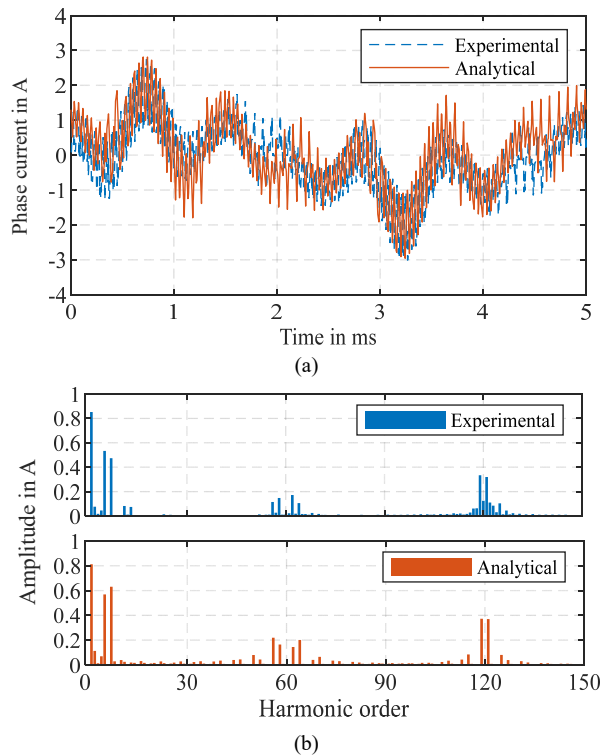
Figure 6.27: Phase current at 12,000 /min when the PWM frequency is 12 kHz and the DC-bus voltage is 100 V. (a) Current waveform. (b) Spectrum of the phase current.

Fig. 6.27 shows that the analytical method can well predict the phase current and the current harmonics generated by PWM inverter. Because of the existence of 5th and 7th EMF harmonics as can be seen in Fig. 6.18, the phase current also consists of high-amplitudes of 5th and 7th current harmonics. Since the low-order current harmonics do not play an important role in the PM EC losses, the current harmonics caused by the PWM inverter are the focus. As aforementioned, the phase current rises and falls twice in one SVPWM period. When the speed of the motor is 12,000 /min, the fundamental frequency at this speed

is 200 Hz of the designed motors. Since the switching frequency is equal to 12 kHz, the phase current consists of high amplitudes of 119th and 121st current harmonics as can be seen in Fig. 6.27(b). This figure also shows that the analytical values of the 119th and 121st current harmonics are a little higher than those of the experimental results. It is because the experimental speed of the prototype is not exactly 12,000 /min, which causes the FFT results of the phase current consisting of high amplitudes of current harmonics around 119th and 121st as shown in Fig. 6.27(b). Hence, the analytical method is feasible for predicting the current harmonics generated by the PWM inverter. This method can be used for predicting the current harmoncs in the motor design stage.

6.4.2 Influence of PWM frequency

According to (5.8) it is known that the amplitudes of the current harmonics generated by the PWM inverter are influenced by the PWM frequency, DC-bus voltage and the rotor speed. When the DC-bus voltage is 100 V, the experimental phase currents at 12,000 /min of different PWM frequencies are presented in Fig. 6.28. It clearly shows that the amplitudes of the current harmonics decrease when the PWM frequency increases, which can be explained by (5.8).
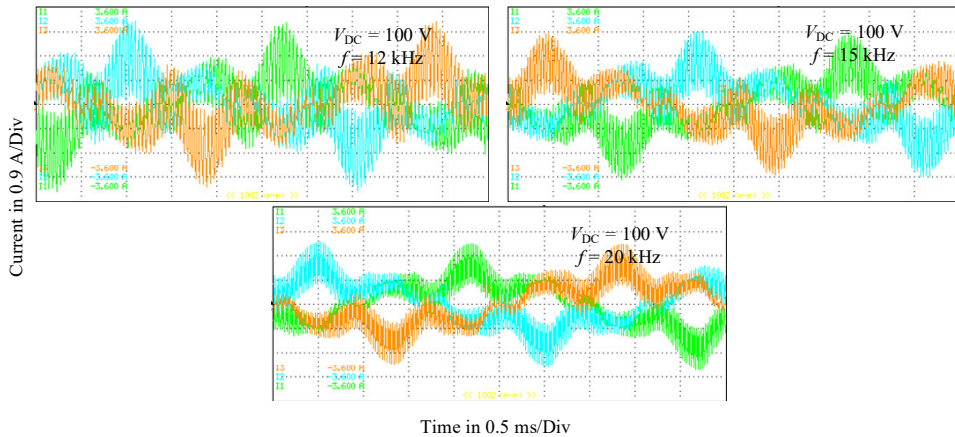
Figure 6.28:   Phase currents at 12,000 /min of different PWM frquencies.

Because experimental measurement of EC losses is very difficult to conduct and the temperature is a reflection of the losses, to verify the analytical results, the temperature rise of the rotor is used. The measurement of the temperature rise of the rotor is made for different PWM frequencies. In order to avoid the influence of the stator copper losses on the rotor temperature, the fundamental current is limited. In the test, q-axis current is equal to 1 A. Due to a low phase resistance of the motor, 0.045 Ω, the total copper losses of the motor

are about 0.07 W. Therefore, the temperature rise of the rotor is mainly due to the PM and the shaft eddy current losses. Then, the predicted PM losses, rotor temperature rises and measured rotor temperature rises at different PWM frequencies are listed in Table 6.2. In this table noload means the PWM is shut down and the tested prototype is driven by another motor and the PM EC losses of the tested prototype are generated by slotting effect.

PWM fre-quency	Predicted PM EC losses	Predicted rotor temperature rise	Experimental rotor tempera-ture rise
Noload	0.01 W	4.5 K	5.3 K
12 kHz	2.64 W	24.6 K	23.0 K
15 kHz	2.41 W	22.7 K	21.8 K
20 kHz	2.09 W	17.1 K	18.6 K

Table 6.2: Predicted PM EC losses and temperature rises of the rotor of different PWM frequencies at 12,000 /min.

The predicted temperature rises of the rotor have a small error with the measurement results. The accuracy of the analytical methods to predict the phase current, the PM EC losses and the temperature rise are proved. Fig. 6.28 and Table 6.2 also illustrate that even though the amplitudes of the current harmonics at a higher PWM frequency are significantly reduced, the PM EC losses and the consequent rotor temperature rise cannot be dramatically decreased. For example, when the PWM frequency is increased from 12 kHz to 20 kHz, the increasement is about 67 %, the temperature rise of the rotor is decreased from 23.0 K to 18.6 K, which is only about 20 %. This is because at a higher PWM frequency, the frequencies of the current harmonics are higher. This means that by increasing the PWM frequency to reduce the PM EC losses of the SPM rotor is not a highly efficient method.

Furthermore, if the influence of the PWM inverter on the PM EC losses is not considered, the predicted PM EC losses are much lower and the predicted rotor temperature rise is much lower than the real temperature rise. This may result in PM irreversible demagnetization due to high temperature. Hence, in the design of the surface-mounted PM motors, the influence of the PWM inverter needs to be considered.

6.4.3 Influence of DC-bus voltage

Generally, the DC-bus voltage is fix and high to cover all the speed and load ranges. For example, to run the two prototypes to the maximum speed at rated torque, the rated voltage required is 500 V. However, because higher DC-bus voltage will induce higher EC losses

of the PMs, in order to avoid a much high temperature of the PMs, it is better to adjust the DC-bus voltage according to the speed and load. When the PWM frequency is 12 kHz, the experimental phase currents of different DC-bus voltages are presented in Fig. 6.29. It clearly shows that the amplitude of the current fluctuation increases when the DC-bus voltage increases. Because the amplitude of the phase back-EMF at 12,000 /min is much lower than the DC-bus voltages applied in the test, the phase current fluctuation increases slightly when the DC-bus voltage is higher than 100 V. This phenomenon can be also explained by (5.8).
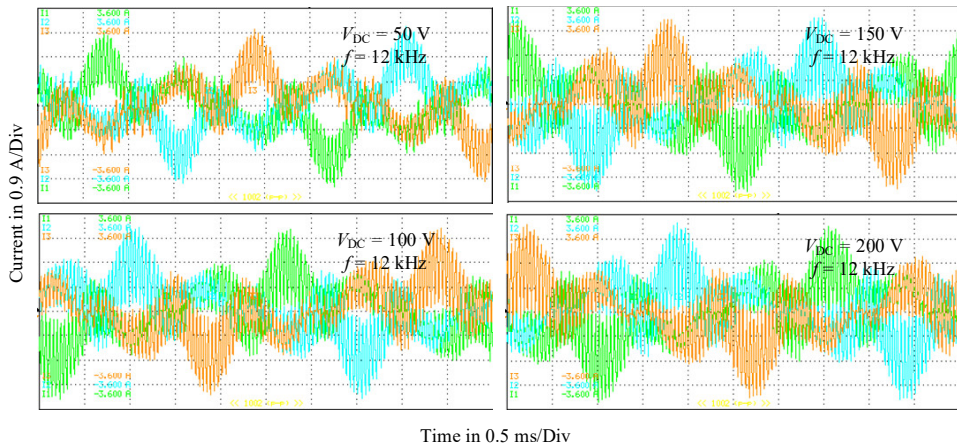
Figure 6.29:   Phase currents of different DC-bus voltage at 12,000 /min.

The predicted PM EC losses and the experimental rotor temperature rise of the rotor of different DC-bus voltage at 12,000 /min are presented in Table 6.3. It shows that the temperature rise of the rotor increases significantly when the DC-bus voltage increases. Even though the DC-bus voltage is only 150 V and the speed is only 12,000 /min and the motor is low load, the rotor temperature rise is high to 36.8 K. Hence, the influence of the DC-bus voltage on the rotor losses is significant and needs to be considered.

DC-bus voltage	Predicted PM EC losses	Predicted rotor temperature rise	Experimental rotor temperature rise
50 V	1.08 W	14.3 K	13.6 K
100 V	2.64 W	24.6 K	23.0 K
150 V	3.91 W	33.5 K	36.8 K

Table 6.3:   Predicted PM EC losses and temperature rises of the rotor of different DC-bus voltages at 12,000 /min.

6.4.4 Influence of rotor speed

Based on (5.8) it is known that when the PWM frequency and the DC-bus voltage are fixed, the amplitudes of the current harmonics caused by the PWM inverter are decided by the rotor speed (corresponds to the back-EMF e_{AN}). When the rotor speed is increased, the amplitude of the current harmonic is firstly increased and then decreased. Since the PWM frequency is fixed and it is much higher than the frequency of fundamental current, the PM eddy current losses are almost proportional to the amplitude of the current harmonic. Consequently, the trend of the rotor temperature rise is similar to that of the amplitude of the current harmonic. When the PWM frequency is 25 kHz, the experimental rotor temperature rise and the amplitude of the current harmonic for different DC-bus voltages as a function of the rotor speed (back-EMF) are presented in Fig. 6.30. The experimental rotor temperature rise is tested when the DC-bus voltage is 150 V. It clearly shows that the rotor temperature rise has a similar trend with the amplitude of the current harmonic. To minimize the rotor temperature, the DC-bus voltage should be regulated according to the speed and load.
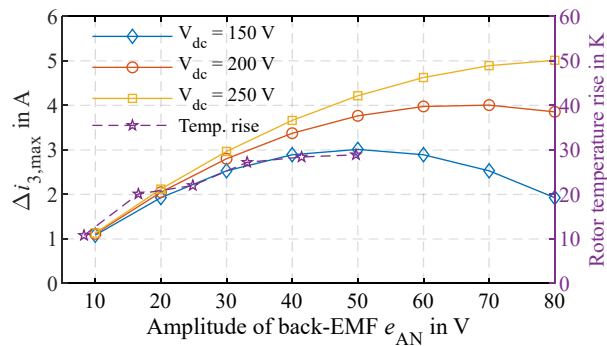
Figure 6.30: Experimental rotor temperature rise and the amplitude of the current harmonic for different DC-bus voltages as a function of the rotor speed (back-EMF).

6.4.5 Comparison of IPM and SPM rotors

The eddy current losses of the SPM motors caused by the PWM inverter have been analyzed in Chapter 5. It is known that the eddy current losses of the PMs caused by the PWM inverter are dominant and they are influenced by the phase inductance, the PWM frequency, the DC-bus voltage and the back-EMF (which corresponds to the rotor speed). Because the IPM rotor has a ferromagnetic rotor core to guide the armature reaction field and the air-gap length of the IPM motor is small, which leads to a high phase inductance and low amplitudes of current harmonics, the eddy current losses of the IPM motor are lower than those of the SPM motor. When the PWM frequency is 20 kHz and the DC-bus

voltage is 150 V, the tested phase currents of the two prototypes at 30,000 /min are compared in Fig. 6.31(a). In the test, one prototype is open circuit and the counter prototype is driven as motor to drive the two co-axial prototypes to a specific speed. The effective currents of the two prototypes are used to overcome the losses of them, including the air-friction losses and the electromagnetic losses of them. The spectrums of the current harmonics are compared in Fig. 6.31(b).
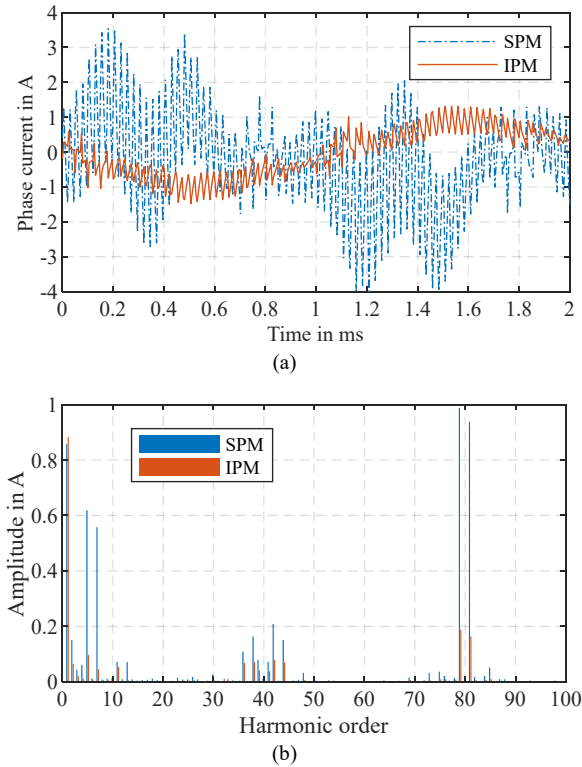
Figure 6.31:   Phase currents of the two prototypes at 30,000 /min, light-load condition. (a) Phase current waveforms. (b) Spectrums of the phase currents.

The FFT results of the phase currents show that the amplitudes of the fundamental currents of the two motors are comparable. However, because the SPM motor consists of high amplitudes of 5th and 7th EMF harmonics, the 5th and 7th current harmonics at no-load condition have high amplitudes. Furthermore, due to lower phase inductance of the SPM motor, the amplitudes of the 79th and the 81st current harmoncis generated by the PWM inverter are about 5 times the IPM motor.

When the DC-bus voltage is 150 V and the PWM frequency is 25 kHz, the temperature rises of the two rotors at low-load condition (amplitude of the phase current of the load

machine is 1 A) as a function of speed are compared in Fig. 6.32. It can be seen that the IPM rotor has lower temperature rise than the SPM rotor. At 36,000 /min, the temperature rise of the IPM motor is about 67% of the SPM motor. The IPM motor shows a better performance in terms of the temperature rise of the rotor.
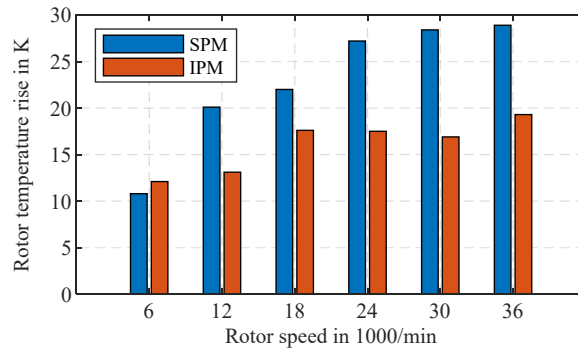
Figure 6.32:   Temperature rises of the two prototypes as a function of rotor speed.

6.5   Efficiency

Based on the torque measurement of the two prototypes as illustrated in Fig. 6.24, it is known that the IPM prototype has higher torque than the SPM prototype when the amplitude of the phase current is higher than 30 A. When the IPM prototype is driven as a motor and the SPM prototype is driven as a generator, at 3,000 /min and 1.08 Nm, the phase currents corresponding to the rotor positions of them are drawn in Fig. 6.33. It can be seen that the IPM has lower current even though it needs to overcome the friction losses of both prototypes.
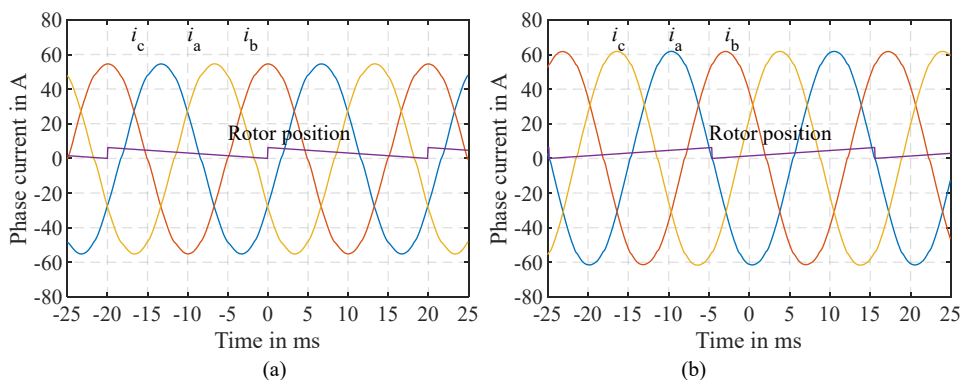
Figure 6.33:   Comparison of the phase currents of the two prototypes at load condition. (a) IPM prototype. (b) SPM prototype.

The efficiency maps of the two prototypes are tested and compared in Fig. 6.34 and Fig. 6.35. It can be noticed that the efficiency of the IPM prototype is about 13 % higher than that of the SPM prototype. It might be mainly because the SPM prototype has much higher amplitudes of current harmonics caused by the PWM inverter as can be seen in Fig. 6.31. The high current harmoincs of the SPM motor lead to higher losses and lower efficiency. Hence, the advantages, such as higher torque density, higher power density and higher efficiency of the proposed IPM rotor made from AMM rotor core are verified.
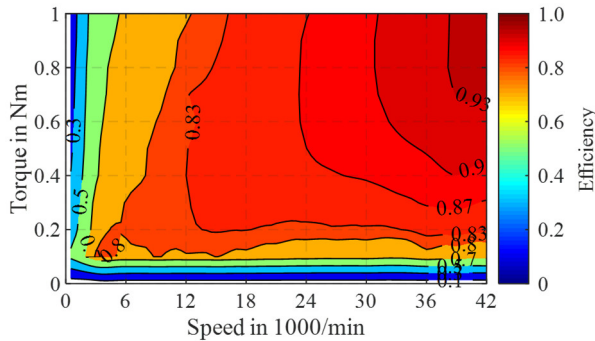
Figure 6.34:   Tested efficiency map of the proposed IPM prototype.
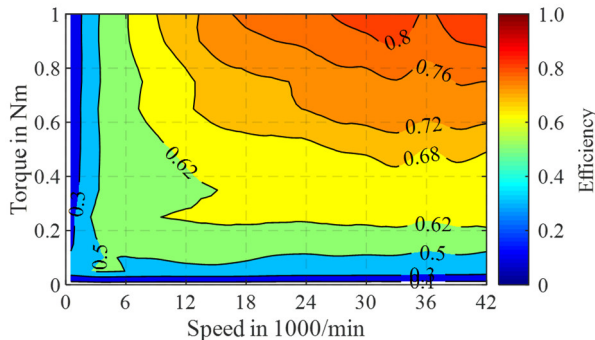
Figure 6.35:   Tested efficiency map of the SPM prototype.

6.6   High-speed operation

To run the motor to a high speed faces with many challenges. Firstly, the rotor dynamic balancing experiment needs to be completed. At the maximum target speed of 125,000 /min, to reach grade G 0.4, the corresponding permissible residual specific unbalance must be lower than 0.04 gmm/kg based on the international standard ISO 1940-1 [167]. To reach grade G 1, the permissible residual specific unbalance must be lower than 0.1 gmm/kg. Currently, we do not have a balancing machine for this target value in our institute. An universal balancing machine Pasio 05 developed by Schenck RoTec GmbH

can reach a minimum residual unbalance of 0.1 gmm/kg and this machine can help to reach a highest grade of G 2.5 and it can be considered for further research. Secondly, to avoid resonance of the motor, both ends of the prototype should be directly fixed to the platform, instead of holded by using two bearings as shown in Fig. 6.11. In this case the torque cannot be measured and the designed testbench needs to be redesigned and built. Thirdly, it is necessary to reduce the influence of the PWM inverter on the losses of the motors. However, currently it is difficult to increase the PWM frequency, because the calculation time of the control strategies and the communication time of the sensors can be hardly reduced in the current configuration of the driver. Another method to reduce the high-frequency losses is to connect a current filter between the motor and the PWM inverter. However the DC-bus voltage needs to be increased and a high frequency current filter is required. It is better to use AMM for this current filter. Currently such a current filter is unavailable in our institute. Fourthly, a high-speed position sensor is needed and the delay of the sensor needs to be compensated. Otherwise, sensorless control strategies are necessary. Because to realize a high-speed PM motor driver also faces with many challenges, it is not developed in this dissertation. Hence, currently, the tested maximum speed is 65,100 /min. In this speed, the surface velocity of the rotor is about 68 m/s. The no-load back-EMF of the load motor at this speed is shown in Fig. 6.36.
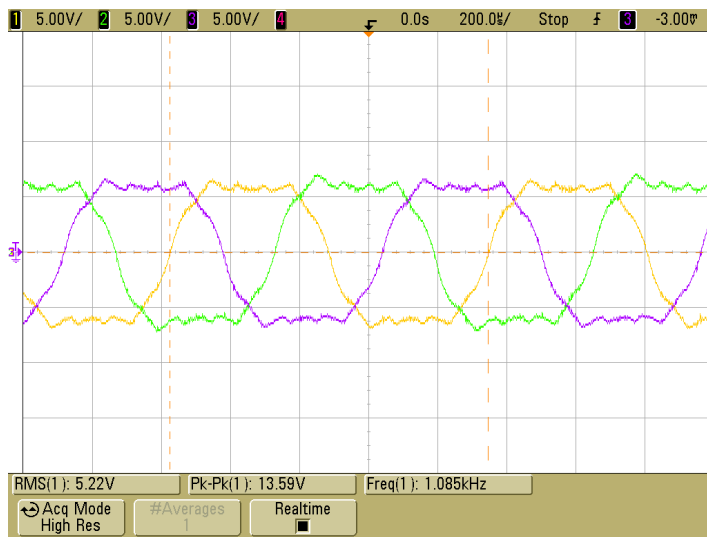
Figure 6.36:   No-load back-EMF of the IPM prototype at 65,100 /min.

Based on the analysis and the experimental results, it is known that the IPM prototype has better performance than the SPM prototype. It can be summarized as follows. Firstly, the proposed IPM rotor has much lower amplitudes of the current harmonics caused by the PWM inverter due to its smaller air-gap length and higher phase inductance. This helps to

reduce the losses of the motor and results in lower temperature rises and higher efficiency. Secondary, the flux-weakening ability of the IPM motor is much better due to higher *d*-axis inductance. Thirdly, since the IPM motor can provide additional reluctance torque, the IPM motor has lower copper losses. It is proved that the proposed IPM rotor made from amorphous core is suitable for the high-speed high-power-density PM motors.

7 Conclusion and outlook

Based on the literature it is known that when the speed of the high-speed PM motors is higher than 50,000 /min, SPM rotors are more frequently applied. Metal sleeves are more commonly used. However, because the solid-conductive sleeves and magnets of the SPM rotors are directly exposed to the armature reaction magnetic field, the eddy current losses of the high-speed SPM rotors are very high. Moreover, since the frequency of the motors at a high speed is high and the modulation ratio of the PWM inverter is low, high amplitudes of current harmonics are generated and these current harmonics result in high eddy current losses in the SPM rotors. Based on the analysis in Chapter 5, it is known that the high-frequency current harmonics due to the PWM inverter play an important role in the rotor eddy current losses. This influence cannot be ignored when a high-speed motor is designed. In order to reduce the eddy current losses, a larger air-gap length is commonly employed for the high-speed SPM motors. However, this method sacrifices the power density of the motor. Moreover, because of low phase inductance, the flux-weakening ability of the SPM motor is poor. Hence, an IPM rotor for high-speed operation is proposed in this dissertation.

AMMs are well-known due to their low core losses and they have been commercially available for decades. However, their application to electrical machines still lack a breakthrough progress. An important property, high mechanical strength of the AMMs, lacks attention. In order to obtain an IPM rotor with high strength and low core losses, AMM is employed to the proposed high-speed IPM rotor. Due to the high strength and relatively low saturation flux density of the AMM, the flux bridges of the AMM IPM rotor are reduced and a low flux leakage is obtained.

In order to better utilize the AMM for the proposed high-speed IPM rotor, the electromagnetic and mechanical properties of the AMM cores are experimentally investigated. For a comparison study, another five materials, including 10JNEX900, M235-35A, M330-35A, M330-50A, and Vacodur 49, are tested as well. It is found that the AMM has the lowest core losses, whereas the 10JNEX900 has the highest permeability and the Vacodur 49 has the highest saturation flux density. The core losses of the AMM are only one seventeenth of the commonly used silicon steel M235-35A. However, the core losses of the AMM cores are easily influenced by the stress. The core losses of a stacked core can be a few times higher than those of the raw AMM ribbon because of high stress induced during the manufacture of the cores. The saturation flux density of the AMM is moderate which is about 1.56 T. It is easily influenced by the working temperature. When the temperature is increased from room temperature to 150 °C, the saturation flux density is reduced by about 10 % for both non-annealed and annealed cores. Positive effects of the high temperature

on the AMM cores are that the core losses are reduced and the relative permeability is increased. When the temperature is increased from room temperature to 150 °C, the core losses of the annealed and non-annealed AMM cores are reduced by about 13.3 % and 6.3 %; the relative permeability of the two cores are increased by about 100 % and 50 %, respectively.

The influence of temperature on M235-35A and 10JNEX900 cores are also tested. It is found that M235-35A has much stable properties when the temperature is changed. When the temperature is increased, the saturation flux density, the relative permeability and the core losses of M235-35A are slightly reduced. The core losses at 150 °C are about 5.6 % lower than those at room temperature. The influence of the temperature on the saturation flux density and the relative permeability of 10JNEX900 is similar to the the conventional silicon iron M235-35A. However, the core losses of 10JNEX900 at a high temperature are higher than those at a low temperature, which is completely different from the AMM and M235-35A cores. When the temperature is increased from room temperature to 150 °C, the core losses of 10JNEX900 are increased by 24.7 % and the relative permeability is reduced by about 60 %.

To ensure the rotor to run at a high speed, the mechanical strength of the AMM core is measured and the tested data is used for the rotor design. Since the AMMs are brittle, they do not have non-linear elastic region. The ultimate tensile strength (UTS) is tested instead of the yield tensile strength. Based on the test it is found that the UTS of the AMM ribbon is normally higher than 800 MPa. However, the mechanical strength of the AMM is very sensitive to the mechanical process. A small defect on the AMM core may crack the core because of its high brittleness. The tested yield strengths of M235-35A, M330-50A and 10JNEX900 are about 450 MPa, 350 MPa and 570 MPa, respectively. Based on the properties study, it is believed that the AMM is the best choice for the high-speed IPM rotor.

To study the feasibility of the proposed IPM rotor made from the AMM rotor core, a demonstrator motor is designed. The electromagnetic, mechanical and thermal performances of the demenstrator motor are fully analyzed. In order to avoid the high rotor losses, integral-slot distributed-winding is adopted. Parallel slots configured with flat wires are employed in order to increase the copper filling factor of the slots and to improve the load performance of the motor. By considering the stress in the PM and the high temperature working condition of the rotor, high temperature NdFeB magnet, whose working temperature is higher than 200 °C is used. A special water-cooled housing is designed in order to increase the wall area of the water channel and the axial stiffness of the housing. The stator is encapsulated with epoxy resin of high thermal conductivity to improve the cooling performance and to reduce the air-friction loss of the rotor. The rotor diameter is determined by the stress of the AMM core while the rotor axial-length is determined by the natural frequencies of the rotor. A high maximum stress of 594 MPa in the rotor core is designed

to verify the high mechanical strength of the AMM core. To evaluate the thermal performance of the motor, the rotor air-friction losses and the heat transfer coefficient of the air gap are calculated. Then the temperature rises of the motor are predicted through 3-dimensional computational fluid dynamic (CFD) simulation.

To evaluate the superiority of the rotor made from the AMM core, the performance of the rotors made from different core materials are compared. Based on the finite element analysis (FEA) it is found that if the AMM core is replaced by a M330-35A core, the thickness of the flux-bridge is larger due to a lower yield strength of M330-35A. Since the saturation flux density of M330-35A is higher, the flux leakage of the rotor is higher. This requires a higher stator electric loading and leads to higher copper losses to generate a specific torque. Moreover, due to higher core losses of M330-35A, the rotor losses of the M330-35A rotor are about 4 times those of the AMM rotor. This leads to a 95 K higher temperature rise of the M330-35A rotor. The superiority of the performance of the AMM rotor over the M330-35A rotor is very clear.

Since the SPM rotors are commonly employed at a high speed, in order to show the advantages of the IPM rotor made from the AMM core, a SPM rotor protected by a high thermal-conductivity carbon fiber sleeve is also designed as a comparison with the proposed motor. The mechanical air-gap lengths and the stators of both motors are identical. The thickness of the sleeve is determined by not only the stress in the sleeve, but also the rotor eddy current losses. In order to avoid high eddy current losses in the SPM rotor, the thickness of the sleeve is a little larger and the maximum stress in the sleeve is about 300 MPa. Even though a thicker sleeve is used, the losses of the SPM rotor are still higher than those of the IPM rotor. Because the SPM motor cannot provide reluctance torque and its air-gap flux density is subjected to the rotor volume and the equivalent air-gap length, it requires a higher electric loading to generate a specific torque than the IPM rotor.

Finally, the designed IPM and SPM motors are built and tested. In order to ensure the success of the AMM prototype, the slotting approaches of the AMM cores, including WEDM, laser and punching approaches are experimentally studied. It is found that WEDM has better cutting quality in terms of electromagnetics and mechanics. Hence, it is adopted for the manufacturing of the IPM prototype with AMM rotor core. A strain gage based torque sensor is connected to the housing of the IPM prototype to measure the output torque. The no-load back-EMFs of the two prototypes are firstly measured. The EMF errors between FEA and experimental results of the IPM motor is about 7.4 %, while the error for the SPM motor is about 1.7 %. The flux linkages as a function of d-axis and q-axis currents of the IPM motor are tested to optimize the torque control of the IPM motor. The torque, the temperature rises and the efficiencies of the two prototypes are tested as well. The FEA

results are consistent well with the experimental results, which proves that the FEA analysis is credible. From the tested results it is found that the IPM motor has about 13% higher efficiency than the SPM motor. The influence of the PWM inverter on the rotor losses are verified. Due to the limitation of the PWM inverter and the testbench, currently, the tested maximum speed of IPM prototype is 65,100 /min. In this case, the circumferential speed is about 68 m/s. Based on the tested data of the prototypes, it is proved that the AMM is suitable for the high-speed motors and the proposed IPM rotor made from AMM has better performance than the SPM rotor.

In order to drive the motor to a higher speed, the PWM inverter needs to be improved and a current filter needs to be designed and built. Since the core losses of the AMM is much lower than the silicon steels, it will be used for the current filter. Our further work about the control of the high-speed motor will be focused on increasing the switching frequency and on developing of the sensorless control strategies. Another work concerning the motor itself is to apply the non-heat-treated AMM core for this IPM rotor. By comparing the performance of the non-heat-treated and the heat-treated rotor cores, we can find out which AMM core is more suitable for the high-speed high-power-density IPM motors. Since the slotting of the AMM is the major problem of the application of the AMM, it is necessary to find out a high-efficiency and high-quality cutting approach. In this work, the WEDM method is recommended for manufacturing of the prototype. When another approach is used to cut the AMM core for the high-speed rotors, it is necessary to test the mechanical strength of the AMM again, as the strength of the AMM is sensitive to the mechanical process. Furthermore, since the high-silicon steel 10JNEX900 has higher strength and much lower core losses than the conventional silicon steels, it has also potential for the high-speed motors and worthes a further research.

List of figures

List of tables

Bibliography

Own publications

[O1]   **J. Ou**, Y. Liu, P. Breining, M. Schiefer and M. Doppelbauer, "Experimental study of the amorphous magnetic material for high-speed sleeve-free PM rotor application," *IEEE Trans. Ind. Electron.*, to be published, doi: 10.1109/TIE.2019.2931282.

[O2]   **J. Ou**, Y. Liu, D. Liang, and M. Doppelbauer, "Investigation of PM eddy current losses in surface-mounted PM motors caused by PWM," *IEEE Trans. Power Electron.*, to be published, doi: 10.1109/TPEL.2019.2895679.

[O3]   **J. Ou**, Y. Liu, M. Schiefer, P. Breining, M. Doppelbauer, and F. Chai, "Application of amorphous cores to DC-excited flux-modulated motors used for electric vehicles," in *2018 IEEE Int. Conf. on Electrical Systems for Aircraft, Railway, Ship Propulsion and Road Vehicles & Int. Transportation Electrification Conf. (ESARS-ITEC)*, Nottingham, 2018, pp. 1-7.

[O4]   **J. Ou**, Y. Liu, R. Qu and M. Doppelbauer, "Experimental and theoretical research on cogging torque of PM synchronous motors considering manufacturing tolerances," *IEEE Trans. Ind. Electron.*, vol. 65, no. 5, pp. 3772-3783, May 2018.

[O5]   **J. Ou**, P. Breining, M. Doppelbauer and M. Schiefer, "New rotor concept for sleeve-free high-speed motors over 125,000 rpm," in *7th VDE/VDI Symposium, Drive Systems 2017*, Karlsruhe, Germany, 2017, pp. 1-6.

[O6]   **J. Ou**, Y. Liu, M. Schiefer and M. Doppelbauer, "A novel PM-free high-speed linear machine with amorphous primary core," *IEEE Trans. Magn.*, vol. 53, no. 11, pp. 1-8, Nov. 2017.

[O7]   **J. Ou**, Y. Liu and M. Doppelbauer, "Torque analysis and slot regions assignment of a DC-excited flux-modulated machine with two stator windings," *AIMS Electronics and Electrical Engineering*, vol. 1, no. 1, pp. 4-17, Nov. 2017.

[O8]   **J. Ou** and M. Doppelbauer, "Torque analysis and comparison of the switched reluctance machine and the doubly-salient permanent magnet machine," in *2016 18th European Conf. on Power Electronics and Applications (EPE'16 ECCE Europe)*, Karlsruhe, 2016, pp. 1-11.

[O9]   Y. Liu, **J. Ou**, M. Schiefer, P. Breining, F. Grilli and M. Doppelbauer, "Application of an amorphous core to an ultra-high-speed sleeve-free interior permanent-magnet rotor," *IEEE Trans. Ind. Electron.*, vol. 65, no. 11, pp. 8498-8509, Nov. 2018.

[O10] Y. Liu, **J. Ou**, F. Grilli; F. Schreiner, V. Zermeno, M. Zhang, and M. Noe, "Comparison of 2D simulation models to estimate the critical current of a coated superconducting coil," *Superconductor Science and Technology*, vol.32, no. 01, 2018, Art. no. 014001.

[O11] Y. Liu, **J. Ou**, F. Schreiner, M. Lao, M. Noe and M. Doppelbauer, "Design of a superconducting DC demonstrator for wind generators," *IEEE Trans. Energy Convers.*, vol. 33, no. 4, pp. 1955-1964, Dec. 2018.

[O12] Y. Liu, **J. Ou** and M. Noe, "A large-scale superconducting DC wind generator considering concentrated/distributed armature winding," *IEEE Trans. Appl. Supercond.*, vol. 27, no. 4, pp. 1-5, Jun. 2017, Art no. 5200405.

[O13] Y. Liu, M. Noe, **J. Ou**, P. Breining, M. Veigel and M. Doppelbauer, "Measurement of magnetic materials at room and cryogenic temperature for their application to superconducting wind generators," *IEEE Trans. Appl. Supercond.*, vol. 28, no. 3, pp. 1-6, Apr. 2018, Art no. 5206006.

Supervised students thesis

[S1] "Rotor losses analysis of high-speed PM machine considering the influence of PWM," Master thesis, 2017.

[S2] "Design of a DC-excited flux-modulated motor with amorphous cores for electric vehicle applications," Master thesis, 2018.

[S3] "Analyses of rotor stress and motor natural frequencies of an interior permanent-magnet high-speed synchronous motor," Master thesis, 2019.

[S4] "Thermal field analysis of an interior permanent-magnet high-speed motor," Master thesis, 2019.

[S5] "Sensorless control of a high-speed interior PM motor," Master thesis, 2019.

Other publications

[1] M. Taniguchi, *et al*., "Development of new hybrid transaxle for compact-class vehicles," *SAE Technical Paper*, 2016-01-1163, 2016.

[2] S. Sano, T. Yashiro, K. Takizawa, and T. Mizutani, "Development of new motor for compact-class hybrid vehicles," *World electric vehicle journal*, vol. 8, pp. 0443-0449, 2016.

[3] C. Zwyssig, J. W. Kolar, and S. D. Round, "Megaspeed drive systems: pushing beyond 1 million r/min," *IEEE/ASME Trans. Mechatronics*, vol. 14, no. 5, pp. 564-574, Oct. 2009.

[4]   C. Wu *et al.*, "Development of amorphous ribbon manufacturing technology," China steel technical report, no. 27, pp. 28-42, 2014.

[5]   Melt spinning process, [Online]. Source: https://metglas.com/company-history/melt-spinning-procress/, Retrieved on 15th of September 2019.

[6]   J. Celie, M. Stie, J. Rens, and P. Sergeant, "Effects of cutting and annealing of amorphous materials for high speed permanent magnet machines," *in 2016 XXII Int. Conf. on Elect. Mach. (ICEM)*, Lausanne, 2016, pp. 1630-1635.

[7]   S. Derlecki, Z. Kuśmierek, M. Dems, and J. Szulakowski, "Magnetic properties of amorphous materials used as corps of electric machines," *Przegląd Elektrotechniczny*, vol. 88, no. 5a, pp. 10-13, 2012.

[8]   G. S. Liew, W. L. Soong, N. Ertugrul, and J. Gayler, "Analysis and performance investigation of an axial-field PM motor utilising cut amorphous magnetic material," in *2010 20th Australasian Universities Power Engineering Conf.*, Christchurch, 2010, pp. 1-6.

[9]   Y. Enomoto, H.Tokoi, T. Imagawa, T. Suzuki, T. Obata, and K. Souma, "Amorphous motor with IE5 efficiency class," *Hitachi Review*, vol. 64, no. 8, pp. 480-487, 2015.

[10]   A. Krings, M. Cossale, A. Tenconi, J. Soulard, A. Cavagnino, and A. Boglietti, "Characteristics comparison and selection guide for magnetic materials used in electrical machines," in *2015 IEEE Int. Electric Machines & Drives Conf. (IEMDC)*, Coeur d'Alene, ID, 2015, pp. 1152-1157.

[11]   D. Gerada, A. Mebarki, N. L. Brown, C. Gerada, A. Cavagnino, and A. Boglietti, "High-speed electrical machines: technologies, trends, and developments," *IEEE Trans. Ind. Electron.*, vol. 61, no. 6, pp. 2946-2959, Jun. 2014.

[12]   D. K. Hong, B. C. Woo, J. Y. Lee, and D. H. Koo, "Ultra high speed motor supported by air foil bearings for air blower cooling fuel cells," *IEEE Trans. Magn.*, vol. 48, no. 2, pp. 871-874, Feb. 2012.

[13]   T. Noguchi and M. Kano, "Development of 150000 r/min, 1.5 kW Permanent-Magnet Motor for Automotive Supercharger," in *2007 7th Int. Conf. on Power Electronics and Drive Systems*, Bangkok, 2007, pp. 183-188.

[14]   T. Noguchi and K. Fujita, "Electrical and mechanical compatible design of 15 kW, 150,000 r/min ultra-high-speed PM motor," in *2019 22th International Conference on Electrical Machines and Systems (ICEMS)*, Harbin, 2019, pp. 1-6.

[15]   K. Fujita and T. Noguchi, "Study on propotion of 15 kW, 150,000 r/min PM motor," in *IEEJ Annual National Conference*, 5-031, Hokkaido, 2019.

[16] D. Gerada, H. Zhang, Z. Xu, G. L. Calzo, and C. Gerada, "Electrical machine type selection for high speed supercharger automotive applications," in *2016 19th International Conference on Electrical Machines and Systems (ICEMS)*, Chiba, 2016, pp. 1-6.

[17] R. Abebe, M. Di Nardo, D. Gerada, G. L. Calzo, L. Papini, and C. Gerada, "High speed drives review: machines, converters and applications," in *IECON 2016 - 42nd Annual Conf. of the IEEE Ind. Electron. Society*, Florence, 2016, pp. 1675-1679.

[18] T. Noguchi, Y. Takata, Y. Yamashita, and S. Ibaraki, "160,000-r/min, 2.7-kW electric drive of supercharger for automobiles," in *2005 Int. Conf. on Power Electron. and Drives Systems*, Kuala Lumpur, 2005, pp. 1380-1385.

[19] D. Krahenbuhl, C. Zwyssig, H. Weser, and J. W. Kolar, "A miniature 500 000-r/min electrically driven turbocompressor," *IEEE Trans. Ind. Appl.*, vol. 46, no. 6, pp. 2459-2466, Nov.-Dec. 2010.

[20] S. M. Jang, H. W. Cho, and S. K. Choi, "Design and analysis of a high-speed brushless DC motor for centrifugal compressor," *IEEE Trans. Magn.*, vol. 43, no. 6, pp. 2573-2575, Jun. 2007.

[21] M. S. Lim, J. M. Kim, Y. S. Hwang, and J. P. Hong, "Design of an ultra-high-speed permanent-magnet motor for an electric turbocharger considering speed response characteristics," *IEEE/ASME Trans. Mechatronics*, vol. 22, no. 2, pp. 774-784, Apr. 2017.

[22] C. Zwyssig, J. W. Kolar, W. Thaler, and M. Vohrer, "Design of a 100 W, 500000 rpm permanent-magnet generator for mesoscale gas turbines," in *Fourtieth IAS Annual Meeting. Conf. Record of the 2005 Ind. Appl. Conf.*, 2005, pp. 253-260, Vol. 1.

[23] W. Lee, E. Schubert, Y. Li, S. Li, D. Bobba, and B. Sarlioglu, "Overview of electric turbocharger and supercharger for downsized internal combustion engines," *IEEE Trans. Transportation Electrification*, vol. 3, no. 1, pp. 36-47, March 2017.

[24] D. Gerada, A. Mebarki, N. L. Brown, K. J. Bradley, and C. Gerada, "Design aspects of high-speed high-power-density laminated-rotor induction machines," *IEEE Trans. Ind. Electron.*, vol. 58, no. 9, pp. 4039-4047, Sep. 2011.

[25] S. Ibaraki, Y. Yamashita, K. Sumida, H. Ogita, and Y. Jinnai, "Development of the "hybrid turbo," an electrically assisted turbocharger," *Mitsubishi Heavy Industries, Ltd. Technical Review*, vol. 43 no. 3, pp. 1-5, Sep. 2006.

[26] J. R. Bumby *et al.*, "Electrical machines for use in electrically assisted turbochargers," in *Second Int. Conf. on Power Electronics, Machines and Drives (PEMD 2004)*, Edinburgh, UK, 2004, pp. 344-349, Vol.1.

[27]   A. Gilson, F. Dubas, D. Depernet, and C. Espanet, "Comparison of high-speed PM machine topologies for electrically-assisted turbocharger applications," in *2016 19th Int. Conf. on Electrical Machines and Systems (ICEMS)*, Chiba, 2016, pp. 1-5.

[28]   Yukio Yamashita *et al.*, "Development of electric supercharger to facilitate the downsizing of automobile engines," *Mitsubishi Heavy Industries Technical Review*, Vol. 47, No. 4, pp. 7-12, Dec. 2010.

[29]   K. Nishiwaki, M. Iezawa, H. Tanaka, and T. Goto, "Development of high speed motor and inverter for electric supercharger," in *SAE 2013 World Congress & Exhibition*, DOI: https://doi.org/10.4271/2013-01-0931.

[30]   T. Noguchi, Y. Takata, Y. Yamashita, Y. Komatsu, and S. Ibaraki, "220,000-rmin, 2-kW Permanent Magnet Motor Drive for Turbocharger," *IEEJ Transactions on Industry Applications*, Vol. 125 No. 9, pp. 854-861, 2005.

[31]   B. An, H. Suzuki, N. Shibata, and M. Ebisu, "Development of two-stage electric turbocharging system for automobiles," *Mitsubishi Heavy Industries Technical Review*, Vol. 52, No. 1, pp. 71-76, Mar. 2015.

[32]   D. Jung, J. Lee, J. Kim, I. S. Jang, J. Lee, and H. Lee, "Design method of an ultra-high speed PM motor/generator for electric-turbo compounding system," *IEEE Trans. Appl. Supercond.*, vol. 28, no. 3, pp. 1-4, Apr. 2018.

[33]   D. Lusignani, D. Barater, G. Franceschini, G. Buticchi, M. Galea, and C. Gerada, "A high-speed electric drive for the more electric engine," in *2015 IEEE Energy Conversion Congress and Exposition (ECCE)*, Montreal, QC, 2015, pp. 4004-4011.

[34]   A. L. Carpenter, T. L. Beechner, B. E. Tews, and P. E. Yelvington, "A high-speed electric drive for the more electric engine," in *ASME 2017 Internal Combustion Engine Division Fall Technical Conf.*, doi:10.1115/ICEF2017-3521.

[35]   W. Lee, E. Schubert, Y. Li, Silong Li, D. Bobba, and B. Sarlioglu, "Electrification of turbocharger and supercharger for downsized internal combustion engines and hybrid electric vehicles-benefits and challenges," in *2016 IEEE Transportation Electrification Conf. and Expo (ITEC)*, Dearborn, MI, 2016, pp. 1-6.

[36]   D. Hong, T. Lee, and Y. Jeong, "Design and experimental validation of a high-speed electric turbocharger motor considering variation of the L/D ratio," *IEEE Trans. Magn.*, vol. 54, no. 11, pp. 1-4, Nov. 2018.

[37]   J. Bumby, S. Crossland, and J. Carter, "Electrically assisted turbochargers: their potential for energy recovery," in *IET - The Institution of Engineering and Technolgy Hybrid Vehicle Conf. 2006*, Coventry, 2006, pp. 43-52.

[38]   J. R. Bumby, E. Spooner, and M. Jagiela, "Equivalent circuit analysis of solid-rotor induction machines with reference to turbocharger accelerator applications," in *IEE Proc. - Electric Power Applications*, vol. 153, no. 1, Jan. 2006, pp. 31-39.

[39]   D. Gerada, Z. Xu, D. Golovanov, and C. Gerada, "Comparison of electrical machines for use with a high-horsepower marine engine turbocharger," in *2018 25th Int. Workshop on Electric Drives: Optimization in Control of Electric Drives (IWED)*, Moscow, 2018, pp. 1-6.

[40]   T. Katrašnik, S. Rodman, F. Trenc, A. Hribernik, and V. Medica, "Improvement of the dynamic characteristic of an automotive engine by a turbocharger assisted by an electric motor," *Journal of Engineering for Gas Turbines and Power*, vol. 125, no. 2, pp. 590-595, Apr. 2003.

[41]   J. R. Bumby, E. Spooner, and M. Jagiela, "Solid rotor induction machines for use in electrically-assisted turbochargers," in *2006 3rd IET Int. Conf. on Power Electronics, Machines and Drives - PEMD 2006*, Dublin, Ireland, 2006, pp. 341-345.

[42]   N. Chayopitak, R. Pupadubsin, S. Karukanan, P. Champa, P. Somsiri, and Y. Thinphowong, "Design of a 1.5 kW high speed switched reluctance motor for electric supercharger with optimal performance assessment," in *2012 15th Int. Conf. on Electrical Machines and Systems (ICEMS)*, Sapporo, 2012, pp. 1-5.

[43]   B. Hanko, P. Drgona, M. Danko, and M. Frivaldsky, "The use of high speed switched reluctance machine for electric turbochargers," in *2017 IEEE Int. Symposium on Sensorless Control for Electrical Drives (SLED)*, Catania, 2017, pp. 207-212.

[44]   M. E. Amiryar and K. R. Pullen, "A review of flywheel energy storage system technologies and their applications," *Applied Sciences*, vol. 7 no. 3, pp. 1-21, Mar. 2017.

[45]   L. Wang, J. Y. Yu, and Y. T. Chen, "Dynamic stability improvement of an integrated offshore wind and marine-current farm using a flywheel energy-storage system," *IET Renewable Power Generation*, vol. 5, no. 5, pp. 387-396, Sep. 2011.

[46]   M. L. Lazarewicz and A. Rojas, "Grid frequency regulation by recycling electrical energy in flywheels," in *IEEE Power Engineering Society General Meeting*, 2004, Denver, CO, 2004, pp. 2038-2042, Vol.2.

[47]   X. Li, N. Erd, and A. Binder, "Design and calculation of a 130 kW high-speed permanent magnet synchronous machine in flywheel energy storage systems for urban railway application," in *2017 6th Int. Conf. on Clean Electrical Power (ICCEP)*, Santa Margherita Ligure, 2017, pp. 452-459.

[48]   B. H. Kenny, P. E. Kascak, R. Jansen, T. Dever, and W. Santiago, "Control of a high-speed flywheel system for energy storage in space applications," *IEEE Trans. Ind. Appl.*, vol. 41, no. 4, pp. 1029-1038, Jul.-Aug. 2005.

[49]   H. A. Toliyat, S. Talebi, P. McMullen, Co Huynh, and A. Filatov, "Advanced high-speed flywheel energy storage systems for pulsed power applications," in *2005 IEEE Electric Ship Technologies Symposium*, Philadelphia, PA, 2005, pp. 379-386.

[50]   C. Huynh, L. Zheng, and P. McMullen, "Thermal performance evaluation of a high-speed flywheel energy storage system," in *IECON 2007 - 33rd Annual Conf. of the IEEE Ind. Electron. Society*, Taipei, 2007, pp. 163-168.

[51]   S. Talebi, B. Nikbakhtian, and H. A. Toliyat, "Analytical model-based analysis of high-speed flywheel energy storage systems for pulsed power applications," in *2009 IEEE Electric Ship Technologies Symposium*, Baltimore, MD, 2009, pp. 65-72.

[52]   C. Zhang, K. J. Tseng, T. D. Nguyen, and S. Zhang, "Design and loss analysis of a high speed flywheel energy storage system based on axial-flux flywheel-rotor electric machines," in *2010 Conf. Proc. IPEC*, Singapore, 2010, pp. 886-891.

[53]   F. Deiana, A. Serpi, I. Marongiu, G. Gatto, and J. Abrahamsson, "Efficiency assessment of permanent magnet synchronous machines for high-speed flywheel energy storage systems," in *IECON 2016 - 42nd Annual Conf. of the IEEE Ind. Electron. Society*, Florence, 2016, pp. 4269-4274.

[54]   R. Okou, G. Mwaba, M. A. Khan, P. Barendse, and P. Pillay, "High speed electromechanical flywheel design for rural electrification in Sub Saharan Africa," in *2009 IEEE Int. Electric Machines and Drives Conf.*, Miami, FL, 2009, pp. 392-398.

[55]   P. Upadhyay and N. Mohan, "Design and FE analysis of surface mounted permanent magnet motor/generator for high-speed modular flywheel energy storage systems," in *2009 IEEE Energy Conversion Congress and Exposition*, San Jose, CA, 2009, pp. 3630-3633.

[56]   K. Itani, A. De Bernardinis, Z. Khatir, and A. Jammal, "Energy management of a battery-flywheel storage system used for regenerative braking recuperation of an Electric Vehicle," in *IECON 2016 - 42nd Annual Conf. of the IEEE Ind. Electron. Society*, Florence, 2016, pp. 2034-2039.

[57]   E. Muljadi and V. Gevorgian, "Flywheel energy storage - dynamic modeling," in *2017 Ninth Annual IEEE Green Technologies Conf (GreenTech)*, Denver, CO, 2017, pp. 312-319.

[58]   W. Gengji and W. Ping, "Rotor loss analysis of PMSM in flywheel energy storage system as uninterruptable power supply," *IEEE Trans. Appl. Supercond.*, vol. 26, no. 7, pp. 1-5, Oct. 2016,

[59]   M. A. Sokolov *et al.*, "Analytical method for design and thermal evaluation of a long-term flywheel energy storage system," in *2016 Int. Symposium on Power Electronics, Electrical Drives, Automation and Motion (SPEEDAM)*, Anacapri, 2016, pp. 270-275.

[60]   C. Chapelsky, J. Salmon, and A. Knight, "Control of a high-inertia flywheel as part of a high capacity energy storage system," in *2007 Canadian Conf. on Electrical and Computer Engineering*, Vancouver, BC, 2007, pp. 1437-1440.

[61]   M. Strasik *et al.*, "Design, fabrication, and test of a 5-kWh/100-kW flywheel energy storage utilizing a high-temperature superconducting bearing," *IEEE Trans. Appl. Supercond.*, vol. 17, no. 2, pp. 2133-2137, Jun. 2007.

[62]   X. Zhang and J. Yang, "A DC-link voltage fast control strategy for high-speed PMSM/G in flywheel energy storage system," in *2017 IEEE Int. Electric Machines and Drives Conf. (IEMDC)*, Miami, FL, 2017, pp. 1-7.

[63]   X. Zhang and J. Yang, "An improved discharge control strategy with load current and rotor speed compensation for high-speed flywheel energy storage system," in *2014 17th Int. Conf. on Electrical Machines and Systems (ICEMS)*, Hangzhou, 2014, pp. 318-324.

[64]   J. Li *et al.*, "Influence of load on discharge performance of high-speed flywheel energy storage system," in *2017 20th Int. Conf. on Electrical Machines and Systems (ICEMS)*, Sydney, NSW, 2017, pp. 1-5.

[65]   D. R. Kelsall, "Pulsed power provision by high speed composite flywheel," in *IEE Symposium on Pulsed Power 2000 (Digest No. 2000/053)*, London, UK, 2000, pp. 16/1-16/5.

[66]   A. S. Nagorny, N. V. Dravid, R. H. Jansen, and B. H. Kenny, "Design aspects of a high speed permanent magnet synchronous motor / generator for flywheel applications," in *2005 IEEE Int. Conf. on Electric Machines and Drives*, San Antonio, TX, 2005, pp. 635-641.

[67]   B. Kou, H. Cao, D. Zhang, W. Li, and X. Zhang, "Structural optimization of high speed permanent magnet synchronous motor for flywheel energy storage," in *2012 16th Int. Symposium on Electromagnetic Launch Technology*, Beijing, 2012, pp. 1-7.

[68]   W. Gengji, Q. Qinglei, W. Ping, and W. Xiaoyuan, "Analysis of the rotor loss in a high speed permanent magnet motor for flywheel energy storage system," in *2015 18th Int. Conf. on Electrical Machines and Systems (ICEMS)*, Pattaya, 2015, pp. 2040-2044.

[69]   Z. Q. Zhu and D. Howe, "Halbach permanent magnet machines and applications: a review," in *IEE Proc. - Electric Power Applications*, vol. 148, no. 4, pp. 299-308, July 2001.

[70]   Y. Yali, W. Yuanxi, and S. Feng, "The latest development of the motor/generator for the flywheel energy storage system," in *2011 Int. Conf. on Mechatronic Science, Electric Engineering and Computer (MEC)*, Jilin, 2011, pp. 1228-1232.

[71]   X. Zhang and J. Yang, "A robust flywheel energy storage system discharge strategy for wide speed range operation," *IEEE Trans. Ind. Electron.*, vol. 64, no. 10, pp. 7862-7873, Oct. 2017.

[72]   P. Yulong, L. Xing, L. Yi, and C. Feng, "Effect of air gap eccentricity on rotor eddy current loss in high speed PMSM used in FESS," in *2014 17th Int. Symposium on Electromagnetic Launch Technology*, La Jolla, CA, 2014, pp. 1-6.

[73]   M. Jiang, J. Salmon, and A. M. Knight, "Design of a permanent magnet synchronous machine for a flywheel energy storage system within a hybrid electric vehicle," in *2009 IEEE Int. Electric Machines and Drives Conf.*, Miami, FL, 2009, pp. 1736-1742.

[74]   T. D. Nguyen, K. J. Tseng, S. Zhang, and C. Zhang, "A flywheel cell for energy storage system," in *2008 IEEE Int. Conf. on Sustainable Energy Technologies*, Singapore, 2008, pp. 214-219.

[75]   Perry Tsao, M. Senesky, and S. R. Sanders, "An integrated flywheel energy storage system with homopolar inductor motor/generator and high-frequency drive," *IEEE Trans. Ind. Appl.*, vol. 39, no. 6, pp. 1710-1725, Nov.-Dec. 2003.

[76]   R. F. Thelen, A. Gattozzi, D. Wardell, and A. Williams, "A 2-MW motor and ARCP drive for high-speed flywheel," in *APEC 07 - Twenty-Second Annual IEEE Applied Power Electronics Conf. and Exposition*, Anaheim, CA, USA, 2007, pp. 1690-1694.

[77]   L. Piroddi, A. Leva, and F. Casaro, "Vibration control of a turbomolecular vacuum pump using piezoelectric actuators," in *Proc. of the 45th IEEE Conf. on Decision and Control*, San Diego, CA, 2006, pp. 6555-6560.

[78]   A. Boglietti, R. I. Bojoi, A. Cavagnino, P. Guglielmi, and A. Miotto, "Analysis and modeling of rotor slot enclosure effects in high-speed induction motors," *IEEE Trans. on Ind. Appl.*, vol. 48, no. 4, pp. 1279-1287, Jul.-Aug. 2012.

[79]   Weiss Spindle Motors, [Online]. Source: https://www.weissgmbh.com/fileadmin/user_upload/downloads/prospekte/en/Spindelloesungen_en.pdf, Retrieved on 23th of September 2019.

[80] R. Abebe, M. Di Nardo, D. Gerada, G. L. Calzo, L. Papini, and C. Gerada, "High speed drives review: machines, converters and applications," in *IECON 2016 - 42nd Annual Conf. of the IEEE Ind. Electron. Society*, Florence, 2016, pp. 1675-1679.

[81] C. Zwyssig, M. Duerr, D. Hassler, and J. W. Kolar, "An ultra-high-speed, 500000 rpm, 1 kW electrical drive system," in *2007 Power Convers. Conf. - Nagoya*, Nagoya, 2007, pp. 1577-1583.

[82] T. Noguchi, Y. Takata, Y. Yamashita, Y. Komatsu, and S. Ibaraki, "220,000-r/min, 2-kW PM motor drive for turbocharger," *Electrical Engineering in Japan*, Vol. 161, No. 3, pp. 854–861, 2007.

[83] P. D. Pfister and Y. Perriard, "Very-high-speed slotless permanent-magnet motors: analytical modeling, optimization, design, and torque measurement methods," *IEEE Trans. Ind. Electron.*, vol. 57, no. 1, pp. 296-303, Jan. 2010.

[84] T. Abe, T. Higuchi, K. Shigematsu, and J. Oyama, "The system simulation for small size and ultra-high speed motor drive system using coupled analysis," in *2007 European Conf. on Power Electron. and Appl.*, Aalborg, 2007, pp. 1-8.

[85] T. Noguchi and T. Wada, "1.5-kW, 150,000-r/min ultra high-speed PM motor fed by 12-V power supply for automotive supercharger," in *2009 European Conf. on Power Electron. and Appl.*, Barcelona, 2009, pp. 1-10.

[86] T. Schneider and A. Binder, "Design and evaluation of a 60 000 rpm permanent magnet bearingless high speed motor," in *2007 7th Int. Conf. on Power Electron. and Drive Systems*, Bangkok, 2007, pp. 1-8.

[87] S. Jumayev, M. Merdzan, K. O. Boynov, J. J. H. Paulides, J. Pyrhönen, and E. A. Lomonova, "The effect of PWM on rotor eddy-current losses in high-speed permanent magnet machines," *IEEE Trans. Magn.*, vol. 51, no. 11, pp. 1-4, Nov. 2015.

[88] A. Tüysüz, M. Steichen, C. Zwyssig, and J. W. Kolar, "Advanced cooling concepts for ultra-high-speed machines," in *2015 9th Int. Conf. on Power Electron. and ECCE Asia (ICPE-ECCE Asia)*, Seoul, 2015, pp. 2194-2202.

[89] J. H. Ahn, J. Y. Choi, C. H. Park, C. Han, C. W. Kim, and T. G. Yoon, "Correlation between rotor vibration and mechanical stress in ultra-high-speed permanent magnet synchronous motors," *IEEE Trans. Magn.*, vol. 53, no. 11, pp. 1-6, Nov. 2017.

[90] C. Zwyssig, S. D. Round, and J. W. Kolar, "An ultra-high-speed, low power electrical drive system," *IEEE Trans. Ind. Electron.*, vol. 55, no. 2, pp. 577-585, Feb. 2008.

[91] L. Zhao *et al.*, "A highly efficient 200 000 rpm permanent magnet motor system," *IEEE Trans. Magn.*, vol. 43, no. 6, pp. 2528-2530, June 2007.

[92]   A. Binder, "Elektrische Hochdrehzahlantriebe-Auslegungsgrundlagen und Bei-spiele aus der Praxis," [Online]. Source: https://www.ew.tu-darmstadt.de/me-dia/ew/vortrge/High_speed_KIT_2018_3.pdf, Retrieved on 15th of September 2019.

[93]   A. Binder, T. Schneider, and M. Klohr, "Fixation of buried and surface-mounted magnets in high-speed permanent-magnet synchronous machines," *IEEE Trans. Ind. Appl.*, vol. 42, no. 4, pp. 1031-1037, Jul.-Aug. 2006.

[94]   T. Abe, T. Higuchi, K. Shigematsu, and J. Oyama, "The system simulation for small size and ultra-high speed motor drive system using coupled analysis," in *2007 European Conf. on Power Electron. and Appl.*, Aalborg, 2007, pp. 1-8.

[95]   J. Kim, I. Jeong, K. Nam, J. Yang, and T. Hwang, "Sensorless control of PMSM in a high-speed region considering iron loss," *IEEE Trans. Ind. Electron.*, vol. 62, no. 10, pp. 6151-6159, Oct. 2015.

[96]   F. R. Ismagilov, N. Uzhegov, V. E. Vavilov, V. I. Bekuzin, and V. V. Ayguzina, "Multidisciplinary design of ultra-high-speed electrical machines," *IEEE Trans. Energy Convers.*, vol. 33, no. 3, pp. 1203-1212, Sep. 2018.

[97]   K. Kim, H. Park, S. Jang, D. You, and J. Choi, "Comparative study of electromagnetic performance of high-speed synchronous motors with rare-earth and ferrite permanent magnets," *IEEE Trans. Magn.*, vol. 52, no. 7, pp. 1-4, Jul. 2016.

[98]   S. Xu, X. Liu, and Y. Le, "Electromagnetic design of a high-speed solid cylindrical permanent-magnet motor equipped with active magnetic bearings," *IEEE Trans. Magn.*, vol. 53, no. 8, pp. 1-15, Aug. 2017.

[99]   Z. Zhang, Z. Deng, Q. Sun, C. Peng, Y. Gu, and G. Pang, "Analytical modeling and experimental validation of rotor harmonic eddy-current loss in high-speed surface-mounted permanent magnet motors," *IEEE Trans. Magn.*, doi: 10.1109/TMAG.2018.2882514.

[100] K. Wang, M. A. Rahman, and J. X. Shen, "Control of high-speed sensorless PM brushless DC motors," in *2010 IEEE Ind. Appl. Society Annual Meeting*, Houston, TX, 2010, pp. 1-7.

[101] G. Munteanu, A. Binder, T. Schneider, and B. Funieru, "No-load tests of a 40 kW high-speed bearingless permanent magnet synchronous motor," in *2010 Int. Symposium on Power Electronics, electrical Drives, Automation and Motion*, Pisa, 2010, pp. 1460-1465.

[102] Y. Fu, M. Takemoto, S. Ogasawra, and K. Orikawa, "Investigation of efficiency enhancement of an ultra-high-speed bearingless motor at 100,000 r/min by high

switching frequency using SiC-MOSFET," in *2018 IEEE Energy Conversion Congress and Exposition (ECCE)*, Portland, OR, 2018, pp. 2306-2313.

[103] S. Kim, Y. Kim, G. Lee, and J. Hong, "A novel rotor configuration and experimental verification of interior PM synchronous motor for high-speed applications," *IEEE Trans. Magn.*, vol. 48, no. 2, pp. 843-846, Feb. 2012.

[104] Y. Honda, S. Yokote, T. Higaki, and Y. Takeda, "Using the halbach magnet array to develop an ultrahigh-speed spindle motor for machine tools," in *IAS '97. Conf. Record of the 1997 IEEE Ind. Appl. Conf. Thirty-Second IAS Annual Meeting*, New Orleans, LA, USA, 1997, pp. 56-60 vol.1.

[105] L. A. Johnson, "Utilization of amorphous metals in electric motors," prepared by General electric company Corporate research and development for OAK ridge national laboratory Power systems technology program Energy division, March 1984.

[106] T. R. Haller, M. G. Jones, G. B. Kliman, and R. E. Tompkins, "Cutting amorphous metal by crystallization with a laser or electron beam," U. S. Patent, 4 328 411 A, May 4, 1982.

[107] N. Ertugrul, R. Hasegawa, W. L. Soong, J. Gayler, S. Kloeden, and S. Kahourzade, "A novel tapered rotating electrical machine topology utilizing cut amorphous magnetic material," *IEEE Trans. Magn.*, vol. 51, no. 7, pp. 1-6, Jul. 2015.

[108] N. J. DeCristofaro, D. A. Ngo, R. L. Bye, Jr., P. J. Stamatis, and G. E. Fish, "Amorphous metal stator for radial-flux electric motor," U. S. Patent, 6 960 860 B1, Nov. 1, 2005.

[109] C. C. Jensen, F. Profumo, and T. A. Lipo, "A low-loss permanent-magnet brushless DC motor utilizing tape wound amorphous iron," *IEEE Trans. Ind. Appl.*, vol. 28, no. 3, pp. 646-651, May/Jun 1992.

[110] R. A. Caamaño, "Electric motor or generator," U. S. Patent, 5 731 649, Mar. 24, 1998.

[111] Z. Wang *et al.*, "Development of a permanent magnet motor utilizing amorphous wound cores," *IEEE Trans. Magn.*, vol. 46, no. 2, pp. 570-573, Feb. 2010.

[112] Z. Wang *et al.*, "Development of an axial gap motor with amorphous metal cores," *IEEE Trans. Ind. Appl.*, vol. 47, no. 3, pp. 1293-1299, May-June 2011.

[113] H. Tokoi *et al.*, "Highly efficient industrial 11kW permanent magnet synchronous motor without rare-earth metals," in *Proc. of the 8th Int. Conf. EEMODS'2013 Energy Efficiency in Motor Driven Systems*, 2013, pp. 117-128.

[114] B. L. Damsky and J. Stein, "Magnetic annealing of amorphous alloy for motor stators," U. S. Patent, 5 671 524, Sep. 30, 1997.

[115] H. H. Liebermann, P. G. Frischmann, and G. M. Rosenberry, "Patterned helical metallic ribbon for continuous edge winding applications," U. S. Patent, 4 380 572, Apr. 19, 1983.

[116] A. Chiba *et al*., "Test results of an SRM made from a layered block of heat-treated amorphous alloys," *IEEE Trans. Ind. Appl.*, vol. 44, no. 3, pp. 699-706, May-Jun. 2008.

[117] Y. Enomoto *et al*., "Evaluation of experimental permanent-magnet brushless motor utilizing new magnetic material for stator core teeth," *IEEE Trans. Magn.*, vol. 41, no. 11, pp. 4304-4308, Nov. 2005.

[118] H. Hayashi, K. Nakamura, A. Chiba, T. Fukao, K. Tungpimolrut, and D. G. Dorrell, "Efficiency improvements of switched reluctance motors with high-quality iron steel and enhanced conductor slot fill," *IEEE Trans. Energy Convers.*, vol. 24, no. 4, pp. 819-825, Dec. 2009.

[119] T. Fukao, A. Chiba, and M. Matsui, "Test results on a super-high-speed amorphous-iron reluctance motor," *IEEE Trans. Ind. Appl.*, vol. 25, no. 1, pp. 119-125, Jan./Feb. 1989.

[120] R. Kolano *et al*., "Amorphous soft magnetic core for the stator of the high-speed PMBLDC motor with half-open slots," *IEEE Trans. Magn.*, vol. 52, no. 6, pp. 1-5, Jun. 2016.

[121] S. Okamoto, N. Denis, Y. Kato, M. Ieki, and K. Fujisaki, "Core loss reduction of an interior permanent-magnet synchronous motor using amorphous stator core," *IEEE Trans. Ind. Appl.*, vol. 52, no. 3, pp. 2261-2268, May-June 2016.

[122] T. Fan, Q. Li, and X. Wen, "Development of a high power density motor made of amorphous alloy cores," *IEEE Trans. Ind. Electron.*, vol. 61, no. 9, pp. 4510-4518, Sep. 2014.

[123] C. Zhang, W. Tong, X. Ma, R. Tang, and J. Zhu, "Development of a high-speed permanent magnet machine using amorphous alloy cores," in *2016 IEEE Vehicle Power and Propulsion Conf. (VPPC)*, Hangzhou, 2016, pp. 1-5.

[124] D. K. Hong, D. Joo, B. C. Woo, Y. H. Jeong, and D. H. Koo, "Investigations on a super high speed motor-generator for microturbine applications using amorphous core," *IEEE Trans. Magn.*, vol. 49, no. 7, pp. 4072-4075, Jul. 2013.

[125] M. Dems and K. Komeza, "Performance characteristics of a high-speed energy-saving induction motor with an amorphous stator core," IEEE Trans. Ind. Electron., vol. 61, no. 6, pp. 3046-3055, Jun. 2014.

[126] M. Veigel, P. Winzer, J. Richter, and M. Doppel-bauer, "New FPGA-based and inline-capable measuring method for the identification of magnetic losses in electrical steel," in *2015 5th Int. Electric Drives Production Conf. (EDPC)*, Nuremberg, 2015, pp. 1-6.

[127] B. Zhang, "Soft magnetic composites in novel designs of electrical traction machines," Ph.D. dissertation, Dept. Elektrotechnik und Informationstechnik, Karlsruher Institut für Technologie, Karlsruhe, Germany, 2016.

[128] Frequently asked questions, [Online]. Source: https://metglas.com/frequently-asked-questions/, Retrieved on 15th of September 2019.

[129] N. Bagrets, W. Goldacker, S. I. Schlachter, C. Barth, and K. P. Weiss, "Thermal properties of 2G coated conductor cable materials," *Cryogenics*, vol. 61; 2014. pp. 8–14.

[130] Nyilas A. "Transducers for sub-micron displacement measurements atcryogenic temperatures," in *Conf. proc. 824 advances in cryogenic engineering: trans. of the int. cryogenic materials conf.-ICMC*, vol. 52; 2006. pp. 27–34

[131] Skin effect calculator, [Online]. Source: https://chemandy.com/calculators/skin-effect-calculator.htm, Retrieved on 15th of September 2019.

[132] Magnetic materials, [Online]. Source: https://metglas.com/magnetic-materials/, Retrieved on 15th of September 2019.

[133] Neorem magnets, [Online]. Source: http://neorem.fi/wp-content/uploads/2018/12/NdFeB_PhysicalProperties_of_NdFeB_material.pdf, Retrieved on 15th of September 2019.

[134] Arnold magnetic technologies, [Online]. Source: https://www.arnoldmagnetics.com/products/recoma-samarium-cobalt-magnets/, Retrieved on 15th of September 2019.

[135] Songke technic for magnet, [Online]. Source: http://www.songke.com/DE/product.aspx?jsid=4, Retrieved on 15th of September 2019.

[136] VAC VACUUMSCHMELZE permanent magnets, Source: https://vacuumschmelze.com/Products/Permanent-Magnets, Retrieved on 18th of September 2019.

[137] E. Swanson, C. D. Powell, and S. Weissman, "A practical review of rotating machinery critical speeds and modes," *Sound and Vibration*, pp. 10-17, May 2005.

[138] J. Saari, "Thermal analysis of high-speed induction machines," Ph.D. dissertation, Dept. Elect. Commun. Eng., Helsinki Univ. Technol., Espoo, Finland, 1998.

[139] Z. Huang, J. Fang, X. Liu, and B. Han, "Loss calculation and thermal analysis of rotors supported by active magnetic bearings for high-speed permanent-magnet electrical machines", *IEEE Trans. Ind. Electron.*, vol. 63, no. 4, pp. 2027-2035, Apr. 2016.

[140] A. Kahveci, P. Szary, F. Herget, A. K. Putri, and K. Hameyer, "Methods for hysteresis losses determinations at non-standard ring core geometries equivalent to Epstein measurements", in *2016 6th Int. Electric Drives Production Conf. (EDPC)*, Nuremberg, 2016, pp. 135-142.

[141] J. C. Dixon, "The shock absorber handbook", second edition, Chichester, England, John Wiley & Sons, Ltd, 2007, Appendix B, pp. 376-377.

[142] D. A. Howey, P. R. N. Childs, and A. S. Holmes, "Air-gap convection in rotating electrical machines", *IEEE Trans. Ind. Electron.*, vol. 59, no. 3, pp. 1367-1375, Mar. 2012.

[143] M. Fénot, Y. Bertin, E. Dorignac, and G. Lalizel, "A review of heat transfer between concentric rotating cylinders with or without axial flow", *Int. Journal of Thermal Sciences*, vol. 50, no. 7, pp. 1138-1155, Jul. 2011.

[144] S. R. Mgardiner and R. H. Sabersky, "Heat transfer in an annular gap", *Int. Journal of Heat and Mass Transfer*, vol. 21, no. 12, pp. 1459-1466, Dec. 1978.

[145] Z. Kolondzovski, "Thermal and mechanical analysis of high-speed permanent-magnet electrical machines," Ph.D. dissertation, Dept. Elect. Eng., Aalto Univ., Helsinki, Finland, 2010.

[146] M. S. Rylko, K. J. Hartnett, J. G. Hayes, and M. G. Egan, "Magnetic material selection for high power high frequency inductors in DC-DC converters," in *2009 Twenty-Fourth Annual IEEE Applied Power Electronics Conf. and Exposition*, Washington, DC, 2009, pp. 2043-2049.

[147] B. Funieru and A. Binder, "Thermal design of a permanent magnet motor used for gearless railway traction," in *2008 34th Annual Conf. of IEEE Ind. Electron.*, Orlando, FL, 2008, pp. 2061-2066.

[148] Y. Zhang, I. Belov, M. Bakowski, J. K. Lim, P. Leisner, and H. P. Nee, "Investigation of a finned baseplate material and thickness variation for thermal performance of a SiC power module," in *2014 15th Int. Conf. on Thermal, Mechanical and Mulit-Physics Simulation and Experiments in Microelectronics and Microsystems (EuroSimE)*, Ghent, 2014, pp. 1-8.

[149] S. Li, X. Yu, H. Bao, and N. Yang, "High thermal conductivity of bulk epoxy resin by bottom-up parallel-linking and strain: a molecular dynamics study," *The Journal of Physical Chemistry C*, DOI: 10.1021/acs.jpcc.8b02001

[150] CarbonForce, [Online]. Source: https://www.carbonforce.de/produkte/carbon-glasfaserrohre/cfk-rohre/rund/, Retrieved on 15th of September 2019.

[151] K. Narita, T. Yamada, Y. Sakashita, and K. Akatsu, "Iron loss calculation of PM motor by coupling analysis between magnetic field simulator and control simulator," in 2008 Int. Conf. on Electrical Machines and Systems, Wuhan, 2008, pp. 3301-3306.

[152] M. Mirzaei, A. Binder, B. Funieru, and M. Susic, "Analytical calculations of induced eddy currents losses in the magnets of surface mounted PM machines with consideration of circumferential and axial segmentation effects," *IEEE Trans. Magn.*, vol. 48, no. 12, pp. 4831-4841, Dec. 2012.

[153] X. Ding and C. Mi, "Modeling of eddy current loss in the magnets of permanent magnet machines for hybrid and electric vehicle traction applications," in *2009 IEEE Vehicle Power and Propulsion Conf.*, Dearborn, MI, 2009, pp. 419-424.

[154] R. Liu, C. C. Mi, and D. W. Gao, "Modeling of eddy-current loss of electrical machines and transformers operated by pulsewidth-modulated inverters," *IEEE Trans. Magn.*, vol. 44, no. 8, pp. 2021-2028, Aug. 2008.

[155] M. Markovic and Y. Perriard, "A simplified determination of the permanent magnet (PM) eddy current losses due to slotting in a PM rotating motor," in *2008 Int. Conf. on Electrical Machines and Systems*, Wuhan, 2008, pp. 309-313.

[156] A. A. Qazalbash, S. M. Sharkh, N. T. Irenji, R. G. Wills, and M. A. Abusara, "Calculation of no-load rotor eddy-current power loss in PM synchronous machines," *IEEE Trans. Magn.*, vol. 50, no. 9, pp. 1-8, Sep. 2014.

[157] Z. Q. Zhu, K. Ng, N. Schofield, and D. Howe, "Improved analytical modelling of rotor eddy current loss in brushless machines equipped with surface-mounted permanent magnets," in *IEE Proc. - Electric Power Appl.*, vol. 151, no. 6, pp. 641-650, 7 Nov. 2004.

[158] J. D. Ede, K. Atallah, G. W. Jewell, J. B. Wang, and D. Howe, "Effect of axial segmentation of permanent magnets on rotor loss in modular permanent-magnet brushless machines," *IEEE Trans. Ind. Appl.*, vol. 43, no. 5, pp. 1207-1213, Sep.-oct. 2007.

[159] D. Ishak, Z. Q. Zhu, and D. Howe, "Eddy-current loss in the rotor magnets of permanent-magnet brushless machines having a fractional number of slots per pole," *IEEE Trans. Magn.*, vol. 41, no. 9, pp. 2462-2469, Sep. 2005.

[160] X. Liu, H. Hu, J. Zhao, A. Belahcen, and L. Tang, "Armature reaction field and inductance calculation of ironless BLDC motor," *IEEE Trans. Magn.*, vol. 52, no. 2, pp. 1-14, Feb. 2016.

[161] F. Dubas and A. Rahideh, "Two-dimensional analytical permanent-magnet eddy-current loss calculations in slotless PMSM equipped with surface-inset magnets," *IEEE Trans. Magn.*, vol. 50, no. 3, pp. 54-73, Mar. 2014.

[162] M. Markovic and Y. Perriard, "Analytical solution for rotor eddy-current losses in a slotless permanent-magnet motor: the case of current sheet excitation," *IEEE Trans. Magn.*, vol. 44, no. 3, pp. 386-393, Mar. 2008.

[163] S. S. Nair, J. Wang, R. Chin, L. Chen, and T. Sun, "Analytical prediction of 3-D magnet eddy current losses in surface mounted PM machines accounting slotting effect," *IEEE Trans. Energy Convers.*, vol. 32, no. 2, pp. 414-423, Jun. 2017.

[164] S. Jumayev, M. Merdzan, K. O. Boynov, J. J. H. Paulides, J. Pyrhönen, and E. A. Lomonova, "The effect of PWM on rotor eddy-current losses in high-speed permanent magnet machines," *IEEE Trans. Magn.*, vol. 51, no. 11, pp. 1-4, Nov. 2015.

[165] Z. Q. Zhu, K. Ng, N. Schofield, and D. Howe, "Analytical prediction of rotor eddy current loss in brushless machines equipped with surface-mounted permanent magnets. I. Magnetostatic field model," in *ICEMS 2001. Proc. of the Fifth Int. Conf. on Electrical Machines and Systems*, vol.2, pp. 806-809, Shenyang, 2001.

[166] M. Kawabe, T. Nomiyama, A. Shiozaki, H. Kaihara, N. Takahashi, and M. Nakano, "Behavior of Minor Loop and Iron Loss Under Constant Voltage Type PWM Inverter Excitation," *IEEE Trans.Magn.*, vol. 48, no. 11, pp. 3458-3461, Nov. 2012.

[167] International standard ISO 1940-1, [Online].Source: https://www.dcma.mil/Portals/31/Documents/NPP/Forms/ISO_1940-1.pdf, Retrieved on 20th of September 2019.